

Manabu Kiguchi *Editor*

---

# Single- Molecule Electronics

An Introduction to Synthesis,  
Measurement and Theory

 Springer

# Single-Molecule Electronics



Manabu Kiguchi

Editor

# Single-Molecule Electronics

An Introduction to Synthesis,  
Measurement and Theory

 Springer

*Editor*

Manabu Kiguchi  
Department of Chemistry  
Graduate School of Science  
and Engineering  
Tokyo Institute of Technology  
Tokyo  
Japan

ISBN 978-981-10-0723-1      ISBN 978-981-10-0724-8 (eBook)  
DOI 10.1007/978-981-10-0724-8

Library of Congress Control Number: 2016939969

© Springer Science+Business Media Singapore 2016

This work is subject to copyright. All rights are reserved by the Publisher, whether the whole or part of the material is concerned, specifically the rights of translation, reprinting, reuse of illustrations, recitation, broadcasting, reproduction on microfilms or in any other physical way, and transmission or information storage and retrieval, electronic adaptation, computer software, or by similar or dissimilar methodology now known or hereafter developed.

The use of general descriptive names, registered names, trademarks, service marks, etc. in this publication does not imply, even in the absence of a specific statement, that such names are exempt from the relevant protective laws and regulations and therefore free for general use.

The publisher, the authors and the editors are safe to assume that the advice and information in this book are believed to be true and accurate at the date of publication. Neither the publisher nor the authors or the editors give a warranty, express or implied, with respect to the material contained herein or for any errors or omissions that may have been made.

Printed on acid-free paper

This Springer imprint is published by Springer Nature  
The registered company is Springer Science+Business Media Singapore Pte Ltd.

# Preface

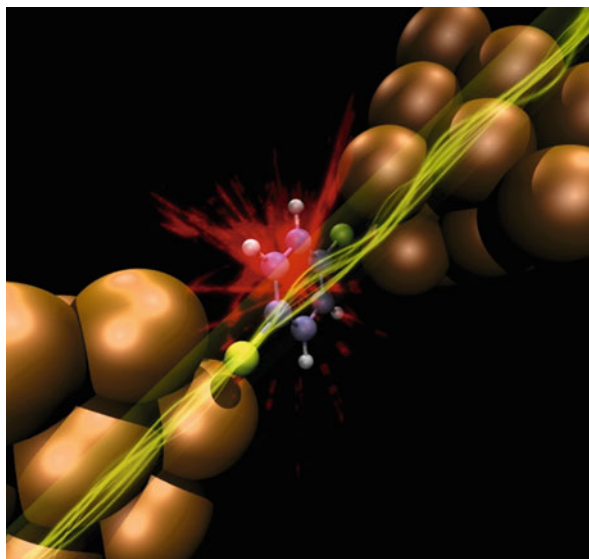
Governing individual molecules and their utilization is one of the scientific dreams of our age. The realization of this dream could open the door to a miniaturization revolution in electronics. Molecular electronics pursues the use of individual molecules as fundamental electronic components. The inherent properties of molecules such as nano-size, low cost, scalability, and self-assembly are seen by many as a perfect complement to conventional silicon electronics. In addition, molecules can be designed with the desired functionality and prepared using common elements such as carbon, nitrogen and oxygen, without the need for rare earth metals. Understanding and governing the charge-transfer phenomena occurring at the molecular level could revolutionize a number of related fields, including energy harvesting, data storage, batteries, sensing devices, and displays. For these reasons, molecule-based electronics has captured the attention of a broad cross section of the scientific community.

Molecular electronics is an interdisciplinary science that requires researchers from different backgrounds to work together. This cooperation includes the design of molecules with the desired functionality, the measurement of the electronic and structural properties of individual molecules, and the integration of molecules into operational devices. The feedback loop between molecular design, measurement, and ultimately device fabrication, is crucial for the development of the field.

The workhorse of molecular electronics is the molecular junction, where a single or few molecules are suspended across the gap between two metal electrodes (Fig. 1). The interaction between molecule and metal gives rise to novel functionality. A clear example of the importance of one metal–molecule interface is heterogeneous catalysis. Molecular junctions, featuring two metal–molecule interfaces are exceptional systems where novel phenomena can take place. Hence, molecular junctions can be regarded as new materials that include the suspended molecule and both metal electrodes. The study of these systems can lead to the development of new scientific fields.

The broadness of the field, resulting from the vast amount of work done in recent years, makes it impossible to include every point of view in a single book. Here, we focus on the basic science from a chemistry point of view. This book contains

**Fig. 1** Single molecular junction



the contribution of specialists in the areas of design and synthesis, single-molecule measurements, and charge-transfer theory. In addition, Prof. Jan van Ruitenbeek, one of the molecular electronics pioneers, discusses the state of the art as well as the future development of functioning devices based on molecular electronics technology.

We would like to thank Springer for the opportunity to prepare this book, especially Dr. Shinichi Koizumi and Ms. Risa Takizawa. We would also like to express our deep gratitude to each of the authors who have contributed with their time and outstanding knowledge to make this book possible. Also, thanks to Dr. Santiago Marqués-González for the helpful discussions during the preparation of the book. Finally, we hope that the readers of this book will find it both useful and delightful.

Tokyo, Japan  
January 2016

Manabu Kiguchi

# Contents

<b>1</b>	<b>Molecular Electronics: A Brief Overview of the Status of the Field ...</b>	<b>1</b>
	Jan M. van Ruitenbeek	
<b>2</b>	<b>Methods to Determine Electrical Conductance of Single-Molecule Junctions .....</b>	<b>25</b>
	Ryo Yamada	
<b>3</b>	<b>Characterization of the Single Molecular Junction .....</b>	<b>61</b>
	Manabu Kiguchi and Shintaro Fujii	
<b>4</b>	<b>Molecular Wires: An Overview of the Building Blocks of Molecular Electronics .....</b>	<b>87</b>
	Paul J. Low and Santiago Marqués-González	
<b>5</b>	<b>Insulated Oligothiophenes .....</b>	<b>117</b>
	Yutaka Ie	
<b>6</b>	<b>Synthesis and Physical Properties of Three-Dimensionally Insulated Molecular Wires .....</b>	<b>141</b>
	Jun Terao	
<b>7</b>	<b>Orbital Rule for Electron Transport of Molecular Junctions .....</b>	<b>165</b>
	Tomofumi Tada	
<b>8</b>	<b>Theoretical Aspects of Quantum Transport and Computational Modeling of Molecular Electronic Device .....</b>	<b>191</b>
	Hisao Nakamura	
<b>9</b>	<b>Single-Molecule Sequencing .....</b>	<b>217</b>
	Masateru Taniguchi	

# Chapter 1

## Molecular Electronics: A Brief Overview of the Status of the Field

Jan M. van Ruitenbeek

**Abstract** The developments in the field of molecular electronics have seen many successes and many setbacks, but the field continues to inspire scientists around the world, now more than ever. The interest is, certainly, for a large part in the fundamental issues: molecules as conducting elements bring together questions from various fields of study and lead to profound new questions. However, this interest alone would not suffice to explain the large efforts in research. Indeed, the prospects of developing electronics with better performance, higher density, and new functionality are what motivates most of the research. In this introductory chapter, I will attempt to take stock of the field, to evaluate what has been achieved, and to identify the interesting challenges that lie ahead.

**Keywords** Molecular electronics • Organic electronics • Applications of molecular electronics • Fundamental questions of molecular electronics

### 1.1 Definition of Molecular Electronics

Before we do so, we need to specify what we mean by the words molecular electronics. Polymers [1] and organic molecular compounds [2] have been studied widely for applications in electronics. Polymer and printable electronics are already commercially available, and organic compounds are found in many commercial organic light-emitting diode (OLED) displays. Plastic photovoltaic cells are in production and are continuously improving in performance. Organic layers can be spin coated or drop casted, where the organic matter in these structures is randomly packed in the form of thin films, usually in contact with a metallic electrode at the top and bottom of the layers. The thickness of these films is many times the molecular diameter, so that only a small fraction of the molecules is in contact with the electrodes.

---

J.M. van Ruitenbeek (✉)

Huygens-Kamerlingh Onnes Laboratory, Leiden University, Niels Bohrweg 2, 2333 CA Leiden, The Netherlands

e-mail: [ruitenbeek@physics.leidenuniv.nl](mailto:ruitenbeek@physics.leidenuniv.nl)

We will refer to this wide field of study and technology as *organic electronics*. The applications mentioned above illustrate the relevance of these developments, but there is a prospect for more advanced exploitation of the properties of molecular building blocks when we connect just a single molecule, or a self-assembled single layer of molecules, between metal electrodes. This adds serious technical challenges, but provides access to the full quantum mechanics of electron transport at the molecular scale, even at room temperature. This is expected to provide new opportunities, e.g., in terms of functionality and miniaturization of electronics, and opens up new areas of study of electron transport at the interface between chemistry and physics.

In order to specify this latter field of study, we will call this *molecular electronics*, or *single-molecule electronics*, which we consider as a subfield of organic electronics. Molecular electronics is concerned with devices which have each of the molecules connected to electrodes at both their ends. This can be either in a single-molecule configuration (for a comprehensive review, see [3]) or in large assemblies of molecules, i.e., self-assembled monolayers (SAMs) [4]. In such SAMs, each molecule is connected to both the top and bottom electrodes placed above and below the layer. In contrast to the many concrete applications already found in organic electronics, the subfield of molecular electronics is still in an earlier, exploratory phase. Although first niche applications are entering the market here, for its full potential to be developed, a lot of research is still needed, as I will argue below.

## 1.2 A Brief History

### 1.2.1 Molecular Monolayers: Langmuir-Blodgett Technique

As early as 1974, ideas were discussed of using organic molecules as electronic circuit elements. The theoretical ideas outlined in the seminal paper by Aviram and Ratner [5] could not be tested in experiments on individual molecules until much later, because the technology had not yet been developed. On the other hand, many steps had already been taken for studying the electrical transport properties of monolayers of molecules. Based on earlier work by Lord Rayleigh and by Agnes Pockels, Langmuir [6] and Blodgett [7, 8] had shown in the 1920s and 1930s that it is possible to form ordered monolayers of amphiphilic molecules at the liquid-air interface and that these layers can be homogeneously transferred to cover solid surfaces. By this Langmuir-Blodgett (LB) technique, Mann and Kuhn [9] first succeeded in reproducibly measuring the electrical resistance of a monolayer of a fatty acid on top of aluminum bottom contacts. The top contact was applied, either in the form of a liquid Hg electrode or it was formed by evaporation and deposition of metals such as Au, Pb, and Al.

Aviram and Ratner had considered a  $\sigma$  bridged donor-acceptor molecule, with TTF (tetrathiafulvalene) as the donor and TCNQ (7,7,8,8-tetracyano-p-quinone-

dimethane) as the acceptor. This combination has never been realized literally in this form but many donor- $\sigma$ -acceptor molecules have since been synthesized and tested for diode characteristics. The first experimental observations of rectification by an LB monolayer were reported in 1990, using hexadecylquinolinium tricyanoquinodimethanide as the active molecular layer between Mg and Pt electrodes [10] and even between Al electrodes on both sides [11]. The mechanism for the observed effects has remained under debate because the direction of rectification does not match that of the mechanism proposed by Aviram and Ratner.

One of the central concerns in the experiments has been the role of the metal contacts, notably the top contact. This remains also one of the challenges in more recent experiments, as will be discussed below. The problems are threefold. First, any defects in the LB film are likely to lead to the formation of a metallic short-circuit connection between the top and bottom electrodes. By careful preparation of the LB film and the metallic contacts, this problem can be controlled [12]. Second, once a defect-free device has been achieved, the atoms in the metallic leads have a tendency to migrate under the influence of the very strong electric fields. Indeed, the electric field for an LB film thickness of 2 nm at an applied bias of 2V is as high as  $10^9$  V/m. As a result, shorts develop after one or more current-voltage cycles. The problem arises for metals with a high room-temperature atom mobility at the surface such as gold, but also for Ti top contacts [13]. The third problem relates to the deposition of metals by evaporation: under-coordinated metal atoms landing from a hot source onto the top of the molecular layer are very reactive and likely to damage the molecular structure of the LB film. Although many experiments suggest that the results are independent of the method of applying a top contact, this is a critical issue that should be considered.

Concerning the latter problem, several solutions have been tested over the years. Metzger and his team have developed a system that allows cold deposition of metals from the vapor phase [14]. The trick they introduced was to have the hot source facing the reverse side of the sample, inside a chamber filled with an inert gas that serves to thermalize the metal vapor and to allow the metal to deposit by diffusion on the farside. The efficiency of this process is very low and this is perhaps the reason why it has not been widely employed. The use of liquid Hg electrodes, as already pioneered by Mann and Kuhn [9], was further developed into a versatile method by Rampi and Whitesides [15]. The latter group elaborated the Hg electrode into a mechanically adjustable microdrop and improved the technique by substituting Hg with a Ga-In eutectic (EGaIn) [16], which marries the advantages of the flow of a metal with the stability of a solid. Although Hg-drop and EGaIn electrodes are very well suited for testing of the molecular layer conductivity, it is not a proper solution for building microfabricated devices.

In order to circumvent the first two problems listed above, Akkerman et al. have introduced the use of conducting polymers (PEDOT:PSS) as top contacts [17]. The junctions show very high stability and reproducibility and a long shelf life. Another original approach was taken by McCreery and colleagues [18], using  $sp^2$  carbon as electrode material.

A first demonstration of a device structure presented by Collier et al. [19] attracted wide attention to the field. They used the LB technique to deposit a layer of rotoxanes, which were expected to switch between two conductance states upon applying a suitable bias voltage. The LB layer was deposited on top of microfabricated Al/Al<sub>2</sub>O<sub>3</sub> wires and covered by crossed wires in a second lithography step, by deposition of a Ti/Al layer. Although the device showed the expected switching behavior, follow-up experiments showed that similar switching effects can be obtained in devices containing LB monolayers of nonspecific molecules, including alkanes [20]. The mechanism of switching has been attributed to migration of metal atoms in the electrodes, highlighting one of the main problems mentioned above. The observed switching effect is interesting by itself for application purposes, but it is not a specific molecular device property that we want to discuss here.

### ***1.2.2 Molecular Monolayers: Self-Assembly***

A chemistry-based method for growing molecular monolayers introduced in the 1980s has become very popular in recent years. In their 1983 paper, Nuzzo and Allara [21] showed that sulfides adsorb onto Au surfaces from solution and form densely packed coverages. Through later work as reviewed, e.g., by Love et al. [22], the method of forming self-assembled monolayers (SAM) was extended to many different substrate materials and many different anchoring groups. Under proper conditions, many combinations of metal substrates, anchoring groups, and molecular structures allow the formation of regular two-dimensional lattice structures on metal surfaces. The molecules can be deposited from the gas phase as well as from solution and bind by proper choice of a functional head group that has specific affinity for the exposed surface. The functional head group is commonly referred to as the anchor group, and molecules can be synthesized to have anchor groups at both ends, such that binding to the top surface of the SAM is enabled. Specifically the combination of Au surfaces with thiol anchoring groups has been very popular due to the low chemical activity of the gold surface for most contaminants and the specificity of the thiol binding.

Some of the first electrical measurements on SAM were done for *n*-alkyltrichlorosilane molecules, which form a dense layer on oxidized Si substrates [23]. While electron transport appeared to be extremely low, which was suggested to be of use for improving insulation in silicon electronics, later experiments using metal substrates showed a more systematic dependence of conductance as a function of length of the molecules [24, 25]. We will return to this systematics below.

### 1.2.3 *Single Molecules*

The development of scanning tunneling microscopy (STM) by Rohrer and Binnig in 1981 [26] has largely shaped many areas of nanoscience. Looking back it seems a natural and logic step to study individual molecules by STM, but it still took about 15 years before the first experiments were performed by Joachim, Gimzewski, and coworkers [27]. They succeeded in imaging and contacting individual  $C_{60}$  molecules, employing an STM operating at room temperature under ultra-high vacuum (UHV).

The fullerene  $C_{60}$  is a rather unusual molecule, which does not have a specific functional group for anchoring to the metal electrodes. In order to broaden the spectrum towards a wider range of molecular wires, the formation of SAM was combined with STM [28–31] and conducting-tip atomic force microscopy (AFM) [32]. In the approaches by Bumm et al. [28] and by Leatherman et al. [32], a suitable substrate, usually Au(111), was covered by self-assembly with a dense layer of alkanethiolate. The length of the alkanethiolate is tuned to match the length of the molecule of interest, and the latter is inserted as isolated molecules, again by self-assembly, at defect positions in the alkane lattice. Since the alkanethiolates have a very low electronic conductance, the molecules of interest, usually conjugated molecular wire structures having delocalized  $\pi$ -electrons, are observed as points of high conductance in the STM images. Although the interface between the molecules and the metal substrate is well-defined and stable by the self-assembly process, the top contact is only made by tunneling over an ill-defined barrier distance. In order to remedy this problem, Cui et al. [33] introduced a second self-assembly step, where the top thiol group was allowed to bind with Au nanoparticles. The Au nanoparticles are clearly visible in the AFM images and can be contacted by the conducting tip of the AFM. Although this approach improves the measurements of the single-molecule characteristics, the contact between the AFM tip and the Au nanoparticles remains a source of variability.

The essential feature of STM and AFM is the capability to adjust the tip-sample distance to the size of a molecule. The molecules of interest have a size in the range from 0.5 to 10 nm, which is too small for standard lithographic techniques. Several other methods have been developed to solve the problem of creating nanogaps between two electrodes to match the size of the molecules, out of which the mechanically controllable break junction (MCBJ) technique and the electromigration break junction (EBJ) technique are the most popular. Since the gap size between the electrodes and the positioning of the molecule cannot be done top down, some form of self-assembly process is involved in all the techniques. The MCBJ technique was originally developed in my group for the study of metallic and superconducting atomic contacts [34, 35]. It was first applied by Reed et al. for the study of single-molecule transport, by measuring the conductance across a junction formed by breaking a gold wire in a solution of benzenedithiol [36]. The MCBJ technique was later refined by introducing microfabrication [37, 38], which made it more widely applicable.

The EBJ technique was invented by Park et al. and first applied for the study of electron transport across a single  $C_{60}$  molecule [39]. The technique makes use of the electromigration force, by which a large current density is capable of displacing the atoms of the current-carrying wire. Breaking a microfabricated wire by control of the current through the wire creates a small tunneling gap, and when molecules have been introduced to the surface of the wire, they are frequently found to bridge this gap. A more elaborate discussion of single-molecule techniques will be presented in Chap. 2.

Although the 1997 work by Reed et al. [36] is regarded as the first single-molecule conductance experiment, in the strict sense of having a single molecule that is chemically bonded between two metallic leads, for several years, it remained difficult to demonstrate unambiguously that the observed signals are associated with a single molecule of the type targeted in the experiment. In 2002, within a year's time, several papers appeared that clarified this problem using all three major single-molecule techniques and opened new avenues for research. Employing the EBJ technique, Park et al. [40] and Liang et al. [41] independently published data on a metal-organic complex between metallic leads, where the doped Si substrate serves as a gate electrode. By control of the gate potential, it was possible to control the charge state of the molecule, and a conductance peak appeared at the crossing point between charge states. In experiments employing the MCBJ technique, Smit et al. [42] studied the simple model system of a single  $H_2$  molecule bound between Pt electrodes. The simple structure and low mass of the  $H_2$  allowed identifying its presence uniquely by vibration mode signals in the differential conductance and by isotope shifts of these signals. Although the hydrogen molecule will not be useful for electronics applications, the experiment provides a model system for which the junction can be characterized in great detail.

Finally, employing an STM setup at ambient conditions in a solution of bipyridine molecules, Xu and Tao demonstrated a method for statistically identifying the conductance of a single molecule [43]. The procedure relies on making and breaking cycles of contact between a Au tip and a Au sample immersed in a solution of the molecules. During the breaking process, a single molecule frequently bridges the gap between the metal electrodes, which is identified as a peak in histograms of conductance values.

### ***1.2.4 Present Status of the Field***

The three experimental techniques described in the last paragraph have been at the basis of most of the experiments that followed. The repeated breaking of atomic contacts by STM in the presence of molecules allowed Venkataraman et al. [44] to demonstrate a beautiful systematic exponential decrease of the electronic conductance of alkanediamines. The conductance decreases as  $\exp(-\beta N)$ , where  $N$  is the number of carbons in the molecular chain and the factor  $\beta$  was determined as  $\beta = 0.91 \pm 0.03$ . Many similar experiments have confirmed this exponential

dependence with length, at least up to  $N = 12$  [45]. There is wide consensus that the factor  $\beta$  for alkanes lies close to 1, which also agrees with results from DFT-based theoretical analysis [46]. For conjugated molecular chain structures,  $\beta$  is significantly smaller [47].

The same experimental technique was also successfully employed for demonstrating other systematics. In a series of molecules synthesized such that the angle  $\phi$  between the planes of two adjacent phenyl rings could be varied, controlled by chemical substitutions, it was shown that the conductance increases as  $\cos^2(\phi)$  and that this agrees with the results from model calculations [48, 49].

Once the methods were developed to introduce molecules with specific anchor groups at both ends into the gap between the electrodes in an MCBJ setup [50], this opened the way for detailed experiments and investigation of molecule-specific properties. Among many other works, it led to the discovery of single-molecule conductance switching under the influence of light by Dulić et al. [51]. The combination of optics and molecular junctions was further exploited by detecting the Raman signal associated with the molecule in a junction for which the conductance was measured simultaneously, either in an EBJ setup [52] or an MCBJ device [53].

The later experiments provide examples of the many new tools that have been developed for characterizing the molecular junctions and investigating their properties. Indeed, it was soon realized that the main limitation of most MCBJ, STM, or EBJ experiments is that the information obtained is limited to values of conductance only, which leaves a lot of ambiguity in interpretation. Additional properties that have been explored, illustrated in Fig. 1.1, include vibration mode spectroscopy [42, 54–56], shot noise [57], mechanical force spectroscopy [59], thermopower [60], electrostatic gating [61, 62], redox chemistry at the single-molecule level monitored by conductance [63, 64], and local thermometry [65].

While most of the STM experiments are performed under ambient conditions or in solution, recent work shows a promising development of more sophisticated STM experiments under UHV conditions at helium temperatures [66–69]. These techniques will be described in more detail in Chap. 2.

All this work starts with the design and synthesis of the appropriate molecular compounds, which has advanced very rapidly as will be presented in Chaps. 4, 5, and 6. Theory has progressed at equal pace, where concepts and techniques from Landauer theory and mesoscopic physics were married with those from theoretical chemistry [70–74]. Many predictions have been made of interesting new phenomena that are uniquely uncovered by single-molecule junctions, including the prediction [75] and observation [76] of Franck–Condon blockade, large negative differential conductance [77], and the prediction [78, 79] and observation [80, 81] of quantum interference between molecular orbitals. A more extensive discussion of theoretical progress is given in Chaps. 7 and 8.

Summarizing, as a field of science, molecular electronics is starting to mature. Robust probes have now been developed to study molecular conductance, both in SAM and on the single-molecule level. Results on the same molecular species are now being reproduced in different labs, and the toolbox of the research field is

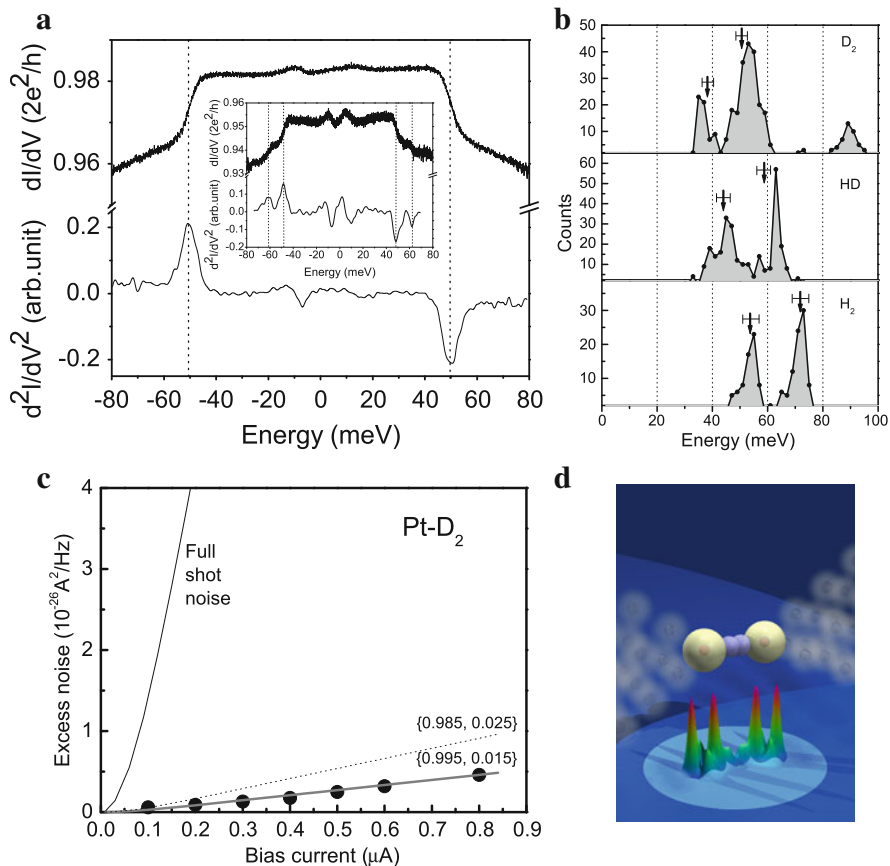


**Fig. 1.1** A single hydrogen molecule bridging two Pt electrodes forms a model system that permits many detailed tests. The differential conductance **(a)** shows sharp drops at characteristic frequencies associated with the vibration modes of the molecule. The *inset* shows an example where two modes are observed for the same molecular junction. The position of the steps in the conductance for many experiments is shown in **(b)**, and the interpretation of the features in the differential conductance as vibration mode energies can be tested using isotope substitutions of the molecule. The shift of the modes between  $H_2$  and  $D_2$  is close to the value of  $\sqrt{2}$ , as expected. This permits verifying that the molecule forming the bridge is indeed hydrogen. By further experiments exploiting shot noise **(c)**, it is possible to show that the conductance is carried by a single conductance channel. More precisely, the total conductance for this particular junction is  $1.01G_0$ , which is the result of a dominant conductance channel with transmission 0.995 and a small additional tunneling contribution of 0.015. This demonstrates that the bridge is formed by just a single hydrogen molecule. Panel **(d)** illustrates the configuration that matches the data, together with a calculation of the local density of states on the bridge (Reproduced by permission from Refs. [42, 57, 58])

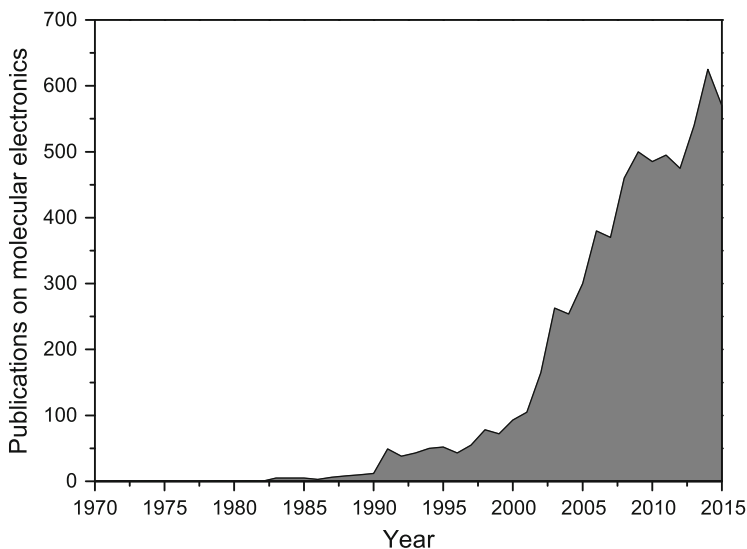


**Fig. 1.2** Number of publications on molecular electronics in each year of publication (Data based upon ISI Web of Science, Thomson Reuters)

rapidly expanding. Figure 1.2 shows the evolution of the numbers of publications each year having “molecular electronics” as topic. The total number exceeds 6500, making molecular electronics one of the large research areas of nanoscience, and the interest clearly continues to grow.

Before we continue to discuss which are the attractive issues for further studies towards deeper fundamentals understanding and for developing applications, I will first argue against the widespread suggestion that molecular electronics may one day replace silicon electronics. This is not intended as discouragement, but intended to highlight the realistic prospects for applications.

### 1.3 Will Self-Assembled Molecular Circuits Replace Silicon?

Semiconductor technology is driving a large part of the world economy, and the fact that there are many signs that we are arriving at the end of the roadmap underlying Moore’s law is making the industry nervous [82]. The industry is in urgent need of new ideas and possibly revolutionary approaches. Molecular electronics is one of the possible ways to go forward, but as I will argue here, it will not proceed by simply replacing silicon transistors by molecular equivalents.

The initial excitement around molecular electronics derived from the vague notion that molecules would someday replace transistors in today’s complementary metal-oxide-semiconductor (CMOS)-based silicon technology, an idea that was sometimes even voiced explicitly. Design of the proper links between the molecular building blocks and choice of proper processing conditions would permit self-

assembly of the complete circuit. Furthermore, the tools of organic chemistry would allow design of the properties of all circuit elements, they could be produced such that they are all identical at mole quantities, and they would represent the ultimate limit in miniaturization. The self-assembly process would obviate the need for investments in wafer-stepper machines, for which the costs explode as the sizes of the smallest circuit details shrink. Although many of these attractive aspects of molecules in electronics remain true and may be exploited in applications of some form, as I will argue below it is useful to be aware that the initial dream in this sense will never become a reality. This has been admitted by many, but has only seldom been stated very explicitly.

One of the main reasons why this scheme cannot work, even in principle, is the fact that the electronic wave functions on a molecule are phase coherent. This is one of the reasons why many believe that molecules may be very attractive in electronics, but phase coherence also implies that the properties of two circuit elements coupled in series do not simply behave as the connection of two classical circuit elements in series. When coupling two molecules together, the wave functions of the two combine into a coherent superposition that modifies the properties of both [83]. In general, the electronic transmission of a molecule is only defined in combination with the properties of the connections and the strength of the coupling.

One possibility of circumventing this problem would be offered by reducing the strength of the coupling of the molecule to its surrounding circuit. A molecule will normally have a single conductance channel that dominates transport, which provides a conductance of one quantum unit,  $2e^2/h$ , or about 0.1 mS under conditions of perfect transmission. When we want to decouple the molecule enough to prevent modification of its wave functions, we will need to introduce barriers that reduce the transmission by typically three orders of magnitude at all connections. The net conductance between any two leads then becomes of the order of 0.1 nS. When, in addition, we want to conserve the operating voltage at about 1 V and the clock frequency of silicon electronics to values of several GHz, we notice that the amount of charge transmitted within a clock cycle is of the order of a single electron. This will produce unwanted statistical fluctuations of the results of the computing operations, will be extremely difficult to control the next circuit elements reliably, and will impose a serious limitation on the fan-out, i.e., the number of next-stage circuit elements that can be controlled by the present one.

The strategy of reducing the coupling between molecular circuit elements to such a degree also implies that the single-electron description of coherent transmission breaks down and that electron-electron interactions need to be taken into account. Coulomb blockade will be important, even at room temperature. This means that the properties of the circuit cannot be described by combining independent circuit elements, but can only be described at the level of the complete circuit, which brings us back to the problem that we started from.

Another approach for decoupling the molecular circuit elements could be provided by placing metallic islands between each molecular stage, large enough to provide decoherence of the phase of the wave functions. This has two serious drawbacks: First, we lose most of the small-size advantage of the molecules.

Second, we would need to arrange for the coupling between the molecules and the metal islands to be strong in order for the electron current to remain large enough to drive the next stage, as argued above. This will result in significant broadening of the molecular level, which will wash out a lot of the specific molecular energy level structure that we would like to exploit for the active device-specific operations.

Even if we were able to find solutions to handle these problems, the difficulty remains of catching up with all the technology invested in CMOS in circuit design taking care of heat dissipation, capacitive cross talk, and much more. For all of these reasons, it seems obvious that molecular electronics can only work if we consider entirely different circuit architectures or different applications that permit relaxing some of the requirements and take advantage of the specific properties of molecular circuit elements. Some of these ideas are briefly outlined below.

## 1.4 Intrinsically Quantum

After these critical remarks, it is important to emphasize that there are many application perspectives and that between the present time and future applications, there is fascinating science on our path. A large part of the fascination lies in the fact that molecules are intrinsically quantum objects and that we may explore and exploit this fact, even at ambient conditions.

An exciting aspect of molecular conduction is the fact that the energy scales involved are such that quantum effects are expected at room temperature. In this sense, single-molecule electronics forms a natural extension of mesoscopic physics. An illustrative example is the observation of quantum interference in charge transport. In mesoscopic physics, interference has been shown to govern the conductance in gold rings with a diameter of 1 micrometer at cryogenic temperatures [84]. In molecules with sizes as small as 1, nanometer interference effects are expected at room temperature. This has first been recognized in theoretical works [79] and very recently, the first experiments have been done [80]. New switchable devices or sensors come within reach once destructive interference (with low conductance) can be turned on and off in a controlled way. However, the consequences of quantum interference reach much further as it may govern thermoelectric properties or spin-spin interaction, enabling new functionality [85].

A molecular wire is maximally exposed to its environment, which poses challenges in incorporating the environment in the description. A molecule exchanges energy with its surroundings through the exchange of vibration modes (phonons), electromagnetic modes (photons), electronic excitations, and composite excitations such as plasmons. It is also influenced by static and dynamic electric fields, magnetic fields, pH and chemical composition in general, temperature, and more. Their influence on transport properties is not understood in detail and provides one of the main challenges of the field. On the other hand, the strong interaction with the environment also creates a lot of opportunities. Some molecular devices show switchability, while the molecule in the junction has no built-in functionality [85].

In this case, the interaction with the electrodes, either via the electric field or via the current, induces the necessary bistability for switch operation. By control of the environment, a fully symmetric molecule can function as a strongly asymmetric diode [86].

Another tantalizing possibility arises from non-conservative current-induced forces. Such forces are held responsible for electromigration in microscopic metal wires. However, more recent work by Tchavdar Todorov and others suggests an interesting connection with the presence of nearly degenerate vibration modes that could be engineered for switching properties in an organic molecule or even for driving nanoscale motors by a dc current [87, 88].

The intrinsic quantum nature of molecules highlights two legitimate goals for further research: fundamental understanding and applications. Below a sketch of promising developments for both directions is given.

## 1.5 Challenges for Applications

Self-assembly will be an essential part of most molecular electronics applications, and this process needs to be optimized for success rates at the single-molecule level. A clear advantage of SAM devices is that the molecular building blocks are all identical, while the variations in coupling of the individual molecules are averaged away. In addition, functionalities can be built in by chemical design, examples of which include switches, rectifiers, and sensors. However, to fully exploit this potential, a good understanding of the molecule-electrode interface is crucial. Single-molecule devices serve as model systems to study these interfaces, as they do, for instance, not suffer from pinhole shorts that SAMs may have. Importantly, single-molecule devices can provide the feedback loop to make the required steps in our understanding and control. In an ideal feedback loop, synthesis of molecules is followed by experimental characterization of single-molecule junctions, for which by now various approaches are available. The experimental results form the input for theoretical modeling and the latter would dictate the synthesis of a new class of molecules with improved performance. In this way, single-molecule electronics becomes an enabling field for large-area device applications based on molecules. These include both SAM-based devices and organic electronic devices, as will be illustrated below.

The metal-molecule interface plays a crucial role in understanding molecular device behavior. This holds not only for the mechanical coupling but also for the electronic coupling, governing charge transport through the junction. The mechanical coupling is based on the stability of chemical bonds, which provide the driving force for self-assembly. Traditionally, the Au-S bond has been the most popular one, but recent research focuses on alternative binding schemes. In fact, this has become an active field of current research that has seen a strong development in the last couple of years [89]. Apart from the mechanical stability, the binding configuration also determines the electronic properties of the junction. Coupling a

molecule to metallic electrodes has two important effects on the molecular energy levels. First, the molecular levels are broadened and, generally speaking, the broader the levels, the higher the off-resonance conductance. Second, charge transfer near the interface may lead to significant shifting of the molecular levels. This shifting has important implications for transport, as the position of the molecular levels with respect to the Fermi energy of the electrodes determines its charge transport properties. In fact, this is used in current organic devices to optimize injection barriers by a methodology that we call interface engineering. For example, an SAM sandwiched between an organic layer and a metal electrode acts as an intermediate, reducing the injection barrier [90].

The perspectives for applications naturally separate into short-term and long-term perspectives. The first applications of molecular electronics have started to appear [91] and, just as this example illustrates, the earliest applications will most likely not rely on single-molecule junctions. In addition, applications of single-molecule layers formed by self-assembly are already being explored for the engineering of work functions of metallization layers. Charge injection into organic conducting layers, such as those being developed for solar cells, can be optimized by a proper choice of molecular surface coating [92]. Although the principles of the process are now reasonably well understood, the optimization and detailed understanding require still a large effort. A third promising application near the horizon is the use of redox-active molecules to improve properties of flash memory in combination with standard silicon transistors [93, 94].

One of the most attractive proposals for employing molecules in electronics is the use of cross-bar array architectures [95, 96], as illustrated in Fig. 1.3. It opens the way towards high-density memory, which could be implemented initially as

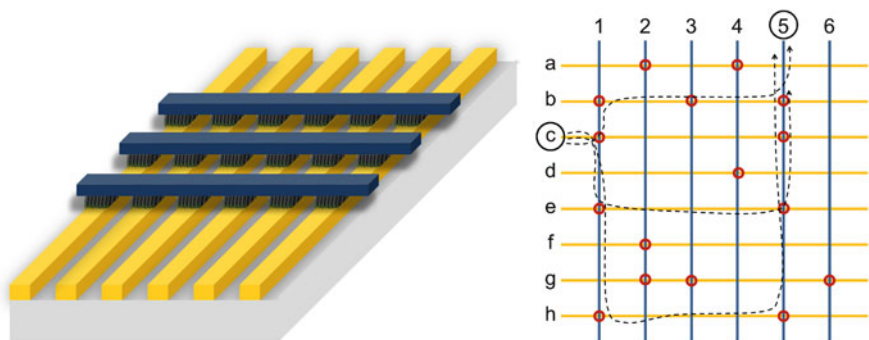


**Fig. 1.3** Schematic structure of a cross-bar array structure employing a layer of molecules as active components at the nodes. Ideally the molecules switch between high-conductance and low-conductance states above a threshold value of the applied bias. The *right panel* illustrates the need for blocking current through parallel paths. When the *circled* nodes are in the high-conductance state and we want to read the information in node C5, the information read will be confounded by parallel current paths as shown by the *dashed lines*. The larger the array, the more abundant are such parallel paths

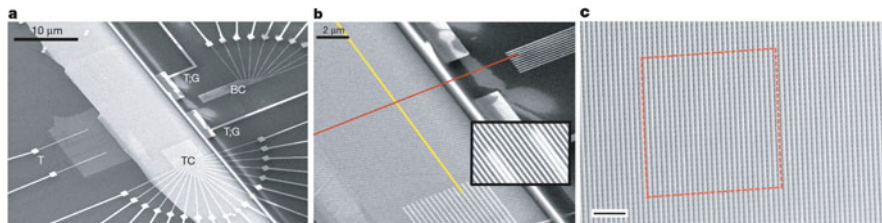


**Fig. 1.4** Scanning electron micrographs of a 160 kbit molecular memory device. It contains 400 Si bottom nanowire electrodes having a 33 nm pitch, seen as the *light gray area* connected by “T” in (a), and 400 Ti nanowires on top with the same pitch, visible as the light band diagonally stretching the image. The nodes are formed by about 100 rotaxane molecules deposited as an LB layer. Panel (b) is a zoom of the central area with a top wire highlighted as red and a bottom wire as yellow. The further zoom in (c) shows the central area of about 2500 bits, where the scale bar is 200 nm (Reproduced by permission from [96])

relatively small arrays incorporated into and added onto standard CMOS circuits. A test structure containing 160,000 molecular junctions was fabricated by Green et al. [96] using an LB monolayer of rotaxanes as the active component; see Fig. 1.4. Although only 25 % of the junctions tested showed an on/off ratio larger than 1.5, the work demonstrates that some of the hurdles can be taken. Apart from the application as memory, such cross-bar arrays can be used for processing, using reconfigurable logic [95].

In its simplest implementation, each node is connected to a single bottom wire and a single cross wire on top. The problem of defective molecular junctions can be accommodated by the embedding structure into a fault-tolerant architecture. Nevertheless, reducing the number of defective junctions will greatly enhance the success of the devices, and this problem is probably predominantly associated with improvement of the deposition and bonding of the top contact wires to the molecular layer and the quality of the SAM.

The schematic in Fig. 1.3 shows the basic structure. The minimal requirements are the need for a molecule that can be self-assembled into a densely ordered layer and deposited on the bottom wires and a molecule that behaves as a well-defined switch between a low-conductance and a high-conductance state upon application of a bias voltage above a suitable threshold value. Although the rotaxanes demonstrate some intrinsic switching behavior, there is much room to improve the on/off ratio and the reliability by searching for other molecular components.

For a practical device, we will need to add further components, which could also be implemented as molecular layers. First, it will be necessary to add a diode in series with the switches at each node [97]. The need for such diodes is illustrated in the right panel of Fig. 1.3. Without diodes, a large cross-bar array would have a multitude of parallel conduction paths that would mask the information for individual bits. We further need to demand a high rectification ratio  $R_{rr}$  between forward and reverse bias for these diodes because the number of parallel current paths scales with the size of the array. In the worst case, when all nodes have

their switch closed (i.e., “on”), the ratio of the signal current to the current through parallel paths is  $2/(N - 1) + R_{rr}/(N - 1)^2$  for an  $N \times N$  array. Even for a modest 1 MBit memory, the requirements would be  $R_{rr} > 10^6$ , which is quite demanding. The solution will be to implement large numbers of smaller arrays embedded into CMOS electronics.

Finally, when we introduce a diode, it impedes the process of writing information to the molecular switch by a current bias of either polarity. This could be taken care of by a molecular Zener diode. Although such Zener diodes have not been discussed widely in the context of molecular electronics, the principle may also be implemented by combining two resonant tunneling diodes [98].

Apart from considering different computer architectures, there are ample further possibilities for which optimization in speed is not required, such as for disposable or wearable electronics. As argued above, electronics based on such molecular SAM are not expected to outperform existing silicon devices, but they will be complementary, will profit from cheap processing technologies, and will enable new applications and functionality. ” For electronics applications that rely less on dense packing of bits and high switching speed, such as disposable electronics, the requirements will be different than those for high-density computing and memory applications. The former will typically make use of SAM of molecules over relatively large areas. It will, then, be important to reduce defects in the SAM or make the device structure insensitive to them.

An aspect that is seldom discussed is the fact that the molecular compounds that have been studied to date at the single-molecule level have a conductance that is far too high for such applications. The conductance for single-molecule junctions usually covers a range down to  $10^{-7}$  of the conductance quantum or  $10^{-7}$  S. SAM of molecules having a conductance at this bottom end of the range and covering an area of  $1 \text{ mm}^2$  would make a total conductance of 10 S. In other words, at a bias of only 1 V, this device would draw a current of 10 A. The conclusion should be that for such applications, it will be necessary to extend the range of investigation of molecular conductance towards much smaller values.

For the longer term, it remains very attractive to investigate truly single-molecule electronics applications. One of the main difficulties that we will need to address is that of keeping single molecules stable at a reproducible transmission. It is likely that metal electrodes will not be the best choice to deal with this problem. Possibly covalent bonds can be explored for bonding to other electrode materials such as Si [99, 100] or graphene [101, 102]. While single-molecule junctions are ideal for testing concepts, for applications, it will be necessary to solve the problem of interfacing the molecules with lithography or find other solutions for creating stable gaps between the electrodes. A lot of progress in this direction has already been made as recently reviewed by Cui et al. [103]. Such single-molecule devices will also need to be forgiving in the variability and fluctuations in the molecular anchoring and conformations.

Most of the research directions discussed above are connected to electronics in some way. However, there are important developments that connect to very different fields such as microbiology and medicine. Sequencing and read-out of DNA and

other biopolymers has evolved into a main field of research and development. The techniques currently in use in sequencers rely almost exclusively on biochemical methods. The advantages of a direct read-out of biopolymers by physical methods are obvious, and several groups are working towards these goals [104–108]. One of the approaches taken is the read-out of sequences of monomers by differentiating the levels of tunneling current [105, 106, 108]. Ideally one would like to controllably drag a biopolymer past a nanometer-size gap between two metallic electrodes and read off the nature of each of the building blocks passing by. Many steps in this direction have been taken, and larger consortia are now being formed for bringing this application to the market. A more extensive discussion is given in Chap. 9.

## 1.6 Challenges for Fundamental Understanding

Obviously, as applies to all of the discussions in this chapter, it is not possible to give an exhaustive list of all points of interest. The items given below are inevitably colored by personal preference, but should still serve to outline the scope of challenges open for research.

Starting with one of the most fundamental issues, the question of whether an accurate prediction of electronic conductance of a molecular junction can be given is still open. For molecules having a strong hybridization of the molecular orbitals with the metallic states of the leads, a coherent transport description works very well [42]. At the other end of the spectrum, molecules that have only a weak tunnel coupling to the leads can be understood within the framework of Coulomb blockade of discrete charge states of the molecule [109]. The intermediate regime has been understood at the level of idealized models, but experiments on individual molecules are usually compared with theory for one of the two extreme conditions. For most molecules for which the off-resonant zero-bias conductance is measured, the results are compared with DFT-based calculations that take electron-electron interaction into account only at a mean field level. Equally important, the role of image charges is very large and has only started to be included in the discussion [61, 110]. For a more extensive discussion of these open problems, I recommend the book by Cuevas and Scheer [3].

The nature of the bond between the molecule and the metal electrodes is of obvious importance. We have only partial understanding of the nature of the binding of the molecules to electrodes (anchoring) in terms of bond strength and electronic transport. The interesting question is whether these two are correlated in any way. This is a critical question for interface engineering and well-defined SAM for applications. The answer to this question will depend on the nature of the electrode material, where metals should probably be distinguished from materials such as graphene, which allow for covalent bonding.

In regular metallic transport experiments, it is very difficult to set up an electron distribution that is locally very far from equilibrium. Molecular junctions open this window toward electron transport far from equilibrium. Under these conditions, we

can probe the details of electron-phonon interactions, dissipation, and relaxation. As a result of the large voltage bias and the associated large current density, electrons have access to many types of relaxation mechanisms, including vibration modes, photons, plasmons, and spin excitations. This coupling works also in the other direction: because the molecule is exposed to the environment, electron transport is sensitive to fields of all these types. These effects can be further amplified by quantum effects such as interference of transport through multiple atomic orbitals [81].

In this way, single molecules form an exceptional platform for testing many phenomena under extreme conditions. There is a wide interest in spin transport, and interaction of the electron spin with the electronic and nuclear spins on the molecule, where the research connects to the field of spintronics [111, 112]. Seebeck coefficients and thermal transport can be engineered and investigated at the single-molecule scale, which will boost progress in thermoelectric energy conversion [113]. Electrochemistry can be investigated down to the single-molecule level [64], and more generally the specificity of the interaction of the molecule with its chemical environment can be investigated through its electronic conductance. The extreme current densities open the way for microscopic investigations of electromigration, where recent predictions suggest that such forces could be harnessed for developing dc-current driven nanomotors, acting as waterwheels in the electron flow [87].

Finally, many important challenges connected to applications stand out: molecular junctions having diode characteristics [114], voltage-controlled switching [85], and negative differential conductance [77] have been demonstrated, but in view of the applications discussed above, there is much need for improvement of these properties and for investigation of other principles leading to the desired properties.

## 1.7 Outlook and Conclusions

Many of the points mentioned above have been widely discussed and are part of active research worldwide. Thinking further into the future, it will be attractive to consider the possibilities of building three-dimensional networks by self-assembly. Can we come up with mechanisms and architectures to do this? Some inspiration may come from the self-assembly of two-dimensional networks that employ the recognition and selective bonding of engineered strands of DNA [115]. Although DNA serves the purpose of self-assembly very well, it is a very poor conductor, if not a very good insulator. We would need, instead, to use flexible conducting molecular wires and find new avenues for targeted self-assembly. Examples of such long self-assembling conducting wires have been demonstrated by Tuccitto et al. [116], and other examples are discussed in Chaps. 5 and 6. Ideally, the target connections would be controllably activated by setting its electrical potentials or by reversible chemical modifications. Such 3D reconfigurable networks would have very interesting properties and offer perspectives for signal processing through

neuromorphic networks. The challenge is clearly formidable and the time scale for achieving this is likely longer than any of the other applications discussed.

From a scientific point of view, as well as from an applications perspective, the conclusion should be that the future of the field of molecular electronics is bright. At which point we find ourselves in the development of the field, we can only answer with certainty much later, but Fig. 1.2 and the list of interesting open problems discussed here suggest that the field will continue to grow for some time to come.

**Acknowledgements** I have profited from many discussions with Sense Jan van der Molen, Herre van der Zant, Ferdinand Evers, Mehdi Tahoori, Alfredo Levy Yeyati, Dago de Leeuw, Juan Carlos Cuevas, Duncan Stewart, and Manabu Kiguchi.

## References

1. Skotheim TA, Elsenbaumer RL, Reynolds JR (eds) (1998) Handbook of conducting polymers. Marcel Dekker, New York/Basel
2. So F (ed) (2010) Organic electronics, materials, processing, devices and applications. CRC Press, Boca Raton
3. Cuevas JC, Scheer E (2010) Molecular electronics, an introduction to theory and experiment. World Scientific, Hackensack
4. Gooding JJ, Ciampi S (2011) The molecular level modification of surfaces: from self-assembled monolayers to complex molecular assemblies. *Chem Soc Rev* 40:2704–2718
5. Aviram A, Ratner MA (1974) Molecular rectifiers. *Chem Phys Lett* 29:277–283
6. Langmuir I (1920) The mechanism of the surface phenomena of flotation. *Trans Faraday Soc* 15:62
7. Blodgett KB (1934) Monomolecular films of fatty acids on glass. *J Am Chem Soc* 56:495–495
8. Blodgett KB (1935) Films built by depositing successive monomolecular layers on a solid surface. *J Am Chem Soc* 57:1007–1022
9. Mann B, Kuhn H (1971) Tunneling through fatty acid salt monolayers. *J Appl Phys* 42:4398
10. Geddes NJ, Sambles JR, Jarvis DJ, Parker WG (1990) Fabrication and investigation of asymmetric current-voltage characteristics of a metal/Langmuir-Blodgett monolayer/metal structure. *Appl Phys Lett* 56:1916
11. Metzger RM, Chen B, Höpfner U, Lakshmikantham MV, Vuillaume D, Kawai T et al (1997) Unimolecular electrical rectification in hexadecylquinolinium tricyanoquinodimethanide. *J Am Chem Soc* 119:10455–10466
12. Metzger RM (1999) Electrical rectification by a molecule: the advent of unimolecular electronic devices. *Acc Chem Res* 32:950–957
13. Lau CN, Stewart DR, Williams RS, Bockrath M (2004) Direct observation of nanoscale switching centers in metal/molecule/metal structures. *Nano Lett* 4:569–572
14. Metzger RM, Xu T, Peterson IR (2001) Electrical rectification by a monolayer of hexadecylquinolinium tricyanoquinodimethanide measured between macroscopic gold electrodes. *J Phys Chem B* 105:7280–7290
15. Rampi MA, Whitesides GM (2002) A versatile experimental approach for understanding electron transport through organic materials. *Chem Phys* 281:373–391
16. Chiechi RC, Weiss EA, Dickey MD, Whitesides GM (2007) Eutectic Gallium-Indium (EGaIn): a moldable liquid metal for electrical characterization of self-assembled monolayers. *Angew Chemie* 120:148–150

17. Akkerman HB, Blom PWM, de Leeuw DM, de Boer B (2006) Towards molecular electronics with large-area molecular junctions. *Nature* 441:69–72
18. Yan H, Bergren AJ, McCreery R, Della Rocca ML, Martin P, Lafarge P, Lacroix JC (2013) Activationless charge transport across 4.5 to 22 nm in molecular electronic junctions. *Proc Natl Acad Sci* 110:5326
19. Collier CP, Wong EW, Belohradsky M, Raymo FM, Stoddart JF, Kuekes PJ, Williams RS, Heath JR (1999) Electronically configurable molecular-based logic gates. *Science* 285:391–394
20. Stewart DR, Ohlberg DAA, Beck PA, Chen Y, Williams RS, Jeppesen JO, Nielsen KA, Stoddart JF (2004) Molecule-independent electrical switching in Pt/Organic Monolayer/Ti devices. *Nano Lett* 4:133–136
21. Nuzzo RG, Allara DL (1983) Adsorption of bifunctional organic disulfides on gold surfaces. *J Am Chem Soc* 105:4481–4483
22. Love JC, Estroff LA, Kriebel JK, Nuzzo RG, Whitesides GM (2005) Self-assembled monolayers of thiolates on metals as a form of nanotechnology. *Chem Rev* 105:1103–1169
23. Boulas C, Davidovits JV, Rondelez F, Vuillaume D (1996) Suppression of charge carrier tunneling through organic self-assembled monolayers. *Phys Rev Lett* 76:4797
24. Wold DC, Frisbie CD (2001) Fabrication and characterization of metal-molecule-metal junctions by conducting probe atomic force microscopy. *J Am Chem Soc* 123:5549–5556
25. Cui XD, Zarate X, Tomfohr J, Sankey OF, Primak A, Moore AL, Moore TA, Gust D, Harrias G, Lindsay SM (2002) Making electrical contacts to molecular monolayers. *Nanotechnology* 13:5
26. Binnig G, Rohrer H, Gerber Ch, Weibel E (1982) Surface studies by scanning tunneling microscopy. *Phys Rev Lett* 49:57
27. Joachim C, Gimzewski JK, Schlittler RR, Chavy C (1995) Electronic transparency of a single C<sub>60</sub> molecule. *Phys Rev Lett* 74:2102
28. Bumm LA, Arnold JJ, Cygan MT, Dunbar TD, Burgin TP, Jones L, Allara DL, Tour JM, Weiss PS (1996) Are single molecular wires conducting? *Science* 271:1705–1707
29. Datta S, Tian W, Hong S, Reifenberger R, Henderson JI, Kubiak CP (1997) Current-Voltage characteristics of self-assembled monolayers by scanning tunneling microscopy. *Phys Rev Lett* 79:2530–2533
30. Han W, Durantini EN, Moore TA, Moore AL, Gust D, Rez P, Leatherman G, Seely GR, Tao N, Lindsay SM (1997) STM contrast, electron-transfer chemistry, and conduction in molecules. *J Phys Chem B* 101:10719
31. Donhauser ZJ, Mantooth BA, Kelly KF, Bumm LA, Monnell JD, Stapleton JJ, Price DW Jr, Rawlett AM, Allara DL, Tour JM, Weiss PS (2001) Conductance switching in single molecules through conformational changes. *Science* 292:2303
32. Leatherman G, Durantini EN, Gust D, Moore TA, Moore AL, Stone S, Zhou Z, Rez P, Liu YZ, Lindsay SM (1999) Carotene as a molecular wire- conducting atomic force microscopy. *J Phys Chem B* 103:4006–4010
33. Cui XD, Primak A, Zarate X, Tomfohr J, Sankey OF, Moore AL, Moore TA, Gust D, Harris G, Lindsay SM (2001) Reproducible measurement of single-molecule conductivity. *Science* 294:571
34. Muller CJ, van Ruitenbeek JM, de Jongh LJ (1992) Conductance and supercurrent discontinuities in atomic-scale metallic constrictions of variable width. *Phys Rev Lett* 69:140–143
35. Muller CJ, van Ruitenbeek JM, de Jongh LJ (1992) Experimental observation of the transition from weak link to tunnel junction. *Physica C* 191:484–504
36. Reed MA, Zhou C, Muller CJ, Burgin TP, Tour JM (1997) Conductance of a molecular junction. *Science* 278:252–254
37. van Ruitenbeek JM, Alvarez A, Piñeyro I, Grahmann C, Joyez P, Devoret MH, Esteve D, Urbina C (1996) Adjustable nanofabricated atomic size contacts. *Rev Sci Instrum* 67 108–111
38. Kergueris C, Bourgoin J-P, Palacin S, Esteve D, Urbina C, Magoga M, Joachim C (1999) Electronic transport through a metal-molecule-metal junction. *Phys Rev B* 59:12505–12513

39. Park H, Park J, Lim AKL, Anderson EH, Alivisatos AP, McEuen PL (2000) Nanomechanical oscillations in a single C60 transistor. *Nature* 407:57–60
40. Park J, Pasupathy AN, Goldsmith JJ, Chang C, Yaish Y, Petta JR, Rinkoski M, Sethna JP, Abruña HD, McEuen PL, Ralph D (2002) Coulomb blockade and the Kondo effect in single-atom transistors. *Nature* 417:722–725
41. Liang W, Shores MP, Bockrath M, Long JR, Park H (2002) Kondo resonance in a single-molecule transistor. *Nature* 417:725–729
42. Smit RHM, Noat Y, Untiedt C, Lang ND, van Hemert MC, van Ruitenbeek JM (2002) Measurement of the conductance of a hydrogen molecule. *Nature* 419:906
43. Xu B, Tao NJ (2003) Measurement of single-molecule resistance by repeated formation of molecular junctions. *Science* 301:1221–1223
44. Venkataraman L, Klare JE, Tam IW, Nuckolls C, Hybertsen MS, Steigerwald ML (2006) Single-molecule circuits with well-defined molecular conductance. *Nano Lett* 6:458–462
45. Haiss W, Martin S, Scullion LE, Bouffier L, Higgins SJ, Nichols RJ (2009) Anomalous length and voltage dependence of single molecule conductance. *Phys Chem Chem Phys* 11:10831–10838
46. Picaud F, Smogunov A, Dal Corso A, Tosatti E (2003) Complex band structures and decay length in polyethylene chains. *J Phys Cond Mat* 15:3731
47. Choi SH, Kim B, Frisbie CD (2008) Electrical resistance of long conjugated molecular wires. *Science* 320:1482–1486
48. Venkataraman L, Klare JE, Nuckolls C, Hybertsen MS, Steigerwald ML (2006) Dependence of single-molecule junction conductance on molecular conformation. *Nature* 442:904
49. Michenko A, Vonlanthen D, Meded V, Bürkle M, Li C, Pobelov IV, Bagrets A, Viljas JK, Pauly F, Evers F, Mayor M, Wandlowski T (2010) Influence of conformation on conductance of Biphenyl-Dithiol single-molecule contacts. *Nano Lett* 10:156–164
50. Reichert J, Weber HB, Mayor M, Löhneysen Hv (2003) Low-temperature conductance measurements on single molecules. *Appl Phys Lett* 82:4137
51. Dulić D, van der Molen SJ, Kudernac T, Jonkman HT, de Jong JJD, Bowden TN, van Esch J, Feringa BL, van Wees BJ (2003) One-way optoelectronic switching of photochromic molecules on gold. *Phys Rev Lett* 91:207402
52. Ward DR, Halas NJ, Cizek JW, Tour JM, Wu Y, Nordlander P, Natelson D (2008) Simultaneous measurements of electronic conduction and raman response in molecular junctions. *Nano Lett* 8:919–925
53. Konishi T, Kiguchi M, Takase M, Nagasawa F, Nabika H, Ikeda K, Uosaki K, Ueno K, Misawa H, Murakoshi K (2013) Single molecule dynamics at a mechanically controllable break junction in solution at room temperature. *J Am Chem Soc* 135:1009–1014
54. Osorio EA, O’Neill K, Stuhr-Hansen N, Nielsen OF, Bjornholm T, van der Zant HSJ (2007) Addition energies and vibrational fine structure measured in electromigrated single-molecule junctions based on an oligophenylenevinylene derivative. *Adv Mater* 19:281–285
55. Tal O, Krieger M, Leerink B, van Ruitenbeek JM (2008) Electron-vibration interaction in single-molecule junctions: from contact to tunneling regimes. *Phys Rev Lett* 100:196804
56. Kim Y, Pietsch T, Erbe A, Belzig W, Scheer E (2011) Benzenedithiol: a broad-range single-channel molecular conductor. *Nano Lett* 11:3734–3738
57. Djukic D, van Ruitenbeek JM (2006) Shot noise measurements on a single molecule. *Nano Lett* 6:789–793
58. Djukic D, Thygesen KS, Untiedt C, Smit RHM, Jacobsen KW, van Ruitenbeek JM (2005) Stretching dependence of the vibration modes of a single-molecule Pt-H<sub>2</sub>-Pt junction. *Phys Rev B* 71:161402
59. Aradhya SV, Frei M, Hybertsen MS, Venkataraman L (2012) Van derWaals interactions at metal/organic interfaces at the single-molecule level. *Nat Mater* 11:872–876
60. Reddy P, Jang, S-Y, Segalman RA, Majumdar A (2007) Thermoelectricity in molecular junctions. *Science* 315:1568–1571
61. Perrin ML, Verzijl CJO, Martin CA, Shaikh AJ, Eelkema R, van Esch JH, van Ruitenbeek JM, Thijssen JM, van der Zant HSJ, Dulić D (2013) Large tunable image charge effects in single-molecule junctions. *Nat Nanotechnol* 8:282–287

62. Xiang D, Jeong H, Kim D, Lee T, Cheng Y, Wang Q, Mayer D (2013) Three-terminal single-molecule junctions formed by mechanically controllable break junctions with side gating. *Nano Lett* 13:2809–28113
63. Li Y, Baghernejad M, Qusiy, Al-G, Zsolt Manrique D, Zhang G, Hamill J, Fu Y, Broekmann P, Hong W, Wandlowski T, Zhang D, Lambert C (2015) Three-state single-molecule naphthalenediimide switch: integration of a pendant redox unit for conductance tuning. *Angew Chem Int Ed.* 54:1–5
64. Osorio HM, Catarelli S, Cea P, Gluyas JBG, Hartl F, Higgins SJ, Leary E, Low PJ, Martin S, Nichols RJ, Tory J, Ulstrup J, Vezzoli A, Zeng Q, Costa Milan D (2015) Electrochemical single-molecule transistors with optimized gate coupling. *J Am Chem Soc* 137:14319–14328
65. Lee W, Kim K, Jeong W, Zotti LA, Pauly F, Cuevas JC, Reddy P (2013) Heat dissipation in atomic-scale junctions. *Nature* 498:209–213
66. Temirov R, Lassise A, Anders FB, Tautz FS (2008) Kondo effect by controlled cleavage of a single-molecule contact. *Nanotechnology* 19:065401
67. Schull G, Dappe YJ, González C, Bulou H, Berndt R (2011) Charge injection through single and double carbon bonds. *Nano Lett* 11:3142–3146
68. Schmaus S, Bagrets A, Nahas Y, Yamada TK, Bork A, Bowen M, Beaurepaire E, Evers F, Wulfhekel W (2011) Giant magnetoresistance through a single molecule. *Nature Nanotechnol* 6:185–189
69. Kitaguchi Y, Habuka S, Okuyama H, Hatta S, Aruga T, Frederiksen T, Paulsson M, Ueba H (2015) Controlled switching of single-molecule junctions by mechanical motion of a phenyl ring. *Beilstein J Nanotechnol* 6:2088
70. Lang ND (1995) Resistance of atomic wires. *Phys Rev B* 52:5335–5342
71. Galperin M, Ratner MA, Nitzan A, Troisi A (2008) Nuclear coupling and polarization in molecular transport junctions: beyond tunneling to function. *Science* 319:1056–1060
72. Emberly E, Kirczenow G (1998) State orthogonalization by building a Hilbert space: a new approach to electronic quantum transport in molecular wires. *Phys Rev Lett* 81:5205–5209
73. Tröster P, Schmitteckert P, Evers F (2012) Transport calculations based on density functional theory, Friedel’s sum rule, and the Kondo effect. *Phys Rev B* 85:115409
74. Thygesen KS, Rubio A (2007) Non-equilibrium GW approach to quantum transport in nano-scale contacts. *J Chem Phys* 126:091101
75. Koch J, von Oppen F (2005) Franck-Condon Blockade and Giant Fano Factors in Transport through Single Molecules. *Phys Rev Lett* 94:206804
76. Burzurí E, Yamamoto Y, Warnock M, Zhong X, Park K, Cornia A, van der Zant HSJ (2014) Franck-Condon blockade in a single-molecule transistor. *Nano Lett* 14:3191–3196
77. Perrin ML, Frisenda R, Koole M, Seldenthuis JS, Celis Gil JA, Valkenier H, Hummelen JC, Renaud N, Grozema FC, Thijssen JM, Dulić D, van der Zant HSJ (2014) Large negative differential conductance in single-molecule break junctions. *Nat Nanotechnol* 9:830–834
78. Lee H-W (1999) Generic transmission zeros and in-phase resonances in time-reversal symmetric single channel transport. *Phys Rev Lett* 82:2358–2361
79. Solomon GC, Andrews DQ, Goldsmith RH, Hansen T, Wasielewski MR, Van Duyne RP, Ratner MA (2008) Quantum interference in acyclic systems: conductance of cross-conjugated molecules. *J Am Chem Soc* 130:17301
80. Guedon CM, Valkenier H, Markussen T, Thygesen KS, Hummelen JC, van der Molen SJ (2012) Observation of quantum interference in molecular charge transport. *Nat Nanotechnol* 7:305–309
81. Ballmann S, Härtle R, Coto PB, Elbing M, Mayor M, Bryce MR, Thoss M, Weber HB (2012) Experimental evidence for quantum interference and vibrationally induced decoherence in single-molecule junctions. *Phys Rev Lett* 109:05680
82. Guha S (2015) Moore’s Law turns 50, but will it soon cease to exist? *Fortune* 19 Apr 2015 <http://for.tn/1PYZsVa>
83. Joachim C, Gimzewski JK, Aviram A (2000) Electronics using hybrid-molecular and mono-molecular devices. *Nature* 408:541–548

84. Webb RA, Washburn S, Umbach CP, Laibowitz RB (1985) Observation of  $h/e$  Aharonov-Bohm oscillations in normal-metal rings. *Phys Rev Lett* 54:2696
85. van der Molen SJ, Liljeroth P (2010) Charge transport through molecular switches. *J Phys Condens Matter* 22:133001–133001
86. Capozzi B, Xia J, Adak O, Dell EJ, Liu Z-F, Taylor JC, Neaton JB, Campos LM, Venkataraman L (2015) Single-molecule diodes with high rectification ratios through environmental control. *Nat Nanotechnol* 10:522–528
87. Dundas D, McEniry EJ, Todorov TN (2009) Current-driven atomic waterwheels. *Nat Nanotechnol* 4:99–102
88. Lü J-T, Brandbyge M, Hedegård P (2010) Blowing the fuse: Berry's phase and runaway vibrations in molecular conductors. *Nano Lett* 10:1657–1663
89. Kaliginedi V, Rudnev AV, Moreno-García P, Baghernejad M, Huang C, Hong W, Wandlowski T (2014) Promising anchoring groups for single-molecule conductance measurements. *Phys Chem Chem Phys* 16:23529–23539
90. Cahen D, Kahn A (2003) Electron energetics at surfaces and interfaces: concepts and experiments. *Adv Mater* 15:271–277
91. <http://www.chem.ualberta.ca/~mccreery/media.html>
92. Ho PKH, Kim J-S, Burroughes JH, Becker H, Li SFY, Brown TM, Cacialli F, Friend RH (2000) Molecular-scale interface engineering for polymer light-emitting diodes. *Nature* 404:481–484
93. Busche C et al (2014) Design and fabrication of memory devices based on nanoscale polyoxometalate clusters. *Nature* 515:545–549
94. Zhu H et al (2015) Redox-active molecular nanowire flash memory for high-performance and high-density non-volatile memory applications. *ACS Appl Mater Interfaces* 7:27306–27313
95. Heath JR, Kuekes PJ, Snider GS, Williams RS (1998) A defect-tolerant computer architecture: opportunities for nanotechnology. *Science* 280:1716–1721
96. Green JE et al (2007) A 160-kilobit molecular electronic memory patterned at  $10^{11}$  bits per square centimetre. *Nature* 445:414–417
97. Parkin SSP et al (1999) Exchange-biased magnetic tunnel junctions and application to nonvolatile magnetic random access memory. *J Appl Phys* 85:5828–5833
98. Perrin ML, Galan E, Eelkema R, Grozema F, Thijssen JM, van der Zant HSJ (2015) Single-molecule resonant tunneling diode. *J Phys Chem C* 119:5697–5702
99. Li Q, Mathur G, Gowda S, Surthi S, Zhao Q, Yu L, Lindsey JS, Bocian DF, Misra V (2004) Multibit memory using self-assembly of mixed ferrocene/porphyrin monolayers on silicon. *Adv Mater* 16:133–137
100. Zhao Q, Luo Y, Surthi S, Li Q, Mathur G, Gowda S, Larson PR, Johnson MB, Misra V (2005) Redox-active monolayers on nano-scale silicon electrodes. *Nanotechnology* 16:257–261
101. Ullmann K, Coto PB, Leitherer S, Molina-Ontoria A, Martín N, Thoss M, Weber HB (2015) Single-molecule junctions with epitaxial graphene nanoelectrodes. *Nano Lett* 15:3512–3518
102. Jia C, Ma B, Xin N, Guo X (2015) Carbon Electrode–Molecule junctions: a reliable platform for molecular electronics. *Acc Chem Res* 48:2565–2575
103. Cui A, Dong H, Hu W (2015) Nanogap electrodes towards solid state single-molecule transistors. *Small* 11:6115–6141
104. Xiao X, Xu B, Tao N (2004) Conductance titration of single-peptide molecules. *J Am Chem Soc* 126:5370–5371
105. Ohshiro T, Matsubara K, Tsutsui M, Furuhashi M, Taniguchi M, Kawai T (2012) Single-molecule electrical random resequeing of DNA and RNA. *Sci Rep* 2:501
106. Ohshiro T, Tsutsui M, Yokota K, Furuhashi M, Taniguchi M, Kawai T (2014) Detection of post-translational modifications in single peptides using electron tunnelling currents. *Nat Nanotechnol* 9:835–840
107. Livshits GI et al (2014) Long-range charge transport in single G-quadruplex DNA molecules. *Nat Nanotechnol* 9:1040–1046
108. Zhao Y et al (2014) Single-molecule spectroscopy of amino acids and peptides by recognition tunnelling. *Nat Nanotechnol* 9:466–473

109. Kubatkin S, Danilov A, Hjort M, Cornil J, Brédas J-L, Stuhr-Hansen N, Hedegård P, Bjørnholm T (2003) Single-electron transistor of a single organic molecule with access to several redox states. *Nature* 425:698–701
110. Kaasbjerg K, Flensberg K (2008) Strong polarization-induced reduction of addition energies in single-molecule nanojunctions. *Nano Lett* 8:3809
111. Wolf SA, Awschalom DD, Buhrman RA, Daughton JM, Molnár S, von Roukes ML, Chtchelkanova AY, Treger DM (2001) Spintronics: a spin-based electronics vision for the future. *Science* 294:1488–1495
112. Vardimon R, Klionsky M, Tal O (2015) Indication of complete spin filtering in atomic-scale nickel oxide. *Nano Lett* 15:3894–3898
113. Murphy P, Mukerjee S, Moore J (2008) Optimal thermoelectric figure of merit of a molecular junction. *Phys Rev B* 78:161406
114. Yuan L, Nerngchamnong N, Cao L, Hamoudi H, del Barco E, Roemer M, Sriramula RK, Thompson D, Nijhuis CA (2015) Controlling the direction of rectification in a molecular diode. *Nat Commun* 6:6324
115. Braun E, Eichen Y, Sivan U, Ben-Yoseph G (1998) DNA-templated assembly and electrode attachment of a conducting silver wire. *Nature* 391:775–778
116. Tuccitto N, Ferri V, Cavazzini M, Quici S, Zhavnerko G, Licciardello A, Rampi MA (2009) Highly conductive ~40-nm-long molecular wires assembled by stepwise incorporation of metal centres. *Nat Mater* 8:41–46

# Chapter 2

## Methods to Determine Electrical Conductance of Single-Molecule Junctions

Ryo Yamada

**Abstract** In this chapter, three major experimental methods, i.e., a break junction (BJ) method, an electromigration (EM) method, and an ultrahigh-vacuum low-temperature scanning tunneling microscopy (UHV-LT-STM), to measure electrical properties of single-molecule junctions are explained with some remarkable example of studies. The BJ method is the most widely used technique and explained including statistical analytical methods to analyze data. Studies of molecular switch and temperature dependence are shown as examples of studies based on statistical analysis as well as examples of static current-voltage measurements with external field modulations. Techniques related to the BJ method such as distance modulation and electromechanical response measurements are also introduced. Although the EM method can suffer from several problems, it is still useful to measure electrical gate effects and in the preparation of nanoscale gap electrodes. A novel application of the EM method to create in-plane nano-holes that would open a new application field of the single-molecule measurement techniques is shown. The UHV-LT-STM is capable of forming single-molecule junctions on single-crystal surfaces and manipulating molecules on the surface that enables researchers to study single-molecule junctions under controlled and well-defined structures and environments.

**Keywords** Break junction • Electromigration • Scanning tunneling microscope • Statistical analysis • Conductance histogram • Two-dimensional histogram • Cross-correlation analysis • Distance modulation

### 2.1 Introduction

One of the great challenges in single-molecule electronics is the preparation of single-molecule junctions. In the early stages of experimental studies, metal contacts were deposited on top of monolayers prepared on metal surfaces by Langmuir-Blodgett and self-assembly techniques to investigate the charge transport through monolayers [1]. Other techniques including nano-pore technique [2],

---

R. Yamada (✉)

Graduate School of Engineering Science, Osaka University, Osaka, Japan  
e-mail: [yamada@moletronics.jp](mailto:yamada@moletronics.jp)

metal-nanoparticle contact [3–5], and cross wire contact [6] were developed. Although interesting characteristics of the single-molecule and monolayer junctions were reported, these techniques suffered low yield of working device and reproducibility. The poor reproducibility is attributed not only to the difficulty of experimental procedure itself but also to the nature of single-molecule junctions that have a wide variety of structures and flexibility.

A mechanical break junction method enabled researchers to obtain a large number of experimental results on the electrical conductance of the single-molecule junctions and to discuss results on both the statistics and the detailed static measurements on a single-molecule junction [7–10]. In this technique, a single-molecule junction is formed during the breaking of metal electrodes with molecules adsorbed on them by mechanical actuation mechanisms such as a scanning probe microscope and specially designed devices. Actuating mechanisms allow the broken electrodes to be reconnected so that measurements can be repeated. This technique enables researchers to conduct measurements on a large number of single-molecule junctions that make statistical analysis of the observed conductance possible in various environments such as vacuum, air, and solutions and at different temperatures. This technique can also be used to sustain a single-molecule junction to measure detailed current-voltage measurements and apply other important measurement techniques introduced in Chap. 3. The ability to tune the distance between two electrodes also used to control conformations of the junction mechanically.

In this chapter, techniques and the data analysis method used for the break junction methods are explained followed by brief introductions of other important measurement techniques, i.e., an electromigration technique and a scanning tunneling microscope, to fabricate single-molecule junctions. Summaries for other measurement techniques can be found in review articles [11–14].

## 2.2 Mechanical Break Junction Method

### 2.2.1 *Principle and Instruments for the Break Junction Method*

In the mechanical break junction (BJ) technique, a contact between two metal electrodes is broken by a precise mechanical control of a distance between the electrodes [7–10]. The BJ is conducted either scanning tunneling microscope (SMT-BJ) [15] and 3-point bending machines to break a metal contact prepared on an elastic substrate (mechanically controllable break junction (CBJ)) [16]. In this section, instruments and remarkable results on these techniques are explained.

### 2.2.1.1 Scanning Tunneling Microscope-Break Junction (STM-BJ)

In the STM-BJ, the STM tip is brought into contact with the substrate and the current during the retracting process is recorded. Figure 2.1a shows the relation between the current transient and structure of the junction during the breaking process. Initially, the electrical current decreases continuously following Ohm's law as the junction is stretched. When the dimension of the contact is as small as an atomic scale, stepwise decrease of the current is observed at the integer multiples of the quantum conductance  $G_0 = 2e^2/h$ . The exponential decay of the current is observed due to the tunneling transport after breaking the atomic contact of the electrodes (a dashed curve in Fig. 2.1a). When the molecule is adsorbed on the electrodes or existed in surrounding medium, conductance plateaus at conductance values below  $1 G_0$  are occasionally observed due to the formation of the single-molecule junction (a black curve in Fig. 2.1a). The single-molecule junction is broken by the further retraction of the STM tip. The break junction process can be repeated by making the STM tip contacted to the substrate repeatedly. The so-called current-distance or Z spectroscopy function implemented to most of commercial STM can be used to conduct the STM-BJ measurement.

The conductance of the single-molecule junction is determined based on the conductance histogram created from hundreds to thousands of the current transient curves (Fig. 2.1b). To create the conductance histogram, the number of data points measured at a certain range of conductance (bin-width of the histogram) is counted in a conductance transient curve. A conductance plateau enhances the count of the data points around the conductance value around it and a peak is formed in the conductance histogram. The current transients showing without any plateaus are sometimes removed to make the peak clearer.

Figure 2.2 shows conductance transient curves and conductance histograms obtained for 4,4'-bipyridine using gold electrodes. The conductance steps above  $1 G_0$  showing the formation of a gold atomic contact are evident in the conductance

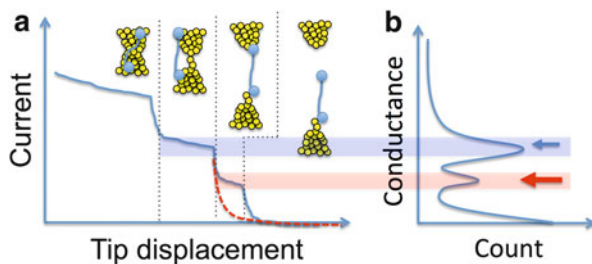


**Fig. 2.1** (a) Scheme of a current transient observed during the retraction of the STM tip. Inset schematics show structures of the junction corresponding to the current steps. A *dashed smooth curve* shows the current decay without molecules. (b) A conductance histogram corresponding to the current transient shown in (a). The peaks indicated by *small* and *large arrows* correspond to the conductance of an atomic point contact, i.e.,  $1 G_0$  for gold, and single-molecule junction, respectively

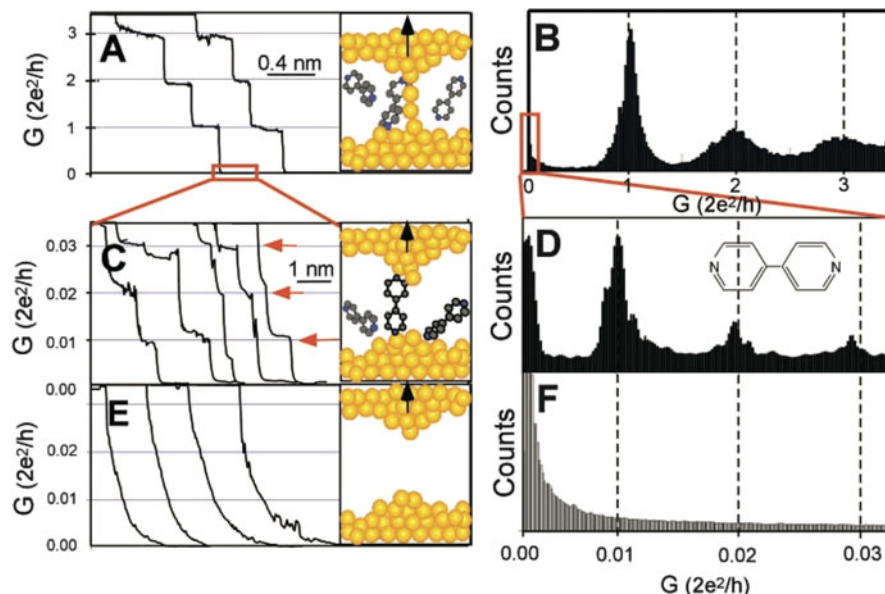


**Fig. 2.2** (a) Conductance transient curves and (b) corresponding conductance histogram above  $1 G_0$  region measured by STM-BJ method using gold electrodes. (c), (d) represent conductance transient curves and corresponding conductance histogram below  $1 G_0$  region with the presence of 4,4'-bipyridine, respectively, whereas (e), (f) show them without any molecules [15]

transient curve (Fig. 2.2a) and histogram (Fig. 2.2b). The conductance transient curves pose additional plateaus below  $1 G_0$  with the presence of molecules as shown in Fig. 2.2c, and corresponding peak is found in the conductance histogram (Fig. 2.2d), whereas no plateaus are found without the presence of molecules (Fig. 2.2e, f). The conductance histogram shows multiple peaks at the integer multiples of the fundamental conductance of  $0.01 G_0$ . The second and third peaks are attributed to two and three molecule junctions in parallel and considered as a strong evidence of the formation of a single-molecule junction at the fundamental conductance peak.

The detailed analysis of the conductance histogram sometimes reveals multiple sets of peaks [17–19]. Figure 2.3 shows conductance transient curves and histograms observed for Au/nonane-dithiol/Au junctions. The conductance plateaus are observed at different conductance ranges. The conductance histogram shows multiple peaks that can be assigned to three fundamental conductance values, indicated as L1, M1, H1, and their multiples. By comparing theoretical models, these peaks are attributed to the junction structures with different contact geometry as shown in Fig. 2.3e. The H1 and M1 correspond to the molecule junction in which the contact is formed at a bridge and an atop site, respectively. The L1 peak is assigned to the structure with bending in alkyl chain.

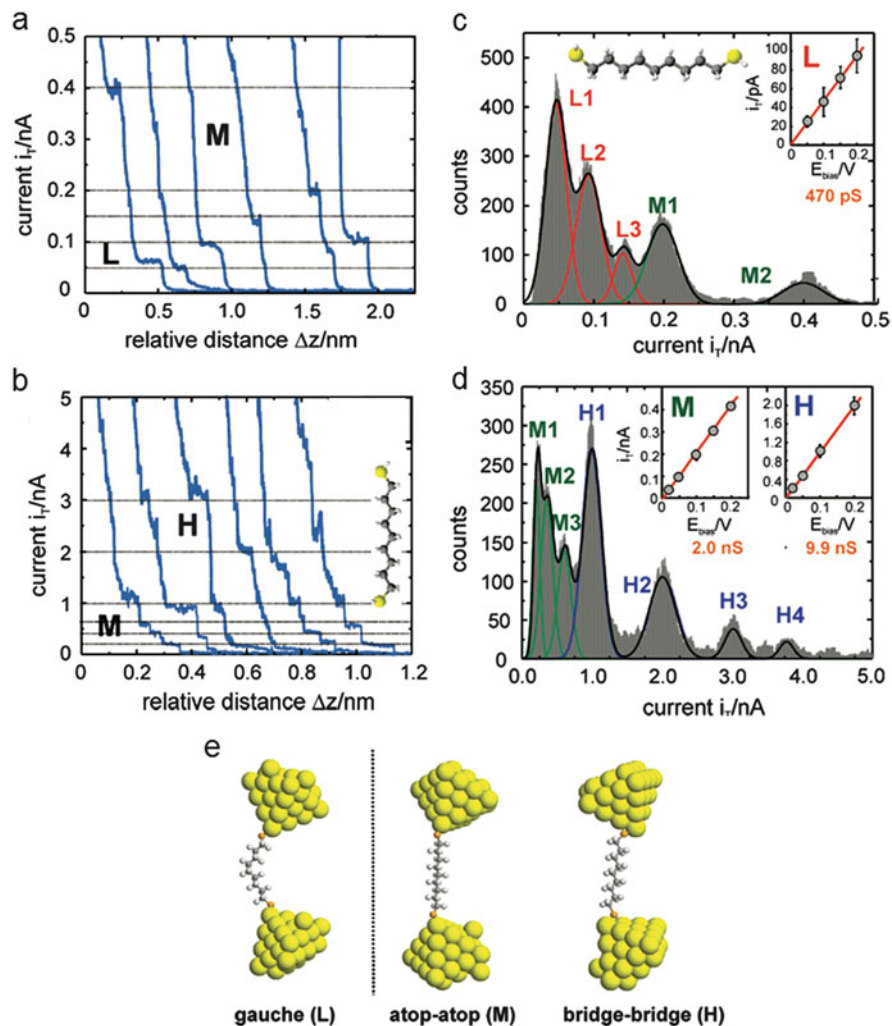


**Fig. 2.3** Current transient curves observed low (a) and high (b) conductance regions and corresponding histograms (c, d). e Proposed models showing H, M and L conductance values [19]

The statistical method using the BJ method provided a way to quantify the single-molecule conductance and is now considered as the most standard method. Based on this technique, the charge transport mechanisms in the single-molecule junction such as length dependence [15, 20, 21], twisting between adjoining  $\pi$ -orbitals [22], anchoring chemistry [23, 24], and orbital energy shift by substituent group [25] have been investigated.

The temperature dependence of the electrical conductance is one of the most basic and important characteristics to understand the charge transport mechanisms.

In the single-molecule junction, tunnel transport is usually dominant. However, thermal hopping charge transport mechanism, i.e., the thermally activated motion of the localized charge injected in a molecule, is also expected to exist. As the thermal hopping transport would open a path to create new device functions such as hysteresis (memory) [26], it is important to clarify the existence of it in the single-molecule junction.

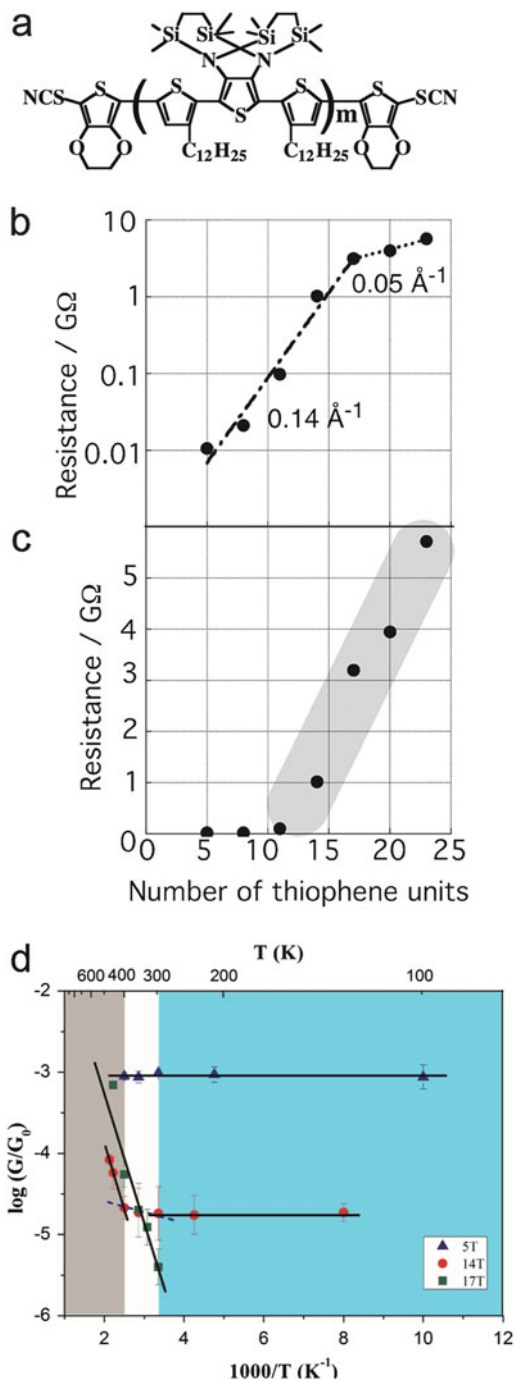
The hopping transport would prevail the tunnel transport at a long distance because the resistance due to the tunnel and hopping transport increases exponentially and linearly, respectively [27]. Temperature dependence of the resistance would give direct evidence for the hopping transport because the tunnel transport is basically a temperature-independent process, although it should be noted that weak temperature dependence can be observed even for the tunnel transport due to thermal excitation of electrons in electrodes [28].

However, it has been difficult to evaluate the temperature dependence because the change of the temperature would cause thermal fluctuations of a molecule and deformations of device structures. The BJ method in which single-molecule junctions are created at each measurement does not suffer from these problems.

The crossover between the tunneling and hopping transport was investigated using oligothiophene molecule (Fig. 2.4a) [29, 30]. The exponential increase of the resistance as a function of the molecular length with  $\beta = 1.4 \text{ nm}^{-1}$  is observed between 5 and 14 mer ( $m = 1 \sim 4$ ) which is attributed to the tunnel transport following  $R_{\text{tunnel}} = R_0 \exp(\beta l)$  where  $R_0$  is constant,  $\beta$  is a tunnel decay constant, and  $l$  is molecular length as shown in Fig. 2.4b. The much weaker slope with  $\beta = 0.5 \text{ nm}^{-1}$  is observed for longer molecules suggesting the change of the transport mechanism to hopping. In fact, the resistance of the longer molecules shows linear dependence on the molecular length as shown in Fig. 2.4c that is expected for the hopping transport.

To confirm the hopping transport, temperature dependence of the conductance was measured for 5- ( $m = 1$ ), 14- ( $m = 4$ ), 17-mer ( $m = 5$ ) molecules. Figure 2.4d shows the Arrhenius plot of the conductance values measured. The conductance of 5-mer molecule does not show clear temperature dependence, whereas that of 17-mer molecule shows clear temperature dependence with an activation energy of 0.3 eV. The conductance of 14-mer molecule is temperature independent below 300 K and starts to increase as temperature is raised. Above 400 K, the slope in the Arrhenius plot is equivalent to that observed for 17-mer molecule. Their result clearly demonstrated the crossover between tunneling and hopping transport as a function of not only molecular length but also temperature.

**Fig. 2.4** (a) The structure of oligothiophene molecule used in the measurement. (b), (c) show resistance values as a function of molecular length in semilog and linear scale, respectively [29]. (d) The Arrhenius plot of the conductance for 5-, 14-, and 17-mer molecules [30]



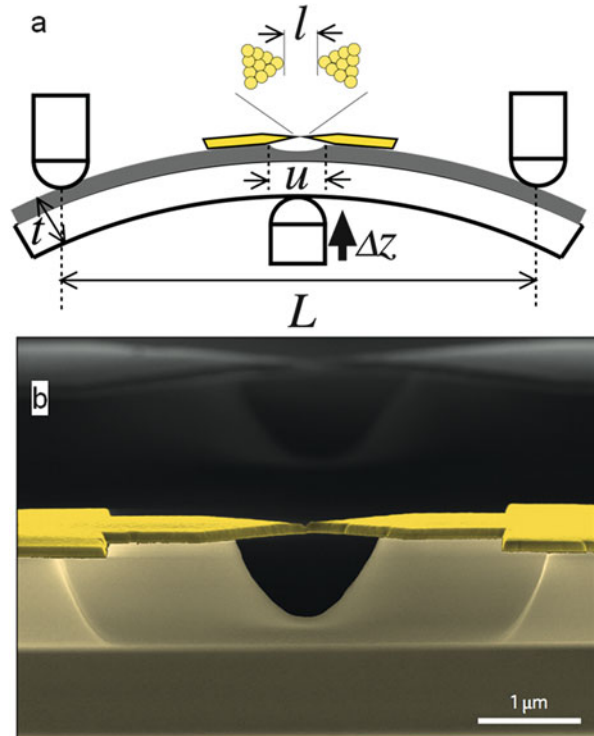
### 2.2.1.2 Mechanically Controllable Break Junction

The MCBJ method uses a suspended metal contact fabricated on an elastic substrate as shown in Fig. 2.5a [7–10]. The substrate is placed in the three-point bending machine. The rod (pushing rod) at the center of the substrate is moved vertically by a screw and/or piezo-actuator to bend the substrate. The bending of the substrate elongates and finally breaks the metal contact.

The elastic substrate is usually made of metal sheets such as phosphor bronze and spring stainless steel. The surface of the metal substrate is insulated by polymer, typically polyimide. Then, the metal electrodes are fabricated by either putting metal wires with a notch created by etching or mechanical cutting or micro/nano-lithography process. The latter is more popular because it can achieve higher resolution. In case of using the lithography process to fabricate the electrode, the insulating layer (polyimide) underneath the electrode is etched using the reactive ion etching (RIE) method to make the electrodes suspended (Fig. 2.5b).

The advantage of MCBJ technique is high resolution and stability. The vertical motion of the pushing rod is converted to the lateral motion with an attenuation factor that is determined by the geometry of the chip. With a configuration shown in Fig. 2.5a, the attenuation factor ( $a$ ) is estimated by  $a = \Delta l / \Delta z \sim 6ut / L^2$ , where

**Fig. 2.5** (a) A schematic of a MCBJ setup. (b) A scanning electron microscopy image of a suspended electrode for MCBJ measurements prepared by lithography and etching technique [58]



$\Delta z$  is the displacement of the pushing rod,  $\Delta l$  is the change of the gap distance,  $u$  is the length of the suspended bridge,  $t$  is the thickness of the support materials, and  $L$  is the length between two supporting points in the three-point bending configuration [31].

For example,  $L = 15$  mm,  $u = 4$   $\mu\text{m}$ , and  $t = 100$   $\mu\text{m}$  give  $a = 10^{-5}$ . The pushing rod can be controlled within an accuracy of 1 nm by using piezoelectric actuator, and thus, sub-pm resolution can be achievable theoretically. In addition to the high distance resolution, the MCBJ setup is more robust against external vibrations and thermal fluctuations than STM because mobile parts are assembled in a small space and the bending machine itself can be also designed to be compact which is favorable to make the device mechanically robust and achieve high mechanical resonant frequency.

The resolution of the MCBJ method can be evaluated by measuring the decay of the tunneling current at low bias voltages [32]. The tunneling current ( $I$ ) at the low bias voltages is described as

$$I \propto \exp\left(-2l \sqrt{2m\phi} / \hbar\right) \sim \exp\left(-10.2l \sqrt{\phi} (eV)^{-0.5} \text{ nm}^{-1}\right),$$

where  $l$  is the gap distance,  $m$  is the electron effective mass, and  $\phi$  is the tunneling barrier height. The decay of the tunneling current from  $I_1$  to  $I_2$  according to the change of the gap distance from  $l_1$  to  $l_2$  is expressed as

$$I_1/I_2 \propto \exp\left\{-10.2 (l_1 - l_2) \sqrt{\phi} (eV)^{-0.5} \text{ nm}^{-1}\right\}$$

By fitting the observed current decay as a function of the motion of the pushing rod with assuming barrier height to be a few eV, the actual attenuation factor can be obtained. Typically, actual distance resolution of MCBJ method is in the order of tens of pm.

Due to the high distance resolution and stability, MCBJ is frequently used to measure current-voltage characteristics of the single-molecule junctions. Figure 2.6 shows results on current-voltage (IV) measurements of 9,10-dihydroanthracene bridged between gold electrodes carried out under the elongation of the gap distance at 6 K [33]. The IV characteristics show negative differential resistance (NDR) which is caused by breaking of the resonance tunneling between two  $\pi$ -conjugating units under the bias voltage as shown in Fig. 2.6a. As the gap distance increases, the NDR is weakened and disappeared. The stable IV measurements under precise control of the gap distance allows us to create the conductance transient by plotting the conductance determined from the IV characteristics at low bias regions as shown in Fig. 2.6b and to find the relation between NDR behaviors and structure of the conductance plateaus which will be helpful to understand the structure of the junction. Also, detailed IV characteristics and other interesting transport properties such as inelastic tunneling spectroscopy and noise spectroscopy are measured, which is discussed in Chap. 3.

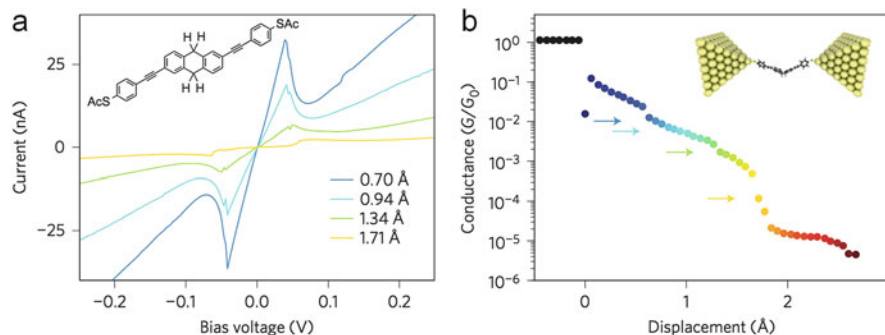


**Fig. 2.6** (a) Current-voltage characteristics of the single-molecule junction of 9,10-dihydroanthracene using gold electrodes as a function of different gap separations at 6 K. Inset shows the structure of the molecule. (b) A conductance transient curve created from the IV characteristics at different gap distances. *Colored arrows* show positions where the current-voltage curves with the same color in (a) are taken [33]

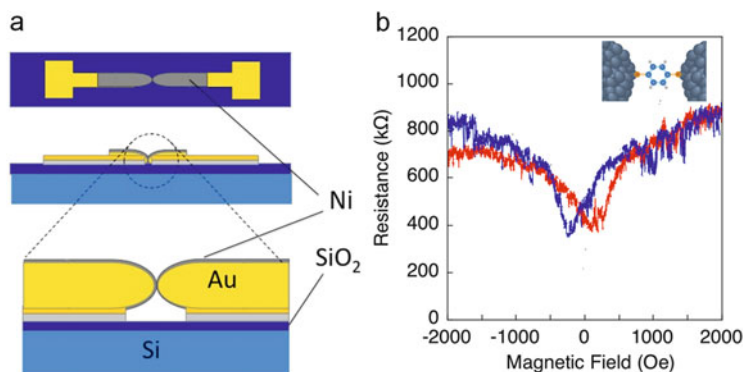


**Fig. 2.7** (a) A schematic of a structure of the electrode used to measure MR effect in the MCBJ setup. (b) Resistance as a function of external magnetic fields (MR loop) observed for a benzenedithiol single-molecule junction using Ni electrodes

MCBJ is also useful to measure effects of external fields on the charge transport characteristics such as magnetic and electrostatic fields. However, the mechanical deformations of the electrodes caused by the external fields should be avoided. For example, to measure the magnetic field effects on single-molecule junctions using ferromagnetic electrodes (magnetoresistance (MR)), mechanical deformations of the electrode due to magnetic force and magnetostriction should be avoided [34, 35].

Figure 2.7a shows the structure of the electrode used to measure the MR effect of single-molecule junctions using Ni electrodes [36]. Initially gold electrodes with a gap separation of 4  $\mu\text{m}$  were prepared by conventional photolithography. Then, the gap separation was reduced to  $\sim 0.5 \mu\text{m}$  by electrodeposition of gold onto the electrode pattern. Then, a ferromagnetic layer (Ni) was electrochemically deposited

to form a nano-contact of Ni. In this electrode structure, the supporting gold electrodes are robust enough to avoid the deformation due to the magnetic fields, and the Ni layer is thin enough to remove the effect due to magnetostriction. By using this device structure, MR loop is successfully measured as shown in Fig. 2.7b. Device structures for electrostatic field will be explained in Sect. 2.3.3.

## 2.2.2 Statistical Data Analysis

Since the current transient measured during the break junction process can be originated from various junction structures formed during the breaking process, a statistical analysis is usually used to determine the conductance of a single-molecule junction. The statistical analysis also reveals useful information such as sequences of the structures appearing during the breaking process. In this section, typical analysis methods in addition to the conductance histogram are explained.

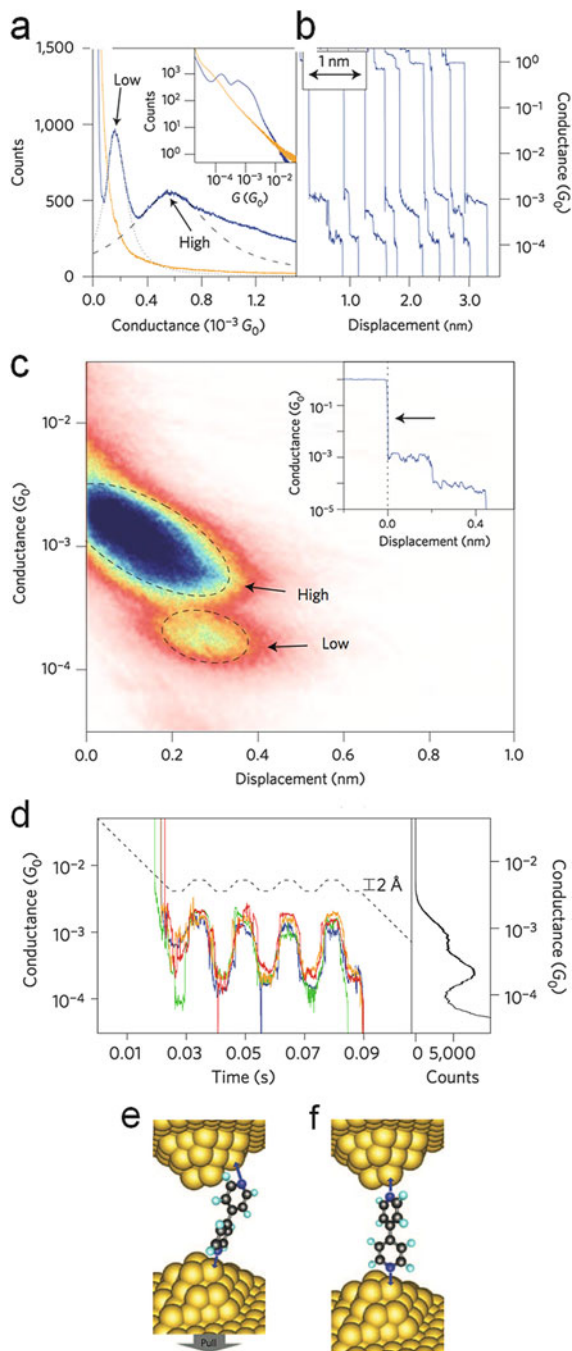
### 2.2.2.1 Distance and Conductance: Two-Dimensional Histogram

The conductance transient curves contain information not only on conductance but also on distance. Since changes of the gap distance can alter structures of a single-molecule junction, dependence of conductance values on the gap distance would give fruitful information on the structure of the single-molecule junction. Two-dimensional (2D) histograms are useful to analyze distribution of the conductance as a function of gap distance (or stretching length) [37].

Figure 2.8a shows conductance histogram obtained for 4,4'-bipyridine using gold electrodes [38], showing two peaks as indicated as low and high. The conductance transients (Fig. 2.8b) show a trend that the low conductance plateaus appear after the high conductance plateaus.

The distance distribution of the high and low conductance states is evident in the conductance 2D histogram shown in Fig. 2.8c. In the 2D histogram, the number of data points at a certain conductance and distance is counted and shown as a color map. A huge peak is observed around the position where the displacement is 0.2 nm and the conductance is  $10^{-3} G_0$  which corresponds to the high conductance state observed in the conductance histogram shown in Fig. 2.8a. The small peak which corresponds to the low conductance state is observed just below the huge peak. From this 2D histogram, it is found that the high conductance state appears just after the breaking of the junction, whereas the low conductance state appears after the gap distance is separated more than 0.2 nm. In fact, these two conductance states can be reversibly switched by controlling the gap distance as shown in Fig. 2.8d. With the help of theoretical calculation, the transition between the high and low conductance states is attributed to the sliding of the bonding site of nitrogen on the gold tip (Fig. 2.8e).

**Fig. 2.8** Conductance histogram (a) and transient curves (b) observed for 4,4'-bipyridine using gold electrodes. (c) 2D histogram of the conductance transient curves observed. The displacement is measured with respect to the position where the conductance drops from  $1 G_0$ . (d) Conductance measured with a distance modulation showing reversible conductance switching between high and low conductance states. *Dashed curve* represents motion of the STM tip. The colored curves show the conductance measured in different experiments. (e) Schematic models of the junction for high and low conductance states [38]



### 2.2.2.2 Cross Correlation and Conditional Histogram Analysis

The conductance transient curves contain information on dynamics of the junction formation. For example, in the molecular mechanical switch shown in Fig. 2.8, the low conductance plateau appears following to the high conductance plateau. This kind of correlation between different conductance values is useful to understand the formation dynamics of the junction and is evaluated by cross correlation analysis in which correlation between each bin of the conductance histogram for all conductance transient curves is evaluated. In this section, the interpretation of the cross correlation analysis is briefly explained by some examples because methods to create cross correlation histogram are too technical to be explained here. For more details, readers may refer other articles [39–41].

Figure 2.9a, b shows the conductance transient and histogram obtained between Co tip and Ge substrate, respectively [39]. The conductance histogram reveals several sharp peaks indicated by *a-g*. The conductance transient curves tend to have certain sets of sequence of the plateaus, such as *f-c-a* and *f-d-a*.

This trend is clearly resolved in cross correlation histogram shown in Fig. 2.9c. In this histogram, the co-relation between two conductance values indicated in horizontal and vertical axes is shown. White color (or bright area) corresponds to positive values. The peaks at diagonal correspond to the peaks in the conductance histogram shown in Fig. 2.9b. For example, when one looks at the horizontal position at the conductance peak *a*, a strong peak is found at the location of the peak *c*. On the other hand, there are no peaks observed at location of the peak *b*. This result indicates that the peak *c* appears in accordance with the peak *a* but not *b*.

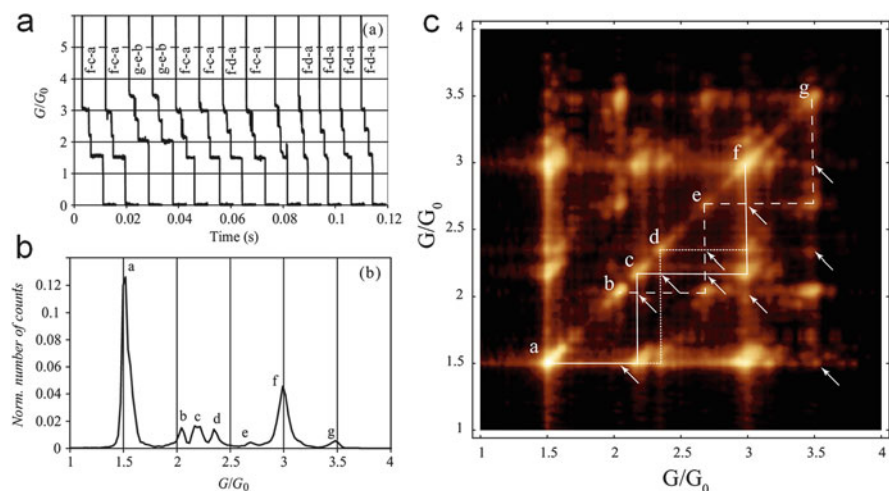


**Fig. 2.9** Conductance transient curves (a) and histogram (b) obtained for Co-Ge junction. (c) Conductance co-relation histogram. Typical scenarios of breaking sequence are indicated by *solid*, *dotted*, and *dashed* lines [39]

We can also find a peak between the peak c and the peak f. Therefore, a sequence f-c-a is expected during the break junction process. Similarly, sequences g-e-b and f-d-a are identified. This analysis gives information on the formation dynamic of the junction.

The detailed analysis of the cross correlation on the break junction data revealed that the cross correlation histogram shows not only the correlation in the occurrence of the plateau but also that of the plateau lengths. Although two conductance values are correlated in occurrence, the cross correlation value can be negative due to negative correlation in plateau length, e.g., long plateau followed by short plateau. The correlation in the occurrence can be evaluated by creating conditional histograms that are made from data sets contributing to certain histogram peaks of interest [40]. If two histogram peaks, A, B, possess anticorrelation (correlation) in occurrence, the histogram created from the data contributing to peak A does not (does) show peak B. The histogram created in this manner is called conditional histogram.

Figure 2.10 show an example of correlation analysis on 4,4'-bipyridine molecule junction shown in Fig. 2.8 [40]. The conductance histogram (Fig. 2.10a, black shadowed) shows two distinct peaks. The cross correlation histogram (Fig. 2.10c) shows negative value for these two peaks, which indicates anticorrelation of

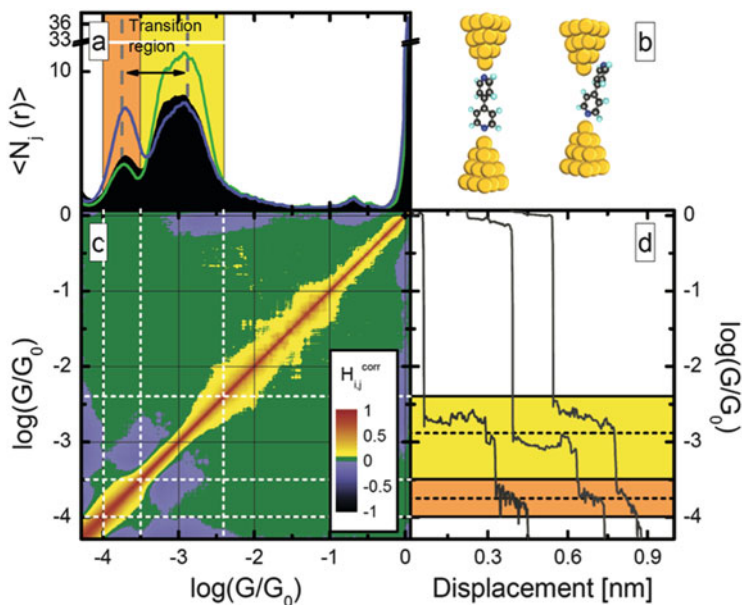


**Fig. 2.10** Correlation analysis of the conductance of 4,4'-bipyridine molecule junction using gold electrodes. (a) Whole conductance histogram (*black shaded*) and conditional histogram for low conductance (*green line*) and high conductance (*blue line*). (b) Proposed model for high and low conductance states. (c) Two-dimensional correlation histogram. (d) Typical conductance transient curves [40]

occurrence or plateau length. As the conditional histogram for the small conductance peak (Fig. 2.10a, blue curve) shows high conductance peak and vice versa, the negative correlation is attributed to the anticorrelation of plateau length. Therefore, the correlation in occurrence exists between the high and low conductance states which support the proposed mechanism of the conductance switching.

## 2.2.3 Related Techniques

### 2.2.3.1 Distance Modulations

In the break junction measurement, formations of single-molecule junctions are detected by the conductance plateaus that can be basically evident only after the breaking of the junctions. A distance modulation technique [42] provides useful information on the formation of the single-molecule junctions and convenient especially when one would like to conduct static measurements such as current-voltage measurements on a single-molecule junction.

In this technique, the distance between two electrodes is modulated at a certain frequency and the AC component of the current synchronizing to the gap distance modulation is measured. In brief, when a current ( $I$ ) is measured at a gap distance ( $D = d_0$ ), the amplitude of the AC current corresponds to  $dI/dD$  at  $d_0$  that should be close to 0 where the conductance plateau is formed.

The total current  $I$  is described as

$$I = I_{\text{DC}} + dI/dD A_0 \cos \omega t,$$

where  $I_{\text{DC}}$ ,  $A_0$ , and  $\omega$  are the measured DC current, amplitude of the distance modulation, and angular frequency, respectively.

First of all, the expression for  $dI/dD$  in case of the vacuum tunneling is discussed. In this case, this technique is equal to the barrier height measurement used in the conventional STM measurement [43]:

$$I_{\text{DC}} \sim I_0 \exp(-\beta D),$$

where  $\beta$  is the tunneling decay constant and  $I_0$  is a constant.

$$dI_{\text{DC}}/dD = -I_0 \beta \exp(-\beta D) = -\beta I_{\text{DC}}$$

Therefore,

$$\beta = -dI/dD/I_{\text{DC}}$$

In the single-molecule junction, the current response with respect to distance is not expressed by a simple equation because it can contain various effects such as

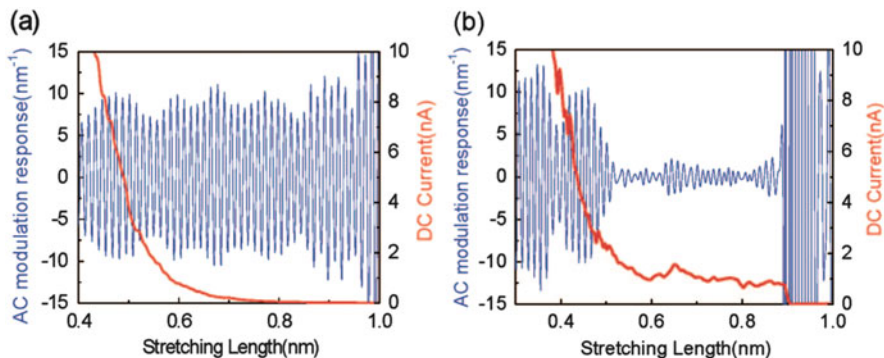


**Fig. 2.11**  $I_{DC}$  (red) and  $I_{AC}/I_{DC}$  (blue) measured in the break junction measurement without (a) and with (b) the presence of 1,8'-octanedithiol. The amplitude or peak value of  $I_{AC}/I_{DC}$  gives  $\alpha$  [42]

mechanical elongation of the junctions and piezoelectric response of molecules [44]. However,  $dI/dD/I_{DC}$  is still a convenient parameter to describe mechanical response of the single-molecule junction since  $dI/dD$  should be normalized and referred as  $\alpha$ .

Figure 2.11 shows  $I_{DC}$  and  $I_{AC}/I_{DC}$  whose amplitude represents  $\alpha$  observed in the experiment using 1,8'-octanedithiol [42]. When no molecules are contained in the measurement system (Fig. 2.11a), only exponential decay of  $I_{DC}$  and almost constant  $\alpha$  are observed. In the presence of 1,8'-octadecanedithiol (Fig. 2.11b),  $I_{DC}$  shows stepwise changes (plateaus) and  $\alpha$  becomes small at the plateau region. After the break down of the plateau,  $\alpha$  suddenly increased. These results demonstrate  $\alpha$  is a good indicator to monitor the formation of the single-molecule junctions.

The ability of the distance modulation technique was demonstrated in the measurements of a molecular diode [45]. It is necessary to know the orientation of the molecular diode with respect to the bias voltage to understand the rectification behavior. However, it is not possible to maintain or identify the orientation of the molecule in the break junction measurement. Therefore, the measurement was conducted by gently contacting the STM tip to the surface of the self-assembled monolayer of the diode molecule whose orientation is controlled by a sequential two-step chemical deprotection method as shown in Fig. 2.12a. When the position of the STM tip is held at the conductance of the single diode molecule determined by the conventional break junction method, the  $\alpha$  and  $I_{DC}$  stochastically change (Fig. 2.12b). The jump of  $I_{DC}$  to higher value is accompanied by the jump of  $\alpha$  to smaller value, which indicates the formation of the molecule junction, allowing the detection of the formation of the molecule junctions. The current-voltage characteristic is measured when the junction is formed (Fig. 2.12b). The modulation in parallel to the substrate in the STM setup is used to evaluate the lateral coupling between molecules and substrate [46].

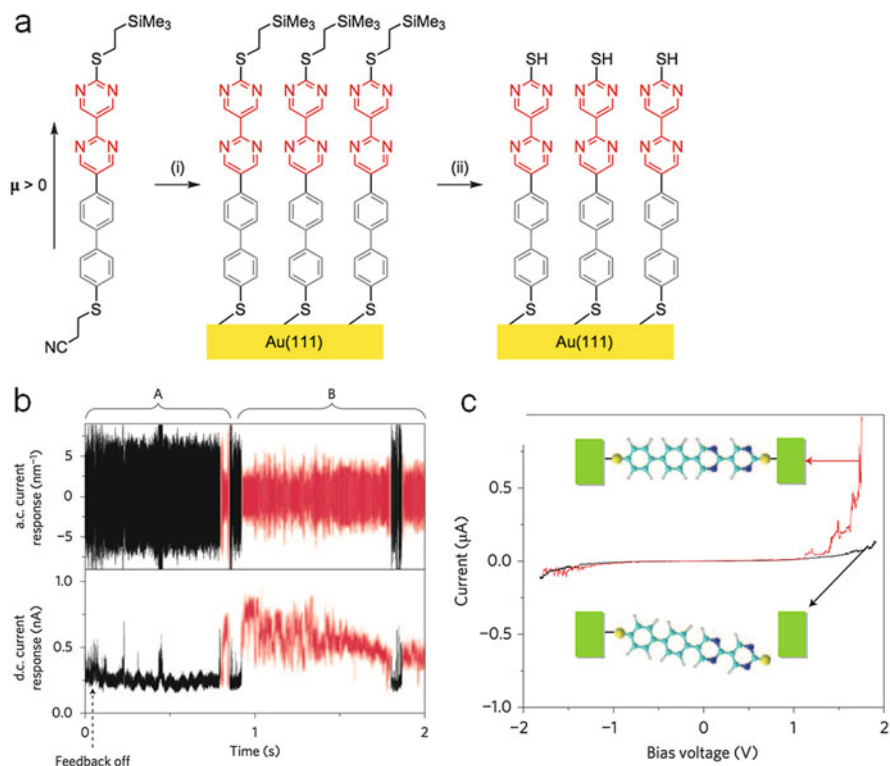


**Fig. 2.12** (a) A method to prepare a monolayer of diode molecule (dipyrimidinyl-diphenyl molecule). A thiol group at the top of the molecule in the figure is deactivated by a protecting group so that the molecules adsorbed only through sulfur atoms at the bottom end of the molecule (step I). After the formation of the monolayer, the protecting group is chemically detached and SH groups which can bind to metal electrodes is generated on *top* of the molecule. (b)  $I_{AC}/I_{DC}$  and  $I_{DC}$  measured. The gap distance was held during the measurement. (c) Current-voltage characteristics measured at the region A (black) and B (red) in (b), which corresponds to the junction with a tunnel gap and the single-molecule junction, respectively [45]

### 2.2.3.2 Electromechanical Responses

The breaking process of the junction is studied in more detail by using an atomic force microscope (AFM) [47–51]. The force observed during the breaking process combined with the electrical conductance gives information on the bonding structure between molecules and electrodes. This measurement is also interesting to understand changes of electrical characteristics caused by mechanical perturbations, i.e., electromechanical responses, of the single-molecule junction that can be used to design single-molecule electronic devices. In this section, the procedure and an example of the measurement are briefly introduced. More detailed discussion is given in Chap. 3.

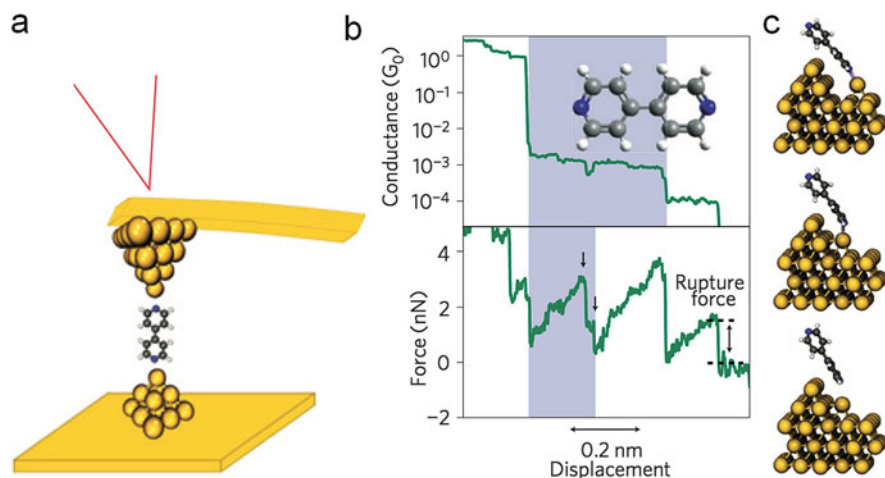


**Fig. 2.13** (a) A schematic of the AFM-BJ method. The deflection of the cantilever is monitored by the position of a laser reflected from the backside of the cantilever. The bias voltage is applied between the tip and the substrate. (b) A conductance transient curve obtained for 4,4'-bipyridine junction using Au electrodes and force measured simultaneously. (c) Model structures representing the force rupture event observed in the middle of the conductance plateau indicated by *arrows* [50]

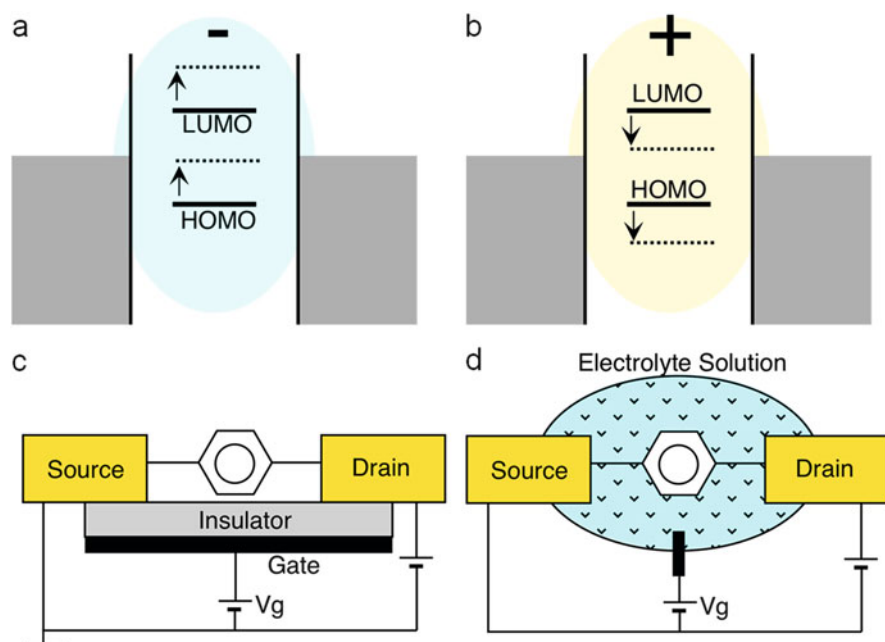
Figure 2.13a shows a scheme of the measurement system. The BJ measurement is carried out with a metal-coated AFM tip. The force acting on the tip is measured from the deflection of a cantilever by a conventional AFM setup. A bias voltage is applied between the AFM tip and the substrate and electrical current is measured simultaneously with the force.

Figure 2.13b shows the conductance and force transient obtained for 4,4'-bipyridine junction using Au electrode [50]. The conductance transient shows clear two-step plateaus and sharp decrease of force is observed at the conductance steps where the bonding between molecules and electrodes is broken. In addition, another sharp drop in the force transient is observed in the middle of the first long conductance plateau at  $10^{-3} G_0$  where a small dip of the conductance is observed. This result indicates that structural changes of the molecule junction without causing significant changes in the conductance can be detected by the force measurement. A proposed model for this structural change is shown in Fig. 2.13c. After the breaking of the gold atomic contact, the molecule can bind to rough gold surface through both specific bonding through N atom and van der Waals interaction through carbon ring. Upon elongation of the gap distance, the van der Waals bonding ruptures and causes a drop of force, whereas the conductance does not change a lot. More detailed and quantitative analysis of the rupture force can be used to deduce the strength of the bonding between electrode and molecule as discussed in Chap. 3.

### 2.2.3.3 Electrical and Electrolyte Gating

An application of an electrostatic gate field shifts the energy of the system and hence the transport characteristics. When the junction is positively (negatively) charged, the energy levels would be shifted to higher (lower) levels (Fig. 2.14a, b). The gate effect is not only useful to investigate transport mechanism but also an important step to realize active devices [52]. Fabrication of a solid-state gate electrode to nm-scale junctions such as shown in Fig. 2.14c is still challenging [53]. To prepare single-molecule junctions on solid-state gate electrodes, electromigration which is explained in Sect. 3.1 and shadow mask techniques [54] have been used. However, application of gate electric fields in the MCBJ setup has been desired.

When electric field is applied to source and drain electrodes from a gate electrode placed underneath them in the MCBJ setup (Fig. 2.15a), electrostatic force causes deformations of the cantilever-shape source and drain electrodes, and the atomic contact can be reversibly opened and closed by the application of gate field as shown in Fig. 2.15b [55]. A side gate structure was developed by electron-beam lithography as shown in Fig. 2.15c [56]. However, the distance, typically in the order of tens of nm, between the gate electrode and the molecule junction is too large



**Fig. 2.14** Energy shifts of a molecule junction when negatively gated (a) and positively gated (b). Schemes for solid-state gate (c) and electrolyte gate (d). HOMO and LUMO represent highest occupied and lowest unoccupied molecular orbitals, respectively

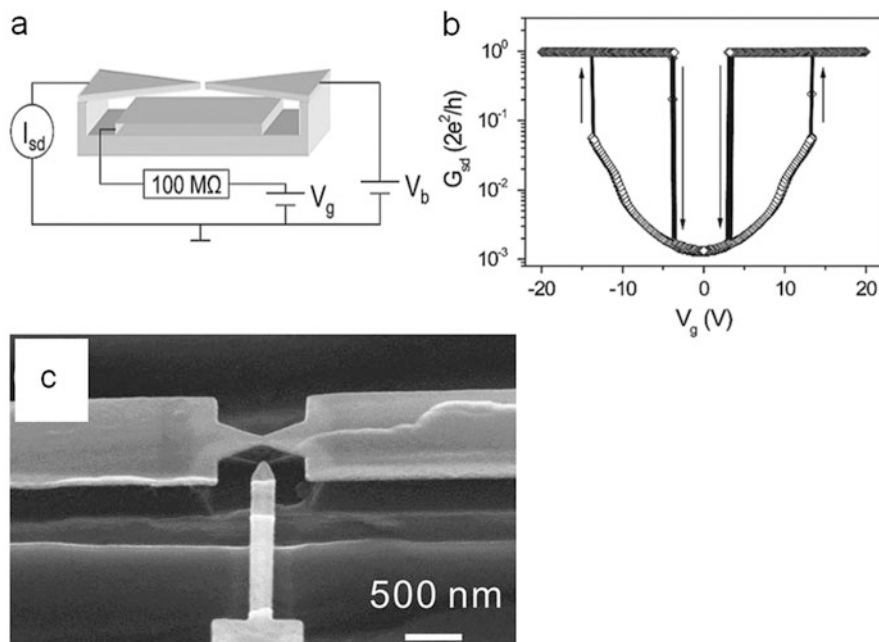


**Fig. 2.15** (a) Schematic of the device structure and measurement circuit. (b) Switching characteristics of the device under the application of the gate voltage. (c) A scanning electron microscopy image of a MCBJ device with a side gate. (a), (b) [55,56]

to generate electric fields effective to tune the electronic structure of the molecule junctions.

To realize the effective electrostatic gate effect without deformation of the source and drain electrodes, the sandwich-type electrode structure was developed [57, 58]. In this structure, the source and drain electrodes are fabricated on the gate electrode covered with aluminum oxide layer and whole electrode is suspended (Fig. 2.16a). Under the bending of the supporting substrate, only the source and drain electrode can be broken allowing the BJ measurement.

Performance of the MCBJ with the stacked gate electrode is demonstrated by using the thiol-terminated zinc-porphyrin molecule [Zn(5,15-di(p-thiolphenyl)-10,20-di(p-tolyl)porphyrin)] (ZnTPPdT) (Fig. 2.16b) [58]. The current-voltage characteristics of the single-molecule junction of ZnTPPdT shows Coulomb blockade as shown in (Fig. 2.16c). Figure 2.16d and e shows color maps of the differential conductance under the application of the source and drain voltages and gate voltages. Note that peaks appearing in the differential conductance correspond to the voltages where the current start to increase in the current-voltage characteristics shown in Fig. 2.16c and, thus, energy levels of transport channels. Figure 2.16d shows peak shifts to higher energy under the application of positive gate voltages, whereas peak shifts toward lower energy is observed in Fig. 2.16e. The observed

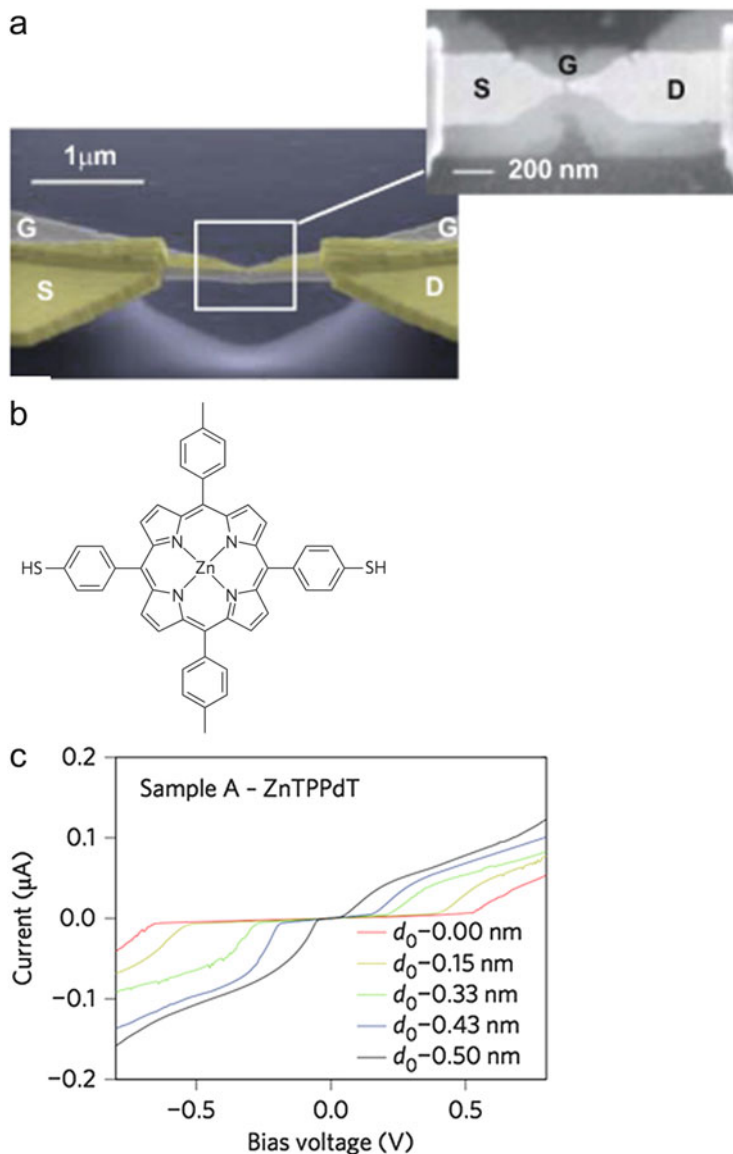


**Fig. 2.16** (a) Scanning electron microscopy images of a MCBJ electrode. A gate electrode is attached underneath suspended source (*S*) and drain (*D*) electrodes through an oxide layer [57]. (b) Structure of ZnTPPdT. (c) Typical current-voltage characteristics of the single-molecule junction of zinc porphyrin measured at various gap separations showing Coulomb blockade. (d), (e)  $dI/dV$  color maps under the application of gate voltages (horizontal axis) and source-drain voltage (vertical axis). (f) An energy diagram showing the effect of a gate voltage,  $V_g$ . The  $b$  in the figure represents the effective gate coupling strength which is used to estimate the effective electrostatic field from the applied gate voltage [58]

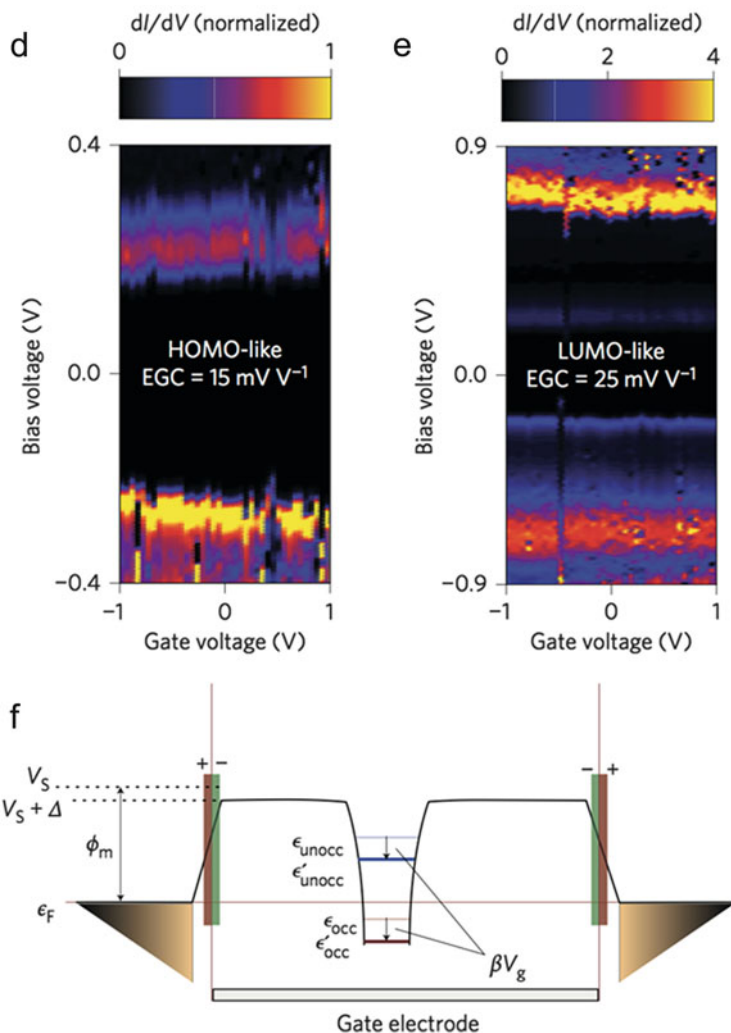


**Fig. 2.16** (continued)

behavior is explained using energy diagram shown in Fig. 2.16f. When positive gate voltage is applied, energy levels in the molecule are shifted to lower energy. The downward shift opens the gap between Fermi level and highest occupied molecular orbital (HOMO)-like transport channel, resulting in the shift of the peak in differential conductance toward higher energy, which is observed in Fig. 2.16d. On the contrary, the gap between Fermi level and lowest unoccupied molecular orbital (LUMO)-like transport channel would become small under the application of positive gate voltage, which is observed in Fig. 2.16e. Note that HOMO-like and LUMO-like indicate the energy levels of the molecule in the junction used for the

charge transport that does not always correspond to the HOMO and LUMO of the molecule in gas phase.

The electric field effect can be also studied by using electrochemical environment, i.e., in electrolyte solutions, as shown in Fig. 2.14d [59]. In this method, the gate electric field (electrochemical potential) is applied through the electric double layer formed by ions in the solution. In terms of electrochemistry, electrochemical potentials of source and drain electrodes are controlled with respect to the reference electrode put in the solution. There are two possible gating mechanisms in electrochemical environment. One of the mechanisms uses the electric field applied through electric double layers formed by ions whose thickness can be reduced in the order of 0.1 nm, allowing the generation of strong electric field for the gating. In the electrochemistry term, this process corresponds to the potential scan in the so-called double-layer region where no electrochemical reactions (or Faradic current) take place. In another mechanism, the electrochemical reaction of the molecule takes place, i.e., the electronic state of the junction is tuned by the charge injection into the molecule. The former and the latter are sometimes referred as electrolyte and electrochemical gating, respectively.

The electrolyte gating is convenient because it can be applicable for both STM-BJ and MCBJ. However, one should pay attention that the charge transport mechanism can be affected by polar solvents. For example, single-molecule junctions of perylene tetracarboxylic diimide (PTCDI) derivatives show temperature-independent tunneling transport and temperature-dependent hopping transport in nonpolar and polar solvent, respectively [60].

## 2.3 Other Experimental Methods to Prepare Single-Molecule Junctions

### 2.3.1 Electromigration Technique

When sufficient electrical current is applied in a narrow metal wire and a critical temperature is reached by Joule heating, metal atoms in the metal wire become mobile and start to drift due to the transfer of momentum of electron [53, 61]. The drift of the metal atoms results in the gradual reduction of the size of the wire and eventually formation of atomic contact and a gap. This process is called electromigration.

To fabricate a gapped electrode by this technique, a necked wire pattern is prepared where the gap should be created (Fig. 2.17a). When a voltage applied to the wire is increased, the electrical current starts to collapse at a certain voltage (Fig. 2.17b, denoted 1) where the electromigration process begins. The voltage should be quickly decreased to avoid the catastrophic breaking of the wire (Fig. 2.17b, denoted 2–3) and then increased again to cause the next electromigration process (Fig. 2.17b, denoted 4). By repeating this cycle, the wire is narrowed to reach atomic size and finally a gap is formed. This process can be monitored

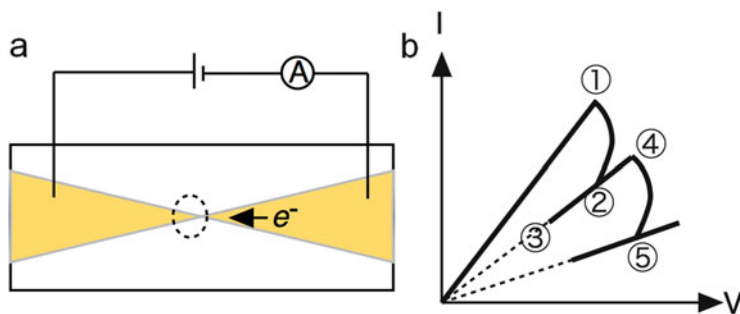


**Fig. 2.17** (a) Scheme of an electrode subjected to the electromigration. Atoms at the necked region will be stacked around the area indicated by a *dotted circle*. (b) A scheme of electrical current observed under the successive electromigration process

from the stepwise decrease of the conductance by a quantum conductance after the electromigration process. A fast feedback control of the electrical power during the electromigration process followed by spontaneous self-breaking of atomic contacts enables researchers to prepare an atomic contact and an electrode gap with a separation of a few or less than nm [62–64]. When molecules are adsorbed on metal electrodes before breaking, molecule junctions can be formed after the breaking of the wire.

The advantage of this technique is that one can prepare single-molecule junctions on a gate insulator as explained in detail below. The disadvantages are as follows: fake signals are sometimes obtained by metal particles and grains generated in electromigration process [65]; yield of molecule junction is low, typically a few %; and the conductance of a single-molecule junction should be determined by different techniques such as the BJ techniques.

Using electromigration techniques, a single-molecule junction can be prepared on a gate insulator as schematically shown in Fig. 2.18 inset [66]. In this structure, an electrode pattern subjected to the electromigration process is fabricated on an  $\text{Al}_2\text{O}_3$  layer formed on an Al electrode which is used as a gate electrode. The electromigration was performed to prepare molecule junctions of 1,4-benzenedithiol (BDT). The formation of the molecule junction is confirmed by inelastic tunneling spectroscopy (IETS) that is explained in Chap. 3. The gate-modulated current-voltage characteristics were successfully observed as shown in Fig. 2.18.

The electromigration technique may have a potential for a mass production of gap arrays with a separation less than 1 nm which is difficult to be fabricated by

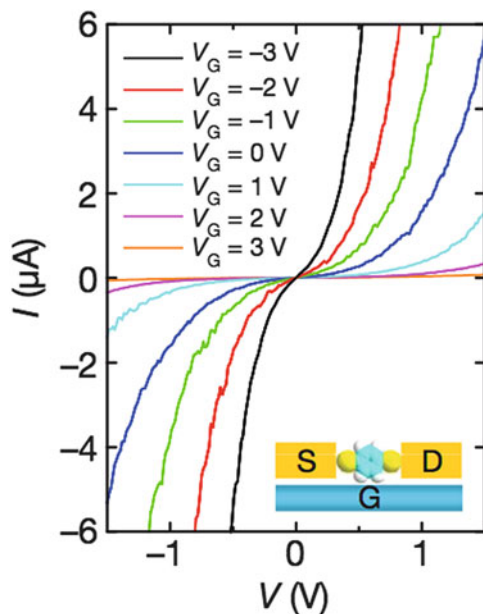
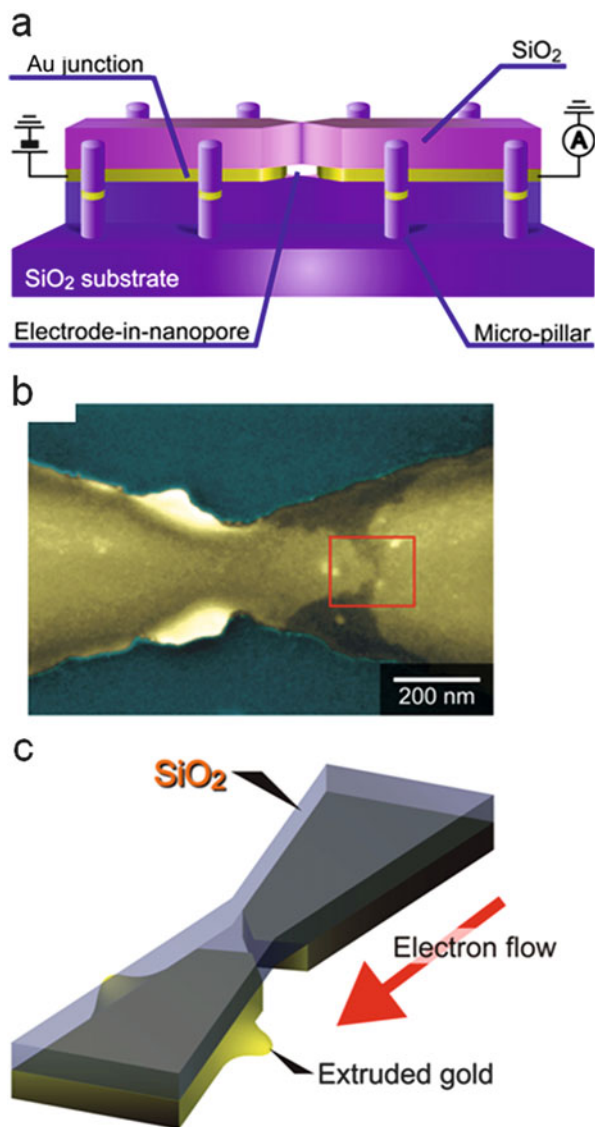


**Fig. 2.18** Schematic of device (inset) and current-voltage characteristics of a BDT molecule junction at various gate voltages.  $S$  and  $D$  represents source and drain electrodes created by the electromigration of the gold electrode.  $G$  represents Al gate electrode. An  $\text{Al}_2\text{O}_3$  layer is formed on the Al electrode by oxidation [66]

lithographic technique since sophisticated methods avoiding generation of metal nanoparticles are developed [63, 64]. The technique to control crystallinity of the electrode edge is under progress [67]. Moreover, this technique is utilized to create a novel lateral in-plane nano-hole that allows single molecules to flow in it [68]. Figure 2.19 shows the device structure. The electrode for the electromigration is sandwiched between oxide insulating layers. When the electrical current is applied, the electrode is narrowed by electromigration process. The gold atoms drift in the space confined by two insulating layers and spill over at the side of the electrode pattern (Fig. 2.19c). After the resistance of the metal electrode becomes higher than  $1 \text{ k}\Omega$ , the bias voltage is held at  $0.1 \text{ V}$  to cause spontaneous breaking of the electrode which results in the formation of regulated gap fitting to a size of single molecules [64]. By combining a fluidic channel fitting to this structure, single molecules passing through the gap in solutions are detected by measuring the electrical current between the gap. Identification of molecules is possible by analyzing the current. This technique opens a new application field for single-molecule electrical measurement techniques as an analytical tool for single molecules as explained in Chap. 9.

**Fig. 2.19** (a) Scheme of the device to create an in-plane nano-hole. Thickness of a gold layer is 15 nm. (b) A scanning electron microscopy image of the junction subjected to the electromigration process followed by spontaneous breaking. (c) Scheme of the junction imaged in (b) [68]



### 2.3.2 Ultrahigh-Vacuum and Low-Temperature Scanning Tunneling Microscope

A scanning tunneling microscope (STM) is a powerful technique to observe surfaces with atomic resolution in real space. It is, therefore, natural to use STM to measure electrical properties of single-molecule junctions. Although the stability of the instruments has been an issue, recently, commercial ultrahigh-vacuum low-

temperature (UHV-LT) STM possesses sufficient stability to create, maintain, and measure single-molecule junctions. The advantages of UHV-LT-STM are as follows: one of the electrodes can be a single-crystal surface, i.e., a well-defined structure; the existence of a molecule is confirmed directly by imaging; the location of the electrical contact in the molecule is controlled with intramolecular resolution; and the position of molecules can be manipulated on a surface. The possible drawbacks of UHV-LT-STM are as follows: it requires ultraclean environments and low temperature that requires very specialized and sophisticated knowledge and techniques; it is very time consuming, e.g., a surface should be imaged to find molecules which takes hours; and good probe tip conditions are needed for reliable measurements, which is always the case for UHV-LT-STM measurements.

In this section, some remarkable examples showing the benefit of UHV-LT-STM are briefly explained. For basic principles and mechanism of STM, readers might refer other books [69].

Manipulation of atoms and molecules is one of the fascinating and unique capabilities of UHV-LT-STM that enables researchers to investigate effects of surrounding molecules on the conductance of a single-molecule junction. Figure 2.20a shows STM images of three phenol molecules adsorbed on Cu(110) surface taken at 4.5 K [70]. The three bright spots represent each phenol molecule. The dark area observed at the right of the bright spots in Fig. 2.20a corresponds to the oxygen of phenol from which orientation of molecules can be identified. The lattice lines indicate the position of Cu atoms. Two molecules sit next to each other and one molecule is isolated. When the STM tip is approached to the molecule indicated by 1 in Fig. 2.20a, the tunneling current suddenly jumps up to around 35 nA as shown in the curve 1 in Fig. 2.20c. At this point, the molecule 1 adsorbed on the STM tip by  $\pi$ -bonding of benzene ring and STM tip. When the same measurement was carried out on the molecule 3, i.e., the isolated molecule, the current reaches around 40 nA. This result indicates the neighboring molecule reduced the conductance of the molecule. To make sure the molecule 1 is identical to the molecule 3, the neighboring molecule was flipped to be separated from the molecule 1. The flip of the molecule can be done by lifting the molecule by approaching the tip and then moving laterally. Now, the molecule 1 is isolated as shown in Fig. 2.20b and indicated as 2. When the molecule junction is formed using the molecule 2, the measured current is the same with that observed for the molecule 3. This result clearly demonstrates the effect of neighboring molecules on the conductance of the single-molecule junction. The energy level shift caused by the electrostatic potential of neighboring molecules including dipole moment is attributed to the reduction of the conductance.

A difficult issue in handling single molecules with UHV-LT-STM is sample preparation. Most of the measurements are limited to molecules that can be sublimated in vacuum conditions. Although techniques to introduce large molecules into vacuum, such as pulse valve [71] and electrospray [72, 73], were developed, it is difficult to find right conditions to put molecules on the substrate without damages and contaminations.

For studies of large molecules by STM, on-surface polymerization is useful [74–76]. In this technique, firstly, unit molecular structures that can be sublimated are

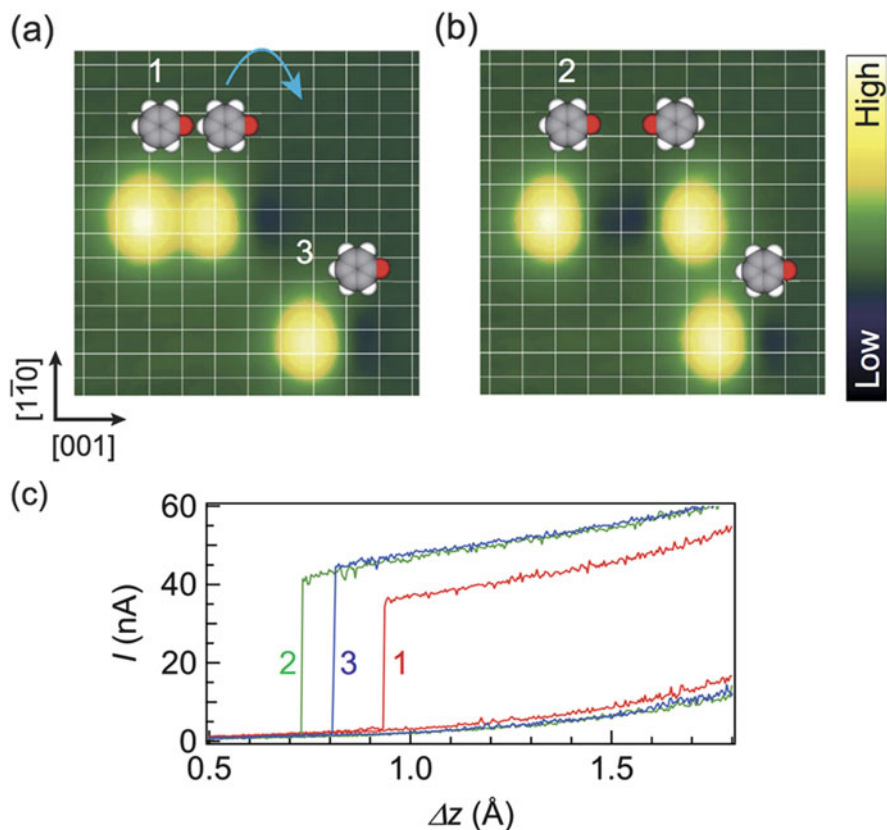


**Fig. 2.20** STM images of phenoxy molecules on Cu(110) surface taken at 4.5 K before (a) and after (b) the flip of molecule next to the one denoted 1. (c) Current transient observed during approaching the STM tip to the molecules denoted 1, 3(a), and 2(c) at the center position of each molecule. The curves not indicated by numbers are current transient taken at clean Cu(110) surface with the same STM tip used to form molecule junctions.  $\Delta z$  is displacement of the tip normal to the surface plane from the feedback point. Positive values correspond to the direction approaching to the surface [70]

adsorbed on a surface. And then, the surface is heated to cause chemical reactions between molecular units. Figure 2.21a shows an example of the molecular unit, dibromoterfluorene (DBTF), for the on-surface polymerization [75]. Figure 2.21b and c shows an experimental and calculated STM image of the DBTF molecule on an Au(111) surface at 10 K. Three intense lobes corresponding to the dimethyl groups connecting two phenyl rings in the DBTF molecule are imaged. When the Au(111) surface is heated, Br atoms dissociate from the molecule and C-C bond is formed between the molecules which thermally diffuse and collapse. Figure 2.21d, e shows STM images after heating the Au(111) surface at 520 K for 5 min. It is evident from the image that the long well-defined fluorene oligomer more than 100 nm is synthesized on the surface. The electrical conductance of the oligomer can be

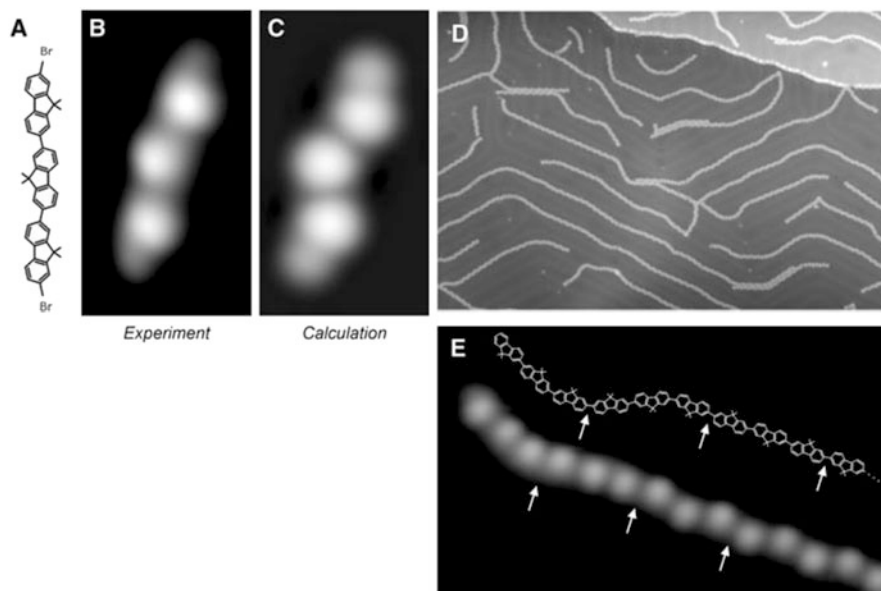


**Fig. 2.21** Chemical structure (a) and observed (b) and calculated (c) STM images of DBTF. (d) STM image of gold surface after on-surface polymerization. (e) Magnified STM image for a polyfluorene oligomer and its molecular structure [75]

measured by contacting the STM tip with one end of the oligomer and lifting the molecule.

The on-surface polymerization is useful not only for preparation of samples for STM measurements but also for synthesizing molecules that are not prepared in solutions. In fact, the long fluorene polymer shown in Fig. 2.21d cannot be prepared in solutions due to the lack of solubility.

## 2.4 Summary and Perspective

In this chapter, three representative methods used to measure electrical properties of single-molecule junctions are explained. The major difficulty of measuring single-molecule junction is confirmation of single-molecule junctions and low yield of formation of the junction. The STM-BJ and MCBJ techniques solve these problems by using mobile electrodes and have become the standard methods. Conductance traces observed during the breaking of the metal wire by mechanical motion of the electrode enable researchers to detect the formation of single-molecule junctions and also repeat measurements for many times sufficient for statistical analysis. The STM-BJ is suitable for the statistical determination of the molecular conductance because the STM setup affords thousands of measurements contentiously. Even

simple statistical analysis using conductance histogram reveals interesting nature of the single-molecule junctions such as relation between conductance and contact geometries. More sophisticated analysis such as correlation analysis and conditional histogram would provide information to understand formation process of single-molecule junctions with different configurations. The MCBJ method is capable of sustaining a single-molecule junction for a long time enough to measure current-voltage characteristics and apply more sophisticated measurement methods introduced in Chap. 3.

External modulations such as electrostatic fields and magnetic fields of single-molecule junctions are still challenging. For this purpose, the MCBJ method encounters difficulties, although some challenges have been done. Different techniques such as electromigration are used. However, the capability of distance modulation is essential to confirm the formation of single-molecule junctions, and the method to measure external modulation with MCBJ should be developed.

The stability and imaging capability of UHV-LT-STM allows researchers not only to confirm the existence of a molecule and bonding site on a substrate but also to identify orientation of molecule that is essential for the study of molecular diodes. The electromechanical properties should be also investigated more precisely by using UHV-LT-AFM. Although it still is difficult to put large molecules on surfaces without contaminations, on-surface polymerization opens a new path to prepare large molecules on clean surfaces in vacuum.

The statistical approach to determine the conductance of a single molecule by the BJ method is reliable and successful. However, the deviation of the conductance histogram often reaches several orders of magnitude. Although this deviation can be justified because conductance values for a wide variety of structures are involved in the conductance histogram, it is not straightforward to understand what the peak value and width of the histogram represent. It can represent the most frequently observed plateau and/or the most long-lasting plateau in conductance transient curves. This difference can be problematic especially in low-temperature MCBJ measurements of long molecules because various metastable structures can be stably sustained. Other analytical method should be applied to understand the meaning of plateaus in the conductance transient and peak of the conductance histogram as discussed in Chap. 3. Design of molecule junctions showing small conductance deviations should be developed for creating single-molecule devices. For this purpose, new anchor structures such as tripods [77, 78] and insulation of conductive path in a molecule should be studied such as discussed in Chaps. 5 and 6.

Fabrication of stable solid-state single-molecule devices is the most challenging topic remained. For this purpose, well-defined electrodes in atomic scale and robust contacts between electrodes and molecules are required. These requirements can be potentially fulfilled by using graphene and nanoribbons as electrodes [79]. Devices possessing functions of single molecules would be also produced by using self-assembled monolayers [80, 81].

## References

1. Ashwell GJ, Sambles JR, Martin AS, Parker WG, Szablewski M (1990) Rectifying characteristics of  $\text{Mg}[(\text{C}_{16}\text{H}_{33}\text{-Q3CNQ LB film})|\text{Pt}]$  structures. *J Chem Soc Chem Commun* 19:1374. <http://doi.org/10.1039/c39900001374>
2. Wang W, Lee T, Reed MA (2004) Elastic and inelastic electron tunneling in alkane self-assembled monolayers. *J Phys Chem B* 108(48):18398–18407. <http://doi.org/10.1021/jp048904k>
3. Cui XD (2001) Reproducible measurement of single-molecule conductivity. *Science* 294(5542):571–574. <http://doi.org/10.1126/science.1064354>
4. Dadosh T, Gordin Y, Krahn R, Khivrich I, Mahalu D, Frydman V, Bar-joseph I (2005) Measurement of the conductance of single conjugated molecules. *Nature* 436:2–6. <http://doi.org/10.1038/nature03898>
5. Jafri SHM, Löfås H, Blom T, Wallner A, Grigoriev A, Ahuja R, Leifer K (2015) Nanofabrication of molecular electronic junctions by targeted modification of metal-molecule bonds. *Sci Rep* 5:14431. <http://doi.org/10.1038/srep14431>
6. Kushmerick JG, Holt DB, Yang JC, Naciri J, Moore MH, Shashidhar R (2002) Metal-molecule contacts and charge transport across monomolecular layers: measurement and theory. *Phys Rev Lett* 89(8):086802. <http://doi.org/10.1103/PhysRevLett.89.086802>
7. Schwarz F, Lörtscher E (2014) Break-junctions for investigating transport at the molecular scale. *J Phys Condens Matter* 26(47):474201. <http://doi.org/10.1088/0953-8984/26/47/474201>
8. Xiang D, Jeong H, Lee T, Mayer D (2013) Mechanically controllable break junctions for molecular electronics. *Adv Mater* 25(35):4845–4867. <http://doi.org/10.1002/adma.201301589>
9. Tsutsui M, Taniguchi M (2012) Single molecule electronics and devices. *Sensors* (Basel, Switzerland) 12(6):7259–7298. <http://doi.org/10.3390/s120607259>
10. Van Ruitenbeek J, Scheer E, Weber HB (2005) Contacting individual molecules using mechanically controllable break junctions. *Lect Notes Phys* 680:253
11. Selzer Y, Allara DL (2006) Single-molecule electrical junctions. *Annu Rev Phys Chem* 57(1):593–623. <http://doi.org/10.1146/annurev.physchem.57.032905.104709>
12. Tao NJ (2006) Electron transport in molecular junctions. *Nat Nanotechnol* 1(3):173–181. <http://doi.org/10.1038/nnano.2006.130>
13. McCreery RL (2004) Molecular electronic junctions. *Chem Mater* 16(23):4477–4496. <http://doi.org/10.1021/cm049517q>
14. Metzger RM (2015) Unimolecular electronics. *Chem Rev* 115(11):5056–5115. <http://doi.org/10.1021/cr500459d>
15. Xu B (2003) Measurement of single-molecule resistance by repeated formation of molecular junctions. *Science* 301(5637):1221–1223. <http://doi.org/10.1126/science.1087481>
16. Reed MA (1997) Conductance of a molecular junction. *Science* 278(5336):252–254. <http://doi.org/10.1126/science.278.5336.252>
17. Li X, He J, Hihath J, Xu B, Lindsay SM, Tao N (2006) Conductance of single alkanedithiols: conduction mechanism and effect of molecule–electrode contacts. *J Am Chem Soc* 128(6):2135–2141. <http://doi.org/10.1021/ja057316x>
18. Ishtzuka K, Suzuki M, Fujii S, Takayama Y, Sato F, Fujihira M (2006) Effect of molecule–electrode contacts on single-molecule conductivity of  $\pi$ -conjugated system measured by scanning tunneling microscopy under ultrahigh vacuum. *Jpn J Appl Phys Part 1* 45(3 B):2037–2040. <http://doi.org/10.1143/JJAP.45.2037>
19. Li C, Pobelov I, Wandlowski T, Bagrets A, Arnold A, Evers F (2008) Charge transport in single Au|Alkanedithiol|Au junctions: coordination geometries and conformational degrees of freedom. *J Am Chem Soc* 130(17):19. <http://doi.org/10.1021/ja0762386>
20. He J, Chen F, Li J, Sankey OF, Terazono Y, Herrero C, Lindsay SM (2005) Electronic decay constant of carotenoid polyenes from single-molecule measurements. *J Am Chem Soc* 127(5):1384–1385. <http://doi.org/10.1021/ja043279i>

21. Yamada R, Kumazawa H, Noutoshi T, Tanaka S, Tada H (2008) Electrical conductance of oligothiophene molecular wires. *Nano Lett* 8(4):1237–1240. <http://doi.org/10.1021/nl0732023>
22. Venkataraman L, Klare JE, Nuckolls C, Hybertsen MS, Steigerwald ML (2006) Dependence of single-molecule junction conductance on molecular conformation. *Nature* 442(7105):904–907. <http://doi.org/10.1038/nature05037>
23. Chen F, Li X, Hihath J, Huang Z, Tao N (2006) Effect of anchoring groups on single-molecule conductance: comparative study of thiol-, amine-, and carboxylic-acid-terminated molecules. *J Am Chem Soc* 128(49):15874–15881. <http://doi.org/10.1021/ja065864k>
24. Park YS, Whalley AC, Kamenetska M, Steigerwald ML, Hybertsen MS, Nuckolls C, Venkataraman L (2007) Contact chemistry and single-molecule conductance: a comparison of phosphines, methyl sulfides, and amines. *J Am Chem Soc* 129(51):15768–15769. <http://doi.org/10.1021/ja0773857>
25. Venkataraman L, Park YS, Whalley AC, Nuckolls C, Hybertsen MS, Steigerwald ML (2007) Electronics and chemistry: varying single-molecule junction conductance using chemical substituents. *Nano Lett* 7(2):502–506. <http://doi.org/10.1021/nl062923j>
26. Troisi A, Ratner MA (2006) Molecular signatures in the transport properties of molecular wire junctions: what makes a junction “molecular”? *Small* 2(2):172–181. <http://doi.org/10.1002/sml.200500201>
27. Luo L, Choi SH, Frisbie CD (2011) Probing hopping conduction in conjugated molecular wires connected to metal electrodes. *Chem Mater* 23(3):631–645. <http://doi.org/10.1021/cm102402t>
28. Poot M, Osorio E, O’Neill K, Thijssen JM, Vanmaekelbergh D, van Walree CA, van der Zant HSJ (2006) Temperature dependence of three-terminal molecular junctions with sulfur end-functionalized tercylohexylidenes. *Nano Lett* 6(5):1031–1035. <http://doi.org/10.1021/nl0604513>
29. Yamada R, Kumazawa H, Tanaka S, Tada H (2009) Electrical resistance of long oligothiophene molecules. *Appl Phys Express* 2(2). <http://doi.org/10.1143/APEX.2.025002>
30. Lee SK, Yamada R, Tanaka S, Chang GS, Asai Y, Tada H (2012) Universal temperature crossover behavior of electrical conductance in a single oligothiophene molecular wire. *ACS Nano* 6(6):5078–5082. <http://doi.org/10.1021/nm3006976>
31. Vrouwe S, van der Giessen E, van der Molen S, Dulic D, Trouwborst M, van Wees B (2005) Mechanics of lithographically defined break junctions. *Phys Rev B* 71(3):1–7. <http://doi.org/10.1103/PhysRevB.71.035313>
32. Zhou C, Muller CJ, Deshpande MR, Sleight JW, Reed M a (1995) Microfabrication of a mechanically controllable break junction in silicon. *Appl Phys Lett* 67(8):1160. <http://doi.org/10.1063/1.114994>
33. Perrin ML, Frisenda R, Koole M, Seldenthuis JS, Gil JA, Valkenier H, van der Zant HSJ (2014) Large negative differential conductance in single-molecule break junctions. *Nat Nanotechnol* 9(10):830–834. <http://doi.org/10.1038/nnano.2014.177>
34. Egle S, Bacca C, Pernau HF, Huefner M, Hinzke D, Nowak U, Scheer E (2010) Magnetoresistance of atomic-size contacts realized with mechanically controllable break junctions. *Phys Rev B - Condens Matter Mater Phys* 81(13):1–11. <http://doi.org/10.1103/PhysRevB.81.134402>
35. Jammalamadaka SN, Kuntz S, Berg O, Kittler W, Kannan UM, Chelvane JA, Sürgers C (2015) Remote control of magnetostriction-based nanocontacts at room temperature. *Sci Rep* 5:13621. <http://doi.org/10.1038/srep13621>
36. Yamada R, Noguchi M, Tada H (2011) Magnetoresistance of single molecular junctions measured by a mechanically controllable break junction method. *Appl Phys Lett* 98(5). <http://doi.org/10.1063/1.3549190>
37. Martin CA, Ding D, Sørensen JK, Bjørnholm T, van Ruitenbeek JM, van der Zant HSJ (2008) Fullerene-based anchoring groups for molecular electronics. *J Am Chem Soc* 130(40):13198–13199. <http://doi.org/10.1021/ja804699a>
38. Quek SY, Kamenetska M, Steigerwald ML, Choi HJ, Louie SG, Hybertsen MS, Venkataraman L (2009) Mechanically controlled binary conductance switching of a single-molecule junction. *Nat Nanotechnol* 4(4):230–234. <http://doi.org/10.1038/nnano.2009.10>

39. Wawrzyniak M, Martinek J, Susla B, Ilnicki G (2009) Correlation histograms in conductance measurements of nanowires formed at semiconductor interfaces. *Acta Phys Pol A* 115(1):384–386
40. Makk P, Tomaszewski D, Martinek J, Balogh Z, Csonka S, Wawrzyniak M, Halbritter A (2012) Correlation analysis of atomic and single-molecule junction conductance. *ACS Nano* 6(4):3411–3423. <http://doi.org/10.1021/nm300440f>
41. Mishchenko A, Zotti LA, Vonlanthen D, Bürkle M, Pauly F, Cuevas JC, Wandlowski T (2011) Single-molecule junctions based on nitrile-terminated biphenyls: a promising new anchoring group. *J Am Chem Soc* 133(2):184–187. <http://doi.org/10.1021/ja107340t>
42. Xia JL, Díez-Pérez I, Tao NJ (2008) Electron transport in single molecules measured by a distance-modulation assisted break junction method. *Nano Lett* 8(7):1960–1964. <http://doi.org/10.1021/nl080857a>
43. Binnig G, Rohrer H, Gerber C, Weibel E (1982) Tunneling through a controllable vacuum gap. *Appl Phys Lett* 40(2):178–180. <http://doi.org/10.1063/1.92999>
44. Bruot C, Palma JL, Xiang L, Mujica V, Ratner MA, Tao N (2015) Piezoresistivity in single DNA molecules. *Nat Commun* 6(May):8032. <http://doi.org/10.1038/ncomms9032>
45. Díez-Pérez I, Hihath J, Lee Y, Yu L, Adamska L, Kozhushner MA, Tao N (2009) Rectification and stability of a single molecular diode with controlled orientation. *Nat Chem* 1(8):635–641. <http://doi.org/10.1038/nchem.392>
46. Díez-Pérez I, Hihath J, Hines T, Wang Z-S, Zhou G, Müllen K, Tao N (2011) Controlling single-molecule conductance through lateral coupling of  $\pi$  orbitals. *Nat Nanotechnol* 6(4):226–231. <http://doi.org/10.1038/nnano.2011.20>
47. Xu B, Xiao X, Tao NJ (2003) Measurements of single-molecule electromechanical properties. *J Am Chem Soc* 125(52):16164–16165. <http://doi.org/10.1021/ja038949j>
48. Xu BQ, Li XL, Xiao XY, Sakaguchi H, Tao NJ (2005) Electromechanical and conductance switching properties of single oligothiophene molecules. *Nano Lett* 5(7):1491–1495. <http://doi.org/10.1021/nl050860j>
49. Frei M, Aradhya SV, Koentopp M, Hybertsen MS, Venkataraman L (2011) Mechanics and chemistry: single molecule bond rupture forces correlate with molecular backbone structure. *Nano Lett* 11(4):1518–1523. <http://doi.org/10.1021/nl1042903>
50. Aradhya SV, Frei M, Hybertsen MS, Venkataraman L (2012) Van der Waals interactions at metal/organic interfaces at the single-molecule level. *Nat Mater* 11(10):872–876. <http://doi.org/10.1038/nmat3403>
51. Yoshida K, Pobelov IV, Manrique DZ, Pope T, Mészáros G, Gulcur M, Wandlowski T (2015) Correlation of breaking forces, conductances and geometries of molecular junctions. *Sci Rep* 5:9002. <http://doi.org/10.1038/srep09002>
52. Perrin ML, Burzurí E, van der Zant HSJ (2015) Single-molecule transistors. *Chem Soc Rev* 44(4):902–919. <http://doi.org/10.1039/C4CS00231H>
53. Cui A, Dong H, Hu W (2015) Nanogap electrodes towards solid state single-molecule transistors. *Small* 11(46):6115–6141. <http://doi.org/10.1002/sml.201501283>
54. Kubatkin S, Danilov A, Hjort M, Cornil J, Brédas J-L, Stuhr-Hansen N, Bjørnholm T (2003) Single-electron transistor of a single organic molecule with access to several redox states. *Nature* 425(6959):698–701. <http://doi.org/10.1038/nature02010>
55. Martin CA, Smit RHM, van der Zant HSJ, van Ruitenbeek JM (2009) A nanoelectromechanical single-atom switch. *Nano Lett* 9(8):2940–2945. <http://doi.org/10.1021/nl901355y>
56. Xiang D, Jeong H, Kim D, Lee T, Cheng Y, Wang Q, Mayer D (2013) Three-terminal single-molecule junctions formed by mechanically controllable break junctions with side gating. *Nano Lett* 13(6):2809–2813. <http://doi.org/10.1021/nl401067x>
57. Martin CA, van Ruitenbeek JM, van der Zant HSJ (2010) Sandwich-type gated mechanical break junctions. *Nanotechnology* 21(26):265201. <http://doi.org/10.1088/0957-4484/21/26/265201>
58. Perrin ML, Verzijl CJO, Martin CA, Shaikh AJ, Eelkema R, Van Esch JH, Dulić D (2013) Large tunable image-charge effects in single-molecule junctions. *Nat Nanotechnol* 8(4):282–287. <http://doi.org/10.1038/nnano.2013.26>

59. Huang C, Rudnev AV, Hong W, Wandlowski T (2015) Break junction under electrochemical gating: tested for single-molecule electronics. *Chem Soc Rev* 44:889–901. <http://doi.org/10.1039/C4CS00242C>
60. Li X, Hihath J, Chen F, Masuda T, Zang L, Tao N (2007) Thermally activated electron transport in single redox molecules. *J Am Chem Soc* 129(37):11535–11542. <http://doi.org/10.1021/ja072990v>
61. Lloyd JR (1997) Electromigration in thin film conductors. *Defect Diffus Forum* 143–147:1661–1672. <http://doi.org/10.4028/www.scientific.net/DDF.143-147.1661>
62. Strachan DR, Smith DE, Johnston DE, Park T-H, Therien MJ, Bonnell D a, Johnson AT (2005) Controlled fabrication of nanogaps in ambient environment for molecular electronics. *Appl Phys Lett* 86(4):043109. <http://doi.org/10.1063/1.1857095>
63. O'Neill K, Osorio EA, Van Der Zant HSJ (2007) Self-breaking in planar few-atom au constrictions for nanometer-spaced electrodes. *Appl Phys Lett* 90(13). <http://doi.org/10.1063/1.2716989>
64. Tsutsui M, Taniguchi M, Kawai T (2008) Fabrication of 0.5 nm electrode gaps using self-breaking technique. *Appl Phys Lett* 93(16):1–4. <http://doi.org/10.1063/1.3006063>
65. Houck AA, Labaziewicz J, Chan EK, Folk JA, Chuang IL (2005) Kondo effect in electromigrated gold break junctions. *Nano Lett* 5(9):1685–1688. <http://doi.org/10.1021/nl050799i>
66. Song H, Kim Y, Jang YH, Jeong H, Reed MA, Lee T (2009) Observation of molecular orbital gating. *Nature* 462(7276):1039–1043. <http://doi.org/10.1038/nature08639>
67. Suga H, Sumiya T, Furuta S, Ueki R, Miyazawa Y, Nishijima T, Naitoh Y (2012) Single-crystalline nanogap electrodes: enhancing the nanowire-breakdown process with a gaseous environment. *ACS Appl Mater Interfaces* 4(10):5542–5546. <http://doi.org/10.1021/am301441a>
68. Tsutsui M, Rahong S, Iizumi Y, Okazaki T, Taniguchi M, Kawai T (2011) Single-molecule sensing electrode embedded in-plane nanopore. *Sci Rep* 1:46. <http://doi.org/10.1038/srep00046>
69. Chen CJ (1993) Introduction to scanning tunneling microscopy. Oxford University Press, New York
70. Kitaguchi Y, Habuka S, Okuyama H, Hatta S, Aruga T, Frederiksen T, Ueba H (2015) Controlling single-molecule junction conductance by molecular interactions. *Sci Rep* 5:11796. <http://doi.org/10.1038/srep11796>
71. Tanaka H, Kawai T (1997) Scanning tunneling microscopy imaging and manipulation of DNA oligomer adsorbed on Cu(111) surfaces by a pulse injection method. *J Vac Sci Technol B* 15(3):602. <http://doi.org/10.1116/1.589299>
72. Yokoyama T, Kogure Y, Kawasaki M, Tanaka S, Aoshima K (2013) Scanning tunneling microscopy imaging of long oligothiophene wires deposited on Au(111) using electrospray ionization. *J Phys Chem C* 117(36):18484–18487. <http://doi.org/10.1021/jp405411f>
73. Rinke G, Rauschenbach S, Schrettl S, Hoheisel TN, Blohm J, Gutzler R, Kern K (2014) Soft-landing electrospray ion beam deposition of sensitive oligoynes on surfaces in vacuum. *Int J Mass Spectrom* 377:228–234. <http://doi.org/10.1016/j.ijms.2014.06.026>
74. Grill L, Dyer M, Lafferentz L, Persson M, Peters MV, Hecht S (2007) Nano-architectures by covalent assembly of molecular building blocks. *Nat Nanotechnol* 2(11):687–691. <http://doi.org/10.1038/nnano.2007.346>
75. Lafferentz L, Ample F, Yu HB, Hecht S, Joachim C, Grill L (2009) Conductance of a single conjugated polymer as a continuous function of its length. *Science* 323(5918):1193–1197. <http://doi.org/10.1126/science.1168255>
76. Nacci C, Ample F, Blegler D, Hecht S, Joachim C, Grill L (2015) Conductance of a single flexible molecular wire composed of alternating donor and acceptor units. *Nat Commun* 6:7397. <http://doi.org/10.1038/ncomms8397>
77. Ie Y, Hirose T, Nakamura H, Kiguchi M, Takagi N, Kawai M, Aso Y (2011) Nature of electron transport by pyridine-based tripodal anchors: potential for robust and conductive single-molecule junctions with gold electrodes. *J Am Chem Soc* 133(9):3014–3022. <http://doi.org/10.1021/ja109577f>

78. Ie Y, Tanaka K, Tashiro A, Lee SK, Testai HR, Yamada R, Aso Y (2015) Thiophene-based tripodal anchor units for hole transport in single-molecule junctions with gold electrodes. *J Phys Chem Lett* 6(18):3754–3759. <http://doi.org/10.1021/acs.jpcclett.5b01662>
79. Ullmann K, Coto PB, Leitherer S, Molina-Ontoria A, Martin N, Thoss M, Weber HB (2015) Single-molecule junctions with epitaxial graphene nanoelectrodes. *Nano Lett* 15(5):3512–3518. <http://doi.org/10.1021/acs.nanolett.5b00877>
80. Ru J, Szeto B, Bonifas A, McCreery RL (2010) Microfabrication and integration of diazonium-based aromatic molecular junctions. *ACS Appl Mater Interfaces* 2(12):3693–3701. <http://doi.org/10.1021/am100833e>
81. Seo S, Min M, Lee SM, Lee H (2013) Photo-switchable molecular monolayer anchored between highly transparent and flexible graphene electrodes. *Nat Commun* 4(May):1920. <http://doi.org/10.1038/ncomms2937>

# Chapter 3

## Characterization of the Single Molecular Junction

Manabu Kiguchi and Shintaro Fujii

**Abstract** The single molecular junction is becoming an increasingly attractive research target owing to the structural tunability, flexibility, low cost, and compatibility with electronics. From a scientific point of view, the single molecular junction gives us platform to access and investigate physical phenomena appearing at the low-dimensional nano-junction on a single molecular scale. In this chapter, we focus on the recent research progress in the characterization of the single molecular junction. One of the main issues in the single molecular junction studies is structural uncertainty in the junction. This is because there is no straightforward way to visualize and identify ultrasmall structure of a molecule trapped in nanogap electrodes. To overcome this issue and to reliably measure physical properties of the single molecular junction, researchers have developed a variety of characterization techniques. We start by introducing structure-related characterizations and analyses of plateau length, point-contact spectroscopy, inelastic electron tunneling spectroscopy, action spectroscopy, and surface-enhanced Raman spectroscopy. Then, electronic characterizations and analyses of current–voltage characteristics, thermopower measurement, and shot noise measurement are presented. Finally, we touch on force measurement, whose development is still in progress, but it provides understanding of the structure–conductance relationship in a single molecular junction.

**Keywords** Single molecular junction • Single molecular spectroscopy • Atomic and electronic structure

### 3.1 Introduction

Since the early 1970s, researchers have looked toward to construct electronic circuits using individual molecules as building blocks [1, 2]. However, the researches in the molecular electronics have been hampered by significant experimental

---

M. Kiguchi (✉) • S. Fujii  
Department of Chemistry, Graduate School of Science and Engineering, Tokyo Institute of Technology, Tokyo, Japan  
e-mail: [kiguti@chem.titech.ac.jp](mailto:kiguti@chem.titech.ac.jp)

challenges, and practical application in electronic devices has remained elusive. Recent development in experimental technique of the single molecular junctions allows us to discover a variety of remarkable electronic functionalities at the single molecular scale. Currently, diode, switch, and transistor properties have been reported for the single molecular junction [3–7]. To improve the device performance as well as understand the working principle, development of a reliable characterization technique at the single molecular scale is of great importance. To unambiguously characterize the single molecular junction, it is necessary to identify the number of molecules in the junctions and structural details including chemical species of the bridging molecules and contact configuration of the electrode–molecule interface. On the basis of the structural analysis, it becomes possible to identify electronic properties of the single molecular junction such as whether charge transports through HOMO or LUMO and energy difference between the conduction orbital and Fermi level of the metal electrodes. This is because atomic and electronic structures govern the transport properties of the single molecular junction. One of the most essential quantities to be clarified in the single molecular junction is the number of molecules bridging between metal electrodes. In early studies, the number of the molecule has been determined by analyzing the conductance trace during the breaking process of the junction. During the breaking process, the conductance trace displays steplike decreases, which are associated with stepwise rupture of multiple molecular junctions. The conductance of the last plateau in the conductance trace is assumed to correspond to the formation of the last single molecular junction [1, 2]. The analysis of the conductance step is not a direct evidence of the formation of the single molecular junction. To confirm the formation of the single molecular junctions as well as characterize molecular-dependent properties, various advanced techniques have been developed in recent years.

In this chapter, we focus on present characterization techniques and analyses of the single molecular junction, including conductance plateau analysis [2], inelastic electron tunneling spectroscopy (IETS) [3], point-contact spectroscopy (PCS) [8], surface-enhanced Raman scattering (SERS) [9], shot-noise measurement [10], current–voltage characteristics [11], thermopower measurement [12], and force measurement [13]. The combination of these techniques fully characterizes the atomic and electronic structure of the single molecular junction.

### ***3.1.1 Plateau Length Analysis***

The length of the atomic contact and single molecular junction can be evaluated by analyzing the conductance changes during the stretching process of the junction. The length of the atomic contact and single molecular junction is fundamental information to obtain structural details of the junction such as formation of an atomic wire and molecular orientation in a molecular junction.

Figure 3.1a shows the typical conductance trace of the Au contact during the stretching process of the contact (conductance trace) [14]. The conductance of the

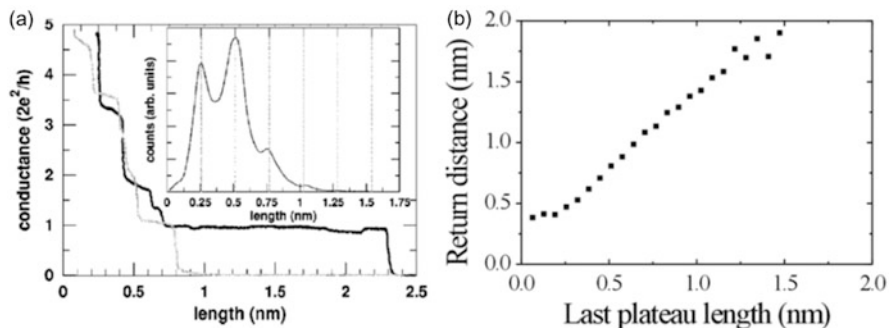


**Fig. 3.1** (a) Evolution of the conductance for an Au contact as a function of the interelectrode distance measured at 4.2 K. The inset shows a length histogram of the  $1 G_0$  plateau [14]. (b) The average of the return distance as a function of the length of the  $1 G_0$  plateau [15]

Au atomic contact is  $1 G_0$  ( $2e^2/h$ ), and the  $1 G_0$  plateau is indicative of the formation of an Au atomic contact. Inset in Fig. 3.1a shows the length histogram of the  $1 G_0$  plateau constructed from 1,000 conductance traces. The Au atomic contact can be stretched up to 1 nm. The distribution shows the peaks at multiples of 0.26 nm. This peak distance agrees with the expected Au–Au bond length in an Au atomic wire. Further information on the atomic wire is captured by the return length analysis. The grey line in Fig. 3.1a shows the return conductance trace of the Au atomic wire during the making of the contact. The electrode needs to return by a little more than the length of the  $1 G_0$  plateau to come back into contact. Figure 3.1b shows the average return lengths as a function of  $1 G_0$  plateau length [15]. The return length is defined as the distance over which the two Au electrodes need to be moved back after the junction breaks in order to reestablish contact. Apart from an offset (0.5 nm) due to the elastic response of the banks, the relation between the plateau length and the return length is approximately proportional. This relationship indicates that a fragile structure is formed with a length corresponding to that of the last plateau. Using this technique, the formation of the atomic wire has been revealed for clean Au, Pt, and Ir wires [16], Co and Pd wires in the presence of hydrogen [17], and Ag and Cu wires in the presence of oxygen [18]. It is noteworthy that the clean Co and Pd do not form atomic wires. The adsorbed hydrogen or oxygen molecule decreases the surface energy of the metal atomic wire and stabilizes the metal atomic wire. This stabilization mechanism leads to the formation of the metal atomic wires, which cannot be formed without molecules.

A similar technique can be applied to single molecular junction [19, 20]. Here, the gap distance or break distance is evaluated from the conductance traces. Figure 3.2a shows the two-dimensional (2-D) conductance histogram for single oligosilane ( $\text{SiMe}_2$  oligomer terminated with 4-(methylthio)phenyl groups) molecular wire constructed from 1,000 conductance traces [20]. For the construction of the 2-D histograms,  $d = 0$  for each trace is set to the point where the conductance drops sharply below  $1 G_0$ . Just after breaking the Au atomic contact ( $d = 0$ ), the gap

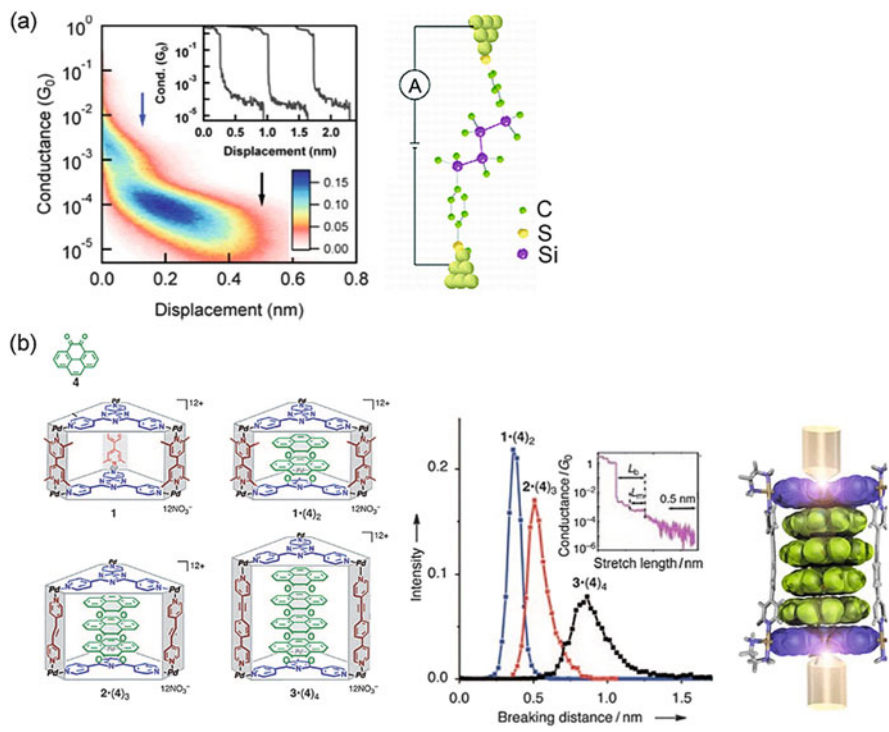


**Fig. 3.2** (a) 2-D conductance histogram for single oligosilane molecular wire. The *inset* shows individual conductance traces. Schematic illustration of the single oligosilane molecular wire is shown on the right side [20]. (b) (*left*) Chemical structure of  $\pi$ -stacked molecular wires:  $1\bullet(4)_2$ ,  $2\bullet(4)_3$ ,  $3\bullet(4)_4$ . (*right*) The distribution of breaking distances ( $L_b$ ) for  $1\bullet(4)_2$ ,  $2\bullet(4)_3$ , and  $3\bullet(4)_4$ , together with the structure model. The *inset* shows typical conductance trace of the Au contact in solution containing  $1\bullet(4)_2$  [21]

size is close to zero. This distance is the stretched length from this breaking point. In Fig. 3.2a, an intense peak appears around  $10^{-4} G_0$  that extends for a distance of ca. 0.5 nm. The gap distance is close to the size of the oligosilane molecule, indicating that single molecular junctions are formed reproducibly and can be elongated over that distance.

Figure 3.2b shows another example of the plateau analysis for  $\pi$ -stacked molecular wire:  $1\bullet(4)_2$ ,  $2\bullet(4)_3$ ,  $3\bullet(4)_4$  [21]. Here,  $\pi$ -stacked molecule **4** is enclosed in the cavity, and the cavity height of the coordination cages **1**–**3** predetermines the number of  $\pi$ -stacked aromatic molecules **4**. The average of the gap size increases by 0.24 nm per  $\pi$ -stacked molecule **4**. The value of 0.24 nm is close to the incremental increase in the molecular height of the  $\pi$ -stacked molecule per  $\pi$ -stacked molecule **4** (0.30 nm). The good agreement between these two values indicates that the top and bottom triangular aromatic panels of the  $\pi$ -stacked molecular wire are bound to the

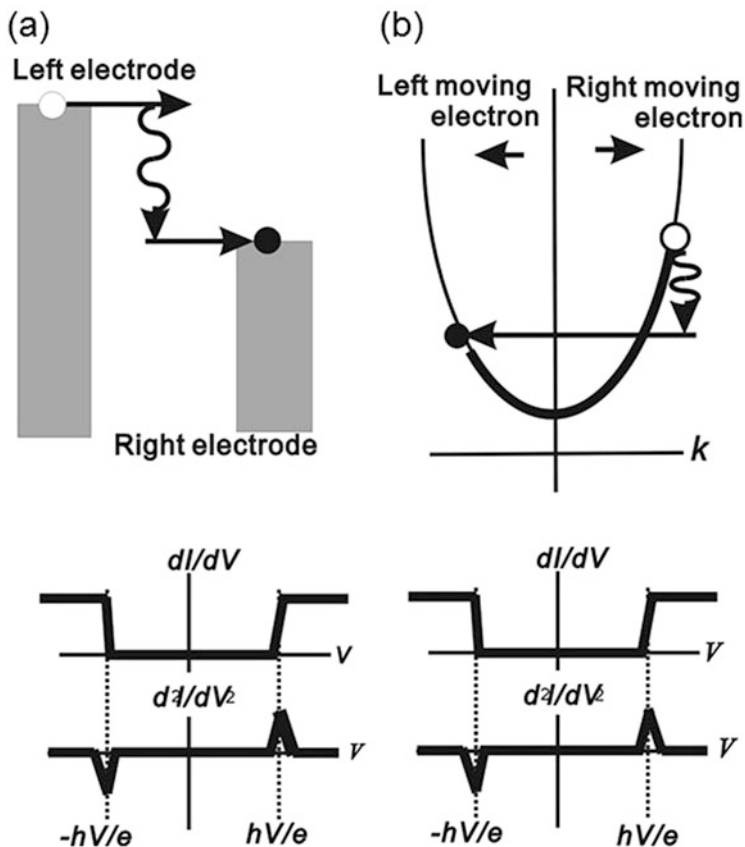
Au electrodes, as shown in Fig. 3.2b. The atomic structure of the single molecular junction can be evaluated by the conductance traces.

### 3.1.2 Point-Contact Spectroscopy and Inelastic Electron Tunneling Spectroscopy

Point-contact spectroscopy (PCS) and inelastic electron tunneling spectroscopy (IETS) are vibrational spectroscopies of single molecular junctions and provide information about the molecular composition in the molecular junction.

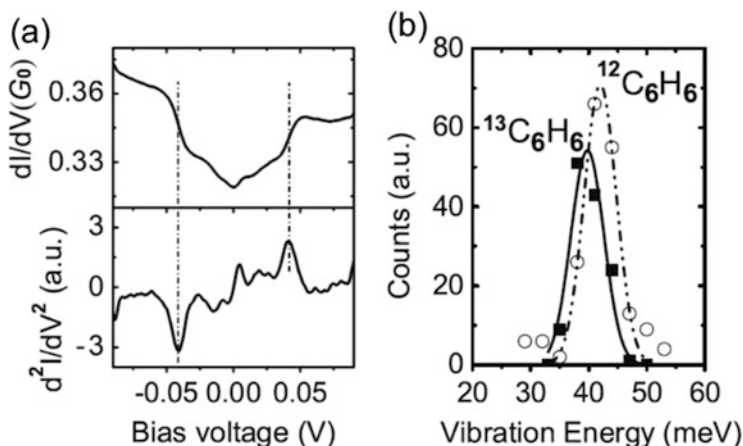
Interactions between molecular vibrations and conduction electron through the single molecular junction modify the molecular conductance. When the differential conductance is measured as a function of the bias voltage across the junction, the conductance changes above the threshold voltage, which corresponds to the excitation of the vibration mode of the junction. We can, thus, get the information of the vibrational energy from the threshold voltage by measuring the current–voltage characteristic of the junction. This is the basic mechanism of the point-contact spectroscopy (PCS) and inelastic electron tunneling spectroscopy (IETS). IETS was first applied to molecules buried in a metal–oxide interface for a metal–oxide–metal tunneling junction [22], while PCS has been applied to metal contacts [8]. The first IETS measurement for a single molecule adsorbed on a metal substrate (not a molecular junction) was reported by Ho’s group with a scanning tunneling microscope (STM) [23]. The first IETS and PCS studies on a single molecular junction were demonstrated for the single hydrogen molecular junction [24]. Since then, IETS and PCS have been applied to various single molecular junctions, including benzene, alkanedithiol, ethylene, and acetylene [3, 25–30].

Figure 3.3 shows a schematic representation of IETS and PCS for the single molecular junctions. In the tunneling regime for IETS (Fig. 3.3a), when the bias voltage is less than the vibrational energy,  $h\nu$ , the electrons can tunnel elastically through the single molecular junction. Above a threshold voltage, where  $h\nu = eV$ , an electron can excite a vibration mode of the single molecular junction. This means that a second inelastic channel opens, in addition to the first elastic channel. The opening of this inelastic channel is accompanied by an increase of the differential conductance ( $dI/dV$ ) at  $eV = \pm h\nu$ . This change is clearly observed in the derivative of the differential conductance,  $d^2I/dV^2$ , where a peak and a dip are observed for the positive and negative biases, respectively. In the ballistic regime for PCS, where the transmission probability is close to one, electrons are delocalized over the two electrodes. The electron transfer process can be considered in the momentum space as shown in Fig. 3.3b. The right-moving electrons occupy higher states than the left-moving electrons, when the bias voltage is applied to the single molecular junction. Above a threshold voltage, the electron can excite a vibration mode of the single molecular junction, as with the case of the tunneling regime. Here, electrons around the top of the right-moving states lose energy via excitation of the vibration mode.



**Fig. 3.3** Schematic view of (a) IETS and (b) PCS, together with  $dI/dV$  and  $d^2I/dV^2$ . IETS: An additional inelastic channel is opened by the excitation of a vibration mode. The differential conductance ( $dI/dV$ ) increases above a threshold voltage. PCS: The right-moving electrons are scattered backward by the excitation of a vibration mode. The differential conductance decreases above the threshold voltage

Electrons should scatter backward, because the right-moving states are occupied at a lower energy. This backscattering leads to the decrease in the differential conductance at  $eV = \pm h\nu$ . This change is observed as a dip and a peak for the positive and negative biases in  $d^2I/dV^2$ , respectively. The conductance change in  $dI/dV$  and spectral shape of  $d^2I/dV^2$  differ from one another in IETS and PCS. In the simple case, where electron transports through a single channel and molecule symmetrically binds to the metal electrodes, the conductance increases along with the excitation of the vibrational mode, when the conductance is smaller than  $0.5 G_0$  (in tunneling regime). In contrast, when the conductance of the contact is higher than  $0.5 G_0$  (in ballistic regime), the conductance decreases by excitation of the vibrational modes. The former and latter cases can be categorized as PCS and IETS,



**Fig. 3.4** (a) Differential conductance (*top*) and its derivative (*bottom*) for a single benzene/Pt junction. The differential conductance is monitored for a fixed contact configuration during sweeping of the DC bias from  $-10$  to  $+100$  mV. (b) Distribution of vibration energy for  $^{12}\text{C}_6\text{H}_6$  and  $^{13}\text{C}_6\text{H}_6$ /Pt junctions [27]

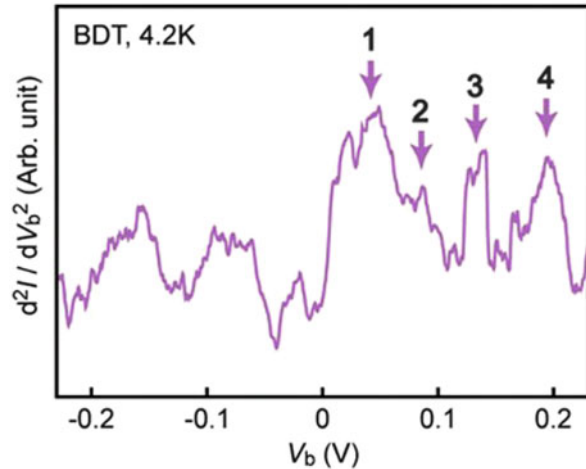
respectively. The transition between PCS and IETS is experimentally shown for the  $\text{H}_2$ ,  $\text{H}_2\text{O}$ , and benzenedithiol junctions [25, 31]. Theoretical analysis reveals that the transition depends on the symmetry and conductance of the single molecular junction.

Figure 3.4a shows an example of IETS spectra for a single benzene/Pt junction [27]. A symmetric upward step in the differential conductance is observed around 40 mV, and peaks are observed in its derivative ( $d^2I/dV^2$ : IETS). The upward steps in the  $dI/dV$  spectrum and the peaks in the  $d^2I/dV^2$  spectrum indicate the excitation of the vibrational mode by conduction electrons with energies of 40 meV. The theoretical calculation shows that the observed vibration mode is attributed to the hindered rotation mode of the benzene molecule bridging between the Pt electrodes. The isotope effect is observed in this system. Figure 3.4b shows the distribution of vibrational energies for single  $^{12}\text{C}_6\text{H}_6$  and  $^{13}\text{C}_6\text{H}_6$ /Pt junctions. The histograms for the single  $^{12}\text{C}_6\text{H}_6$  and  $^{13}\text{C}_6\text{H}_6$ /Pt junctions show peaks at 42 meV and at 40 meV, respectively. The mass ratio of  $^{13}\text{C}_6\text{H}_6$  and  $^{12}\text{C}_6\text{H}_6$  is 84/78. The vibrational mode for the single  $\text{C}_6\text{H}_6$ /Pt junction is predicted to shift from 42 ( $^{12}\text{C}_6\text{H}_6$ ) to 40 meV ( $^{13}\text{C}_6\text{H}_6$ ) with the harmonic oscillator model:

$$\nu = k/\sqrt{m} \quad (3.1)$$

where  $m$  is the mass of benzene molecule and  $k$  is the spring constant of the benzene molecule–Pt electrode, assuming that the electrode is much heavier than benzene molecule. The good agreement between the predicted and experimental values for vibration energies supports that the benzene molecule bridges between the Pt electrodes.

**Fig. 3.5** IETS spectra of single BDT molecular junction measured at 4.2 K [26]. The vibration modes: 1  $\nu_s$  (Au-S), 2  $\delta_s$ (C-C-C), 3  $\delta_s$ (C-C-H), 4  $\nu_s$ (C=C)



Here, it is noted that the single benzene/Pt junction exhibits a conductance value close to  $1 G_0$ , which is close to the conductance value of the metal atomic contact. In the conventional single molecular junctions, where molecules are attached to metal electrodes via an anchoring group (e.g., -SH, -NH<sub>2</sub>), the conductance is below  $0.01 G_0$  [1, 2]. A highly conductive molecular junction is fabricated by the direct binding of a  $\pi$ -conjugated molecule to the metal electrodes without the anchoring group. The  $\pi$ -orbital (conduction orbital) effectively hybridizes with the metal orbital, which leads to the high conductivity of the single molecular junction. Currently, this direct  $\pi$ -binding technique has been applied to various molecules, including ethylene, acetylene, and C<sub>60</sub> [32–34].

Figure 3.5 shows another example of IETS of a single BDT molecular junction [26]. In contrast with the single benzene molecular junction, intramolecule vibration modes are clearly observed in the spectrum. The peaks at 196 mV, 139 mV, and 86 mV are assigned to intramolecule vibration modes of  $\nu_s$ (C=C),  $\delta_s$ (C-C-H), and  $\delta_s$ (C-C-C) in the phenyl ring, respectively. The peak at 45 meV corresponds to metal–molecule vibration modes ( $\nu_s$  (Au-S)). The vibrational modes are fingerprint of molecule, and the observation of the intramolecular vibration modes shows the bridging of the molecule between metal electrodes.

The excitation of the vibration mode by the conduction electron can induce a structural change of the single molecular junctions. Since the conductance of the single molecular junction is sensitive to the atomic structure of the single molecular junction, this structural change causes large conductance change, compared to IETS and PCS, where conductance change is smaller than 1%. The large conductance change induced by structural change is observed as symmetric peaks in the  $dI/dV$  spectra, as shown in Fig. 3.6. As the structural change is induced by the excitation of the vibration mode, the energy of the peak indicates the vibration energy of the single molecular junction. This abrupt change in differential conductance can be used as “action spectroscopy” of the single molecular junctions. In conventional

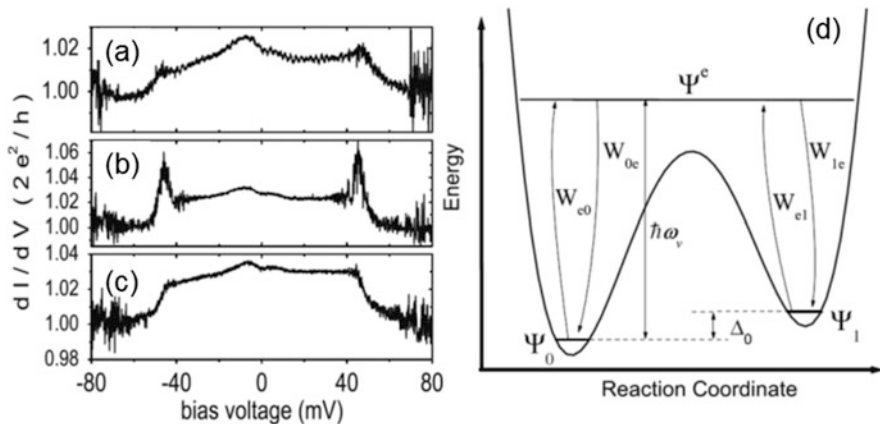


**Fig. 3.6** The gradual change of  $dI/dV$  spectra of a  $D_2/Pt$  junction; panels (b) and (c) show spectra taken for the same junction as (a) after stretching by 0.01 and 0.02 nm, respectively. (d) Energy landscape of a molecule in an atomic contact. The molecule can be vibrationally excited and relax into the other energy minimum [35]

action spectroscopy, the reaction yield is measured as a function of energy. Here, we call this form of spectroscopy “action spectroscopy,” because the action of single molecular junctions is utilized to determine the energy of the vibration mode. Action spectroscopy has some advantages compared to IETS. First, it can detect vibration modes that cannot be detected by IETS. Vibrational modes that are not visible in IETS can be revealed as a response of vibrationally mediated molecular motion to applied bias voltage in the action spectroscopy. Second, action spectroscopy can be applied to a system in which the IETS signal is too weak to detect.

Action spectroscopy of the single molecular junctions was first applied to the  $CO/Pt$  and  $H_2/Pt$  junctions [35]. Figure 3.6a–c shows a sequence of spectra taken, when the  $D_2/Pt$  junction is slightly stretched over 0.02 nm. The small bump on the variation mode shoulder in Fig. 3.6a at 47 meV evolves into full peaks in Fig. 3.6b and subsequently into a regular vibration model spectrum. This change in the spectra indicates that peaks in  $dI/dV$  are caused by the phonon excitation, as in the case with PCS or IETS. The theoretical calculation shows that the observed vibration mode is attributed to the transverse translation mode of the molecule in the Pt–H–H–Pt configuration.

The appearance of symmetric peaks is explained using a model of vibration-induced two-level systems (Fig. 3.6d). In this model, the potential curve of the molecular junction is represented as a double-well potential with a ground state  $\Psi_1$  and a metastable state  $\Psi_2$  in the two energy minima. The two energy minima are separated by the activation barrier ( $E_{AC}$ ). The molecular junction can be vibrationally excited by the conduction electron. If the junction is fully excited, then the junction with ground state  $\Psi_1$  can overcome the activation barrier and change into a junction with metastable  $\Psi_2$ , which leads to the abrupt change in

differential conductance (the peak in the  $dI/dV$  spectrum). The  $\Psi_1$  and  $\Psi_2$  states correspond to junctions with slightly different local geometric configurations, such as the adsorption site of the molecule on the metal electrodes, the molecule tilt angle, and the configuration of the metal electrodes. The action spectroscopy has revealed the bridging of single hydrogen molecule between Au and Cu electrodes [36, 37].

### 3.1.3 Surface-Enhanced Raman Scattering

While IETS, PCS, and action spectroscopy are powerful techniques for identifying single molecular junctions, these techniques require low temperatures. From an application standpoint, vibration spectroscopic characterization under ambient conditions is desirable for single molecular devices working at room temperature. The utilization of interaction between light and molecular vibration is a promising way to detect the vibration mode of the single molecular junction. IR and Raman scattering are typical vibrational spectroscopies to study molecules in bulk sample such as molecular solutions and solids. At the single molecular scale, signals from a molecule in conventional Raman spectroscopy are below the detection limit. However, the enhanced field in the nanogap overcomes this problem, as shown in Fig. 3.7a [9, 38–44]. In a single molecular junction, a single molecule is trapped in the nanogap. When light is shone on the molecular junction, a strong electric field is formed between the nanogap electrodes, which enhances the intensity of the Raman signal. The single molecular junction gives us the best platform to perform SERS [41–43].

We start by focusing on the SERS studies on molecular junctions where several numbers of molecules are bridged between metal electrodes. Figure 3.7b, c

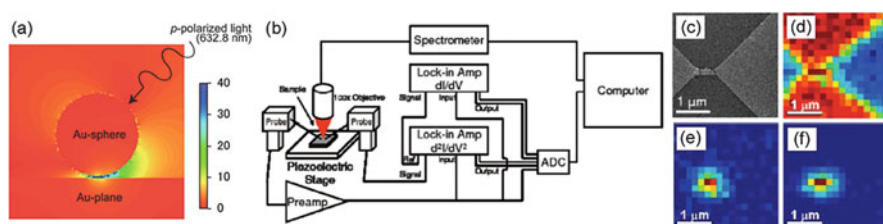


**Fig. 3.7** (a) Electric field distribution obtained by finite-difference time-domain (FDTD) method for a nanogap between Au sphere and Au plane. The gap distance and the diameter of the Au sphere were set to be 1.5 and 50 nm, respectively. Localization of electric field in the gap region is apparent and the local field enhancement is more than 20 [44]. (b) Schematic of the simultaneous SERS and conductance measurement. Lock-in amplifier is an instrument to recover signals that are buried in noise by applying a reference signal at the same frequency as the signal that is being measured. (c) Scanning electron image of Au electrode constriction with a nano-sized gap. (d) Map of the Raman scattering of (d) Si ( $480\text{--}560\text{ cm}^{-1}$ ) and (e) Map of *p*-mercaptoaniline SERS signal from ring mode  $\nu_{\text{C}=\text{C}}$  ( $\sim 1,590\text{ cm}^{-1}$ ). (f) Integrated continuum signal ( $50\text{--}300\text{ cm}^{-1}$ ) [9]

shows the experimental setup of SERS measurement for the molecular junction [9]. The SERS measurements are performed using a scanning confocal Raman microscope in reflection mode using an objective lens (ca. 100 $\times$  magnification). The formation of the molecular junction is confirmed by the conductance measurement. The Au nanogap electrodes are lithographically fabricated onto a Si/SiO<sub>2</sub> wafer. Figure 3.7c–f shows an SEM image of the nanogap electrode, together with maps of the Raman signal from Si (480–560 cm<sup>-1</sup>), SERS signal of molecule, and integrated continuum signal (50–300 cm<sup>-1</sup>). In this experiment, *p*-mercaptoaniline (pMA) molecules are bridged between Au electrodes by immersed in a pMA solution. The SERS signal corresponding to the ring mode  $\nu_{C=C}$  ( $\sim 1,590$  cm<sup>-1</sup>) of pMA is selectively observed at the nanogap, caused by the formation of the strong electric field.

The SERS spectra of the molecular junction are different from that of bulk sample and molecules on metal surface, because the environment of molecule in the single molecular junction is different from other systems. When a molecule interacts with the metallic substrate, a certain degree of charge transfer takes place from the molecular bonding orbital (e.g., HOMO) to the metal unoccupied state and from metal occupied state to the antibonding orbital (e.g., LUMO). While this process secures the molecule to the metal surface, it typically results in the weakening of molecular bonds, leading to the redshift of the vibrational energy. In addition to the shift of the vibrational energy, vibration modes which are not observed in bulk can be observed for molecular junctions. The top and middle portions of Fig. 3.8 show the example of the SERS of the 4,4'-bipyridine (BPY) molecular junction [41]. The spectra shown at the bottom of Fig. 3.8 are normal SERS spectrum of BPY on Au surfaces. The totally symmetric *a* modes are observed for conventional SERS at 1,025, 1,062, 1,217, and 1,296 cm<sup>-1</sup> (bottom of Fig. 3.8). On the other hand, nontotally symmetric *b*<sub>1</sub> modes or *b*<sub>2</sub> modes are observed for the single BPY molecular junction at 840, 998, 1,026, and 1,205 cm<sup>-1</sup> (middle of Fig. 3.8), at 975 cm<sup>-1</sup> (top of Fig. 3.8). The appearance of the nontotally symmetric modes is explained by the photoinduced charge transfer process.

Simultaneous conductance and SERS measurement of molecular junctions has more recently been employed to monitor vibrational mode effective temperatures at the junction [39, 40]. By simultaneously measuring Stokes (S) and anti-Stokes (AS) Raman components, an AS/S ratio can be calculated which represents the steady-state nonequilibrium population in the presence of inelastic tunneling current. This ratio can then be translated into effective temperature ( $T_v^{\text{eff}}$ ) for each vibrational mode.  $T_v^{\text{eff}}$  can be defined as

$$\frac{I_v^{\text{AS}}}{I_v^{\text{S}}} = A_v \frac{(\omega_L + \omega_v)^4}{(\omega_L - \omega_v)^4} \exp(-\hbar\omega_v/k_B T_v^{\text{eff}}) \quad (3.2)$$

where  $I_v^{\text{S}}$  and  $I_v^{\text{AS}}$  are the Stokes and anti-stokes Raman intensities for a given mode,  $\omega_L$  is the incident laser frequency,  $\omega_v$  is the frequency of Raman scattering, and  $A_v$  is a correction factor that accounts for the ratio of the anti-Stokes and Stokes cross sections [39, 40]. For the amine-terminated oligophenylene vinylene

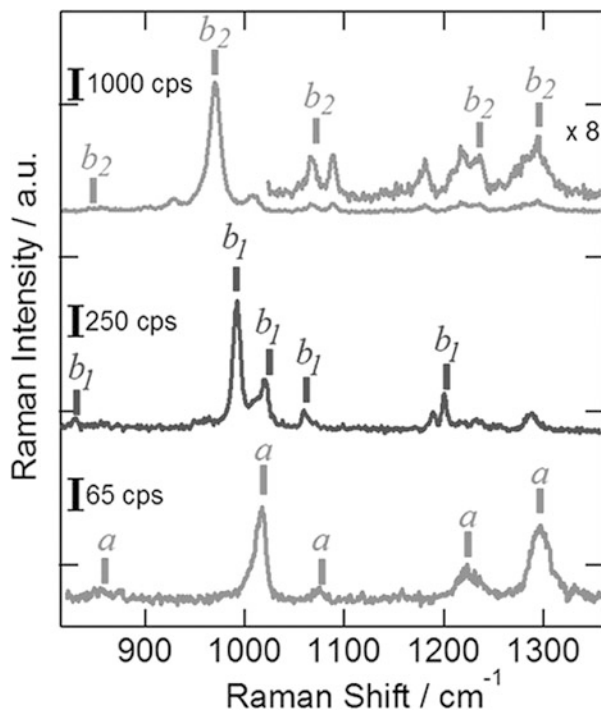
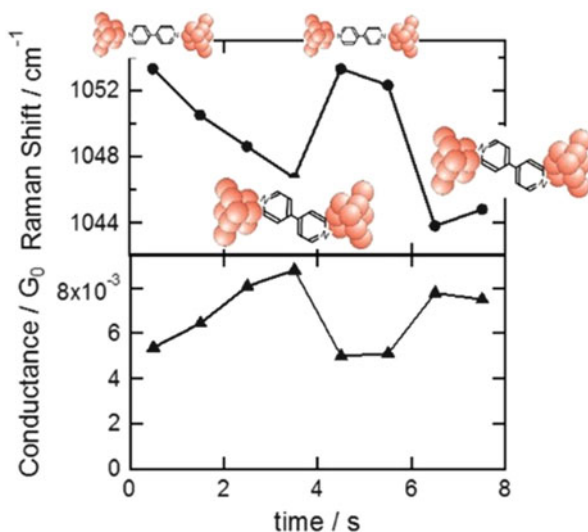


**Fig. 3.8** Three types of SERS spectra of a single 4,4'-bipyridine (BPY) molecular junction (*top* and *middle*). Normal SERS of BPY molecules on Au surface (*bottom*). The nontotally symmetric  $b_2$  mode (*top*) and  $b_1$  mode (*medium*) are observed for the single BPY molecular junction [41]

(OPV) junction, the effective temperature of vibrational modes at  $1,317\text{ cm}^{-1}$  and  $1,625\text{ cm}^{-1}$  increases linearly with the applied bias. It increases up to 600 K at bias voltage of 500 mV [39]. The effective temperature of the vibrational mode at  $1815\text{ cm}^{-1}$  remains bias-independent until the applied voltage exceeds  $\hbar\omega_v$ . For bias voltage greater than  $\hbar\omega_v$ , the effective temperature increases linearly. Although each vibrational mode has to be considered individually, generally speaking, the effective electronic temperature at bias voltages of a few hundred millivolts can reach values up to three times greater than those measured when no bias is applied.

The above discussion is mainly focused on the molecular junction, where several numbers of molecules are bridged between metal electrodes. The next target is SERS study of the single molecular junction. The first SERS measurement of the single molecular junction was reported for the single BPY molecular junction using the “fishing mode” STM technique (FM-STM) [42]. In the FM-STM method, the tip–substrate gap is precisely controlled by placing the tip at the desired position and lowering STM proportionally and the integral gain (ca. 0.03 % of normal values). The thermally induced movements of the molecules on the substrate surface lead to the random formation of the molecular junctions bridging the tip–substrate gap.

**Fig. 3.9** Time course of the energy of the ring breathing mode around  $1,050\text{ cm}^{-1}$  and the conductance of the single BPY molecular junction. Schematics of the relevant molecular orientation are shown as insets [41]



By constantly monitoring the junction conductance and SERS signal, a series of high-frequency current jumps can be correlated with structural details by analyzing related SERS fluctuations. In the case of the SERS of single BPY molecular junction, the C–C stretching mode reversibly splits into a doublet upon increasing the applied bias voltage. This signal splitting is attributed to an asymmetric metal–molecule coupling induced by the applied bias.

Further analysis of the simultaneous conductance and SERS measurements reveals the dynamic motion of single molecular junctions [41]. Figure 3.9 shows the time course of the molecular conductance and the energy of the ring breathing mode around  $1,050\text{ cm}^{-1}$  in the single BPY molecular junction. The energy of the ring breathing mode becomes higher (lower) as the conductance becomes smaller (larger). This anticorrelation between the peak energy and the conductance can be explained by the change in the tilting angle of the molecule to the electrode surface during the time course. At the higher-conductance state at  $t = 3.5\text{ s}$ , BPY features a perpendicular orientation with larger metal–molecule coupling (i.e., smaller energy of the vibrational mode). In the course of the time at  $t = 4.5\text{ s}$ , a tilting of BPY weakens the metal–molecule coupling which leads to the increase in the conductance of the single molecular junction as well as the decrease in the vibrational energy.

### 3.1.4 Current–Voltage Characteristics

Current–voltage measurement provides us information about the electronic structure of the single molecular junction. Energy difference between a conduction orbital

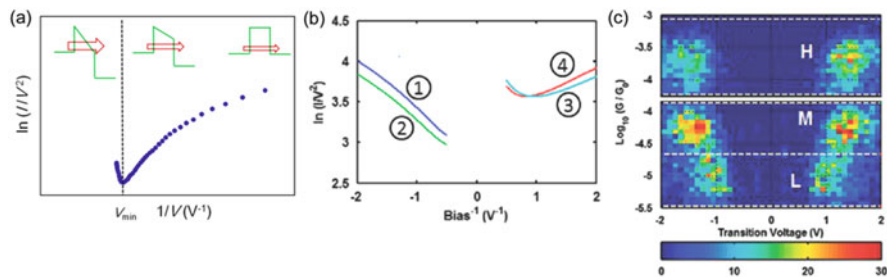


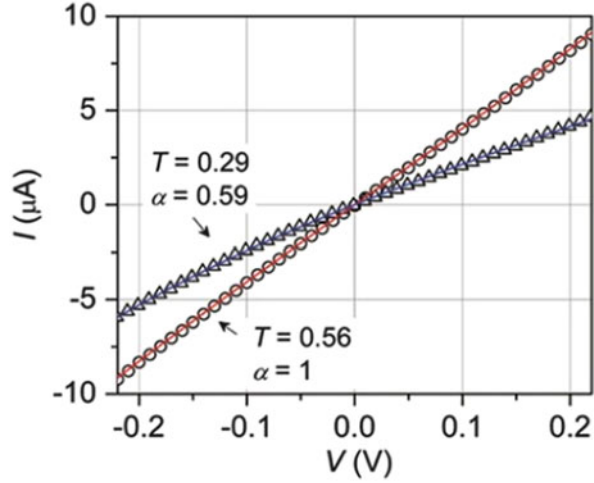
**Fig. 3.10** (a) Schematic illustration of TVS analysis of an  $I$ - $V$  curve. Change in the shape of the tunneling barrier as a function of the bias voltage [46]. For details, see main text. (b) Transition voltage spectroscopy for the single alkanedithiol molecular junction taken at different separation of the electrode ( $I$ -4). (c) 2-D transition voltage histograms for single alkanedithiol molecular junction at three different conductance regimes ( $H$ ,  $M$ ,  $L$ ) [45]

and electrode Fermi level can be determined as an effective tunneling barrier height in a transition voltage spectroscopy (TVS), in which minimum voltage ( $V_{\min}$ ) on a  $(I/V^2)$ - $1/V$  curve (Fowler–Nordheim plot) of  $I$ - $V$  data is associated with tunneling barrier height and the energy-level position of the closest conduction orbital relative to the electrode Fermi level [1, 45, 46]. The minimum voltage (i.e., transition voltage) on the Fowler–Nordheim plot corresponds to the voltage at which the electron transport changes between the direct tunneling and the field emission or F–N tunneling. TVS allows for the determination of the tunneling barrier height, i.e., energy-level alignment between the molecule and the electrodes in single molecular junctions.

Tao et al. have demonstrated TVS for single molecular junctions with different binding geometries with Au electrodes to analyze the tunneling barrier heights and the dependence of the energy-level alignment on the Au–molecule contact geometry in the molecular junction [45]. Figure 3.10 shows the TVS of the alkanedithiol molecular junctions sandwiched by Au electrodes, featuring three conductance values ( $H$ ,  $M$ , and  $L$ ). Despite their lower conductance values, the  $L$ -junctions show smaller transition voltage ( $V_{\min} = 0.7$  V) than those for  $M$ - and  $H$ -junctions ( $V_{\min} = 1.1$  and  $1.4$  V), which indicates that the difference between the HOMO and the Fermi level of the Au electrodes is smaller for  $L$ -junctions than those of  $M$ - and  $H$ -junctions. The  $L$ -junction has been attributed to a gauche conformation, and the theoretical calculation supports a smaller HOMO–Fermi gap for the  $L$ -junctions. The experimental observation that both  $H$ - and  $M$ - junctions exhibit similar transition voltages (energy-level alignments between the molecule and the Au electrodes) and the absence of correlation between the conductance and the transition voltages mean that the conductance variation is primarily due to variation of the contact resistance (i.e., metal–molecule electronic coupling efficiency).

In the tunneling barrier height model of the TVS analysis, the energy-level alignment is discussed. Next, we pay attention to the metal–molecule coupling

**Fig. 3.11** The examples of  $I$ - $V$  curves of BDT molecular junctions at different transmission regimes ( $T = 0.56$  and  $0.29$ ). The best-fit results are shown as lines,  $\Gamma = 253$  meV,  $\varepsilon_0 = 225$  meV for  $T = 0.56$ ,  $\Gamma_R = 75$  meV,  $\Gamma_L = 127$  meV,  $\varepsilon_0 = 317$  meV for  $T = 0.29$  [25]



strength in the single molecular junctions. In a single-level tunneling model,  $I$ - $V$  characteristic of the molecular junction is represented by

$$I(V) = \frac{8e}{h} \frac{\Gamma_L \Gamma_R}{\Gamma_L + \Gamma_R} \left\{ \tan^{-1} \left( \frac{\Gamma_R}{\Gamma_L + \Gamma_R} eV - \varepsilon_0 \right) + \tan^{-1} \left( \frac{\Gamma_L}{\Gamma_L + \Gamma_R} eV + \varepsilon_0 \right) \right\} \quad (3.3)$$

where  $\varepsilon_0$ ,  $\Gamma_L$ , and  $\Gamma_R$  are the energy difference between the conduction orbital and metal orbital and the strength of the coupling between molecule and left and right electrodes, respectively [1, 2]. Figure 3.11 shows the example of the  $I$ - $V$  curve of the single benzenedithiol (BDT) molecular junction [25]. By fitting the experimental result with Eq. 3.3, the  $\Gamma_L$ ,  $\Gamma_R$ , and  $\varepsilon_0$  were determined to be 0.030 eV, 0.033 eV, and  $-0.63$  eV, respectively.

Based on this technique, there is a challenge to study the atomic structure of the metal–molecule interface of the single molecular junction [43]. Figure 3.12a shows the two-dimensional  $I$ - $V$  histogram summarizing the  $I$ - $V$  characteristics of 203 single BDT molecular junctions. The  $I$ - $V$  curves show the three statistically high-probability nonlinear curves, indicating the existence of three metastable states. Figure 3.12b, c shows the distribution of  $\varepsilon_0$  and  $\Gamma$  obtained from fitting 203  $I$ - $V$  characteristics to Eq. 3.3. The distribution of  $\Gamma$  shows three main coupling values, i.e., low (L), medium (M), and high (H), at 0.01, 0.05, and 0.14 eV, respectively. In contrast, the distribution of  $\varepsilon_0$  shows a single peak centered at 0.86 eV. The strength of the coupling is sensitive to the metal–molecule interface. The three different couplings suggest the three different adsorption sites of the BDT molecule. The current–voltage characteristics provide the information about the single molecular junction: conductance,  $\Gamma$ , and  $\varepsilon_0$ . By comparing these three parameters between

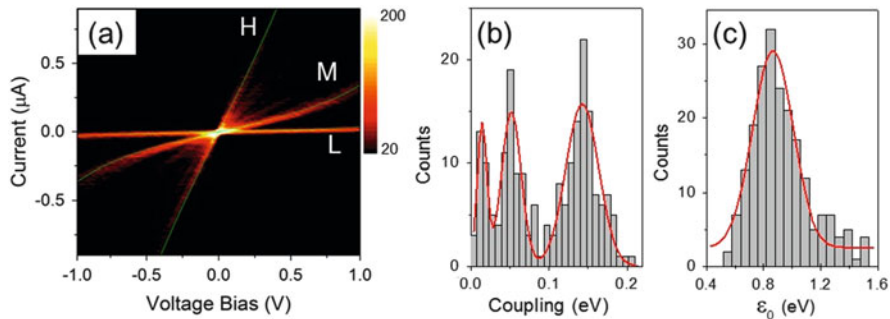


**Fig. 3.12** (a) Two-dimensional  $I$ - $V$  histogram summarizing the  $I$ - $V$  response of 203 single BDT molecular junctions. Three intense bands are clearly observed: high ( $H$ ), medium ( $M$ ), and low ( $L$ ) profiles, respectively. Distribution of (b)  $\Gamma$  and (c)  $\varepsilon_0$  constructed from  $I$  to  $V$  profiles fitted to a single-level tunneling process [43]

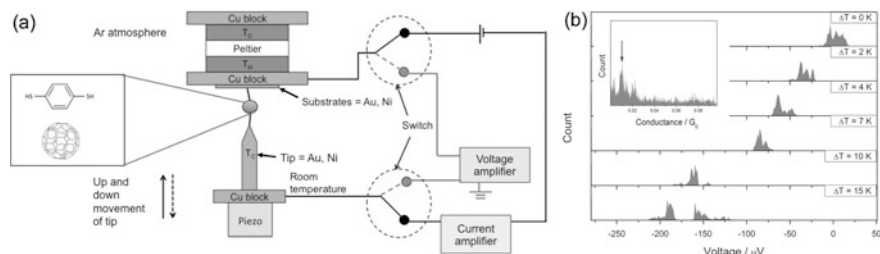
experimental results and theoretical calculation results with the model cluster, H, M, and L states are assigned to the bridge, hollow, and atop site, respectively.

### 3.1.5 Thermopower Measurement

The energy difference between Fermi level and conduction orbital can be investigated by analyzing the current-voltage characteristics. But it does not answer whether Fermi level is above or below the conduction orbital. Thermopower measurement provides this electronic information [12]. Therefore, combining the current-voltage measurement with the thermopower measurement, full characterization of the energy alignment of the conduction orbital is achieved. The Seebeck coefficient of the single molecular junction can be represented by

$$S_{Seebeck} = \frac{-\pi^2 k_B^2 T}{3e} \left. \frac{\partial \ln(t(E))}{\partial E} \right|_{E=E_F} \quad (3.4)$$

where  $k_B$ ,  $T$ , and  $t(E)$  are the Boltzmann constant, temperature, and transmission function, respectively [12]. When the conduction orbital is an occupied state (unoccupied state), the slope of the transmission curve is negative (positive) at Fermi level, and the thermopower becomes positive (negative). Here, it is noteworthy that the conductance is sensitive to the number of molecules bridging the metal electrodes and the strength of the metal-molecule coupling, but the Seebeck coefficient is independent of the number of molecules (see Eq. 3.4., i.e.,  $\partial \ln(t(E)) / \partial E = \partial \ln(nts(E)) / \partial E = \partial \ln(n = \text{const.}) + \partial \ln(ts(E)) / \partial E$  where  $n$  and  $ts(E)$  are the transmission function of a single molecular junction and number of molecules, respectively).



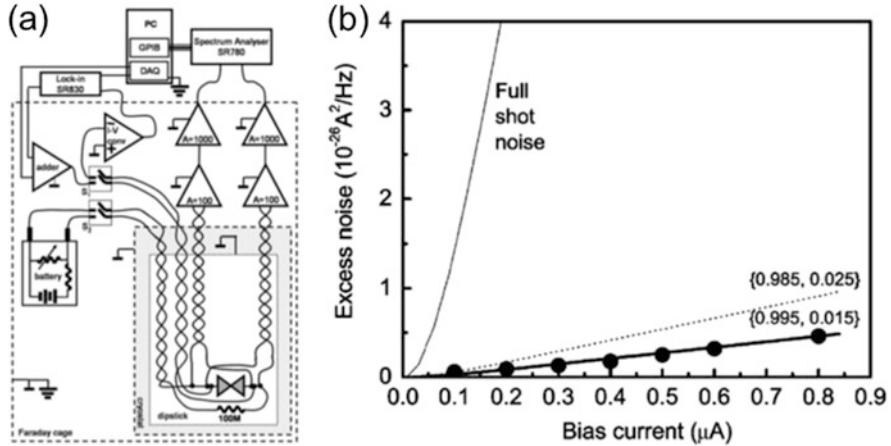
**Fig. 3.13** (a) Schematic diagram of the thermoelectric voltage measurement setup. (b) Thermo-electric voltage histograms for BDT/Ni junctions [47]

Figure 3.13 shows the example of the experimental setup of the thermopower measurement with STM [47]. A difference in temperature between the tip and the substrate is generated by controlling the temperature of the substrate with a Peltier device. The STM tip is mounted on a Cu block and kept at approximately room temperature. The STM tip is brought close to the substrate until it reaches a certain threshold conductance value larger than the conductance of the molecular junctions. Subsequently, the bias voltage source and current amplifier are disconnected, and the voltage amplifier is connected. Figure 3.13b shows the voltage histogram for BDT/Ni junctions. The negative thermoelectric voltage indicates that the charge carriers are electrons. The absolute value of the thermoelectric voltage rises up with increasing the temperature difference across the junction. The Seebeck coefficient is calculated to be in the range of  $-12.5 \pm 1.2$  to  $-14.1 \pm 1.0 \mu\text{V}/\text{K}$  from the slope of the peak voltage in the voltage histograms as a function of the temperature difference across the junction.

The Seebeck coefficient measurement can provide insight into the electronic structure of the single molecular junction with the aid of the theoretical calculation. The *ab initio* theoretical calculation of the model cluster provides the transmission function of the single molecular junction. Using the transmission function, we can calculate the Seebeck coefficient based on Eq. 3.4. By comparing the calculated Seebeck coefficient with the experimentally obtained one, we can determine the position of the conduction orbital. Reddy et al. succeeded to reveal that the Au Fermi-level position is 1.2 eV above the HOMO level of BDT [12].

### 3.1.6 Shot-Noise Measurement

The determination of the number of molecules bridging between metal electrodes is important but a difficult subject. In most of studies, the number of the molecule has been determined by the stepwise conductance change in the conductance trace during the breaking the junction. The conductance of the last plateau is assumed to be a single molecular junction [1, 2]. The analysis of the conductance step is



**Fig. 3.14** (a) Schematic outline of the setup used for simultaneous measurements of point-contact spectroscopy and shot noise on a single molecular junction. (b) Excess noise, that is, the difference between the measured white noise level with and without current, as a function of the applied current. The Poissonian shot-noise level is indicated by the curve marked “full shot noise.” The dashed curve illustrates the sensitivity of the noise to the distribution of transmission probabilities for a slightly different choice ( $\tau_1 = 0.985$ ,  $\tau_2 = 0.025$ ) [10]

not a direct evidence of the formation of the single molecular junction. The shot-noise measurement in combination with the conductance measurement provides an alternative approach to assess the number of the molecular junctions (i.e., the information on the number of the conduction channels and transmission probability of each channel that directly correlates with the number of the molecular junctions) [10, 27, 31]. If the number of the conduction orbital is one, we can know that the number of molecules bridging between metal electrodes is exactly one (see Fig. 3.14 and corresponding text).

The shot noise originates from time-dependent fluctuations in the electrical single-molecule current caused by the discreteness of the electron charge. When electrons flow across the molecular junction, the noise level is determined by the number of available transmission channels across the junction and their transmission probabilities  $\tau_i$ . The total noise level of a quantum point contact for temperature  $T$  and applied bias voltage  $V$  is given as

$$S_{noise} = 2eV \coth\left(\frac{eV}{kT}\right) \frac{2e^2}{h} \sum \tau_i (1 - \tau_i) + 4k_B T \frac{2e^2}{h} \sum \tau_i^2 \quad (3.5)$$

On the other hand, the conductance ( $G$ ) of the molecular junction is given by

$$G = 2 \frac{2e^2}{h} \sum \tau_i \quad (3.6)$$

The shot-noise and the conductance contain information on the transmission probabilities. Here, a set of transition probabilities ( $\tau_i$ ) is described by two independent equations (Eqs. 3.5 and 3.6). Therefore, information on the transmission probability of each channel (i.e., the number of the conduction channels) can be obtained by combining shot-noise and conductance measurement. The simultaneous shot-noise and conductance measurements have been performed for single H<sub>2</sub>, benzene, and water molecular junctions [10, 27, 31].

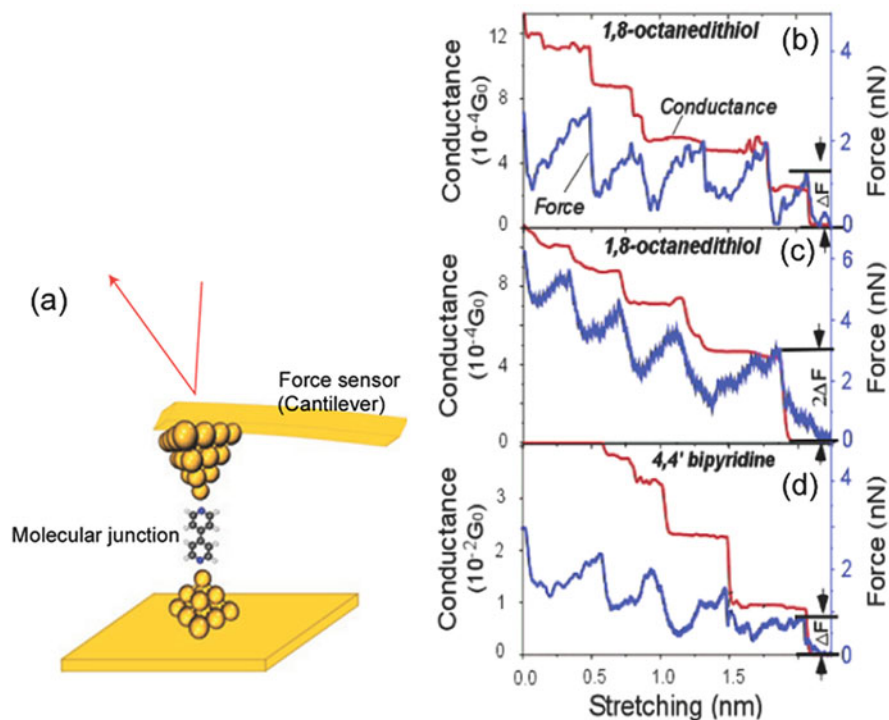
Figure 3.14a shows the experimental setup of the shot-noise measurement. The shot noise is a weak signal, and thus, there are ideas to separate the shot noise from other noises. The cryostat together with the amplifiers is placed in an acoustically shielded Faraday cage to prevent coupling to external vibrations or electromagnetic fields. For shot-noise measurements ( $S_1$  open,  $S_2$  closed), the signal is picked up by two separate Cu wire twisted pairs and then is amplified by two parallel stages of low-noise preamplifiers. The two outputs are sent to a signal analyzer, which takes a Fourier transform of both signals and calculates the cross spectrum of the two signals. By taking the cross spectra, we can efficiently extract the intrinsic shot noise from the signal.

Figure 3.14b shows shot noise for the single D<sub>2</sub>/Pt molecular junctions as a function of bias current [10]. The Poissonian shot-noise level is indicated by the curve marked “full shot noise,” and we observe a strong quantum suppression of the noise. The zero bias conductance for this junction is 1.01  $G_0$ , and the experimental result can be well fitted with theory assuming essentially a single fully open channel, ( $\tau_1 = 0.995$ ,  $\tau_2 = 0.015$ ). The number of channels is close to one, indicating that the number of the molecules bridging Pt electrodes is one.

### 3.1.7 Force Measurement

Simultaneous conductance and force measurement provides an understanding of the structure–conductance relationship in a single molecular junction [13, 48]. Typically, conductance and force are simultaneously measured during the elongation process of a single molecular junction using atomic force microscopy-based BJ (AFM-BJ) method (Fig. 3.15a), where stepwise conductance changes accompany abrupt changes in forces, which are associated with structural rearrangement in the junctions along the deformation and rupture of the junction.

Figure 3.15b–d shows the force curve during breaking of the alkanedithiol molecular junction binds to Au electrodes together with the conductance curve. While the conductance decreases in discrete steps, the corresponding force decreases in sawtooth waves. The force required to break a single alkanedithiol molecular junction (i.e., the final step of the force curve, which is accompanied with a conductance drop to zero) is 1.5 nN. The rupture force is similar to the force required to break an Au–Au bond. Because the Au–S bond is stronger than the Au–Au bond, the Au–Au bond is responsible for the breakdown of the alkanedithiol molecular junction. In contrast, for a single 4,4'-bipyridine (BPY) molecular junction, the



**Fig. 3.15** (a) Schematic representation of a BPY junction formed between a gold-coated cantilever tip and a gold substrate. Au, C, H, and N atoms are shown in yellow, gray, white, and blue, respectively [48]. (b–d) Simultaneously recorded conductance and force curves of (b, c) C8 and (d) BPY junctions during stretching [13]

force required to break a single molecular junction is 0.8 nN, which is considerably smaller than the force required to break an Au–Au bond. The smaller force is expected because BPY binds to Au electrodes via N–Au affinity, which is weaker than the S–Au bond. The force required to break a single molecular junction reveals the bonding nature of the molecule to the electrodes.

The following conductance and force study on the BPY junctions binding to Au electrodes revealed that the single BPY junctions feature two preferential high- and low-conductance states with  $\pi$ –Au and N–Au metal–molecule couplings and the two conductance states exhibit distinct rupture forces of 1.5 and  $\sim 0.8$  nN (Fig. 3.16) [48]. In general rupture force is correlated with chemistry (binding modes) at the metal–molecule interfaces in a single molecular junction. Together with characterizing the charge transport property (conductance), the distinct preferential rupture force measurement is complementary evidence that a “single” molecule is bridging a gap between metal electrodes.

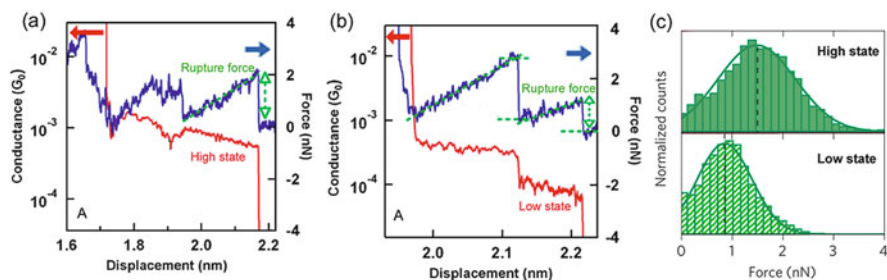


**Fig. 3.16** (a, b) Simultaneous force (blue) and conductance (red) measurements during elongation of the BPY molecular junctions featuring rupture forces of (a) high- and (b) low-conductance junctions. Rupture forces are indicated by up and down arrows. (c) Histograms of rupture forces for BPY molecular junctions with high- ( $1.48 \pm 0.01$  nN) and low-conductance states ( $0.85 \pm 0.01$  nN). Solid lines are Gaussian fits to the data, and dashed lines connecting the peaks of the distributions are provided as visual guides [48]

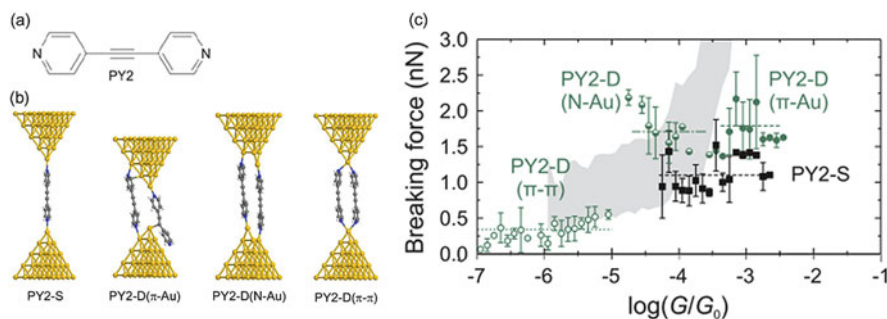


**Fig. 3.17** (a) Chemical structure of the tolane-type molecule with the two pyridine terminal groups (PY2). (b) Structural models of BPY2 junctions. (c) Simulated mean breaking force (symbols) and its standard deviation (error bar) for PY2 molecular junctions as a function of the logarithm of the normalized conductance  $\log(G/G_0)$ . “PY2-S” and “PY2-D ( $\pi$ - $\pi$ )” indicated a single PY2 junction and PY2 dimer junction, respectively. “PY2-D ( $\pi$ -Au)” and “PY2-D (N-Au)” denote PY2 double junctions with  $\pi$ -Au and N-Au couplings (see the models in b). The gray bands mark the experimental data [49]

A very recent combined AFM-BJ experiment and DFT simulation study has demonstrated detailed analysis in rupture forces of tolane (diphenylacetylene)-type molecular junctions with two pyridine terminal groups (Fig. 3.17a) [49]. DFT simulations most quantitatively reproduce the experimental data on the rupture force and conductance of the PY2 molecular junctions (Fig. 3.17b, c). DFT-based rupture force simulation revealed the rupture forces of the tolane-type molecular junction are ca. 1–2 nN and are independent of metal–molecular coupling types of the “N–Au” and “ $\pi$ -Au,” which is in contrast to the BPY junctions. The smaller rupture force  $\sim 0.5$  nN is ascribed to the formation of  $\pi$ - $\pi$ -stacked dimer junction (see PY2-D( $\pi$ - $\pi$ ) in Fig. 3.17b). The simultaneous measurement of conductance and forces in the molecular junctions is still a challenging task as evidenced by the scarcity of

experimental results, requiring further research and development of the current and force detection techniques.

## 3.2 Summary and Future Perspective

In this chapter, we discuss the characterization technique of the single molecular junction (Table 3.1). The chemical species bridging between metal electrodes are determined with the IETS, PCS, and SERS. The length of the single molecular junction and metal atomic contact is determined by the conductance measurement during the breaking process. The number of molecules bridging between metal electrodes is determined by the simultaneous shot-noise and conductance measurement. The atomic structure of the single molecular junction can be identified by the combination of these techniques. The electronic structure of the single molecular junction can be studied with the thermopower measurement and current–voltage characteristics. The thermopower measurement determines whether a conduction orbital is above or below the Fermi level of the electrode (i.e., whether a dominant conduction orbital is HOMO or LUMO and whether a charge carrier is a hole or electron), while the current–voltage characteristic determines the energy difference between a conduction orbital and Fermi level. The force measurement provides information about the bonding nature of the molecule to the metal electrode.

The characterization of magnetic properties of the single molecular junction is becoming an important topic, although we made no mention of this topic. The use of molecular spin state as a quantum information for data storage has attracted considerable attention in the context of next-generation low-power data storage devices. At ultralow temperature, the spin state of the single molecular junction has been investigated with the current–voltage characteristic. The Kondo effect and its manipulation have been reported for single molecular junction with transition metal complex (e.g., Co, Mn) [50].

We consider that the characterization of adsorption site at the metal–molecule interface and time-resolved spectroscopy will become the next important topic in developing the new characterization technique of the single molecular junction. The conductance of the single molecular junction is sensitive to the local contact

**Table 3.1** Summary of the characterization techniques

Characterization technique	Quality and quantity to be measured
IETS, Raman spectroscopy	Junction configuration
Force measurement	
Conductance and shot-noise measurements	Transmission
	Conduction channels (number of molecules)
$I$ – $V$ and thermopower measurements	Electronic structure, charge carriers
IETS, PCS	Transport mechanism

configuration at the metal–molecule interface. A number of theoretical and experimental studies have discussed that the conductance of the single molecular junction changes more than two orders of magnitude depending on the molecular adsorption site on the metal electrodes [43]. The importance of the characterization of the adsorption site is clear. In theory, the vibrational spectroscopy of the single molecular junction can determine the adsorption site, but there are little studies to fix the adsorption site with the vibration spectroscopy up to now. The vibration mode of the metal–molecule bond is susceptible to the molecular adsorption site, and the energy shift of the vibration mode is widely used for identification of the adsorption site in the case of molecules on well-defined surface, such as metal, semiconductor, and metal oxide surface. Similar detailed vibration analysis can fix the adsorption site of the single molecular junction. The current–voltage characteristics also provide information about the metal–molecule interface, as strength of the metal–molecule coupling. This metal–molecule coupling varies with the molecular adsorption site, and thus, the adsorption site can be determined by the current–voltage characteristic measurement, together with the theoretical calculation. One of the big problems in the industrial application of the single molecular devices is the fluctuation of the conductance of the single molecular device. This fluctuation is mainly caused by the change in the molecular adsorption site. The characterization and governing of the molecular adsorption site represents a crucial step toward the reliable single molecular device and integration of single molecular devices into a working device.

The second challenge in the characterization technique of the single molecular junction is the time-resolved spectroscopy. Most of characterization technique of the single molecular junction cannot follow the high-speed event, such as chemical reaction, and phase transition. It is because the signal from the single molecule is weak, and it takes time to get the reliable signal. On the other hand, a timescale of  $\sim$ fs is required to track an atomistic motion of the single molecular junction. The structural changes in the single molecular junctions are directly translated into a change in the properties of the system. The high-speed characterization and controlling the structural fluctuation are much more important for the single molecular junction, compared to conventional organic electronic devices, such as organic field-effect transistor and light-emitting diode. In these organic electronic devices, a number of molecules contribute to the electron transport in the devices, and the character of the individual molecule is smeared out, and thus, the motion of individual molecule is not so important, compared to single molecular devices. In addition to the characterization of the motion of the single molecule, the time-resolved spectroscopy is important to investigate the excited state in photon-to-electron conversion, chemical reaction, and other ultrafast events in the single molecular junction. The pump-probe spectroscopy has been widely used to study the short-lived excited state (e.g., photoinduced phase transition, spin relaxation) [51]. A similar pump-probe spectroscopy would be applied to the single molecular junction. In order to get the signal from the single molecular junction, we think that the voltage pulse (current through the junction) should be the source of the pump or probe.

## References

1. Cuevas JC, Scheer E (2010) *Molecular electronics: an introduction to theory and experiment*. World Scientific Publishing Co. Pte. Ltd, Singapore
2. Kiguchi M, Kaneko S (2013) *Phys Chem Chem Phys* 15:2253
3. Song H, Kim Y, Jang YH, Jeong H, Reed MA, Lee T (2009) *Nature* 462:7276
4. Diez-Perez I, Hihath J, Lee LY, Yu, Adamska L, Kozhushner MA, Oleynik II, Tao N (2009) *Nat Chem* 1:635
5. Kiguchi M, Ohto T, Fujii S, Sugiyasu K, Nakajima S, Takeuchi M, Nakamura H (2014) *J Am Chem Soc* 136:7327
6. Su TA, Li H, Steigerwald ML, Venkataraman L, Nuckolls C (2015) *Nat Chem* 7:215
7. Fujii S, Tada T, Komoto Y, Osuga T, Murase T, Fujita M, Kiguchi M (2015) *J Am Chem Soc* 137:5939
8. Naidyuk Y, Yanson I (2005) *Point-contact spectroscopy*. Springer, New York
9. Ward DR, Halas NJ, Ciszek JW, Tour JM, Wu Y, Nordlander P, Natelson D (2008) *Nano Lett* 8:919
10. Djukic D, van Ruitenbeek JM (2006) *Nano Lett* 6:789
11. Ho Choi S, Kim B, Frisbie CD (2008) *Science* 320:1482
12. Reddy P, Jang SY, Segalman RA, Majumdar A (2007) *Science* 315:1568
13. Xu B, Xiao X, Tao NJ (2003) *J Am Chem Soc* 125:16164
14. Untiedt C, Yanson AI, Grande R, Rubio-Bollinger G, Agrait N, Vieira S, van Ruitenbeek JM (2002) *Phys Rev B* 66:085418
15. Kiguchi M, Djukic D, van Ruitenbeek JM (2007) *Nanotechnology* 18:035205
16. Smit RH, Untiedt C, Yanson AI, van Ruitenbeek JM (2001) *Phys Rev Lett* 87:266102
17. Kiguchi M, Hashimoto K, Ono Y, Taketsugu T, Murakoshi K (2010) *Phys Rev B* 81:195401
18. Thijssen WHA, Strange M, aan de Brugh JMJ, van Ruitenbeek JM (2008) *New J Phys* 10:033005
19. Perrin ML, Prins F, Martin CA, Shaikh AJ, Eelkema R, van Esch JH, Briza T, Kaplanek R, Kral V, van Ruitenbeek JM, van der Zant HS, Dulic D (2014) *Angew Chem Int Ed* 50:11223
20. Klausen RS, Widawsky JR, Steigerwald ML, Venkataraman L, Nuckolls C (2012) *J Am Chem Soc* 134:4541
21. Kiguchi M, Takahashi T, Takahashi Y, Yamauchi Y, Murase T, Fujita M, Tada T, Watanabe S (2011) *Angew Chem Int Ed* 50:5708
22. Jaklevic RC (1966) *J Lambe: Phys Rev Lett* 17:1139
23. Stipe BC, Rezaei MA, Ho W (1998) *Science* 280:1732
24. Smit RHM, Noat Y, Untiedt C, Lang ND, van Hemert MC, van Ruitenbeek JM (2002) *Nature* 419:906
25. Kim Y, Pietsch T, Erbe A, Belzig W, Scheer E (2011) *Nano Lett* 11:3734
26. Tsutsui M, Taniguchi M, Shoji K, Yokota K, Kawai T (2009) *Nanoscale* 1:164
27. Kiguchi M, Tal O, Wohlthat S, Pauly F, Krieger M, Djukic D, Cuevas JC, van Ruitenbeek JM (2008) *Phys Rev Lett* 101:046801
28. Hihath J, Arroyo CR, Rubio-Bollinger G, Tao N, Agrait N (2008) *Nano Lett* 8:1673
29. Taniguchi M, Tsutsui M, Yokota K, Kawai T (2009) *Nanotechnology* 20:434008
30. Pong D, Lazorcik J, Mantooh BA, Hoore M, Ratner MA, Troisi A, Yao Y, Ciszek JW, Tour JM, Shashidhar R (2006) *Nat Mater* 5:11
31. Tal O, Krieger M, Leerink B, van Ruitenbeek JM (2008) *Phys Rev Lett* 100:196804
32. Kiguchi M, Murakoshi K (2008) *J Phys Chem C* 112:8140
33. Nakazumi T, Kaneko S, Matsushita R, Kiguchi M (2012) *J Phys Chem C* 116:18250
34. Kaneko S, Nakazumi T, Kiguchi M (2010) *J Phys Chem Lett* 1:3520
35. Thijssen WH, Djukic D, Otte AF, Bremmer RH, van Ruitenbeek JM (2006) *Phys Rev Lett* 97:226806
36. Kiguchi M, Nakazumi T, Hashimoto K, Murakoshi K (2010) *Phys Rev B* 81:45420
37. Nakazumi T, Kaneko S, Kiguchi M (2014) *J Phys Chem C* 118:7489

38. Tian J-H, Liu B, Xiulan, Yang Z-L, Ren B, Wu S-T, Nongjian, Tian Z-Q (2006) *J Am Chem Soc* 128:14748
39. Ward DR, Corley DA, Tour JM, Natelson D (2011) *Nat Nanotechnol* 6:33
40. Ioffe Z, Shamaï T, Ophir A, Noy G, Yutsis I, Kfir K, Cheshnovsky O, Selzer Y (2008) *Nat Nanotechnol* 12:727
41. Konishi T, Kiguchi M, Takase M, Nagasawa F, Nabika H, Ikeda K, Uosaki K, Ueno K, Misawa H, Murakoshi K (2013) *J Am Chem Soc* 135:1009
42. Liu Z, Ding SY, Chen ZB, Wang X, Tian JH, Anema JR, Zhou XS, Wu DY, Mao BW, Xu X, Ren B, Tian ZQ (2011) *Nat Commun* 2:305
43. Kaneko S, Murai D, Marqués-González S, Nakamura H, Komoto Y, Fujii S, Nishino T, Ikeda K, Tsukagoshi K, Kiguchi M (2016) *J Am Chem Soc* 138:1294
44. Ikeda K, Sato J, Fujimoto N, Hayazawa N, Kawata S, Uosaki K (2009) *J Phys Chem C* 113:11816
45. Guo S, Hihath J, Diez-Perez I, Tao N (2011) *J Am Chem Soc* 133:19189
46. Beebe JM, Kim B, Gadzuk JW, Frisbie CD, Kushmerick JG (2006) *Phys Rev Lett* 97:026801
47. Lee SK, Ohto T, Yamada R, Tada H (2014) *Nano Lett* 14:5276
48. Aradhya SV, Frei M, Hybertsen MS, Venkataraman L (2012) *Nat Mater* 11:872
49. Yoshida K, Pobelov IV, Manrique DZ, Pope T, Meszaros G, Gulcur M, Bryce MR, Lambert CJ, Wandlowski T (2015) *Sci Rep* 5:9002
50. Parks JJ, Champagne AR, Costi TA, Shum WW, Pasupathy AN, Neuscamman E, Flores-Torres S, Cornaglia PS, Aligia AA, Balseiro CA, Chan GK, Abruña HD, Ralph DC (2010) *Science* 328:1370
51. Loth S, Etzkorn M, Lutz CP, Eigler DM, Heinrich AJ (2010) *Science* 329:1628

# Chapter 4

## Molecular Wires: An Overview of the Building Blocks of Molecular Electronics

Paul J. Low and Santiago Marqués-González

**Abstract** Molecular wires are the archetypal components in molecular electronics, performing the simple electronic function of conducting charge from one side of a circuit to the other. At the most basic level, a molecular wire is composed of a backbone through which the transmission of charge can take place, either via a coherent superexchange (tunneling) or incoherent charge-hopping mechanism and binding or anchoring groups to physically attach and electronically couple the wire to the rest of the circuit (typically metal electrodes). However, despite the simplicity of concept, the design of an efficient molecular wire, i.e., one able to conduct charge close to the ideal quantum of conductance  $G_0$  and with extremely low attenuation with distance, in a uniform and reproducible fashion remains a topic of debate and intense investigation. In this chapter an empirical overview of the chemistry of molecular wires is presented, with emphasis on the chemical structures and influence on the electrical properties of the molecular junctions formed from them.

**Keywords** Single-molecule junctions • Charge transfer • Molecular wire design • Metal-molecule interface • Anchoring groups

### 4.1 Introduction

Molecular wires have served as the test-bed components for the concepts, theories, methods of measurement and device fabrication since the earliest days of molecular electronics and continue to be a topic of intense interest and investigation [1]. By analogy with a conventional macroscopic metallic wire, a molecular wire is a simple structure, usually linear in shape, through which charge (i.e., electrons or holes) can be transmitted. A conceptual model for a molecular wire would therefore consist of two terminals, between which charges will be exchanged, linked through a suitable

---

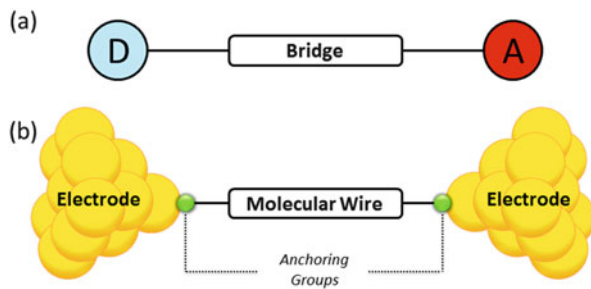
P.J. Low (✉)

School of Chemistry and Biochemistry, University of Western Australia, 35 Stirling Highway, Crawley 6009, Western Australia, Australia  
e-mail: [paul.low@uwa.edu.au](mailto:paul.low@uwa.edu.au)

S. Marqués-González

Department of Chemistry, Graduate School of Science and Engineering, Tokyo Institute of Technology, 2-12-1 W4-10 Ookayama, Meguro-ku, Tokyo, 152-8511, Japan

**Fig. 4.1** (a) Schematic representation of a donor-bridge-acceptor (D-B-A) assembly. (b) Molecular junction schematic view

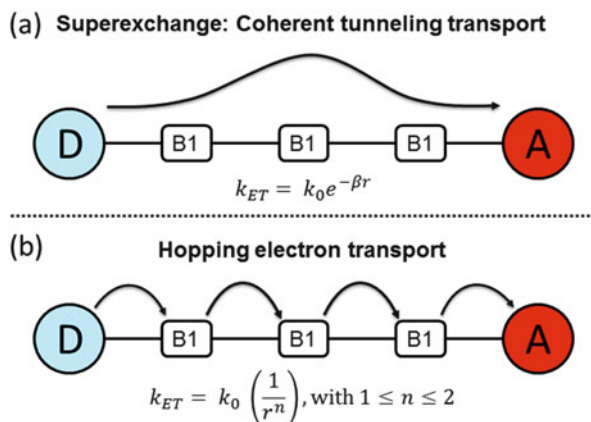


bond or anchoring group to some molecular bridge which mediates the charge exchange (Fig. 4.1). The terminals can be considered as some appropriate electron donor (D) and acceptor (A) combination, or an electrode pair. These two different models are usually represented as donor-bridge-acceptor (D-B-A) assemblies or, since the electrodes are typically metallic (although nonmetallic electrodes such as graphene are gathering attention), as metal-molecule-metal junctions. Charge transfer in classic D-B-A systems can be induced photochemically or thermally. On the other hand, in molecular junctions, charge transfer can be induced by application of a bias voltage.

The concepts of charge transfer in molecular systems are well developed, with Marcus theory providing a conceptual framework around which to relate electron-transfer rates ( $k_{ET}$ ) to the thermodynamic driving force ( $\Delta G^0$ ), the reorganization energy ( $\lambda$ ) which can be further partitioned into the inner-sphere (which arises from changes in molecular structure as a consequence of the change in charge at each site D and A) and outer-sphere (arising from changes in solvent distribution and solvation energies) contributions, and the electronic coupling,  $V$ , between the D and A sites mediated by the bridge, B [2, 3]. In cases where there is significant spatial overlap of the donor HOMO (highest occupied molecular orbital) with the acceptor LUMO (lowest unoccupied molecular orbital) via the bridge and hence the highest coupling terms  $V$ , photoexcitation can lead to charge transfer directly from D to A. In other cases, typically for longer bridges and lower  $V$ , localized photoexcitation is followed by charge (electron) transfer from the photoexcited donor to the acceptor or from the donor to the photoexcited acceptor. This process of charge transfer takes place by one of two general mechanisms: superexchange (tunneling) or hopping (Fig. 4.2).

In the case of electron transfer by tunneling, the unoccupied molecular orbitals of the bridge are too high in energy to be directly populated by the charge being transferred from the donor. Rather, the charge tunnels from donor to acceptor via virtual bridge states, but does not reside on the bridge in any physical sense. The coupling parameter is therefore a function of the interactions D-to-B and also B-to-A, and the overall coupling element  $V_{DA}$  can be further partitioned into coupling terms that explicitly include the donor-bridge ( $V_{DB}$ ) and bridge-acceptor ( $V_{BA}$ ) terms. If the bridge is considered as a series of identical sites, then a third term  $V_{BB}$  representing the coupling between these sites within the bridge can also be

**Fig. 4.2** (a) Schematic representation of the superexchange. (b) Hopping electron-transfer mechanisms



introduced. For  $N$  such sites, it is possible to show that the overall term  $V_{DA}$  can be written as

$$V_{DA} = \frac{V_{DB}V_{BA}}{\Delta E_{DB}} \left( \frac{V_{BB}}{\Delta E_{DB}} \right)^{N-1}$$

where  $\Delta E_{DB}$  is the energy gap for charge injection from the donor into the bridge virtual states [4]. This is an important concept as it underlines the key point that the assessment of a wirelike molecule or comparisons between similar systems need to consider not only the structure of the bridge but also the nature of the end caps.

Electron-transfer rates,  $k_{ET}$ , in the tunneling regime are expressed in the form

$$k_{ET} = k_0 e^{-\beta r_{DA}}$$

where  $k_0$  is the “fundamental” electron-transfer rate at the van der Waals contact distance,  $r_{DA}$  is the separation of the donor and acceptor, and  $\beta$  is the bridge-specific attenuation factor. For effective long-range charge transfer, the attenuation factor should be low. The attenuation factor is determined by measuring electron-transfer rates for a series of closely related D-(B) $_N$ -A molecules across a range of bridge lengths and hence  $r_{DA}$ . Typically, for systems in which tunneling is the dominant transport mechanism, values of  $\beta$  range from 2.0 to 5.0 Å<sup>-1</sup> in vacuum and considerably less for covalently linked molecular bridges, as will be illustrated further in the examples below.

In contrast to the tunneling mechanism, when the bridge orbitals are sufficiently close in energy to the donor, the transferring charge can become localized on the bridge at a suitable redox site for a short period before moving (hopping) to the next. This random walk continues until the charge crosses the bridge. Since the hopping mechanism is a series of redox processes, there is considerable nuclear motion associated with each step, and the charge-transfer rate is temperature dependent. The rate of charge transfer is inversely proportional to the charge-transfer distance

[5]. While in principle such mechanisms should be simple to determine and distinguish, in practice both mechanisms can coexist, with superexchange often found to dominate at shorter charge-transfer distances and hopping becoming more important for longer bridges.

The fundamentals of intramolecular charge transfer determined from studies of D-B-A assemblies, including mixed-valence examples (D-B-D<sup>+</sup> or A<sup>-</sup>-B-A), have provided the basis for an extension to molecular electronic junctions [6], where the donor and acceptor are replaced by macroscopic electrodes under an applied bias. In these cases, rather than discussing an electron-transfer rate,  $k_{\text{ET}}$ , the notion of conductance,  $G$ , is used and usually reported in units of Siemens (S) (or more commonly nano-Siemens (nS)) or as a fraction of the quantum of conductance  $G_0$ :

$$G_0 = \frac{2e^2}{h} = 77481 \text{ nS}$$

Theoretical models of a linear relationship between  $k_{\text{ET}}$  and  $G$  in both tunneling and hopping regimes have been proposed [7–10], although experimentally a power law correlation has been found [11]. These discrepancies have been attributed to differences in the charge-transfer energy barriers between the bridge and the D/A groups or electrode and bridge de-phasing and the potential for multiple mechanisms of charge transfer. The relative charge-transfer rate constants for a bridge obtained from electrochemical or spectroscopic methods may not therefore correlate with the order of conductance values obtained from molecular junction studies. Nevertheless, despite the differences that may characterize the individual terms, similar expressions relating conductance ( $G$ ) to junction length ( $r$ ) in both tunneling ( $G = G_0 e^{-\beta r}$ ) and hopping (where for  $N$  hopping sites, a linear current dependence on  $1/N$  indicates directional hopping and a linear dependence on  $1/N^2$  is indicative of a nondirectional diffusion mechanism) persist [12].

Much of the early work in single-molecule electronics was concerned largely with the chemical nature of the molecular backbone (bridge). However, it is now well established that the electrical performance of a molecule is an ensemble effect of the system, with the electrode-molecule interface playing a major role [13–17]. These contacting groups not only serve to physically attach the molecule to the electrode surface but also serve as the coupling point, or tunnel barrier, between the molecule and the electrode.

Contemporary studies are now beginning to address the processes that take place at the electrode-molecule interface as the junction is formed and also the nature of the particular surface features and binding geometry, molecular alignment and conformation within the junction, and variations in these structural details between individual junctions. The importance of these junction-to-junction variations is clearly evinced in the multiple conductance values often found in single-molecule conductance studies, which can vary between individual measurements by several orders of magnitude. These different conductance values are commonly ascribed to differences in the surface roughness of the electrodes and the different contact geometries [18], although as described below, other deformations including tilting

of the molecule within the junction, molecular stretching or other changes in molecular conformation, electrode contacts to different parts of the molecule, and electrode deformation including extrusion of metal-atom chains from metallic electrode surfaces are all important in considering the particular behavior of any individual junction measurement.

In the simplest case though, we can consider the general scenario arising from the construction of conductance histograms from many (hundreds to tens of thousands) of individual measurements. Very often, three different conductance peaks or values will be observed, which have been termed simply types A, B, and C or low (L), medium (M) and high (H) conductance, respectively (Fig. 4.3). The low-conductance (A) contacts are ascribed to molecule binding at low-coordination surface sites. The medium (B) and higher (C) conductance values are believed to be due to molecule binding at defect sites and which can also include interactions from the  $\pi$ -rich regions of the molecule to defects on the electrode surface in a “side-on” manner. Within each of these conductance peaks further variation can be ascribed to the variations in fine details of the molecular geometry within the junction.

The behavior of molecules within molecular junctions is therefore influenced not only by the structure of the particular “bridge” but also the nature of the electrode; the detail of the electrode-molecule contact, including potential for deformation of the electrode surfaces during junction evolution; and other factors such as local solvent environment which will be discussed in relation to specific examples in the subsequent sections of this chapter. In addition, the ability to vary the electrode separation in various break junction and STM-based junctions allows a degree of mechanical control over the molecular conformation and length. The design of molecular wires therefore needs to take into consideration not only the chemical nature of the species under investigation but also the nature of the measurement.

Molecular electronics is a truly interdisciplinary field of endeavour. Innovative synthetic chemistry has allowed molecules of incredible structural diversity bearing a wide range of surface contacting groups to be prepared. Advanced engineering

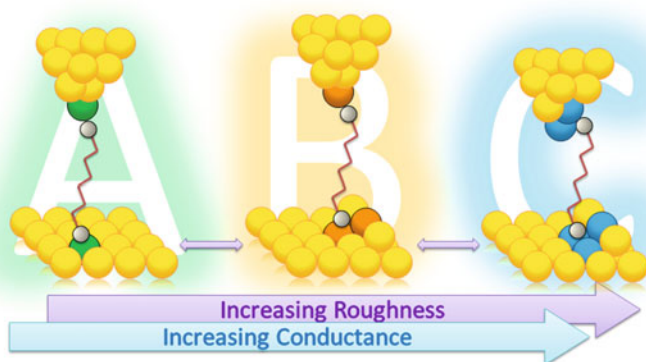


**Fig. 4.3** Schematic representation of a molecular junction showing the A, B, and C binding modes, responsible for the different conductance values typically observed for the same molecular wire

and experimental physics now allow the truly remarkable feat of suspending an individual molecule within a junction and measuring the conductance values over thousands of individual experiments. The range of in situ spectroscopies that allow characterization of these junctions is growing, whilst advances in theory and high-level computation help to interpret the results and inspire and direct new experiments. Together, activities in these areas have brought the field of molecular electronics and the study of molecular wires in particular to an advanced state [19]. Here we will consider the new insights concerning wirelike molecules within molecular junctions that have emerged from recent studies of wirelike molecules based on saturated hydrocarbons, oligo(enes) and oligo(ynes), oligo(arylenes), and oligo(phenylene ethynylenes) and oligo(phenylene vinylenes).

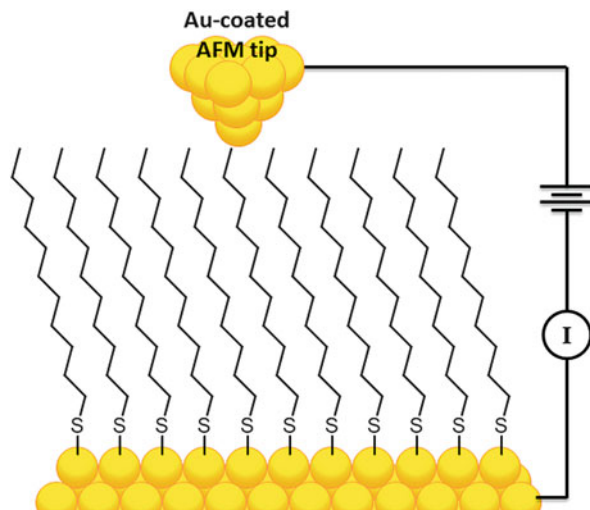
## 4.2 Saturated Hydrocarbon Wires

The first reports of studies of conductance through molecules emerged in the late 1960s. However, the first clear evidence for a consistent, exponential decay of conductance with molecular length is likely due to Mann and Kuhn [20]. These workers succeeded in creating a monolayer junction by depositing Hg, Pb, Au or Al as top-contact electrodes on to a series of Langmuir-Blodgett monolayers of cadmium salts of fatty acids  $\text{CH}_3(\text{CH}_2)_{n-2}\text{CO}_2\text{H}$  ( $n = 18-22$ ) supported on Al-coated glass slides. Since that time, alkanes have maintained a special place as prototypical molecular wires, despite some rather obvious, and perhaps deceptive, apparent shortcomings. The availability of homologous series of alkanes  $\text{CH}_3(\text{CH}_2)_{n-1}\text{X}$  and  $\text{X}-(\text{CH}_2)_n-\text{X}$  where X is some surface binding group has allowed the exponential decay of conductance with length expected for a tunneling transport mechanism to be demonstrated on many occasions, in a wide range of experimental platforms using both monolayers and individual molecules [21]. From across these various studies, for well-packed monolayers and fully extended molecules, a decay factor  $\beta$  of about 1.14–1.5 per methylene ( $-\text{CH}_2-$ ) is commonly observed (Fig. 4.4) [22].

However, both  $\beta$  and conductance values for a given molecule can vary over many orders of magnitude which can be attributed to differences in electrode material and charge injection barriers and details of the individual contacts, solvation, and conformation. For example, the  $\beta$  value of alkane dicarboxylic acids in Pd or Ag junctions under ambient conditions was approximately 1 for the lowest conductance group in each case. The lack of dependence on the electrode material (and in principle the different energy gaps between the electrode Fermi level and the molecular energy levels) can be attributed to pinning of the Fermi levels and the molecular states [23]. However, under electrochemical control, the Fermi levels are changed relative to a reference electrode, while the molecular levels (in the case of redox-innocent alkanes) remain essentially constant. This change in Fermi level and molecular level alignment results in  $\beta$  values which range from 0.95 (Cu) to 0.71 (Ag) to 0.65 (Pd) [24, 25].

In conducting probe-atomic force microscopy (CP-AFM) studies of monolayers of octane- or decane-thiol, the use of a solvent environment (toluene or hexane) [26]

**Fig. 4.4** A typical approach to the measurement of  $I$ - $V$  data in a scanning probe-based molecular junction [22]



decreases the conductance value by up to three orders of magnitude in comparison with similar experiments conducted in ambient environments [27]. This has been proposed to be due to the solvent shell around the tip limiting the electronic coupling of the hydrocarbon “tail” of the molecule to the CP-AFM tip [21]. Interestingly, such differences are not as apparent in analogous studies of alkane dithiols under these different conditions [28, 29]; presumably the stronger chemisorbed contact at both molecule-electrode interfaces limits the effects of tip solvation.

With the mechanism of tunneling clearly established for alkane-based wires, it is possible to design more functional molecules, including surprisingly efficient molecular rectifiers, which can take advantage of a change in mechanism as the bias is switched [30]. Self-assembled monolayers (SAMs) of ferrocene-terminated alkane, 11-(ferrocenyl)-1-undecanethiol, on Ag were top-contacted by a eutectic Ga-In alloy, likely with an interfacial  $\text{Ga}_2\text{O}_3$  layer. Rectification ratios ( $R = |J(-1.0 \text{ V})| / |J(+1.0 \text{ V})|$ ) of ca. 130 were obtained for a large number of junctions. The poor rectification ratios of alkane thiols ( $R = 1-5$ ) in similar devices indicate that the ferrocenyl moiety is involved in the rectification process. It is thought that under positive bias, the ferrocenyl HOMO, which is more strongly coupled with the top electrode with an assumed potential drop of 0.3 V across the van der Waals contact, does not fall between the Fermi levels of the electrodes, and tunneling across the whole molecule dominates the molecular conductance (Fig. 4.5) [30]. However, under positive bias, the HOMO is raised, and initial tunneling from the Fc donor to the Ag electrode (to give an oxidized ferrocenium moiety) is followed by charge hopping from the  $\text{Ga}_2\text{O}_3/\text{EGaIn}$  electrode. This reduces the effective tunnel barrier width and likely promotes the rectification process.

The rather chemically inert nature of the alkane backbone and predominance of studies identifying tunneling mechanisms belie the complexity of molecular

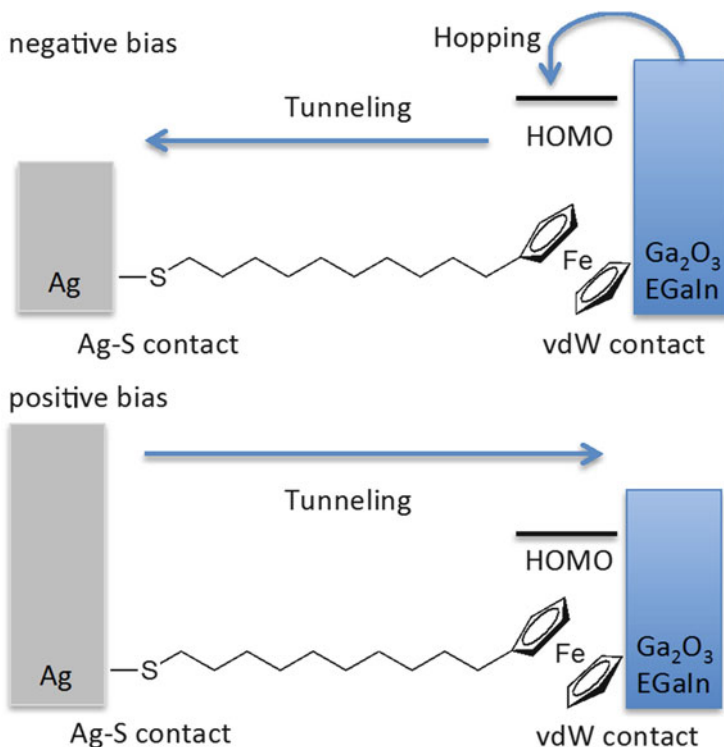


**Fig. 4.5** A simplified energy level diagram illustrating the mechanism of charge transport across Ag|SC<sub>11</sub>Fc|Ga<sub>2</sub>O<sub>3</sub>|EGaIn junctions. The barrier widths of the junctions are defined by the lengths of the C<sub>11</sub> alkyl chain (ca. 13 Å) and the Fc moiety (6.7 Å). At positive bias, the HOMO level of the ferrocene (Fc) group falls out of the gap between the Fermi levels of the electrode, and the entire molecule serves as a tunnel junction. At negative bias, the Fc HOMO falls in the Fermi gap and can undergo a redox process. The charge tunnels from Fc over the 13 Å alkyl moiety to create an oxidized ferrocenium (Fc<sup>+</sup>) fragment. The electron transfer is completed when an electron hops onto the Fc<sup>+</sup>, reducing it back to Fc [30]

junctions based on these conformationally flexible molecules. In the case of alkanes, a large number of molecular conformations are possible, which are related by the relative orientations of the individual methylene (-CH<sub>2</sub>) moieties. These different conformers offer dramatically different lengths. While the access to these different conformations seems less likely in highly ordered SAMs, in true single-molecule junctions, the molecular conductance has been shown to increase sharply as the electrode separation is decreased below the molecular length of the alkane in the “stretched” all-trans configuration. At smaller electrode separations, more conductive *gauche* defects are introduced into the molecular backbone (Fig. 4.6). A significant temperature dependence is observed for alkanes contacted within the narrower gaps, which is consistent with the thermal population of a range of conformers [31, 32]. These proposals are consistent with DFT calculations from

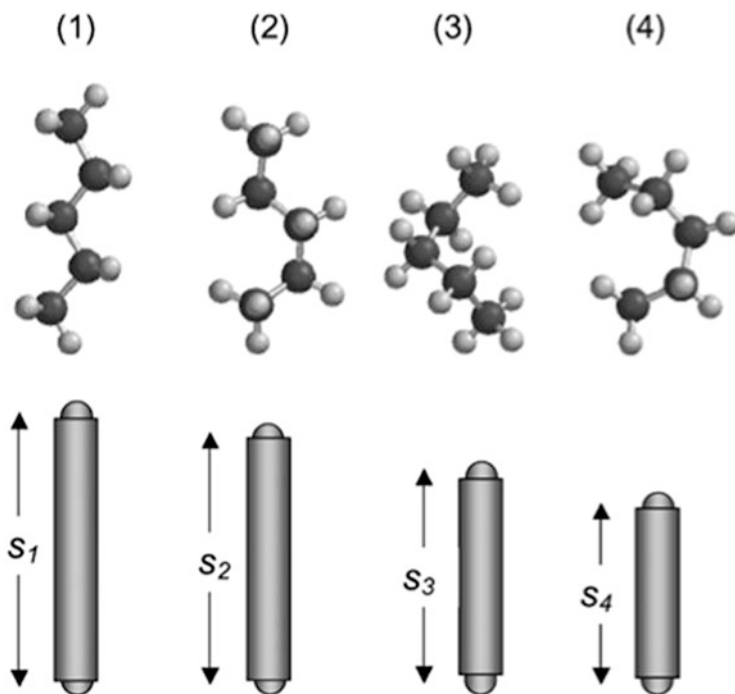


**Fig. 4.6** Ball and stick models of four energetically different conformers of the model alkane pentane ( $\text{CH}_3\text{CH}_2\text{CH}_2\text{CH}_2\text{CH}_3$ ) from all *trans* (1) to all *gauche* (4). The lower portion of the diagram indicates the gradual contraction in molecular length as the number of *gauche* conformer increases (Reproduced from Haiss et al. [32] with permission from the Royal Society of Chemistry)

Jones and Troisi [33], although others have proposed that in fact the all-*trans* conformation is the more conductive form [34, 35].

Regardless, these conformational effects are also superimposed on the variations in contact geometry, further complicating the overall junction behavior [36, 37] and analysis [38]. While the careful mechanical control of the electrode separation may offer a route to modulating or gating conductance through these systems [39], conformational flexibility is likely more a complication to the full characterization of alkane single-molecule junctions. The concept of using structurally rigid, saturated hydrocarbons to promote effective through-bond transmission through long-range  $\sigma^*$ -overlaps predates these findings [40], and measurements of single-molecule conductance of these systems indicate that there is still considerable scope for investigation of these conformationally restricted molecules in molecular wire design strategies [41].

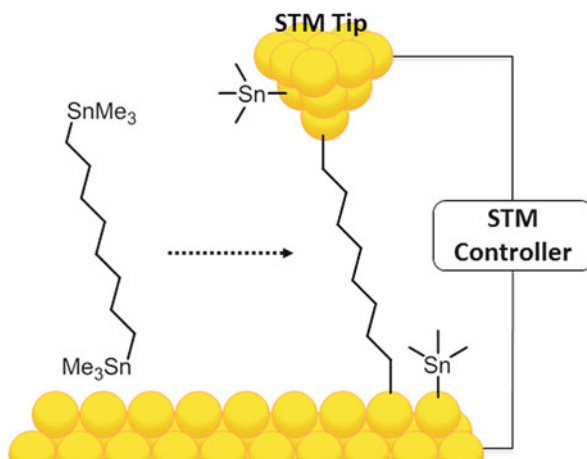
As noted above, common surface binding groups can contact to the electrode surfaces in a number of different ways, leading to distribution of molecular conductance values for each molecule. For alkanedithiols and diamines of various lengths, measured under a wide range of different conditions, these conductance values can

be as high as  $10^{-3} G_0$  for propane dithiol at 4.2 K [42], but more commonly fall in the range of  $10^{-4}$ – $10^{-5} G_0$  for the higher conductance junctions and as low as  $10^{-6} G_0$  for the lower conductance features of decane dithiol [43]. Quite remarkably, the use of  $\alpha,\omega$ -bis(trimethylstannyl)alkanes  $\text{Me}_3\text{Sn}(\text{CH}_2)_n\text{SnMe}_3$  ( $n = 4, 6, 8, 10, 12$ ) as precursors to the formation of molecular junctions on gold using STM-BJ (scanning tunneling microscope break junction) in 1,2,4-trichlorobenzene solution gives junction conductance values of some two orders of magnitude higher than those formed from thiol- or amine-contacted alkanes of the same number of carbon atoms [44]. The decay constant  $\beta$  is close to 1 ( $0.97 \pm 0.02$ ) per methylene group, as is usually found for alkane-based wires. The remarkably high conductance has been attributed to the formation of a direct Au-C bond, with the trimethylstannyl group being lost to the surface, although the precise mechanism remains an open question (Fig. 4.7) [45–47].

The concept of the Au-C bond being formed from such “transmetallation” reactions has an origin in the work of Michl and colleagues with studies of alkyl transfer from tin species of general form  $\text{SnX}(\text{Me})_n(\text{C}_{18}\text{H}_{37})_3-$  ( $n = 0, 1, 2$ ) [48], although the significance of the result was not recognized until later [45]. The Au-C bond formed from transfer of an alkyl group from tin to the gold surface has been confirmed by inelastic electron tunneling spectroscopy (IETS). The role of a radical intermediate and in situ cleavage of the  $\text{SnMe}_3$  group in the junction is suggested by the observation of conductance plateau corresponding to alkanes of twice the length of the as-synthesized species being measured. The high-conductance values have been attributed to the strong resonance feature arising from the Au-C  $\sigma$ -bonds or “gateway” states [49, 50].

Additional features corresponding to junction rearrangement due to mobility of the gold atoms can also be observed in individual conductance traces. A further exciting observation is that similarly highly conductive junctions are formed from  $\alpha,\omega$ -bis(triphenylphosphine)gold alkanes [44]. While the fate of the  $\text{PPh}_3$  ligand

**Fig. 4.7** Schematic representation of the junction formed from 1,4-bis(trimethylstannyl)octane and two gold electrodes [44]



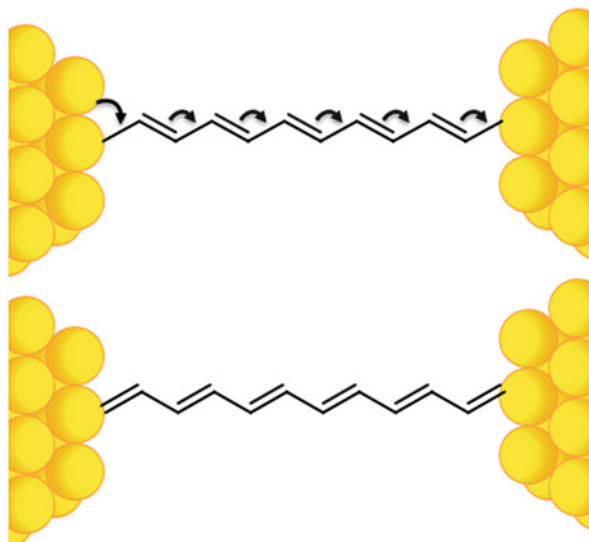
has not yet been ascertained, the potential for such tin and gold (and presumably other) organometallic agents known to undergo transmetallation reactions to serve as precursors for the formation of highly conductive electrode-C contacts is well worth further investigation.

### 4.3 Oligo(enes) and Oligo(ynes)

In moving from alkanes, the most logical extension, if not the most chronological, involves the increasing degrees of unsaturation associated with oligo(enes) and oligo(ynes). The poly(ene), or poly(acetylene), as distinct from poly(ynes), fragment has clear conceptual place as a model molecular wire, offering a well-defined series of alternating single and double bonds through which charge transfer can be readily envisioned through the conventional “curly arrow” descriptions beloved of organic chemists (Fig. 4.8) [51]. These conceptual ideas hold true for different connections in cyclic poly(enes) in which different points of connection can be envisioned [52]. These concepts are also expressed in terms of quantum interference patterns that can be propagated through molecular frameworks [53].

A very recent computational study from the Lambert group has used a small family of poly(ene) compounds to explore the interplay between the inherent “conjugated” pathway that can be drawn between the designated anchor groups through a series of  $\alpha,\omega$ -diphenyloligo(enes) and the variation in electrode-molecule coupling that can arise as electrode gaps are tuned [54]. At small electrode separations, the interaction between the metallic electrode and the  $\pi$ -system of the molecule via a “side-on” contact is significant, and the difference in conductance

**Fig. 4.8** A schematic “curly arrow” depiction of charge transfer through a poly(ene) suspended between two electrodes



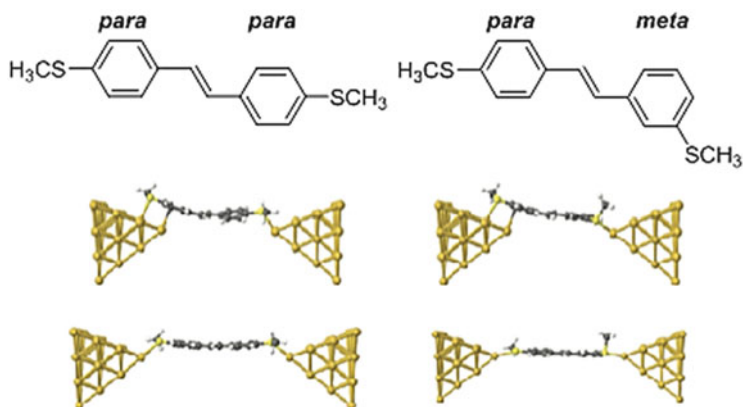


**Fig. 4.9** Examples of two of the compounds from the Lambert study of junction evolution in oligo(enes). The lower parts of the figure show two relaxed junctions for each compound, with a different electrode separation. The electrode-molecule ( $\pi$ ) interaction is clear in the shorter junctions (Adapted from Berritta et al. [54] with permission from The Royal Society of Chemistry)

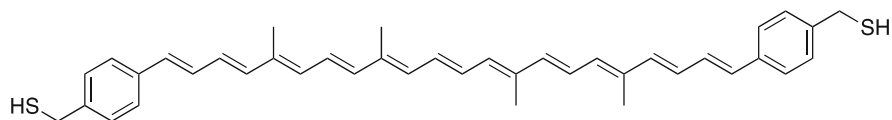


**Fig. 4.10** A carotene-inspired molecular wire

between molecules with *meta*- and *para*-positioned anchor groups is suppressed (Fig. 4.9). As the electrode separation is increased, the metal- $\pi$  interaction gives way to the anchor group-metal coupling. This naturally leads to a suppression of conductance in the *meta* case, due to destructive quantum interference (QI). When the calculations are performed to include fluctuations in the electrode-molecule binding via finite-temperature molecular dynamics, the transition from metal- $\pi$  to anchor-metal coupling takes place at smaller electrode separations, and the destructive QI effects in *meta* isomers again lead to a much lower conductance.

Despite the structural appeal of the oligo(ene) fragment as a molecular wire, the synthesis of well-defined examples of significant length is challenging, and the propensity for such systems to undergo photochemical *cis/trans* isomerization and intermolecular coupling is a substantial barrier. Consequently, there are fewer extensive series of these compounds, and estimates of decay values are therefore more limited than in the case of the alkanes.

Examples of oligo(ene)-based wires studied to date include the thiomethyl-contacted series  $\text{MeSC}_6\text{H}_4(\text{CH}=\text{CH})_n\text{C}_6\text{H}_4\text{SMe}$  ( $n = 1, 2, 3$ ) [55] and the much longer carotene-inspired fragment contacted via benzylthiol moieties (Fig. 4.10) [56] and pyridine [57]. For these latter systems, values of  $\beta$  per  $(\text{CH}=\text{CH})$  moiety are found to be  $0.556 \pm 0.09$  and  $0.43 \pm 0.07$ , respectively, considerably smaller than the values of ca. 1 per methylene ( $\text{CH}_2$ ) in alkane-based wires.

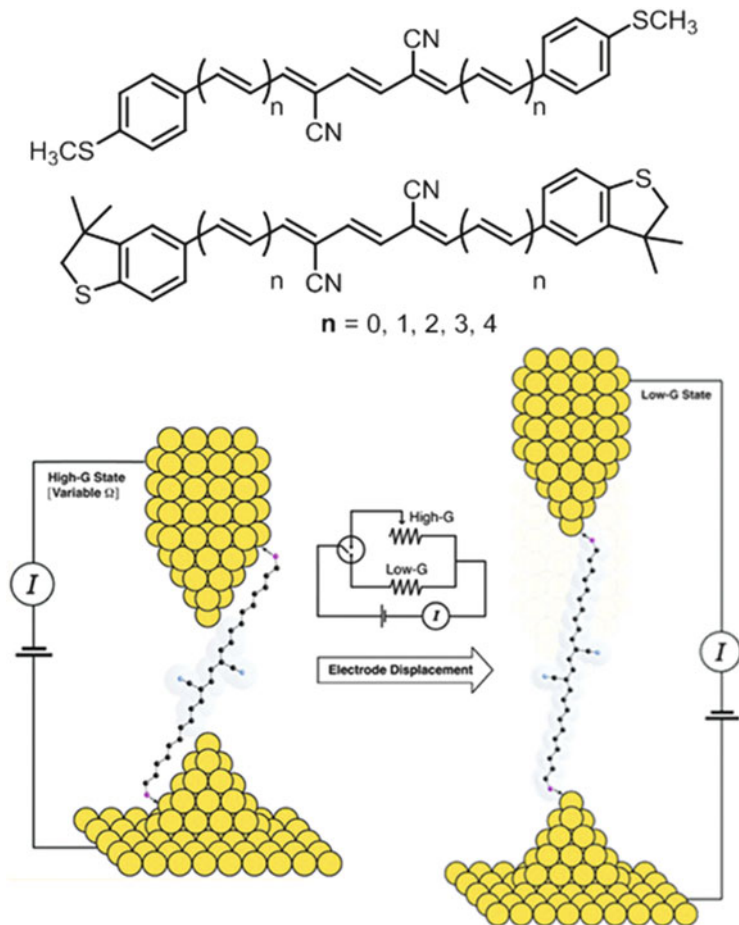


**Fig. 4.11** Schematic representation of the compounds used to demonstrate the variable points of contact along oligo(enes) bearing  $\alpha, \omega$ -anchor groups. The  $\pi$ -metal interaction leads to a higher molecular conductance (high  $G$  state) (Adapted with permission from Meisner et al. [58]. Copyright 2011 American Chemical Society)

In the case of the oligo(enes) shown in Fig. 4.9, the terminal sulfur groups are designated anchor groups in the molecular design, while the oligo(ene) provides the wirelike molecular backbone [58]. However, in shorter junctions, while the sulfur atoms may serve to physically connect the molecule into close proximity of the electrode, the oligo(ene)  $\pi$ -system can electronically couple to the electrode providing an electrode-oligo(ene)-sulfur-electrode tunneling pathway (Fig. 4.11). As the junction length is increased, the molecule can “slide” along the electrodes until such point as the sulfur atoms serve as both mechanical and electronic points of contact, giving a lower conductance state. From this sulfur-sulfur-contacted junction, a decay value  $\beta$  of  $0.2 \text{ \AA}^{-1}$  was estimated.

Perhaps the simplest chemical structure that can be viewed as a molecular wire is the oligo(yne),  $R-(C\equiv C)_n-R$ . The synthetic chemistry of the longer members of the family has been a topic of considerable interest for decades, driven by a desire to better understand the properties of the linear carbon allotrope carbyne [59]. Conceptually, oligo(ynes) are extremely appealing building blocks for construction of molecular wires, offering a cylindrical  $\pi$ -electron system free of the conformational issues noted for alkanes and alkenes, although the low bending force constant associated with the  $-C\equiv C-$  fragment can result in some spectacular and beautifully curved structures in the solid state [60]. The electronic structures of these carbon fragments lead to proposals of the use of such molecules as molecular wires, with predictions of extremely low length dependence of the conductance values [61, 62].

The connection of oligo(ynes) capped by surface binding groups into molecular junctions has been recently achieved, and experimental explorations of conductance have been supported by a range of computational studies [63–65]. In a manner similar to that described for the oligo(enes) in Fig. 4.11, conductance traces and conductance distributions over a family of oligo(ynes) are consistent with the sliding of the anchor groups along the electrodes as the junction length is increased (Fig. 4.12), leading to oscillations in both the electrical conductance and the binding energies of the oligo(yne)-based molecular wires [64].

The experimental attenuation constants  $\beta$  in poly(ynes)  $XC_6H_4-(C\equiv C)_n-C_6H_4X$  ( $X = CN, NH_2$ ), benzodihydrothiophene (BT), and  $NC_5H_4-(C\equiv C)_n-C_5H_4N$  (PY- $(C\equiv C)_n$ -PY) are sensitive to the nature of the binding group, falling between  $0.17 \text{ \AA}^{-1}$  (CN) and  $0.32 \text{ \AA}^{-1}$  (SH), with a trend  $\beta(CN) < \beta(NH_2) < \beta(BT) < \beta(PY) \approx \beta(SH)$  for the higher conductance peak, although chemical stability of the  $NH_2$ - and  $SH$ -substituted oligo(ynes) decreased significantly with increasing

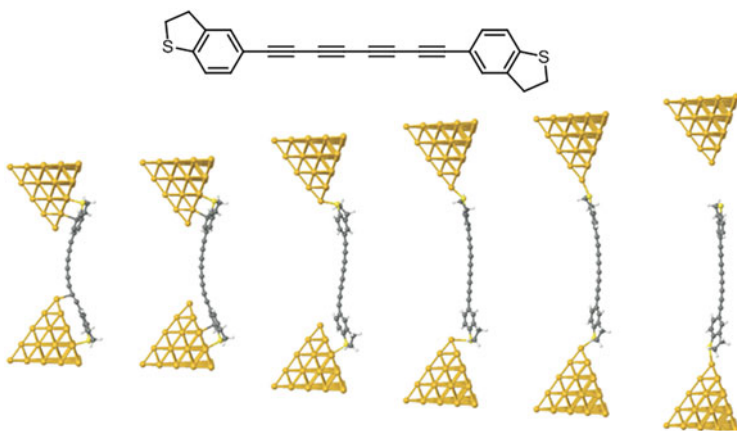


**Fig. 4.12** A bis(benzodihydrothiophene) (BT) functionalized tetrayne and examples of key configurations obtained from DFT modeling of junction evolution. The aryl and alkyne  $\pi$ -system interactions with the electrodes are clearly evident in the shorter junctions (Adapted with permission from Moreno-Garcia et al. [64]. Copyright 2013 American Chemical Society)

molecular length ( $n > 2$ ). The benzodihydrothiophene (BT) contacts were identified as being particularly useful, leading to high junction formation rates and significant conductance values of ca.  $3.1 \cdot 10^{-4} G_0$  in the case of the tetrayne (estimate molecular length 2.08 nm). Interestingly, compared with these STM-BJ experiments conducted in 4:1 1,3,5-trimethylbenzene/THF, a related study with pyridine-contacted oligo(ynes) in air gave a much lower  $\beta$  value of  $0.06 \pm 0.03 \text{ \AA}^{-1}$  [63]. A combined experimental and computational study has been undertaken to explore the influence of the environmental medium on conductance and the decay of conductance ( $\beta$ ) in the trimethylsilyl-contacted oligo(ynes)  $\text{Me}_3\text{Si}-(\text{C} \equiv \text{C})_n-\text{SiMe}_3$  ( $n = 2, 3, 4, 5$ ) [66]. Experimentally, a lower conductance and higher decay constant ( $\beta$  ca  $0.1 \text{ \AA}^{-1}$ ) were observed in mesitylene solvent, with higher conductance values and lower length decay in propylene carbonate ( $\beta$  ca  $0.05 \text{ \AA}^{-1}$ ) and 1,2,4-trichlorobenzene ( $\beta$  ca  $0.01 \text{ \AA}^{-1}$ ). Detailed theoretical and computational investigation using models that explicitly include solvent molecules reveals that the junction conductance and  $\beta$  are very sensitive to the position of the electrode Fermi energies within the molecular HOMO-LUMO gap and that solvent interactions with the molecular bridge via long-range electrostatic interactions are sufficient to gate the electrical properties of the junction. Solvent effects in molecular electronics are not limited to oligo(yne)-based systems and are being increasingly recognized in a wide variety of systems, influencing the electrical properties of junctions through a number of different mechanisms. Thus, while the conductance of octanedithiol is largely independent of solvent, due to the large HOMO-LUMO gap and far-off resonant tunneling behavior [67], in the case of an oligo(thiophene)-containing molecular wire, water molecules are thought to play a large role on the conductance behavior through a more direct interaction with the thiophene  $\pi$ -system which significantly shifts the transport resonances and hence the conductance of the system [68]. Temperature-dependent conductance of a perylene tetracarboxylic diimide-based molecular wire in water solvents, but not toluene, has been attributed to the thermal effects on the hydrogen bond network around the carbonyl moieties of the perylene diimide core [69, 70]. Other studies have considered the role of solvent on the Fermi level of the electrodes and the resulting improved molecular junction level alignment [71]. These various environment contributions to the electrical behavior of molecular junctions may also help explain in part some of the discrepancies between electrical behaviors of a given molecule in different studies.

#### 4.4 Oligo(arylenes)

In moving toward more complex chains as molecular wires, attention is next directed toward oligo(arylene)-based systems [72]. Perhaps the best-known example of a molecular wire constructed from adjacent aromatic rings is 4,4'-bipyridine (Fig. 4.13), studied in Tao's seminal work concerning the development of the STM-BJ method [29]. Here, the pyridine N atoms serve as surface contacting groups, and a conductance value of approximately  $0.01 G_0$  was determined for a single

**Fig. 4.13** (a) Schematic representation of a 4,4'-bipyridine junction, showing the steric interactions between the 2,6-2',6' hydrogen atoms in the "planar" conformation. (b) Lower-energy "twisted" conformation

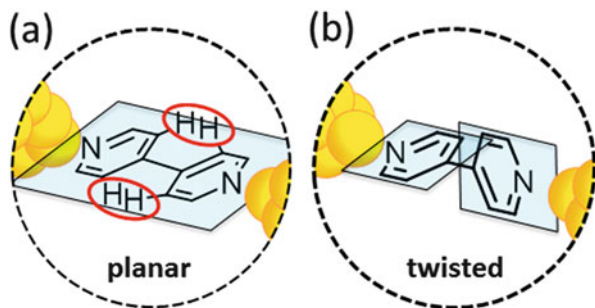
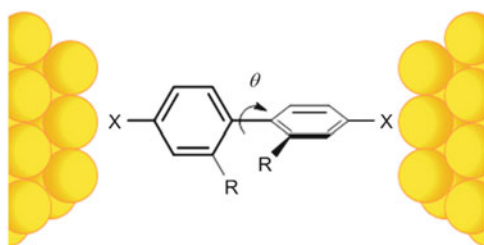


**Fig. 4.14** Schematic view of a biphenyl molecular junction, with anchor groups X (= NH<sub>2</sub> or SH in literature examples), illustrating the nonplanar geometry brought about by steric interactions between substituents, R



bipyridine moiety, although characteristic traces for junctions with two or three molecules within the electrode gap were also apparent.

The presence of the two adjacent aromatic rings in the prototypical 4,4'-bipyridine system immediately raises questions of molecular geometry. A perfectly planar molecular geometry would offer the most efficiently delocalized  $\pi$ -system between the two ring systems, yet the steric interactions between the hydrogen atoms lead to a significant inter-ring torsion (Fig. 4.13). The influence of conformation on the efficacy of charge transfer in donor-acceptor systems has long been established [73], and so there was obvious interest in extending these concepts to single-molecule junctions. A number of biphenyl molecules with amine (-NH<sub>2</sub>) [74] or thiol (-SH) [75] anchor groups and a variety of substituents placed to influence the ground state orientation of the aryl rings with respect to each other (defined by the angle  $\theta$ ; Fig. 4.14) have been studied in STM-BJ-based molecular junctions. The conductance values followed well to the anticipated  $\cos^2\theta$  relationship, with the more planar molecules exhibiting higher conductance values than the more twisted systems. The electronic characteristics of the substituents (R) played a less important role in the conductance when the Fermi level sits between the molecular HOMO and LUMO levels. However, as the HOMO or LUMO resonances come closer to the Fermi level, chemical effects from the substituents which influence the molecular levels become a more significant contributing factor to the electrical performance of the junction [76].

In the case of unconstrained systems, thermal fluctuations which cause population of a dynamic range of molecular conformations are evinced by an increase in the width of the conductance peaks. Thus, the peak width arises from individual junctions sampling a different specific conformation, each with their own specific

and characteristic conductance. The peak in the conductance histograms correspond to the most probable conformations, which are likely similar to the lowest energy conformation. Similar conformational effects have been discussed in the context of intermolecular charge transfer in mixed-valence systems [77], and proposals for the design of molecular switches based on conformational changes, such as the reversible formation and cleavage of a tether between the rings of a biphenyl system, have also been made [78]. However, care must be taken to distinguish conformational switching phenomena from stochastic changes in the electrode-molecule binding groups.

Conformational effects have been observed in other arylene systems, such as those based on oligo(thiophenes). In the case of the small series of thiomethyl-contacted oligo(thiophenes) T1–T6 (T5 and T6 being hexyl substituted for reasons of improved solubility) (Fig. 4.15), some rather unusual effects of increasing length on conductance were observed [79]. While conductance values from T1–T3 to T5 fall more or less in the expected pattern, with a decay constant  $\beta$  of ca.  $0.3 \text{ \AA}^{-1}$ , the conductance of T4 is rather higher than the shorter T3 [79, 80].

The conductance of T6 is rather less than might be expected by extrapolation from T1–T3 to T5. Although the T3/T4 discrepancy was initially interpreted as a result of better alignment of the HOMO of T4 with the electrode Fermi level, electrochemically determined HOMO energies were rather invariant across the series. The lower than expected conductance of T6 was attributed to the steric interactions between the solubilizing hexyl groups, which prevent the attainment of the most conjugated (and conductive) planar forms. In the case of T3 and T4, while the planar and twisted forms of the tetrathiophene have comparable end-to-end lengths, thereby permitting relatively free rotation in the constraints of the anchored junction, the twisted and planar forms of terthiophene T3 are of different lengths, and a molecule of T3 being bound in the junction in the less conductive twisted form will not be able to planarize without rupturing the junction (Fig. 4.15). Although this conformational model is unlikely to be the complete description of the molecules within the junction, it serves to underline the growing awareness of the issues of conformation in molecular electronics and results obtained from measurements taken over many individual junctions.

A comprehensive study of the length dependence of conductance in thiolate-contacted oligo(phenylene) wires in junctions to Au, Ag, and Pt electrodes has permitted a rather complete picture of the tunneling transport in these systems to be derived. The rather strong dipole associated with the M-S bond results in Fermi pinning and a significant shift of the energy of the molecular HOMO. The charge injection barrier height is therefore only weakly correlated with the metal electrode work function [81].

In seeking to improve the coupling between the electrode and the molecule, attention has naturally focused on the nature of the chemical bond at the metal-molecule interface. Direct Au-C bonds are fast emerging as promising candidates, and naturally attention is being quickly turned to explore methods for fabricating such contacts for a wide range of molecular bridges. The reduction of diazonium salts has been identified as a useful route to anchor molecular materials to electrodes

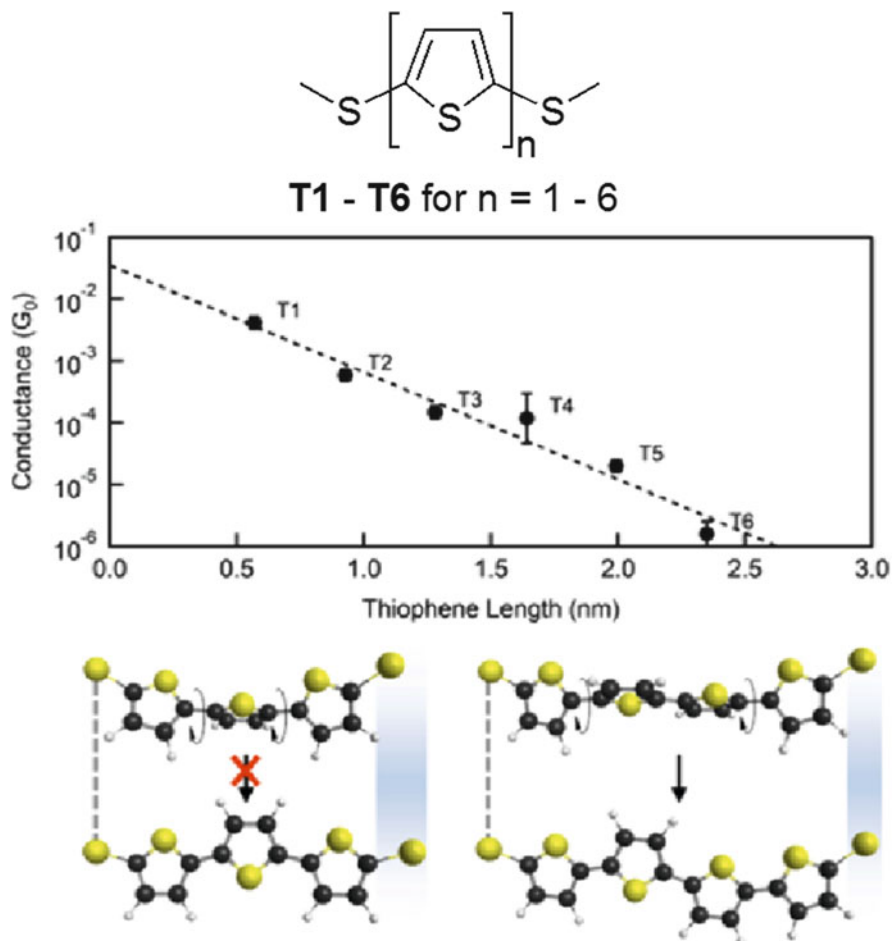
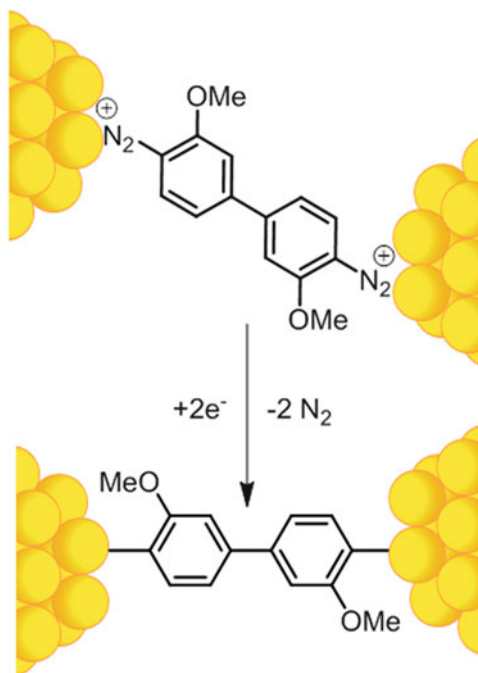


**Fig. 4.15** The oligo(thiophenes) T1–T6 (solubilizing side chains on T5 and T6 omitted for clarity) with a plot of the conductance data extracted from 2-D conductance histograms for the fully elongated junctions. The lowest section of the figure illustrates the hindered rotation of T3 in a junction and the change in molecular length (S...S) compared with the lower-energy rotation and limited change in molecular dimensions for T4 (Adapted with permission from Capozzi et al. [79]. Copyright 2014 American Chemical Society)

via direct electrode-C bonds [82], although care is required to avoid molecule-molecule coupling processes and the formation of dendritic architectures. Reduction of the diazonium group results in liberation of molecular  $N_2$  and formation of an aryl radical, which forms a new bond with the electrode surface. The 3,3'-dimethoxybiphenyl-4,4'-bis(diazonium) compound (commercially available as the zinc tetrachloride salt, also known as Fast Blue B salt) reduced within the BJ

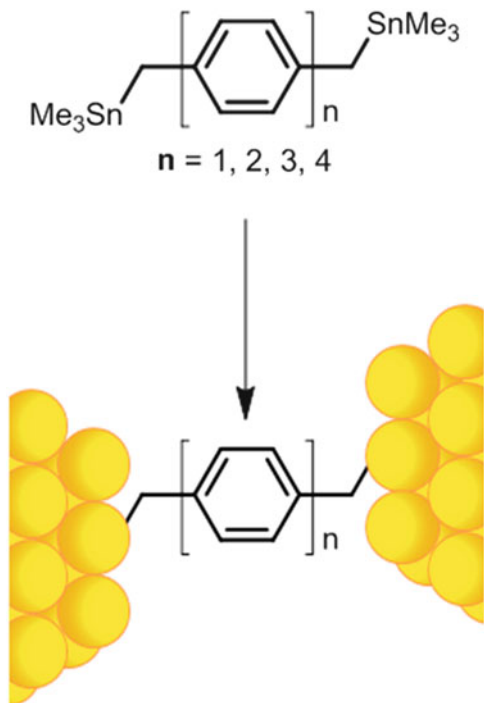
**Fig. 4.16** Schematic illustration of the in situ reduction of the diazonium Fast Blue B salt to create a Au-C-contacted single-molecule junction



gap formed in an electrochemical STM gave robust molecular junctions with conductance of ca.  $2.3 \cdot 10^{-3} G_0$  and median pulling length of 0.34 nm (Fig. 4.16) [83]. This compares with junctions formed from the analogous amine-contacted molecule which gave  $G = 1.4 \cdot 10^{-3} G_0$  and a median pulling length of only 0.18 nm before junction rupture. The rather small increase in conductance perhaps is a good indication that in this case the molecule-electrode coupling, while physically strong, does not take full advantage of the biphenyl  $\pi$ -system and is more dominated by the  $\sigma$ -channel [44].

Trimethylstannyl transfer chemistry may offer a remarkable solution to this issue of creating robust and highly transmissive electrode-molecule contacts [49]. While a direct benzene-gold  $\sigma$ -bond formed in this manner gave a conductance value of ca.  $0.03 G_0$ , this is somewhat lower than obtained for a similarly connected butane ( $-(\text{CH}_2)_4-$  chain (ca.  $0.09 G_0$ ). By interpolating a methylene spacer between the gold electrode and an oligo(phenylene) chain,  $-\text{Au}[\text{CH}_2(\text{C}_6\text{H}_4)_n\text{CH}_2]\text{Au}$  (Fig. 4.17), conductance values as high as  $G_0$  ( $n = 1$ ) are obtained ( $n = 2$ ,  $G = 0.1 G_0$ ;  $n = 3$ ,  $G = 0.014 G_0$ ;  $n = 4$ ,  $G = 0.0022 G_0$ ). The extracted decay constant  $\beta$  is 1.9/phenylene or  $0.43 \text{ \AA}^{-1}$ . A smaller peak due to dimerization of the target molecular fragment was also observed at lower conductance values. Interestingly, by constraining the biphenyl derivative ( $n = 2$ ) into a planar fluorene, the conductance rises to  $0.17 G_0$ . The extraordinarily high-conductance values are attributed to the coupling of the electrode through the Au-C  $\sigma$ -bond and the molecular  $\pi$ -system [49]. These

**Fig. 4.17** A schematic of the in situ formation of Au-C bonds from  $\text{SnMe}_3$  precursors

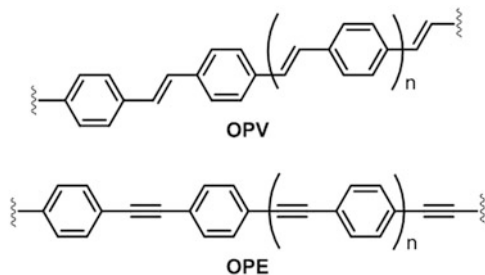


remarkable molecular contacts and the strategy for generation of highly conductive junctions will likely attract considerable attention in the future [84].

#### 4.5 Oligo(phenylene ethynylenes) and Oligo(phenylene vinylenes)

Of the myriad of wirelike molecules that have been prepared and studied in D-B-A, thin film, and single-molecule junctions, the oligo(phenylene vinylene) and oligo(phenylene ethynylene) occupy a particularly prominent position. The ease of synthesis, stability under ambient conditions, ready functionalization with a wide range of electronically and sterically interesting groups, and suitability to form modular structures of regularly increasing length have made these systems ideal workhorses for the explorations of electronic phenomena in molecular systems. There are many reviews and discussion papers that address the chemistry and junction characteristics of these species [85]; a comprehensive description of this molecular class alone would occupy at least an entire volume. Here we focus on a brief overview of this class of molecule, including recent developments concerning the wirelike characteristics of longer molecular species, with molecular lengths that approach near future technological dimensions (ca. 5–10 nm).

**Fig. 4.18** The elementary chemical structures of OPV and OPE



The oligo(phenylene vinylene) (OPV) fragment has long been considered as an excellent candidate structure for the assembly of long molecular wires [86]. The phenylene rings are able to conjugate with the adjacent vinyl moieties and the relatively high barrier to rotation (in comparison with oligo(phenylene ethynylene) (OPE) derivatives) [87], although such low-frequency torsional modes have been found to play a role in long-distance charge transfer in D-B-A models (Fig. 4.18) [88]. Estimates and measurements of the relative decay constants of molecular backbones often place OPV-style molecules at the lower end, indicating their suitability for the construction of long molecular wires, although the crossover from coherent tunneling to incoherent hopping ensures a degree of debate about such comparisons will ensue [89, 90].

Planarizing the OPV system through the introduction of methylene tethers to give “carbon-bridged” oligo(phenylene vinylenes) (COPVs) has been shown to result in dramatic (ca. 840-fold) increase in electron-transfer rates in D-COPV-A systems compared to the analogous D-OPV-A compounds [91]. This rate enhancement is attributed to both enhanced coupling through the planar  $\pi$ -system and contributions from inelastic electron tunneling caused by electron-vibration coupling [92].

While the OPE backbone is thought to offer a wider range of conformations, given the essentially barrierless rotation of the phenylene moieties around the ethynyl axis [93], the great advantage of this fragment is the (relative) simplicity of synthetic approach based on sequential and convergent cross-coupling methods [94]. OPEs, particularly the three ring derivatives based on the 1,4-bis(phenylethynyl)benzene moiety, have been widely explored as wirelike molecules within molecular junctions [95]. However, despite early promise of higher electronic function arising from conformational switching [96] and redox chemistry leading to negative differential resistance (NDR) effects [97], these observations were later traced to stochastic changes in the S-Au bond [98] and metallic filament formation [99], respectively. However, these earlier visionary works were important in creating interest in the field and driving the development of molecular structures and methods through which to explore these observations and underlying phenomena in greater detail. Indeed, through the application of electrochemical STM-based platforms, electrochemical gating of the electrical properties of OPE-based molecular junctions has been realized [100].

The relative ease of synthesis of OPE-type systems has allowed a number of comparative studies that have probed effects of the anchor groups on the formation and evolution of molecular junctions [101, 102]. The simplest “OPE,” diphenylacetylene functionalized with -SH, NH<sub>2</sub>, and -CN binding groups together with the “extended” bipyridine analog NC<sub>5</sub>H<sub>4</sub>C ≡ CC<sub>5</sub>H<sub>4</sub>N (PY-C ≡ C-PY) which presents a model for the pyridine binding group, has been used to explore not only the conductance behavior of the diarylethynyl fragment but also the evolution of the junction during the stretching process that is implicit in both STM-BJ and MCBJ methods [103]. As is commonly the case, and noted elsewhere, the conductance histograms revealed multiple conductance features (H, M, L). The most probable main conductance values H decrease in the following sequence: SH ( $2 \cdot 10^{-3} G_0$ ) > NH<sub>2</sub> ( $8 \cdot 10^{-4} G_0$ ) > PY ( $5 \cdot 10^{-4} G_0$ ) ≫ CN ( $2 \cdot 10^{-5}$ ). The accessible data from the L conductance groups showed the same trend, e.g., SH > NH<sub>2</sub> > PY. However, their values spread over nearly two orders of magnitude between 10<sup>-4</sup> and 10<sup>-6</sup> G<sub>0</sub>. A possible low-conductance feature could not be resolved from the instrument noise for the CN-contacted compound. Careful analysis of 2-D conductance histograms and stretching distances coupled with simulation suggests that as in other studies described above, there is a significant contribution to the junction from not only contact from the anchor group to the gold electrode but also an electronic interaction from the π-system of the aryl ring to the electrode at short electrode separations. Indeed, in all cases except thiol, the π-metal interaction was the most significant contribution to the overall binding energy. As the electrodes are moved apart during the pulling process, the molecules slide along the electrode (modeled as a pyramidal arrangement of gold atoms) until the gap is large enough that the only contact is via the terminal anchor groups and the apex atoms of the gold tip. The strong gold-sulfur bond causes restructuring of the electrode during this evolution process, and this adaption of the surface to maintain good interaction with the sulfur atom is likely a contributing factor to the higher conductance of the molecule contacted by this group. Conversely, the nitrile (-CN) moiety binds in a rather linear fashion, preventing a strong π-metal interaction and likely a cause of the lower conductance generally weaker binding of the molecule to the electrode through this anchor. The general conclusion reached through this study of the shortest members of the OPE family would be that while the fully stretched molecular junctions can be formed, the conductance of this idealized junction configuration is likely rather low. The main conductance features probably arise from a statistical average of junction configurations of higher conductance which involve π-metal interactions between the molecule and the rougher portions of the electrode surface.

In the search for simpler junction behavior, the trimethylsilylethynyl moiety, -C ≡ CSiMe<sub>3</sub>, has been identified [104, 105]. While giving rise to only one apparent conductance peak, the conductance values are quite low (e.g., Me<sub>3</sub>SiC ≡ CC<sub>6</sub>H<sub>4</sub>C ≡ CC<sub>6</sub>H<sub>4</sub>C ≡ CC<sub>6</sub>H<sub>4</sub>C ≡ CSiMe<sub>3</sub>  $G = 2.75 \cdot 10^{-5} G_0$ ). Although initially attributed to a five-coordinate silicon-Au interaction, more recent computational studies suggest that the silicon retains four coordinate tetrahedral geometry, and a side-on contact between the C ≡ C π-system and defects on the electrode surface similar to those described for aryl systems is more important

[66]. Cleavage of the silyl moiety in situ by addition of tetrabutylammonium fluoride (NBu<sub>4</sub>F) gives a transient alkynyl anion which can form a new bond to the (gold) electrode surface [106]. Analysis of the break-off distance and the estimated molecular lengths indicate that binding of the molecule in an upright (vertical or normal to the electrode surface) position is most probable, with Raman spectroscopy providing further support for the Au-C bonding mode. The main conductance feature of a three-ring OPE contacted to gold electrodes in an STM-BJ setup was determined to be  $2.5 \cdot 10^{-4} G_0$ , while analysis of a small series of compounds from one to three rings gave  $\beta = (0.33 \pm 0.01) \text{ \AA}^{-1}$ , which compare well with the value of  $(0.34 \pm 0.01) \text{ \AA}^{-1}$  determined for thiol-contacted OPEs under similar conditions [107]. As with the trimethylstannyl method of engineering Au-C bonds, some evidence for dimerization of the target compounds was also observed with peaks of lower conductance being detected and assigned by comparison with the conductance traces of authentic samples of the putative dimers.

The capacity to synthesize very long OPE derivatives lends naturally to exploration of both  $\beta$  and the potential to observe the transition from tunneling to hopping mechanisms in long molecular wires; similar interests are of course also expressed in related systems [108]. Estimates of  $\beta$  from photoinduced charge transfer studies in D-OPE-A systems based on triarylamine donors and diaryloxadiazole acceptors have given  $\beta = 0.15 \text{ \AA}^{-1}$  [109], consistent with the value obtained from shorter OPEs in molecular junctions (ca.  $0.3 \text{ \AA}^{-1}$ ). In molecular junctions, over a longer range of molecular lengths with amine contacts,  $\beta$  is found to range from ca.  $0.2 \text{ \AA}^{-1}$  in the tunneling regime to  $0.03 \text{ \AA}^{-1}$  as hopping mechanisms begin to dominate [110]. The transition from tunneling to hopping was found to occur around the three- to four-ring compounds (ca. 2.75 nm) in thin films contacted into junctions by contacting with a CP-AFM, although the mechanism of transport in the intermediate length ranges was likely arising from more than one process. Conductance values spanned the range of  $\sim 10^{-3}$  (OPE 1),  $\sim 10^{-4}$  (OPE3), and  $\sim 6 \cdot 10^{-5}$  (OPE7). These behaviors compare with analogous long OPE wires featuring pyridine contacts (in which case the term oligo(arylene ethynylene) (OAE) has been adopted to reflect the presence of the pyridyl anchor group which also forms part of the numbered ring system) measured in single-molecule STM-BJ junctions [111]. Across a series of OAEs from OAE3 (molecular length ca. 1.6 nm) to OAE9 (5.8 nm), conductance values determined from STM-BJ studies in 4:1 (v/v) 1,3,5-trimethylbenzene/tetrahydrofuran fall sharply from ca.  $3 \cdot 10^{-5} G_0$  (OAE3) to  $3 \cdot 10^{-6} G_0$  (OAE4) to  $2 \cdot 10^{-7} G_0$  (OAE5) ( $\beta = (0.33 \pm 0.01) \text{ \AA}^{-1}$ ), before decreasing more slowly from OAE5 to OAE 9 ( $G = 1 \cdot 10^{-7} G_0$ ) ( $\beta = (0.016 \pm 0.008) \text{ \AA}^{-1}$ ). This change in  $\beta$ , and hence mechanism from tunneling to hopping, was found to correspond to molecular lengths of ca. 3 nm.

These remarkable single-molecule experiments conducted on the longer members of the OAE family illustrated several issues which are becoming more frequently recognized as common traits within studies of molecular junctions: the molecular junctions break before the full extension to the idealized “vertical” conformation, likely indicating the preference for pyridyl  $\pi$ -to-metal contacts and the “dragging” of the molecule across the surface that must accompany

translation of the junction in a fixed x,y-coordinate as the electrodes are separated; the conductance peaks are broadened as the degrees of internal freedom of the molecule increase; the junction formation probability decreases with increasing length, reflecting the difficulties in establishing a strong connection as a result of steric interactions with the solubilizing alkyloxy chains that were necessarily introduced during the synthesis to improve handling; and the strong  $\pi$ -interactions between the molecule and the surface which might provide an additional barrier to creating a free-standing molecular junction suspended between the electrodes.

## 4.6 Summary and Outlook

This summary of molecular wires within molecular junctions has set out to provide an overview of the key features of these junctions and the points that are emerging as important criteria and considerations for future molecular designs of wirelike molecules. The initial cartoon depicting a molecular junction (Fig. 4.1) and the partitioning of the system into electrodes, contacts, and bridges can now be seen as rather misleading. The electrical characteristics of the junction cannot be simply arrived at from a sum-of-the-parts modular approach. The anchor should not only provide an effective, robust, and uniform contact but must effectively couple the electrode to the molecular orbitals that propagate the transferring charge with a small barrier to charge injection. The bridge should not only offer a well-defined pathway for charge propagation, but have few degrees of freedom to limit the number of distinct junction types that are formed. The use of solubilizing side chains might be best avoided, as these can interfere with the docking of the electrode to the anchor groups or provide alternative points of contact. Similarly, the use of  $\pi$ -conjugated systems as the conduction channel also provides an alternative point of strong contact between the molecule and metallic electrodes.

In looking ahead we can identify the potential to use insulating groups to shield the conducting  $\pi$ -system of a conjugated wire, the use of large-area contacts that may average over different contact sites on the electrode surface, and advanced spectroscopic methods to better characterize individual junctions to better understand the diversity of contact, molecular conformation, and junction geometry on a junction-to-junction basis. Exciting steps in these directions are discussed in other chapters of this volume and provide a framework for extension of the emerging technology of molecular electronics, where molecules may act either individually or as an ensemble average, to perform a useful electronic function in a true device architecture.

**Acknowledgments** P. J. L. gratefully acknowledges financial support from the ARC and the award of a Future Fellowship. S. M. G. gratefully acknowledges an International Research Fellowship from the Japan Society for the Promotion of Science. We thank our colleagues and coworkers for their ongoing collaborations and insightful discussions.

## References

1. Guldi DM, Nishihara H, Venkataraman L (2015) Molecular wires (editorial). *Chem Soc Rev* 44:842–844
2. Marcus RA (1993) Electron transfer reactions in chemistry: theory and experiment (nobel lecture). *Angew Chem Int Ed Engl* 32:1111–1121
3. Bixon M, Jortner J (1999) Electron transfer—from isolated molecules to biomolecules. In: Prigogine I, Rice SA (eds) *Advances in chemical physics: electron transfer – from isolated molecules to biomolecules. Part 1, vol 106*. Wiley, Hoboken
4. McConnell HM (1961) Intramolecular charge transfer in aromatic free radicals. *J Chem Phys* 35:508–515
5. Adams DM, Brus L, Chidsey CED, Creager S, Creutz C, Kagan CR, Kamat PV, Lieberman M, Lindsay S, Marcus RA, Metzger RM, Michel-Beyerle, Miller JR, Newton MD, Rolison DR, Sankey O, Schanze KS, Yardley J, Zhu XY (2003) Charge transfer on the nanoscale: current status. *J Phys Chem B* 107:6668–6697
6. Gilbert M, Albinsson B (2015) Photoinduced charge and energy transfer in molecular wires. *Chem Soc Rev* 44:845–862
7. Nitzan A (2001) A relationship between electron-transfer rates and molecular conduction. *J Phys Chem A* 105:2677–2679
8. Nitzan A (2002) The relationship between electron transfer rate and molecular conduction 2: the sequential hopping case. *Israel J Chem* 42:163–166
9. Berlin YA, Ratner MA (2005) Intra-molecular electron transfer and electric conductance via sequential hopping: unified theoretical description. *Radiat Phys Chem* 74:124–131
10. Traub MC, Brunschwig BS, Lewis NS (2007) Relationships between the nonadiabatic bridged intramolecular, electrochemical and electrical electron-transfer processes. *J Phys Chem B* 111:6676–6683
11. Wierzbinski E, Venkatramani R, Davis KL, Bezer S, Kong J, Zing Y, Borguet E, Achim C, Beratan DN, Waldeck DH (2013) The single-molecule conductance and electrochemical electron-transfer rate are related by a power law. *ACS Nano* 7:5391–5401
12. Nitzan A (2001) Electron transmission through molecules and molecular interfaces. *Annu Rev Chem* 52:681–750
13. Hong S, Reifengerger, Tian W, Datta S, Henderson J, Kubiak CP (2000) Molecular conductance spectroscopy of conjugated, phenyl-based molecules on Au(111): the effect of end groups on molecular conduction. *Superlattice Microstruct* 28:289–303
14. Ke S-H, Baranger HU, Yang W (2004) Molecular conductance: chemical trends of anchoring groups. *J Am Chem Soc* 126:15897–15904
15. Jia CC, Guo XF (2013) Molecule-electrode interfaces in molecular electronic devices. *Chem Soc Rev* 42:5642–5660
16. Leary E, La Rosa A, Gonzalez MT, Rubio-Bollinger G, Agrait N, Martin N (2015) Incorporating single molecules into electrical circuits. The role of the chemical anchoring group. *Chem Soc Rev* 44:920–942
17. Kaliginedi V, Rudnev AV, Moreno-Garcia P, Baghernejad M, Huang CC, Hong WJ, Wandlowski T (2014) Promising anchoring groups for single-molecule conductance measurements. *Phys Chem Chem Phys* 16:23529–23539
18. Haiss W, Martín S, Leary E, Zalinge HV, Higgins SJ, Bouffier L, Nichols RJ (2009) Impact of junction formation method and surface roughness on single molecule conductance. *J Phys Chem C* 113:5823–5833
19. Chen F, Hihath J, Huang Z, Li X, Tao NJ (2007) Measurement of single molecule conductance. *Annu Rev Phys Chem* 58:535–564
20. Mann B, Kuhn H (1971) Tunneling through fatty acid salt monolayers. *J Appl Phys* 42:4398–4405
21. Salomon A, Cahen D, Lindsay S, Tomfohr J, Engelkes VB, Frisbie CD (2003) Comparison of electronic transport measurements on organic molecules. *Adv Mater* 15:1881–1890

22. Wold DJ, Frisbie CD (2000) Formation of metal-molecule-metal tunnel junctions: microcontacts to alkanethiol monolayers with a conducting AFM tip. *J Am Chem Soc* 122:2970–2971
23. Wang Y-H, Hong Z-W, Sun Y-Y, Li D-F, Zheng J-F, Niu Z-J, Zhou X-S (2014) Tunneling decay constant of alkanedicarboxylic acids: different dependence on the metal electrodes between air and electrochemistry. *J Phys Chem C* 118:18756–18761
24. Wang YH, Zhou XY, Sun YY, Han D, Zheng JF, Niu ZJ, Zhou XS (2014) Conductance measurement of carboxylic acids binding to palladium nanoclusters by electrochemical jump-to-contact STM break junction. *Electrochim Acta* 123:205–210
25. Peng ZL, Chen ZB, Zhou XY, Sun YY, Liang JH, Niu ZJ, Zhou XS, Mao BW (2012) Single molecule conductance of carboxylic acids contacting Ag and Cu electrodes. *J Phys Chem C* 116:21699–21705
26. Cui XD, Zarate X, Tomfor J, Sankey OF, Primak A, Moore AL, Moore TA, Gust D, Harris G, Lindsay SM (2002) Making electrical contacts to molecular monolayers. *Nanotechnology* 13:5–14
27. Beebe JM, Engelkes VB, Miller LL, Frisbie CD (2002) Contact resistance in metal-molecule-metal junctions based on aliphatic SAMs: effects of surface linker and metal work function. *J Am Chem Soc* 124:11268–11269
28. Cui XD, Primak A, Zarate X, Tomfohr J, Sankey OF, Moore AL, Moore TA, Gust D, Nagahara LA, Lindsay SM (2002) Changes in the electronic properties of a molecule when it is wired into a circuit. *J Phys Chem B* 106:8609–8614
29. Xu B, Tao NJ (2003) Measurement of single-molecule resistance by repeated formation of molecular junctions. *Science* 301:1221–1223
30. Nijhuis CA, Reus WF, Barber JR, Dickey MD, Whitesides GM (2010) Charge transport and rectification in arrays of SAM-based tunneling junctions. *Nano Lett* 10:3611–3619
31. Martin S, Haiss W, Higgins S, Cea P, Lopez MC, Nichols RJ (2008) A comprehensive study of the single molecule conductance of  $\alpha$ ,  $\omega$ -dicarboxylic acid-terminated alkanes. *J Phys Chem C* 112:3941–2948
32. Haiss W, van Zalinge H, Bethell D, Ulstrup J, Schiffrin DJ, Nichols RJ (2006) Thermal gating of the single molecule conductance of alkanedithiols. *Faraday Discuss* 131:253–264
33. Jones DR, Troisi A (2007) Single molecule conductance of linear dithioalkanes in the liquid phase: apparently activated transport due to conformational flexibility. *J Phys Chem C* 111:14567
34. Haran A, Waldeck DH, Naaman R, Moons E, Cahen D (1994) The dependence of electron transfer efficiency on the conformational order in organic monolayers. *Science* 263:948
35. Fujihira M, Suzuki M, Fujii S, Nishikawa A (2006) Currents through single molecular junction of Au/hexanedithiolate/Au measured by repeated formation of break junction in STM under UHV: effects of conformational change in an alkylene chain from *gauche* to *trans* and binding sites of thiolates on gold. *Phys Chem Chem Phys* 8:3876
36. Guo S, Hihath J, Diez-Perez I, Tao NJ (2011) Measurement and statistical analysis of single-molecule current-voltage characteristics, transition voltage spectroscopy and tunneling barrier height. *J Am Chem Soc* 133:19189–19197
37. Li C, Pobelov I, Wandlowski T, Bagrets A, Arnold A, Evers F (2008) Charge transport in single Au vertical bar alkanedithiol vertical bar Au junctions: coordination geometries and conformational degrees of freedom. *J Am Chem Soc* 130:318–326
38. Báldea I (2012) Interpretation of stochastic events in single-molecule measurements of conductance and transition voltage spectroscopy. *J Am Chem Soc* 134:7958–7962
39. Kiguchi M, Kaneko S (2013) Single molecule bridging between metal electrodes. *Phys Chem Chem Phys* 15:2253–2267
40. Paddon-Row MN (1994) Investigating long-range electron-transfer processes with rigid, covalently linked donor-(norbornylogous bridge)-acceptor systems. *Acc Chem Res* 27:18–25
41. Darwish N, Paddon-Row MN, Gooding JJ (2014) Surface-bound norbornylogous bridges as molecular rulers for investigating interfacial electrochemistry and as single molecule switches. *Acc Chem Res* 47:385–395

42. Hihath J, Arroyo CR, Rubio-Bollinger G, Tao N, Agraït N (2008) Study of electron – phonon interactions in a single molecule covalently connected to two electrodes. *Nano Lett* 8:1673–1678
43. Metzger RM (2015) Unimolecular electronics. *Chem Rev* 115:5056–5115
44. Cheng Z-L, Skouta R, Vazquez H, Widawsky JR, Schneebeli S, Chen W, Hybertsen MS, Breslow R, Venkataraman L (2011) *In situ* formation of highly conducting covalent Au-C contacts for single-molecule junctions. *Nat Nanotechnol* 6:353–357
45. Kaletova E, Kohutova A, Hajduch J, Kaleta J, Basti Z, Pospisil L, Stibor I, Magnera TF, Michl J (2015) The scope of direct alkylation of gold surfaces with solutions of C1–C4 n-alkylstannanes. *J Am Chem Soc* 137:12086–12099
46. Batra A, Kladnik G, Gorjizadeh N, Meisner J, Steigerwald M, Nuckolls C, Quek SY, Cvetko D, Morgante A, Venkataraman L (2014) Trimethyltin-mediated covalent gold-carbon bond formation. *J Am Chem Soc* 136:12556–12559
47. Foti G, Vazquez H, Sanchez-Portal D, Arnau A, Frederiksen T (2014) Identifying highly conductive Au-C links through inelastic tunneling spectroscopy. *J Phys Chem C* 118:27106–27112
48. Khobragade D, Stensrud ES, Mucha M, Smith JR, Pohl R, Stibor I, Michl J (2010) Preparation of covalent long-chain trialkylstannyl and trialkylsilyl salts and an examination of their adsorption on gold. *Langmuir* 26:8483–8490
49. Chen W, Widawsky JR, Vazquez H, Schneebeli ST, Hybertsen MS, Breslow R, Venkataraman L (2011) Highly conducting  $\pi$ -conjugated molecular junctions covalently bonded to gold electrodes. *J Am Chem Soc* 133:17160–17163
50. Batra A, Darancet P, Chen Q, Meisner JS, Widawsky JR, Neaton JB, Nuckolls C, Venkataraman L (2013) Tuning rectification in single-molecular diodes. *Nano Lett* 13:6233–6237
51. Stuyver T, Fias S, De Proft F, Geerlings P (2015) Back of an envelope selection rule for molecular transmission: a curly arrow approach. *J Phys Chem C* 119:26390–26400
52. Tsuji Y, Movassagh R, Datta S, Hoffmann R (2015) Exponential attenuation of through-bond transmission in a polyene: theory and potential realizations. *ACS Nano* 9:11109–11120
53. Arroyo CR, Frisenda R, Moth-Poulsen K, Seldenthuis JS, Bjornholm T, van der Zant HSJ (2013) Quantum interference effects at room temperature in OPV-based single molecule junctions. *Nanoscale Res Lett* 8:234
54. Berritta M, Manrique DZ, Lambert CJ (2015) Interplay between quantum interference and conformational fluctuations in single-molecule break junctions. *Nanoscale* 7:1096–1101
55. Meisner JS, Ahn S, Aradhya SV, Krikorian M, Parameswaran R, Steigerwald ML, Venkataraman L, Nuckolls C (2012) The importance of direct metal- $\pi$  coupling in electronic transport through conjugated single-molecule junctions. *J Am Chem Soc* 134:20440–20445
56. He J, Chen F, Li J, Sankey OF, Terazono Y, Herrero C, Gust D, Moore TA, Moore AL, Lindsay SM (2005) Electronic decay constant of carotenoid polyenes from single-molecule measurements. *J Am Chem Soc* 127:1384–1385
57. Visoly-Fisher I, Daie K, Terazono Y, Herrero C, Fungo F, Otero L, Durantini E, Silber JJ, Sereno L, Gust D, Moore TA, Moore AL, Lindsay SM (2006) Conductance of a biomolecular wire. *Proc Natl Acad Sci U S A* 103:8686–8690
58. Meisner JS, Kamenetska M, Krikorian M, Steigerwald ML, Venkataraman L, Nuckolls C (2011) A single molecule potentiometer. *Nano Lett* 11:1575–1579
59. Tykwinski RR (2015) Carbyne: the molecular approach. *Chem Rev* 15:1060–1074
60. Szafert S, Gladysz JA (2006) Update 1 of: carbon in one-dimension: structural analysis of the higher conjugated polyynes. *Chem Rev* 106:PR1–PR33
61. Garcia-Suarez VM, Lambert CJ (2008) Non-trivial length dependence of the conductance and negative differential resistance in atomic molecular wires. *Nanotechnology* 19:455203
62. Crljen Z, Baranovic G (2007) Unusual conductance of polyyne-based molecular wires. *Phys Rev Lett* 98:116801
63. Wang C, Batsanov AS, Bryce MR, Martin S, Nichols RJ, Higgins SJ, Garcia-Suarez VM, Lambert CJ (2009) Oligoynes single molecule wires. *J Am Chem Soc* 131:15647–15654

64. Moreno-Garcia P, Gulcur M, Manrique DZ, Pope T, Hong W, Kaliginedi V, Huang C, Batsanov AS, Bryce MR, Lambert C, Wandlowski T (2013) Single-molecule conductance of functionalized oligoynes: length dependence and junction evolution. *J Am Chem Soc* 135:12228–12240
65. Gulcur M, Moreno-Garcia P, Zhao X, Baghernejad M, Basanov AS, Hong WJ, Bryce MR, Wandlowski T (2014) The synthesis of functionalized diaryltetraynes and their transport properties in single-molecule junctions. *Chem Eur J* 20:4653–4660
66. Milan DC, Al-Owaedi O, Oerthel MC, Marques-Gonzalez S, Brooke RJ, Bryce MR, Cea P, Ferrer J, Higgings SJ, Lambert CJ, Low PJ, Manrique DZ, Martin S, Nichols RJ, Schwazacher W, Garcia-Suarez VM (2016) Solvent dependence of the single molecule conductance of oligoyne-based molecular wires. *J Phys Chem C*. doi:10.1021/acs.jpcc.5b08877
67. Li XL, He J, Hihath J, Xu BQ, Lindsay SM, Tao NJ (2006) Conductance of single alkanedithiols: conduction mechanism and effect of molecule-electrode contacts. *J Am Chem Soc* 128:2135–2141
68. Leary E, Hobenreich H, Higgins SJ, Van Zalinge H, Haiss W, Nichols RJ, Finch CM, Grace I, Lambert CJ, Mcgrath R, Smerdon J (2009) Single-molecule solvation-shell sensing. *Phys Rev Lett* 102:086801
69. Li X, Hihath J, Chen F, Masuda T, Zang L, Tao N (2007) Thermally activated electron transport in single redox molecules. *J Am Chem Soc* 129:11535–11542
70. Cao H, Jiang J, Ma J, Luo Y (2008) Temperature-dependent statistical behavior of single molecular conductance in aqueous solution. *J Am Chem Soc* 130:6674–6675
71. Fatemi V, Kamenetska M, Neaton JB, Venkataraman L (2011) Environmental control of single-molecule junction transport. *Nano Lett* 11:1988–1992
72. Weiss EA, Ahrens MJ, Sinks LE, Gusev AV, Ratner MA, Wasielewski MR (2004) Making a molecular wire: charge and spin transport through para-phenylene oligomers. *J Am Chem Soc* 126:5577–5584
73. Benniston AC, Harriman A (2006) Charge on the move: how electron-transfer dynamics depend on molecular conformation. *Chem Soc Rev* 35:169–179
74. Venkataraman L, Klare JE, Nuckolls C, Hybertsen MS, Steigerwald ML (2006) Dependence of single-molecule junction conductance on molecular conformation. *Nature* 442:904–907
75. Mishchenko A, Vonlanthen D, Meded V, Burkle M, Li C, Pobelov IV, Bagrets A, Viljas JK, Pauly F, Evers D, Mayor M, Wandlowski T (2010) Influence of conformation on conductance of biphenyl-dithiol single molecule contacts. *Nano Lett* 10:156–163
76. Finch CM, Sirichantaropass S, Bailey SW, Grace IM, Garcia-Suarez VM, Lambert CJ (2008) Conformation dependence of molecular conductance: chemistry versus geometry. *J Phys Condens Matter* 20:022203
77. Parthey M, Gluyas JBG, Fox MA, Low PJ, Kaupp M (2014) Mixed-valence ruthenium complexes rotating through a conformational Robin-Day continuum. *Chem Eur J* 20:6895–6908
78. Michoff MEZ, Castillo ME, Leiva EPM (2013) A reversible molecular switch based on the biphenyl structure. *J Phys Chem C* 117:25724–25732
79. Capozzi B, Dell EJ, Berkelbach TC, Reichmann DR, Venkataraman L, Campos LM (2014) Length-dependent conductance of oligothiophenes. *J Am Chem Soc* 136:10486–10492
80. Xu BQ, Li XL, Xiao XY, Sakaguchi H, Tao NJ (2005) Electromechanical and conductance switching properties of single oligothiophene molecules. *Nano Lett* 5:1491–1495
81. Xie ZT, Baldea I, Smith CE, Wu YF, Frisbie CD (2015) Experimental and theoretical analysis of nanotransport in oligophenylene dithiol junctions as a function of molecular length and contact work function. *ACS Nano* 9:8022–8036
82. Ranfanathan S, Steidel I, Anariba F, McCreery RL (2001) Covalently bonded organic monolayers on a carbon substrate: a new paradigm for molecular electronics. *Nano Lett* 1:491–494
83. Hines T, Diez-Perez I, Nakamura H, Shimazaki T, Asai Y, Tao NJ (2013) Controlling formation of single-molecule junctions by electrochemical reduction of diazonium terminal groups. *J Am Chem Soc* 135:3319–3322

84. Ramos-Berdullas N, Mandado M (2013) Electronic properties of p-xylylene and p-phenylene chains subjected to finite bias voltages: a new highly conducting oligophenyl structure. *Chem Eur J* 19:3646–3654
85. de Cola L (2005) Molecular wires: from design to properties. *Top Curr Chem*, vol 257. In: de Cola L (ed). Springer, Berlin/Heidelberg
86. Davis WB, Svec WA, Ratner MA, Wasielewski MR (1998) Molecular-wire behavior in p-phenylenevinylene oligomers. *Nature* 396:60–63
87. Bock CW, Trachtman M, George P (1985) A molecular orbital study of the rotation about the C = C bond in styrene. *Chem Phys* 93:431–443
88. Davis WB, Ratner MA, Wasielewski MR (2001) Conformational gating of long distance electron transfer through wire-like bridges in donor-bridge-acceptor molecules. *J Am Chem Soc* 123:7877–7886
89. Nishizawa S, Hasegawa J-Y, Matsuda K (2013) Theoretical investigation of the  $\beta$  value of the  $\pi$ -conjugated molecular wires by evaluating exchange interaction between organic radicals. *J Phys Chem C* 117:26280–26282
90. Giacalone F, Segura JL, Martin N, Guldi DM (2004) Exceptionally small attenuation factors in molecular wires. *J Am Chem Soc* 126:5340–5341
91. Sukegawa J, Schubert C, Zhu XZ, Tsuji H, Guildi DM, Nakamura E (2014) Electron transfer through rigid organic molecular wires enhanced by electronic and electron-vibration coupling. *Nat Chem* 6:899–905
92. Schubert C, Margraf JT, Clark T, Guildi DM (2015) Molecular wires-impact of  $\pi$ -conjugation and implementation of molecular bottlenecks. *Chem Soc Rev* 44:988–998
93. Greaves SJ, Flynn EL, Fitcher EL, Wrede E, Lydon DP, Low PJ, Rutter SR, Beeby A (2006) Cavity ring-down spectroscopy of the torsional motions of 1,4-bis(phenylethynyl)benzene. *J Phys Chem A* 110:2114–2121
94. Diderich F (2005) Acetylene chemistry: chemistry, biology and material science. In: Diderich F, Stang PJ, Tykwinski RR (eds). Wiley-VCH, Weinheim
95. Tour JM (2003) Molecular electronics; commercial insights, chemistry, devices, architecture and programming. World Scientific Publishing Co. Pte. Ltd., Singapore/River Edge/London
96. Donhauser ZJ, Mantooth BA, Kelly KF, Bumm LA, Monnell JD, Stapleton JJ, Price DW Jr, Rawlett AM, Allara DL, Tour JM, Weiss PS (2001) Conductance switching in single molecules through conformational changes. *Science* 292:2303–2307
97. Chen J, Reed MA, Rawlett AM, Tour JM (1999) Large on-off ratios and negative differential resistance in a molecular electronic device. *Science* 286:1550–1552
98. Moore AM, Dameron AA, Mantooth BA, Smith RK, Fuchs DJ, Cizek JW, Maya F, Yao Y, Tour JM, Weiss PS (2006) Molecular engineering and measurements to test hypothesized mechanisms in single molecule conductance switching. *J Am Chem Soc* 128:1959–1967
99. James DK, Tour JM (2004) Electrical measurements in molecular electronics. *Chem Mater* 16:4423–4435
100. Xiao XY, Nagahara LA, Rawlett A, Tao NJ (2005) Electrochemical gate-controlled conductance of single oligo-(phenylene ethynylene)s. *J Am Chem Soc* 127:9235–9240
101. Kushmerick JG, Whitaker CM, Pollack SK, Schull TL, Shashidhar R (2004) Tuning current rectification across molecular junctions. *Nanotechnology* 15:S489–S493
102. Zotti LA, Kirchner T, Cuevas JC, Pauly F, Huhn T, Scheer E, Erbe A (2010) Revealing the role of anchoring groups in the electrical conduction through single-molecule junctions. *Small* 6:1529–1535
103. Hong WJ, Manrique DZ, Moreno-Garcia P, Gulcur M, Mishchenko A, Lambert CJ, Bryce MR, Wandlowski T (2012) Single molecule conductance of tolanes: experimental and theoretical study on the junction evolution dependent on the anchor group. *J Am Chem Soc* 134:2292–2304
104. Pera G, Martin S, Ballesteros LM, Hope AJ, Low PJ, Nichols RJ, Cea P (2010) Metal-molecule-metal junctions in Langmuir-Blodgett films using a new linker: Trimethylsilane. *Chem Eur J* 16:13398–13405

105. Marques-Gonzalez S, Yufit DS, Howard JAK, Martin S, Osorio HM, Garcia-Suarez VM, Nichols RJ, Higgins SJ, Cea P, Low PJ (2013) Simplifying the conductance profiles of molecular junctions: the use of the trimethylsilylethynyl moiety as a molecule-gold contact. *Dalton Trans* 42:338–341
106. Hong WJ, Li H, Liu S-X, Fu YC, Li JF, Kaliginedi V, Decurtins S, Wandlowski T (2012) Trimethylsilyl-terminated oligo(phenylene ethynylene)s: an approach to single-molecule junctions with covalent Au-C s-bonds. *J Am Chem Soc* 134:19425–19431
107. Kaliginedi V, Moreno-Garcia P, Valkenier H, Hong W, Garcia-Suarez VM, Buitter P, Otten JLH, Hummelen JC, Lambert CJ, Wandlowski T (2012) Correlations between molecular structure and single-junction conductance: a case study with oligo(phenylene-ethynylene)-type wires. *J Am Chem Soc* 134:5262–5275
108. Cho AH, Risko C, Delgado MCR, Kim BS, Bredas JL, Frisbie CD (2010) Transition from tunneling to hopping transport in long, conjugated oligo-imine wires connected to metals. *J Am Chem Soc* 132:4358–4368
109. Linton KE, Fox MA, Palsson LO, Bruce MR (2015) Oligo(p-phenyleneethynylene) (OPE) molecular wires: synthesis and length dependence of photoinduced charge transfer in OPEs with triarylamine and diaryloxadiazole end groups. *Chem Eur J* 21:3997–4007
110. Lu Q, Liu K, Zhang HM, Du Z, Wang XH, Wang FS (2009) From tunneling to hopping: a comprehensive investigation of charge transport mechanisms in molecular junctions based on oligo(p-phenylene ethynylene)s. *ACS Nano* 3:3861–3868
111. Zhao X, Huang CC, Gulcur M, Batsanov AS, Baghernejad M, Hong WJ, Bryce MR, Wandlowski T (2013) Oligo(aryleneethynylene)s with terminal pyridyl groups: Synthesis and length dependence of the tunneling-to-hopping transition of single-molecule conductances. *Chem Mater* 25:4340–4347

# Chapter 5

## Insulated Oligothiophenes

Yutaka Ie

**Abstract** Single-molecule electronics have attracted a great deal of attention in terms of the bottom-up construction and potential for ultimate device miniaturization. Development of novel functional components for this application has become an active area of research. Structurally well-defined oligothiophenes have been utilized as a key framework of molecular wires. For this purpose, the encapsulation of the  $\pi$ -conjugated backbones is important to prevent intermolecular electronic communications. In this chapter, I summarize on a series of oligothiophenes for the use in “insulated molecular wire” units, which are essential components of single-molecule electronics. Especially, I focus on the combination of cyclopenta[*c*]thiophene with orthogonally introduced bulky substituents. This novel framework can accomplish the encapsulation of its-containing oligothiophene backbones without disturbing effective conjugation, leading to the construction of ideal insulated molecular wires.

**Keywords** Oligothiophene • Insulated molecular wire • Single-molecule conductance

### 5.1 Introduction

Oligothiophenes have been recognized as an important  $\pi$ -conjugated platform for molecular wires in single-molecule electronics for the following reasons: [1–5] (1) oligothiophene backbones have the longest effective conjugation length among reported organic  $\pi$ -conjugated systems [6], leading to small energy gaps between the highest occupied molecular orbital (HOMO) and lowest unoccupied molecular orbital (LUMO). (2) Their wide synthetic availability and high chemical stability enable us to fine-tune the electronic and electrochemical properties. (3) The high polarizability of the sulfur atom in thiophene effectively stabilizes cationic oligothiophenes in various oxidation states. These characteristics provide advantages for carrier injection from metal electrodes and intramolecular charge-carrier transport

---

Y. Ie (✉)

The Institute of Scientific and Industrial Research, Osaka University, Osaka, Japan  
e-mail: [yutakaie@sanken.osaka-u.ac.jp](mailto:yutakaie@sanken.osaka-u.ac.jp)

properties. Although long oligothiophenes whose molecular lengths far exceed 10 nm have been developed [6–11], there are few reports on the measurement of the electrical conductance of single-molecule oligothiophenes for revealing their electric potential in molecular wires because of the difficulty in designing and synthesizing suitable molecules [12–19]. For example, Ie et al. (2007) [11] synthesized tetrahexylsexithiophene-based oligothiophenes (**1** and **2**) of ca. 10 nm length, bearing anchor units (either a protected thiol group or a trimethylsilylethynyl group) at both terminal positions on the conjugated backbone (Fig. 5.1). The thiol-terminated oligothiophene **1'** was bridged to nanogap gold electrodes by self-assembly, and then, the current–voltage characteristics were measured [14].

However, as shown in Fig. 5.2, the scanning tunneling microscopy (STM) image of **1'** on an Au (111) substrate showed a dense parallel arrangement [20]. This phenomenon is due to the spontaneous aggregation of oligothiophene backbones, making it difficult to elucidate the single-molecule conductance without the influence of aggregated molecules. In order to circumvent these  $\pi$ – $\pi$  interactions, insulation of the conjugated backbones is essential. In this chapter, I summarize

**Fig. 5.1** Chemical structures of anchor-terminated oligothiophenes (**1**, **1'**, and **2**)

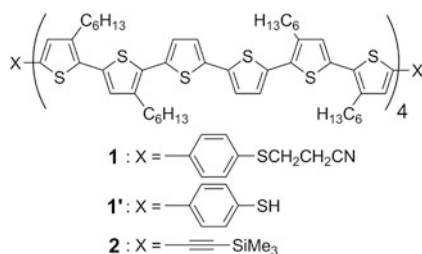
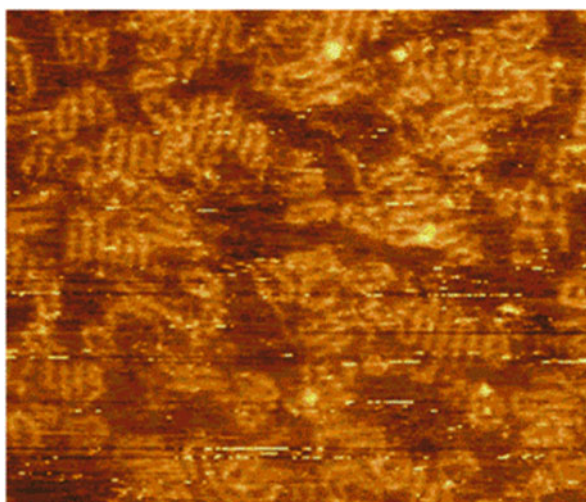


**Fig. 5.2** STM image of **1'** on Au (111)



10 nm

research on the development of insulated oligothiophenes for this purpose, along with their single-molecule conductivity.

## 5.2 Oligothiophenes with Bulky Silyl Substituents as Insulating Units

The introduction of covalently attached insulating groups is advantageous for the tight insulation of the well-defined oligomeric  $\pi$ -conjugated system, thus facilitating investigation of structure–property relationships. As one of the pioneering strategies, bulky dendrons have been utilized for the development of insulated  $\pi$ -conjugated systems [21, 22]. In this context, as shown in Fig. 5.3, dendron-incorporating oligothiophenes **3** and **4** have also been reported by Fréchet et al. (1998, 2000) [23, 24]. Direct introduction of bulky *N*-silyl-protected diamino substituents at both  $\beta$ -positions in the thiophene ring was carried out by Tanaka

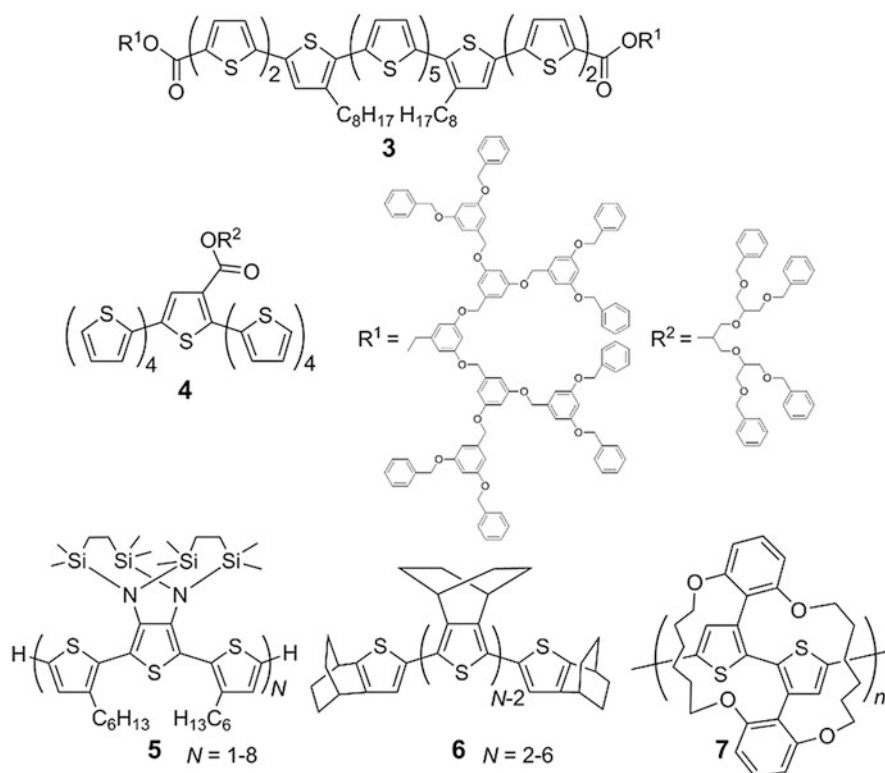
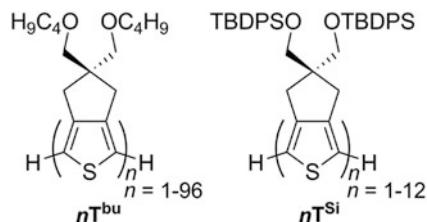


**Fig. 5.3** Representative chemical structures of insulated oligothiophenes and polythiophene with covalently attached bulky substituents

**Fig. 5.4** Chemical structures of  $n\mathbf{T}^{\text{bu}}$  and  $n\mathbf{T}^{\text{Si}}$



and Yamashita (1999) [25]. The terthiophene **5** ( $N = 1$ ) containing this unit was elongated to the nanometer scale for single-molecule measurements [10]. However, its steric bulkiness limited the number of insulating units that could be incorporated in the  $\pi$ -conjugated backbones. In fact, only a few thiophene-based conjugated systems containing the covalently attached insulating groups at *all* repeating units have been reported [10, 26–30]. This is due to the crucial difficulty in designing an appropriate repeating unit that is compatible with the use of bulky substituents for insulation while retaining the effective conjugation of the backbone. Nishinaga et al. (2003) [26, 27] designed bicyclo[2.2.2]octane-annulated thiophene and developed **6**, an oligothiophene based on this thiophene. Sugiyasu et al. (2010) [30] developed a threading-type insulated polythiophene (**7**).

Here, Ie et al. have focused on annulated cyclopentanes at the  $\beta$ -positions in the thiophene ring, because effective conjugation is maintained up to 96 repeating thiophene units for  $n\mathbf{T}^{\text{bu}}$  despite the presence of substituents on every  $\beta$ -site [6]. It is anticipated that the combination of cyclopentane annellation and bulky *t*-butyldiphenylsilyl (TBDPS) groups in the thiophene ring would be an ideal unit for insulated oligothiophene and designed oligothiophenes  $n\mathbf{T}^{\text{Si}}$  based on this (Fig. 5.4) [31]. Note that the TBDPS group is known to exhibit good stability toward oxidative conditions, which is suitable for an insulating group for oligothiophenes. Indeed, iron(III)-mediated oxidative coupling could be used for the synthesis of  $n\mathbf{T}^{\text{Si}}$ .

The electronic absorption spectra of  $2\mathbf{T}^{\text{Si}}$ – $12\mathbf{T}^{\text{Si}}$  in  $\text{CH}_2\text{Cl}_2$  are shown in Fig. 5.5. The absorption maxima of  $n\mathbf{T}^{\text{Si}}$  were bathochromically shifted with chain extension. When the  $\pi$ – $\pi^*$  transition energies ( $E$ ) were plotted against inverse thiophene-ring numbers ( $1/n$ ), a linear relationship was observed with the equation  $E$  (eV) =  $2.03 + 3.86/n$ . This slope was very close to that of the corresponding non-substituted oligothiophenes (3.76) [32]. This result indicates that the introduction of bulky TBDPS groups at the pendant position of cyclopentene ring had little effect on the effective conjugation.

The X-ray crystal structure of  $4\mathbf{T}^{\text{Si}}$  clearly shows the highly coplanar structure of the oligothiophene backbone with all anti-conformation as well as the  $\pi$ -conjugated backbone completely encapsulated by the TBDPS groups (Fig. 5.6).

To evaluate the effect of insulation on suppressing intermolecular interactions, the UV–vis–NIR spectra of radical cationic species of  $6\mathbf{T}^{\text{Si}}$  ( $6\mathbf{T}^{\text{Si}\bullet+}$ ) and uninsulated hex- $6\mathbf{T}^+$  were measured. As shown in Fig. 5.7, the polaronic bands of hex- $6\mathbf{T}^+$  (0.8 and 1.6 eV) at 298 K disappeared along with the concomitant appearance of new bands (1.2 and 1.9 eV) at 223 K. These high-energy shifts of polaronic

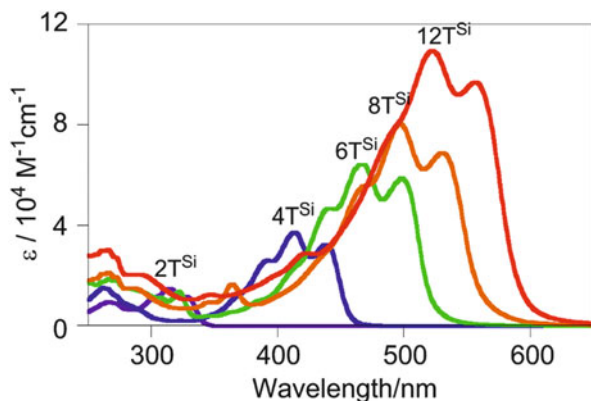


Fig. 5.5 UV-vis absorption spectra of  $n\text{T}^{\text{Si}}$  ( $n = 2, 4, 6, 8,$  and  $12$ ) in  $\text{CH}_2\text{Cl}_2$

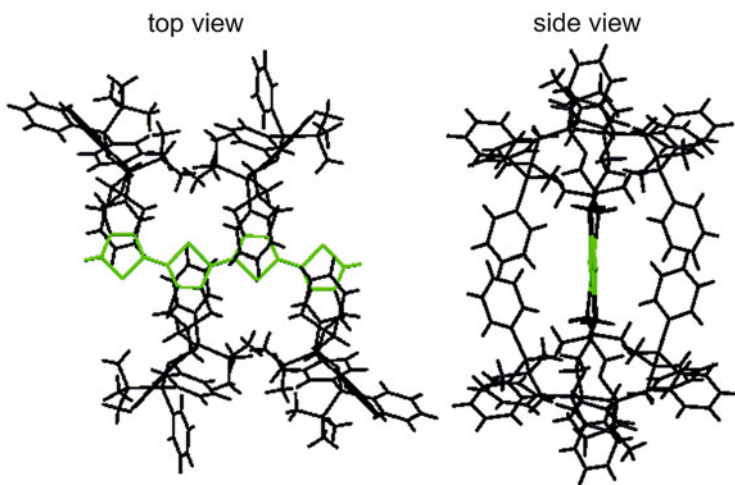
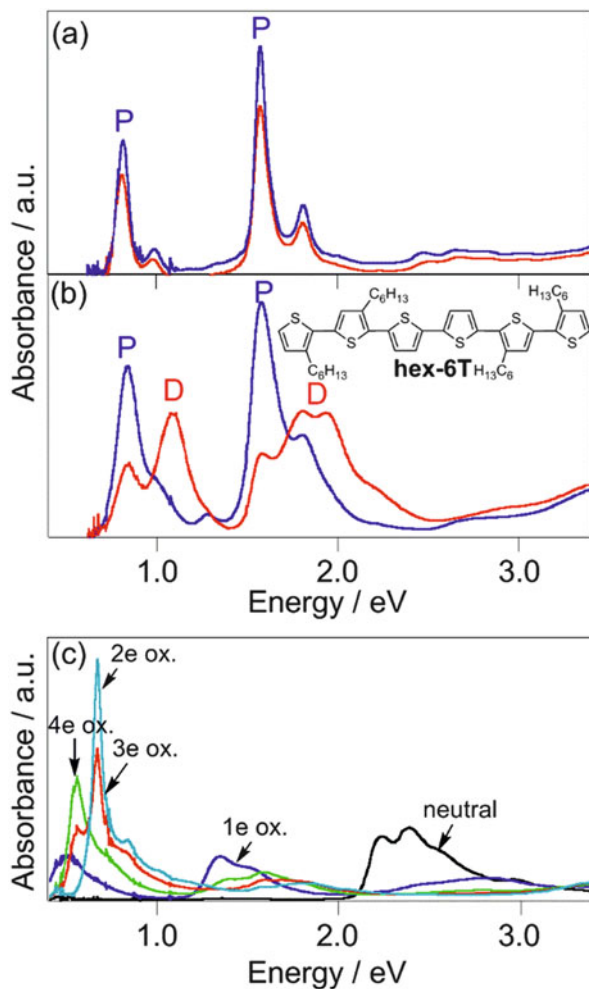


Fig. 5.6 X-ray crystal structure of  $4\text{T}^{\text{Si}}$

bands are typically characteristic of  $\pi$ -dimer formation [33]. On the other hand,  $6\text{T}^{\text{Si}+\cdot}$  exhibited no significant spectral change between 298 and 223 K. This apparent difference can be explained by the insulating effect of the TBDPS group upon suppressing the  $\pi$ -dimer formation of  $6\text{T}^{\text{Si}+\cdot}$ , leading to insulation of the oligothiophene  $\pi$ -conjugated backbone. Importantly, the perfect blocking of  $\pi$ -dimeric intermolecular electronic interactions enabled us to observe further progressive three- and four-electron oxidation of  $12\text{T}^{\text{Si}}$ .

**Fig. 5.7** UV–vis–NIR spectra of radical cationic species for (a) **6T<sup>Si</sup>** and (b) uninsulated **hex-6T** in CH<sub>2</sub>Cl<sub>2</sub> at 298 K and 223 K. P and D denote polaronic and  $\pi$ -dimeric bands, respectively. (c) UV–vis–NIR spectra of **12T<sup>Si</sup>** in CH<sub>2</sub>Cl<sub>2</sub> under oxidation with FeCl<sub>3</sub> at room temperature



### 5.3 Completely Insulated Oligothiophenes with Anchor Units

Single-molecule electronics inevitably require molecule–metal junctions, and thus, the introduction of anchor units to molecular wires is essential for forming metal–molecule–metal junctions for single-molecule conductance measurements. The uninsulated oligothiophenes with thiol anchors have been investigated by Bourgoin et al. (1999) (compound **8**) [34], Tao et al. (2005) (compound **9**) [12], and Campos et al. (2014) (compounds **10–12**) [19] (Fig. 5.8). However, these molecules cannot exclude the presence of intermolecular interactions. Furthermore, Kiguchi et al. (2014) [35] reported that partially insulated oligothiophene **13** showed two types of anchoring geometries in the exposed thiophene rings, indicating that the effective

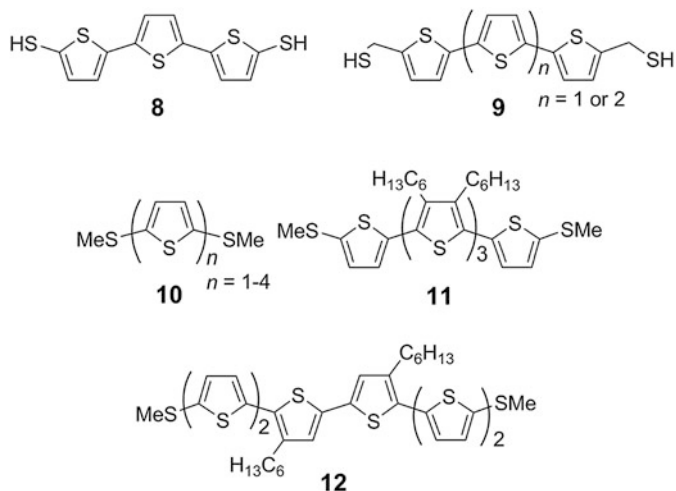


**Fig. 5.8** Reported uninsulated oligothiophenes having anchor units for the single-molecule conductance measurements

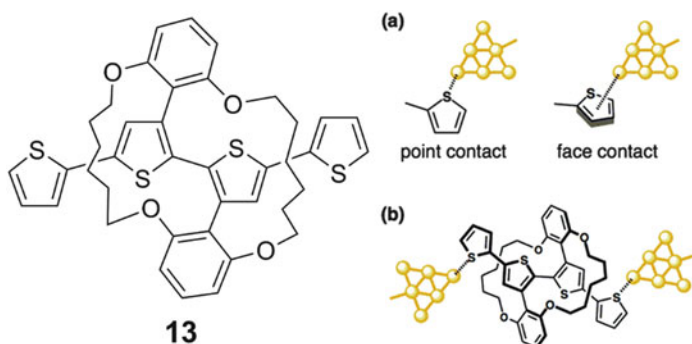


**Fig. 5.9** Chemical structure of partially insulated oligothiophene **13** and schematic illustrations of metal-molecule-metal junctions (Reprinted with the permission from ref. [35]. Copyright 2014 American Chemical Society)

tunneling length was variable via controlling the anchoring positions in the same molecule (Fig. 5.9). The single-molecule conductance measurements of insulated oligothiophene **14** was performed by Yamada et al. (2009) [16] (Fig. 5.10). They successfully observed the crossover between tunneling and hopping. However, the conjugation of **14** is distorted by the bulkiness of silyl substituents.

Under this situation, the Stille coupling reaction of bisstannylated quaterthiophene **15** with 4-(2-cyanoethylthio)bromobenzene (**16**) was attempted to introduce thiol anchors (Fig. 5.11). However, this reaction did not yield the desired product, indicating that the steric bulk of the TBDPS groups inhibited this reaction. Based on the low reactivity of **15**, it is predicted that a planar fluorene group in place of

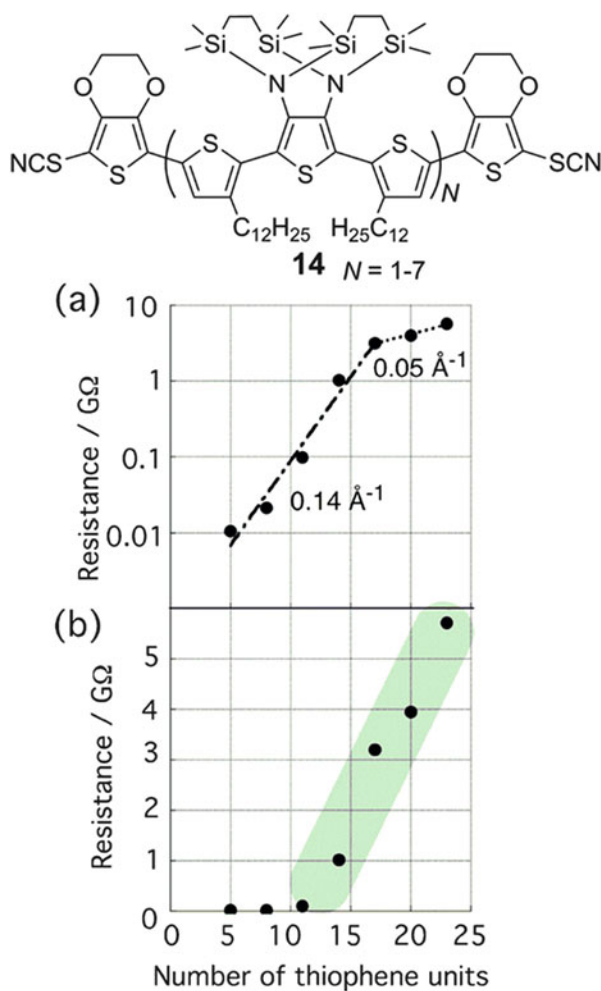


**Fig. 5.10** Chemical structure of insulated oligothiophene **14** and semilog (a) and linear (b) plots of the resistance as a function of the number of thiophene units. Schematic illustrations of metal–molecule–metal junctions (Reprinted with the permission from ref. [16]. Copyright 2009 The Japan Society of Applied Physics)

the TBDPS group as an insulating unit for cyclopentene-annulated thiophene would enhance reactivity at the  $\alpha$ -positions for the Stille coupling reaction. Based on this idea, Ie et al. (2011) [17] developed the oligothiophenes  $n\mathbf{T}^{\text{oct}}$ .

As shown in Fig. 5.12, the X-ray crystal structure of  $2\mathbf{T}^{\text{oct}}$  indicates that it has *trans* conformation and a completely coplanar structure. The octyl groups covered the bithiophene backbone without shielding the reactive terminal  $\alpha$ -positions, leading to oligomers featuring suppressed intermolecular  $\pi$ – $\pi$  interactions while maintaining the versatility of terminal functionalization. As expected, the protected

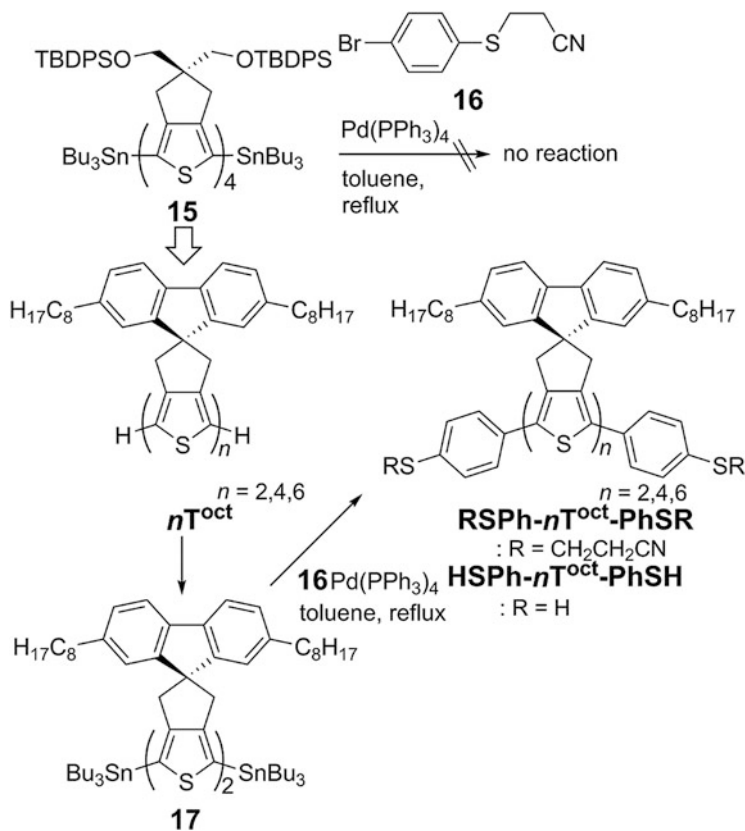


Fig. 5.11 Attempt to introduce anchor units for **15** and insulated oligothiophenes  $n\text{T}^{\text{oct}}$

thiol functional group was successfully introduced to stannylated bithiophene **17** by the Stille coupling reaction with **16** to give the anchoring-group-introduced oligothiophenes **RSPH- $2\text{T}^{\text{oct}}$ -PhSR**. Likewise, the use of Pd-catalyzed homo-coupling or Stille coupling with **16** gave **RSPH- $4\text{T}^{\text{oct}}$ -PhSR** or **RSPH- $6\text{T}^{\text{oct}}$ -PhSR**.

To investigate the photophysical properties of the oligomers, the electronic absorption spectra of  $n\text{T}^{\text{oct}}$  were measured in  $\text{CH}_2\text{Cl}_2$  solutions. As shown in Fig. 5.13, these oligomers exhibited an absorption band in the visible region corresponding to the  $\pi-\pi^*$  transition of the oligothiophene backbones together with the  $\pi-\pi^*$  transition of the fluorene unit centered at 280 nm. The absorption maxima derived from the  $\pi-\pi^*$  transitions of the oligothiophene backbones shifted to a longer wavelength, from 314 to 466 nm, when the number of thiophene rings increased from two to six. The linear relationship of  $E$  against  $1/n$  for  $n\text{T}^{\text{oct}}$  was calculated to be  $E$  (eV) =  $2.03 + 3.85/n$ . The slope of  $n\text{T}^{\text{oct}}$  (3.85) was almost identical to that of  $n\text{T}^{\text{Si}}$  (3.86), indicating that the insulating dioctylfluorene units also had little effect on the effective conjugation of the oligothiophene backbone.

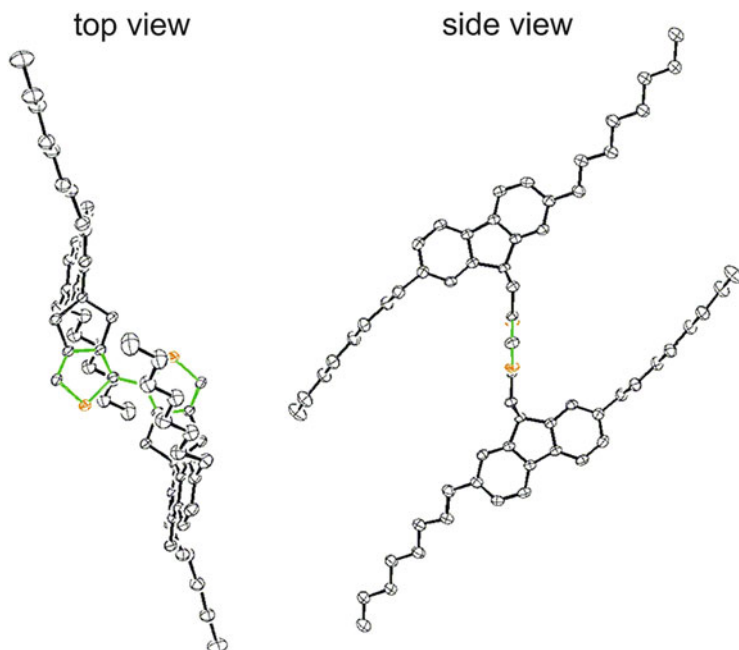


Fig. 5.12 X-ray crystal structure of  $2T^{oct}$

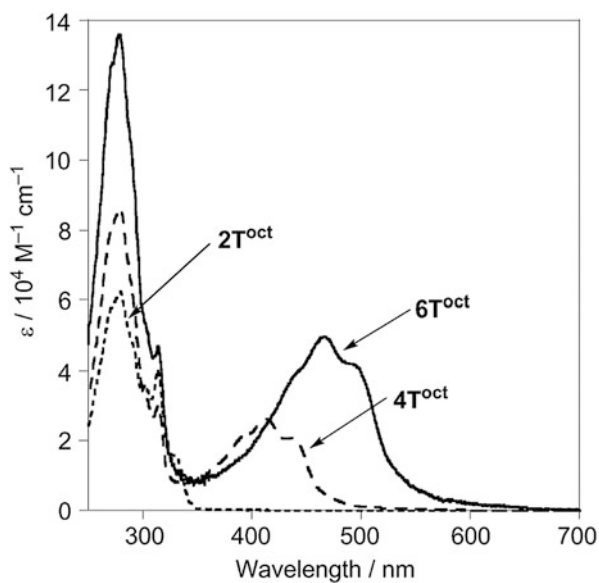
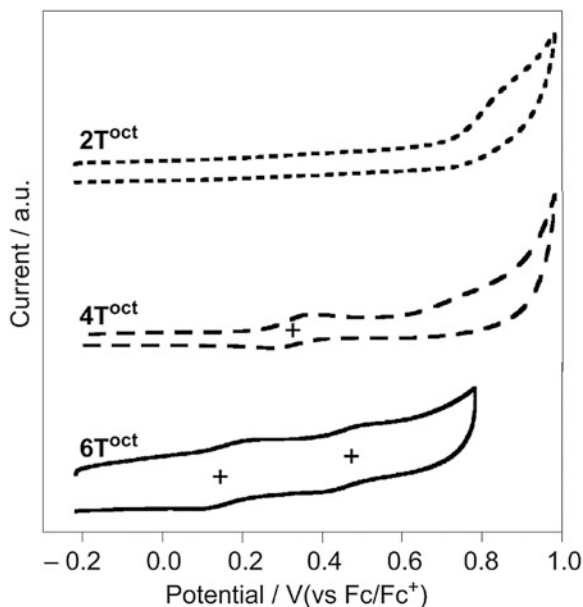


Fig. 5.13 UV-vis spectra of  $nT^{oct}$  in  $CH_2Cl_2$

**Fig. 5.14** CVs of  $n\mathbf{T}^{\text{oct}}$  in  $\text{CH}_2\text{Cl}_2$



The electrochemical properties of  $n\mathbf{T}^{\text{oct}}$  quantified by CV measurement showed that reversible oxidation waves were observed in all oligothiophenes except  $2\mathbf{T}^{\text{oct}}$  (Fig. 5.14). The first oxidation potentials decreased as the number of thiophene rings increased. In order to investigate the encapsulating effect in a similar manner to that for  $n\mathbf{T}^{\text{Si}}$ , the UV-vis-NIR spectrum of the radical cationic species of  $6\mathbf{T}^{\text{oct}}$  was measured. As expected, the polaronic species of  $6\mathbf{T}^{\text{oct}}$  exhibited no spectral band transposition to a higher energy even upon cooling to 223 K, indicating insulation of the conjugated backbone. This trend is in good agreement with that for  $n\mathbf{T}^{\text{Si}}$ .

The single-molecule electrical conductance of  $\mathbf{HSPH}-n\mathbf{T}^{\text{oct}}-\mathbf{PhSH}$  ( $n=2, 4,$  and  $6$ ) was measured using the break junction (BJ) method by STM [17]. This measurement was carried out using mechanically cut gold tips in a  $\sim 0.1 \mu\text{M}$  mesitylene solution of the molecules at room temperature. Figure 5.15 shows the conductance histograms obtained from 500 to 1,000 transient conductance measurements of  $\mathbf{HSPH}-n\mathbf{T}^{\text{oct}}-\mathbf{PhSH}$ . The solid arrows indicate the peak positions attributed to single-molecule conductance. A semilog plot of the conductance as a function of the estimated molecular length indicated an exponential decrease in conductance with molecular length (Fig 5.15d); thus, tunneling transport is evident, which is expressed as  $G \times \exp(-\beta L)$ , where  $\beta$  is a decay constant and  $L$  is the length of the conduction channel. The  $\beta$  value of the  $\mathbf{HSPH}-n\mathbf{T}^{\text{oct}}-\mathbf{PhSH}$  was estimated to be  $1.9 \text{ nm}^{-1}$ . This value is in good agreement with that obtained from theoretical calculations for non-substituted oligothiophenes ( $\beta = 2.11 \text{ nm}^{-1}$ ) [36], indicating that our completely encapsulated oligothiophenes  $\mathbf{HSPH}-n\mathbf{T}^{\text{oct}}-\mathbf{PhSH}$  possessed the intrinsic electronic structures and transport properties of defect-free oligothiophenes with effective conjugation.

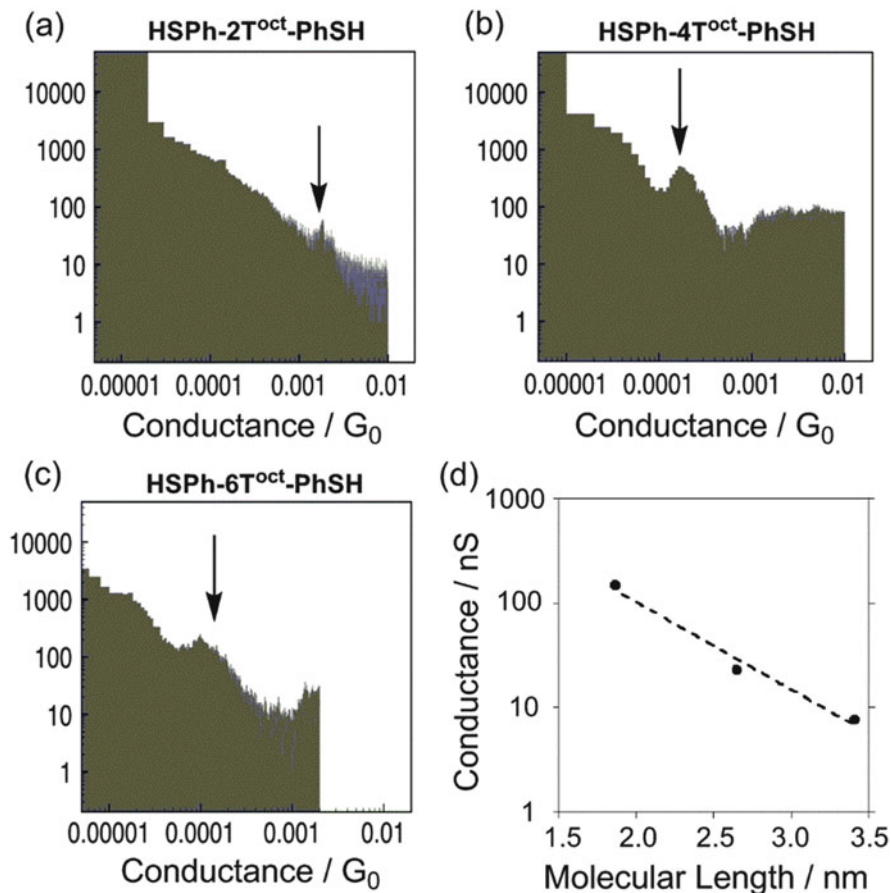


**Fig. 5.15** Conductance histograms for (a) HSPh-2T<sup>oct</sup>-PhSH, (b) HSPh-4T<sup>oct</sup>-PhSH, and (c) HSPh-6T<sup>oct</sup>-PhSH. (d) Conductance of HSPh-*n*T<sup>oct</sup>-PhSH as a function of molecular length

## 5.4 Insulation-Tuned Oligothiophenes

Oligothiophenes have been developed not only as molecular wires for single-molecule electronics [37] but also as semiconducting materials for organic thin-film electronics applications, such as organic field-effect transistors and organic photovoltaics [38, 39]. In the former application, the single-chain properties become crucial for single-molecule conductance. In the latter case, the properties of oligothiophenes in aggregated states influence the charge-carrier mobility of their films. In this context, the cationic species of oligothiophenes, as well as the dimer species of their radical cations ( $\pi$ -dimers), have been extensively investigated to elucidate the electronic structures and conduction mechanisms [27, 40–54]. In this case, it is anticipated that oligothiophenes composed of both cyclopenta[*c*]thiophene

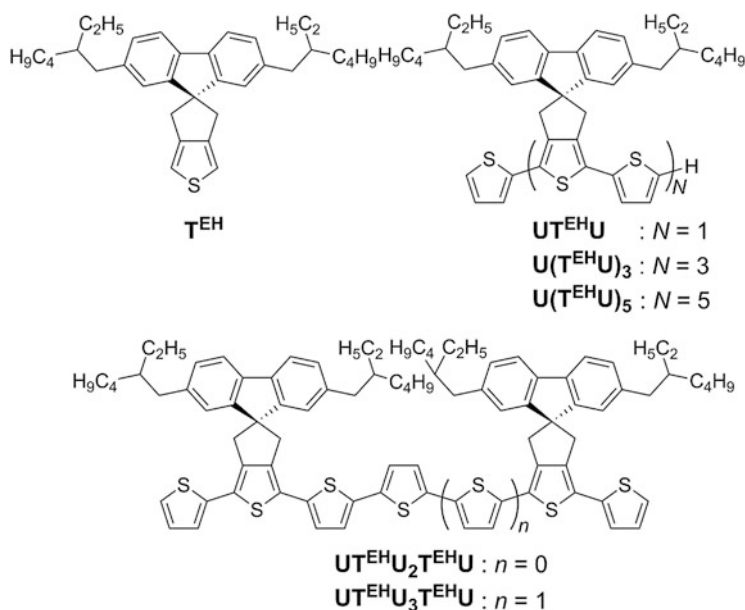
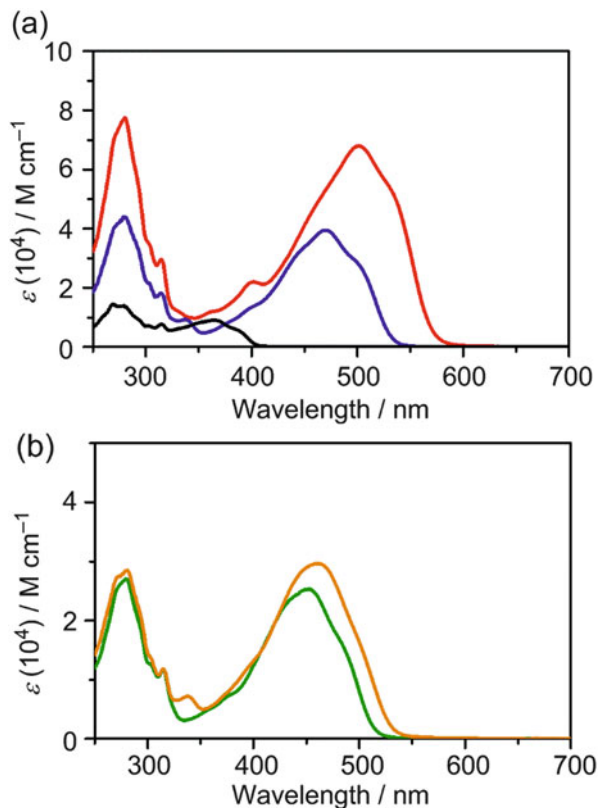


**Fig. 5.16** Chemical structures of  $\text{T}^{\text{EH}}$ -containing oligothiophenes

(**T**) and unsubstituted thiophene (**U**) units would be an appropriate model to elucidate the structure–property relationship of  $\pi$ -dimer formation capability. In order to compensate for the introduction of less soluble **U** units, the octyl-substituted fluorene in  $\text{T}^{\text{oct}}$  was replaced with 2-ethylhexyl-substituted fluorene ( $\text{T}^{\text{EH}}$ ). To investigate the tunability of the  $\pi$ -dimer formation by changing the number and position of the  $\text{T}^{\text{EH}}$  units, Ie et al. (2015) [55] developed a series of oligothiophenes,  $\text{U(T}^{\text{EHU}})_n$  ( $n = 1, 3, \text{ and } 5$ ),  $\text{UT}^{\text{EHU}}_2\text{T}^{\text{EHU}}$ , and  $\text{UT}^{\text{EHU}}_3\text{T}^{\text{EHU}}$  (Fig. 5.16).

Under the assumption that these oligomers take all-*trans* conformations, the orthogonally fused fluorene units are located on one side of the  $\pi$ -conjugated chain for  $\text{U(T}^{\text{EHU}})_n$  and  $\text{UT}^{\text{EHU}}_3\text{T}^{\text{EHU}}$  and on both sides for  $\text{UT}^{\text{EHU}}_2\text{T}^{\text{EHU}}$ . These oligothiophenes could be synthesized by the palladium-catalyzed Stille coupling reaction as a key C–C bond formation step. As shown in Fig. 5.17, the absorption bands of all the compounds were similar to those of  $n\text{T}^{\text{oct}}$ . One band located at 280 nm corresponded to the local  $\pi$ – $\pi^*$  transition of the fluorene unit, and the other band in the visible region was ascribed to the  $\pi$ – $\pi^*$  transition of the oligothiophene backbones. The absorption maxima derived from the oligothiophene backbones were redshifted as the number of thiophene units increased. The value of  $E$  for  $\text{U(T}^{\text{EHU}})_n$  ( $n = 1, 3, \text{ and } 5$ ) against  $1/n$  displayed a linear relationship with the equation of  $E$  (eV) =  $2.11 + 3.83/n$ . Its slope (3.83) was almost the same as that of the abovementioned insulated oligothiophenes. This result indicated that effective conjugation was maintained in the  $\text{U(T}^{\text{EHU}})_n$  conjugated system.

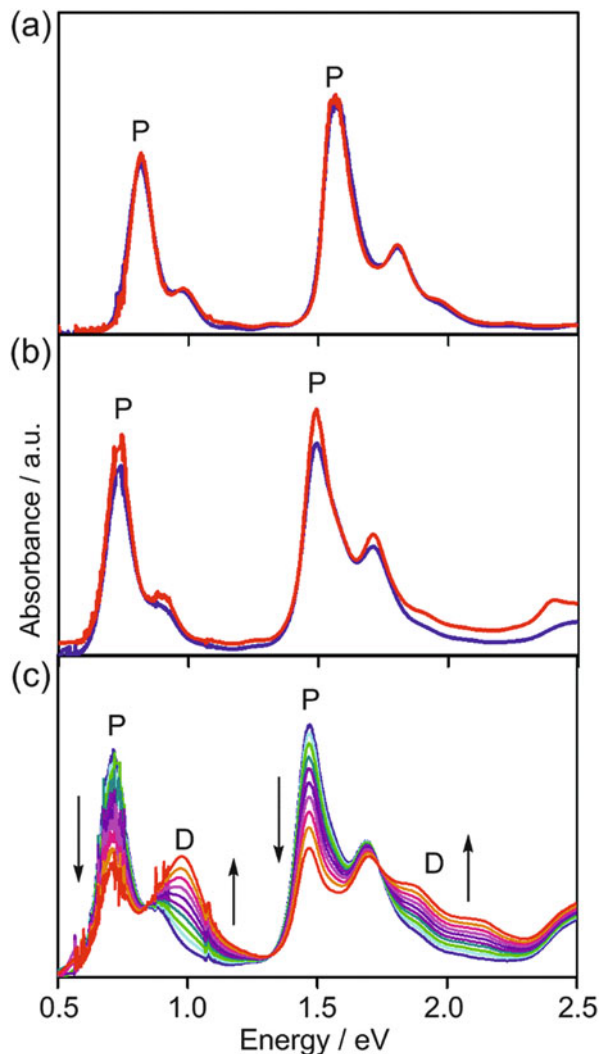
**Fig. 5.17** UV–vis absorption spectra of (a)  $\text{UT}^{\text{EH}}\text{U}$  (black),  $\text{U}(\text{T}^{\text{EH}}\text{U})_3$  (blue),  $\text{U}(\text{T}^{\text{EH}}\text{U})_5$  (red), (b)  $\text{UT}^{\text{EH}}\text{U}_2\text{T}^{\text{EH}}\text{U}$  (green), and  $\text{UTU}_3\text{TU}$  (orange) in  $\text{CH}_2\text{Cl}_2$



To investigate the influence of the  $\text{T}^{\text{EH}}$  unit on the intermolecular interactions, the UV–vis–NIR spectra of positively charged oligothiophenes were measured. As shown in Fig. 5.18a, b, upon lowering the temperature from 298 to 223 K, spectral change corresponding to the formation of  $\pi$ -dimer was not observed from the polaronic species derived from  $\text{U}(\text{T}^{\text{EH}}\text{U})_3$  and  $\text{UT}^{\text{EH}}\text{U}_2\text{T}^{\text{EH}}\text{U}$ . On the other hand, the polaronic bands of  $\text{UT}^{\text{EH}}\text{U}_3\text{T}^{\text{EH}}\text{U}$  were gradually replaced by  $\pi$ -dimer bands (Fig. 5.18c) upon cooling the temperature to 223 K. This interconversion between two species was confirmed by the appearance of isosbestic points. Based on the equilibrium constant value and a van't Hoff plot, the dimerization enthalpy ( $\Delta H_{\text{exp}}$ ) was determined to be  $-7.1 \text{ kcal mol}^{-1}$ .

To gain insight into the  $\pi$ -dimerization behavior of radical cationic species for  $\text{UT}^{\text{EH}}\text{U}_3\text{T}^{\text{EH}}\text{U}$ , theoretical calculations were performed. To ease the calculation, all the alkyl groups were substituted with a methyl group. Nishinaga et al. (2013) [54] reported that the dimer of *cis*-connected conformers with slipped-stacking was the most stable structure for an unsubstituted oligothiophene framework. In this study, the dimer models of (1) the *cis* conformations between the unsubstituted thiophenes (*tct*- $\text{UT}^{\text{m}}\text{U}_3\text{T}^{\text{m}}\text{U}$ ), (2) all-*cis* conformations (*ccc*- $\text{UT}^{\text{m}}\text{U}_3\text{T}^{\text{m}}\text{U}$ ), and (3)

**Fig. 5.18** UV-vis-NIR spectra of (a)  $\text{U}(\text{T}^{\text{EH}}\text{U})_3^{*+}$ , (b)  $\text{UT}^{\text{EH}}\text{U}_2\text{T}^{\text{EH}}\text{U}^{*+}$ , and (c)  $\text{UT}^{\text{EH}}\text{U}_3\text{T}^{\text{EH}}\text{U}^{*+}$  in  $\text{CH}_2\text{Cl}_2$  at 298 K and at 223 K. *P* and *D* denote polaronic and  $\pi$ -dimeric bands, respectively



all-*trans* conformations (*ttt*- $\text{UT}^{\text{m}}\text{U}_3\text{T}^{\text{m}}\text{U}$ ) were investigated among the possible structures. Note that the calculated dimerization enthalpy ( $\Delta H_{\text{calc}}$ ) was estimated against double the enthalpies of the most stable structure *ttt*- $\text{UT}^{\text{m}}\text{U}_3\text{T}^{\text{m}}\text{U}^{*+}$ . The  $\Delta H_{\text{calc}}^{\text{tct}}$  of *tct*- $\text{UT}^{\text{m}}\text{U}_3\text{T}^{\text{m}}\text{U}$  was calculated to be  $-6.1 \text{ kcal mol}^{-1}$  (Fig. 5.19a), which is inconsistent with  $\Delta H_{\text{exp}}$ . In the case of *ccc*- $\text{UT}^{\text{m}}\text{U}_3\text{T}^{\text{m}}\text{U}$ , the optimized dimer model adopted a slipped face-to-face structure (Fig. 5.19b). The  $\Delta H_{\text{calc}}^{\text{ccc}}$  of  $-24.7 \text{ kcal mol}^{-1}$  indicated greater stabilization compared to that for *tct*- $\text{UT}^{\text{m}}\text{U}_3\text{T}^{\text{m}}\text{U}$ . However, the corresponding *ccc*-conformer of  $\text{UT}^{\text{m}}\text{U}_2\text{T}^{\text{m}}\text{U}$  could also construct a similar dimer model without steric hindrance, which is also inconsistent with the experimental results. On the other hand, the dimer model of *ttt*-

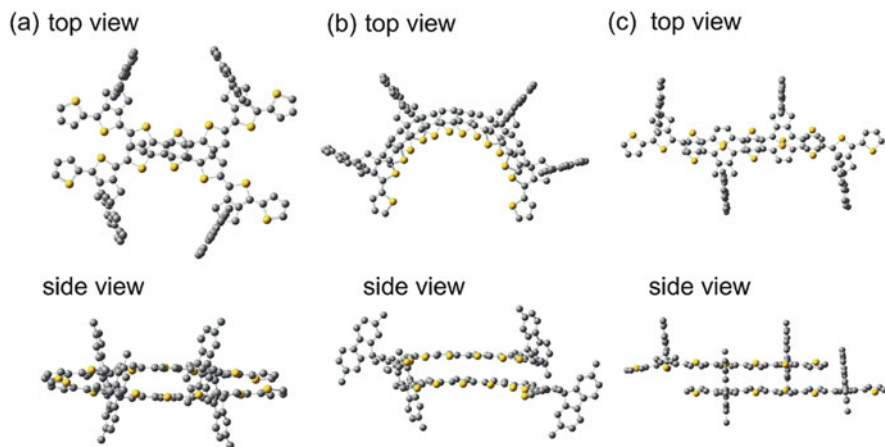


**Fig. 5.19** Top and side views of dimer structure for (a) *tct*- $\text{UT}^m\text{U}_3\text{T}^m\text{U}$ , (b) *ccc*- $\text{UT}^m\text{U}_3\text{T}^m\text{U}$ , and (c) *ttt*- $\text{UT}^m\text{U}_3\text{T}^m\text{U}$  calculated at M06-2X/6-31G(d) level. Hydrogen atoms are omitted for clarity

$\text{UT}^m\text{U}_3\text{T}^m\text{U}$  bearing the slippage structures precluded the steric hindrance between the neighboring cyclopentene rings of  $\text{T}^m$  with a  $\Delta H_{\text{calc}}^{\text{m}}$  value of  $-19.2 \text{ kcal mol}^{-1}$  (Fig. 5.19c), whereas the corresponding *ttt*- $\text{UT}^m\text{U}_2\text{T}^m\text{U}$  showed steric congestion. These phenomena were consistent with the experimental results. Therefore, it was concluded that the combination of the  $\text{U}_3$  unit and an all-*trans* conformation led to a decrease in the steric repulsion between the cyclopentene ring and its opposing thiophene ring in the dimer structure, which may be a crucial factor for the  $\pi$ -dimer formation of oligothiophenes containing  $\text{T}$  units.

## 5.5 Insulated Oligothiophenes with Hopping Conduction

As mentioned in Sect. 2.3, Ie et al. (2011) [17] calculated the  $\beta$ -value of completely insulated oligothiophenes. On the other hand, electrical conductance measurements of oligothiophene in the hopping region are still limited to the result of Yamada et al. (2009) [16] using  $\text{NCS}-(3m+2)\text{T}_{\text{DTD}}\text{-SCN}$  (Fig. 5.10). It was shown that for this molecule, the carrier transport mechanism changes from tunneling to hopping at around thiophene 11~14-mer. However, effective conjugation is disrupted by the presence of bulky insulating substituents. Thus, elucidation of the intrinsic electrical properties of the oligothiophene backbone in the hopping region has been positioned as an important issue. Quite recently, Ie et al. synthesized  $n\text{T}^{\text{EH}}$  ( $n = 2\text{--}24$ ) using the modified Stille coupling reaction (Fig. 5.20) [56]. These oligomers retained effective conjugation, which was inferred from the UV-vis absorption spectra. The single-

**Fig. 5.20** Chemical structures of  $n\mathbf{T}^{\text{EH}}$  ( $n = 2, 4, 6, 8, 12, 16, 20, \text{ and } 24$ ) and  $\text{NCS-}n\mathbf{T}^{\text{EH}}\text{-SCN}$  ( $n = 2, 4, 6, 8, 12, 16, 20, \text{ and } 24$ )

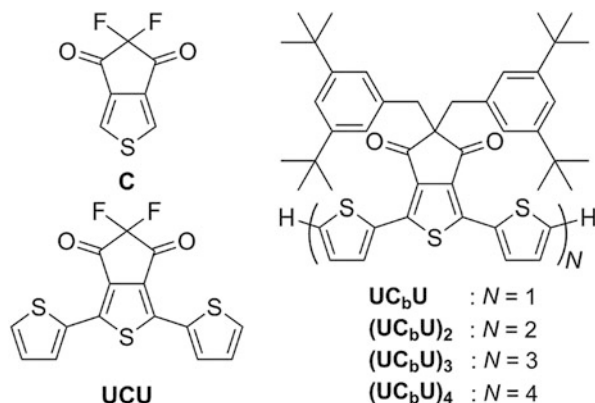


molecule conductance measurements of  $\text{NCS-}n\mathbf{T}^{\text{EH}}\text{-SCN}$  ( $n = 2\text{--}24$ ) using STM will reveal the crossover point between tunneling and hopping conductance.

## 5.6 Insulated Oligothiophenes with Electron-Affinity Characteristics

As mentioned above, Ie et al. have focused on a cyclopenta[*c*]thiophene framework bearing bulky substituents to accomplish insulation of  $\pi$ -conjugated backbones while maintaining effective conjugation. Although the energetic alignment between the work function of metal electrodes and the energy levels of molecular wire has been considered to influence the charge injection, little progress has been made in modification of electronic states in molecular wires. This is especially evident as development of molecular wires with electron-transport characteristics through their LUMO orbital has been limited to nonencapsulated  $\pi$ -conjugated systems [57–60]. Bearing this in mind, Ie et al. developed insulated oligothiophenes with electron affinity suitable for applications of electron-transporting molecular wires. The introduction of electron-withdrawing substituents into oligothiophenes has become a general technique to stabilize the LUMO energy level, leading to an increase in the electron affinity [61, 62]. Ie et al. (2008, 2009) [63, 64] have reported difluorodioxocyclopenta[*c*]thiophene (**C**) as a new electron-accepting unit and oligothiophenes based upon it as electron-transporting organic field-effect transistor materials (Fig. 5.21). It is expected that the replacement of the fluorine atoms in **C** with sterically bulky di-*t*-butylphenyl (DTBP) methyl groups [65, 66] would insulate the backbones while maintaining the electron-accepting properties. Based on this idea, insulated oligothiophenes ( $\text{UC}_b\mathbf{U}$ ) $_N$  ( $N = 1\text{--}4$ ) with high electron affinity (Fig. 5.21) were developed. To construct the key thiophene unit **C<sub>b</sub>**, the alkylation reaction of the 1,3-diketone was utilized. The repeating unit  $\text{UC}_b\mathbf{U}$  was synthesized by the Stille coupling reaction between the dibromo derivative of **C<sub>b</sub>** and tributylstannylthiophene. Palladium-catalyzed direct homocoupling of  $(\text{UC}_b\mathbf{U})_1$  gave extended products. The absorption maxima of  $(\text{UC}_b\mathbf{U})_N$  were redshifted with the chain extension. The plots of  $E$  against  $1/n$  showed

**Fig. 5.21** Chemical structures of **C**-, **UCU**-, and **C<sub>b</sub>**-containing oligothiophenes



linear relationships, indicating that effective conjugation was maintained in these oligomers. However, the quantitative evaluation was rather difficult due to the electronically nonequivalent repeating units [67, 68].

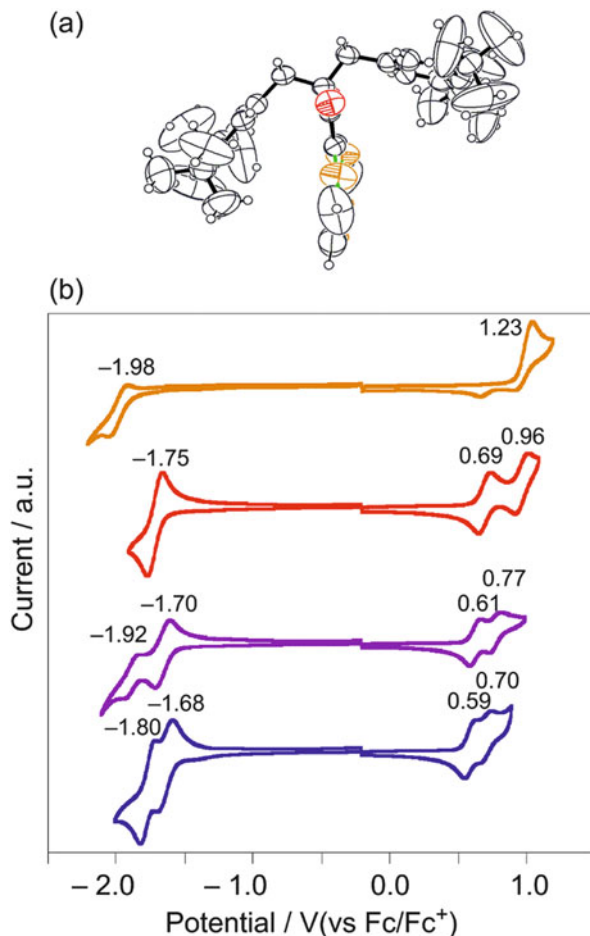
The X-ray crystal structure of **UC<sub>b</sub>U** showed the planar conformation for terthiophenes, irrespective of the introduction of DTBP groups (Fig. 5.22a). As expected, the DTBP groups were positioned perpendicular to the terthiophene unit, implying effective insulation of the conjugated backbone.

As evidenced in the CV measurements, all these oligomers (**UC<sub>b</sub>U**)<sub>N</sub> showed not only oxidation but also reduction processes (Fig. 5.22b). The appearance of reduction waves for these oligomers indicated that the presence of the **C<sub>b</sub>** unit contributed to increasing the electron affinity of the oligothiophene groups. In contrast to a quasi-reversible reduction wave and an irreversible oxidation wave for the CV of **UC<sub>b</sub>U**, the corresponding (**UC<sub>b</sub>U**)<sub>2</sub>, (**UC<sub>b</sub>U**)<sub>3</sub>, and (**UC<sub>b</sub>U**)<sub>4</sub> exhibited both reversible reduction and oxidation processes. Note that the formation of dianionic species was spectroscopically observed by reduction with potassium/graphite under inert conditions. However, the spectral pattern was too unstable to investigate the encapsulation effect. Thus, UV-vis-NIR measurements of radical cationic species (polarons) were performed to investigate the insulation effects of our-developed oligothiophenes. On one-electron oxidation of (**UC<sub>b</sub>U**)<sub>2</sub>, the  $\pi$ - $\pi^*$  transition band of the neutral species was replaced with two bands attributed to polarons. These two bands showed little difference between the spectra recorded at room temperature and at 233 K, which indicated that the presence of sterically bulky DTBP groups disturbed the formation of the  $\pi$ -dimer in (**UC<sub>b</sub>U**)<sub>2</sub><sup>•+</sup>.

## 5.7 Summary

In this chapter, I summarized a series of insulated oligothiophenes to apply to the single-molecule electronics. Especially, I focused on our-developed encapsulated oligothiophenes, whose structures are based on the combination of cyclopentene-

**Fig. 5.22** (a) Side view of X-ray crystal structure of  $\text{UC}_b\text{U}$ . (b) CVs of  $\text{UC}_b\text{U}$  (orange),  $(\text{UC}_b\text{U})_2$  (red),  $(\text{UC}_b\text{U})_3$  (purple), and  $(\text{UC}_b\text{U})_4$  (blue)



annulated thiophene and orthogonally oriented encapsulation units. The influence of the insulation on the molecular properties and single-molecule electrical conductance was investigated by spectroscopic measurements, electrochemical measurements, X-ray analyses, and STM-BJ techniques. All the data exemplified that there is no interruption of conjugation along the oligothiophene backbone. Furthermore, since single-molecule electrical conductance was obtained by the use of highly planar oligothiophenes in the absence of intermolecular interactions, our determined values could become a standard for forthcoming  $\pi$ -conjugated systems. Further studies on the design and synthesis of the molecular structures to gain insight into structure–property–function relationships will pave the way for the development of new insulated oligothiophenes in single-molecule electronics.

**Acknowledgments** My work summarized in this chapter was supported by Grants-in-Aid for Scientific Research from the Ministry of Education, Culture, Sports, Science and Technology, Japan. I greatly acknowledge all my coauthors listed in the references.

## References

1. D. Fichou (1999) In: Handbook of oligo- and polythiophenes. Wiley-VCH, Weinheim
2. Perepichka IF, Perepichka DF (2009) In: Handbook of thiophene-based materials. Wiley-VCH, Weinheim
3. Otsubo T, Aso Y, Takimiya K (2001) Synthesis, optical, and conductive properties of long oligothiophenes and their utilization as molecular wires. *Bull Chem Soc Jpn* 74:1789
4. Mishra A, Ma C-Q, Bäuerle P (2009) Functional oligothiophenes: molecular design for multidimensional nanoarchitectures and their applications. *Chem Rev* 109:1141
5. Rasmussen SC, Evenson SJ, McCausland CB (2015) Fluorescent thiophene-based materials and their outlook for emissive applications. *Chem Commun* 51:4528
6. Izumi T, Kobashi S, Takimiya K, Aso Y, Otsubo T (2003) Synthesis and spectroscopic properties of a series of b-blocked long oligothiophenes up to the 96-mer: reevaluation of effective conjugation length. *J Am Chem Soc* 125:5286
7. Sumi N, Nakanishi H, Ueno S, Takimiya K, Aso Y, Otsubo T (2001) Synthesis and properties of a series of the longest oligothiophenes up to the 48-mer. *Bull Chem Soc Jpn* 74:979
8. Ikemoto J, Takimiya K, Aso Y, Otsubo T, Fujitsuka M, Ito O (2002) Porphyrin-oligothiophene-fullerene triads as an efficient intramolecular electron-transfer system. *Org Lett* 4:309
9. Nakamura T, Fujitsuka M, Araki Y, Ito O, Ikemoto J, Takimiya K, Aso Y, Otsubo T (2004) Photoinduced electron transfer in porphyrin-oligothiophene-fullerene linked triads by excitation of a porphyrin moiety. *J Phys Chem B* 108:10700
10. Tanaka S, Yamashita Y (2001) Novel synthetic approach to 5-10 nm long functionalized oligothiophenes. *Synth Met* 119:67
11. Endou M, Ie Y, Kaneda T, Aso Y (2007) Synthesis of 10-nm scale oligothiophene molecular wires bearing anchor units at both terminal positions. *J Org Chem* 72:2659
12. Xu BQ, Li XL, Xiao XY, Sakaguchi H, Tao NJ (2005) Electromechanical and conductance switching properties of single oligothiophene molecules. *Nano Lett* 5:1491
13. Yasuda S, Yoshida S, Sasaki J, Okutsu Y, Nakamura T, Taninaka A, Takeuchi O, Shigekawa H (2006) Bond fluctuation of S/Se anchoring observed in single-molecule conductance measurements using the point contact method with scanning tunneling microscopy. *J Am Chem Soc* 128:7746
14. Hatanaka N, Endo M, Okumura S, Ie Y, Yamada R, Aso Y, Tanaka K, Tada H (2007) Electrical conductance measurement of oligothiophene molecular wires using nanogap electrodes prepared by electrochemical plating. *Chem Lett* 36:224
15. Yamada R, Kumazawa H, Nobutoshi T, Tanaka S, Tada H (2008) Electrical conductance of oligothiophene molecular wires. *Nano Lett* 8:1237
16. Yamada R, Kumazawa H, Tanaka S, Tada H (2009) Electrical resistance of long oligothiophene molecules. *Appl Phys Exp* 2:025002-1
17. Ie Y, Endou M, Lee SK, Yamada R, Tada H, Aso Y (2011) Completely encapsulated oligothiophenes: synthesis, properties, and single-molecule conductance. *Angew Chem Int Ed* 50:11980
18. Lee SK, Yamada R, Tanaka S, Chang GS, Asai Y, Tada H (2012) Universal temperature crossover behavior of electrical conductance in a single oligothiophene molecular wire. *ACS Nano* 6:5078
19. Capozzi B, Dell EJ, Berkelbach TC, Reichman DR, Venkataraman L, Campos LM (2014) Length-dependent conductance of oligothiophenes. *J Am Chem Soc* 136:10486

20. Ie Y, Endou M, Han A, Yamada R, Tada H, Aso Y (2012) Functional oligothiophenes toward molecular wires in single-molecular electronics. *Pure Appl Chem* 84:931
21. Schlüter AD, Rabe JP (2000) Dendronized polymers: synthesis, characterization, assembly at interfaces, and manipulation. *Angew Chem Int Ed* 39:864
22. Li W-S, Jiang D-L, Aida T (2004) Photoluminescence properties of discrete conjugated wires wrapped within dendrimeric envelopes: "dendrimer effects" on p-electronic conjugation. *Angew Chem Int Ed* 43:2943
23. Malenfant PRL, Groenendaal L, Fréchet JMJ (1998) Well-defined triblock hybrid dendrimers based on lengthy oligothiophene cores and poly(benzylether) dendrons. *J Am Chem Soc* 120:10990
24. Apperloo JJ, Janssen RAJ, Malenfant PRL, Groenendaal L, Fréchet JMJ (2000) Redox states of well-defined p-conjugated oligothiophenes functionalized with poly(benzyl ether) dendrons. *J Am Chem Soc* 122:7042
25. Tanaka S, Yamashita Y (1999) New building unit for rigid and coplanar oligo-aromatic molecular wires with insulating mantle. *Synth Met* 101:532
26. Wakamiya A, Yamazaki D, Nishinaga T, Kitagawa T, Komatsu K (2003) Synthesis and properties of novel oligothiophenes surrounded by bicyclo[2.2.2]octene frameworks. *J Org Chem* 68:8305
27. Nishinaga T, Wakamiya A, Yamazaki D, Komatsu K (2004) Crystal structures and spectroscopic characterization of radical cations and dications of oligothiophenes stabilized by annelation with bicyclo[2.2.2]octene units: sterically segregated cationic oligothiophenes. *J Am Chem Soc* 126:3163
28. Lee D, Swager TM (2003) Defining space around conducting polymers: reversible protonic doping of a canopied polypyrrole. *J Am Chem Soc* 125:6870
29. Lee D, Swager TM (2005) Toward isolated molecular wires: a pH-responsive canopied polypyrrole. *Chem Mater* 17:4622
30. Sugiyasu K, Honsho Y, Harrison RM, Sato A, Yasuda T, Seki S, Takeuchi M (2010) A self-threading polythiophene: defect-free insulated molecular wires endowed with long effective conjugation length. *J Am Chem Soc* 132:14754
31. Ie Y, Han A, Otsubo T, Aso Y (2009) Completely encapsulated oligothiophenes up to 12-mer. *Chem Commun.* 31:3020
32. Bidan G, De Nicola A, Enée V, Guillerez S (1998) Synthesis and UV-visible properties of soluble regioregular oligo(3-octylthiophenes), monomer to hexamer. *Chem Mater* 10:1052
33. Miller LL, Mann KR (1996)  $\pi$ -dimers and  $\delta$ -stacks in solution and in conducting polymers. *Acc Chem Res* 29:417
34. Kergueris C, Bourgoin J-P, Palacin S, Esteve D, Urbina C, Magoga M, Joachim C (1999) Electron transport through a metal-molecule-metal junction. *Phys Rev B* 59:12505
35. Kiguchi M, Ohto T, Fujii S, Sugiyasu K, Nakajima S, Takeuchi M, Nakamura H (2014) Single molecular resistive switch obtained via sliding multiple anchoring points and varying effective wire length. *J Am Chem Soc* 136:7327
36. Peng G, Strange M, Thygesen KS, Mavrikakis M (2009) Conductance of conjugated molecular wires: length dependence, anchoring groups, and band alignment. *J Phys Chem C* 113:20967
37. Luo L, Choi SH, Frisbie CD (2011) Probing hopping conduction in conjugated molecular wires connected to metal electrodes. *Chem Mater* 23:631
38. Murphy AR, Fréchet JMJ (2007) Organic semiconducting oligomers for use in thin film transistors. *Chem Rev* 107:1066
39. Dang MT, Hirsch L, Wantz G (2011) P3HT:PCBM, Best seller in polymer photovoltaic research. *Adv Mater* 23:3597
40. van Haare JAEH, Havinga EE, van Dongen JIJ, Janssen RAJ, Cornil J, Brédas J-L (1998) Redox states of long oligothiophenes: two polarons on a single chain. *Chem Eur J* 4:1509
41. Nakanishi H, Sumi N, Ueno S, Takimiya K, Aso Y, Otsubo T, Komaguchi K, Shiotani M, Ohta N (2001) Spectral properties of the longest oligothiophenes in the oxidation states. *Synth Met* 119:413

42. González SR, Ie Y, Aso Y, López Navarrete JT, Casado J (2011) The frontiers of quinoidal stability in long oligothiophenes: raman spectra of dicationic polaron pairs. *J Am Chem Soc* 133:16350
43. Yu Y, Gunic E, Zinger B, Miller LL (1996) Spectra and reactivity of methoxyoligothiophene cation radicals. *J Am Chem Soc* 118:1013
44. Graf DD, Campbell JP, Miller LL, Mann KR (1996) Single-crystal x-ray structure of the cation radical of 3',4'-dibutyl-2,5''-diphenyl-2,2':5',2''-terthiophene: definitive evidence for p-stacked oxidized oligothiophenes. *J Am Chem Soc* 118:5480
45. Graf DD, Daun RG, Campbell JP, Miller LL, Mann KR (1997) From monomers to p-stacks. A comprehensive study of the structure and properties of monomeric, p-dimerized, and  $\pi$ -stacked forms of the cation radical of 3',4'-dibutyl-2,5''-diphenyl-2,2':5',2''-terthiophene. *J Am Chem Soc* 119:5888
46. Bäuerle P, Segelbacher U, Gaudl K-U, Huttenlocher D, Mehring M (1993) Didodecylsexithiophene-a model compound for the formation and characterization of charge carriers in conjugated chains. *Angew Chem Int Ed* 32:76
47. Bäuerle P, Segelbacher U, Maier A, Mehring M (1993) Electronic structure of mono- and dimeric cation radicals in end-capped oligothiophenes. *J Am Chem Soc* 115:10217
48. Kaikawa T, Takimiya K, Aso Y, Otsubo T (2000) Synthesis and spectroscopic properties of [2.2]quinquethiophenophane as an ideal p-dimer model. *Org Lett* 2:4197
49. Satou T, Sakai T, Kaikawa T, Takimiya K, Otsubo T, Aso Y (2004)  $\alpha$ ,  $\omega$ -Bis(quinquethienyl)alkanes as a p-dimer model of polythiophene. *Org Lett* 6:997
50. Sakai T, Satou T, Kaikawa T, Takimiya K, Otsubo T, Aso Y (2005) Syntheses, structures, spectroscopic properties, and p-dimeric interactions of [n.n]quinquethiophenophanes. *J Am Chem Soc* 127:8082
51. Casado J, Takimiya K, Otsubo T, Ramírez FJ, Quirante JJ, Ortiz RP, González SR, Oliva MM, López Navarrete JT (2008) Raman spectroscopy shows interchain through space charge delocalization in a mixed valence oligothiophene cation and in its  $\Pi$ -dimeric biradicaloid dication. *J Am Chem Soc* 130:14028
52. Knoblock KM, Silvestri CJ, Collard DM (2006) Stacked conjugated oligomers as molecular models to examine interchain interactions in conjugated materials. *J Am Chem Soc* 128:13680
53. Yamazaki D, Nishinaga T, Tanino N, Komatsu K (2006) Terthiophene radical cations end-capped by bicyclo[2.2.2]octene units: formation of bent  $\pi$ -dimers mutually attracted at the central position. *J Am Chem Soc* 128:14470
54. Tateno M, Takase M, Iyoda M, Komatsu K, Nishinaga T (2013) Steric control in the  $\Pi$ -dimerization of oligothiophene radical cations annelated with bicyclo[2.2.2]octene units. *Chem Eur J* 19:5457
55. Ie Y, Okamoto Y, Tone S, Aso Y (2015) Synthesis, properties, and  $\pi$ -dimer formation behavior of oligothiophenes partially bearing orthogonally fused fluorene units. *Chem Eur J* 21:16688
56. Ie Y, Okamoto Y, Tone S, Honda Y, Tanaka S, Lee S. K, Ohto T, Yamada R, Tada H, Aso Y, in preparation
57. Ashwell GJ, Urasinska B, Wang C, Bryce MR, Grace I, Lambert CJ (2006) Single-molecule electrical studies on a 7 nm long molecular wire. *Chem Commun* 45:4706
58. Wang C, Batsanov AS, Bryce MR, Ashwell GJ, Urasinska B, Grace I, Lambert CJ (2007) Electrical characterization of 7 nm long conjugated molecular wires: experimental and theoretical studies. *Nanotechnology* 18:044005
59. Xu B, Tao NJ (2003) Measurement of single-molecule resistance by repeated formation of molecular junctions. *Science* 301:1221
60. Stadler R, Thygesen KS, Jacobsen KW (2005) Forces and conductances in a single-molecule bipyridine junction. *Phys Rev B* 72:241401-1
61. Facchetti A, Yoon MH, Stern CL, Hutchison GR, Ratner MA, Marks TJ (2004) Building blocks for N-type molecular and polymeric electronics. Perfluoroalkyl- versus alkyl-functionalized oligothiophenes (nts; n = 2-6). Systematic synthesis, spectroscopy, electrochemistry, and solid-state organization. *J Am Chem Soc* 126:13480

62. Yoon MH, DiBenedetto SA, Russell MT, Facchetti A, Marks TJ (2007) High-Performance n-channel carbonyl-functionalized quaterthiophene semiconductors: thin-film transistor response and majority carrier type inversion via simple chemical protection/deprotection. *Chem Mater* 19:4864
63. Ie Y, Umemoto Y, Okabe M, Kusunoki T, Nakayama K-i, Pu Y-J, Kido J, Tada H, Aso Y (2008) Electronegative oligothiophenes based on difluorodioxocyclopentene-annelated thiophenes: synthesis, properties, and n-type fet performances. *Org Lett* 10:833
64. Ie Y, Okabe M, Umemoto Y, Tada H, Aso Y (2009) Electronegative oligothiophenes having difluorodioxocyclopentene-annelated thiophenes as solution-processable n-type ofet materials. *Chem Lett* 38:460
65. Langlais VJ, Schlittler RR, Tang H, Gourdon A, Joachim C, Gimzewski JK (1999) Spatially resolved tunneling along a molecular wire. *Phys Rev Lett* 83:2809
66. Shi ZF, Wang LJ, Wang H, Cao XP, Zhang HL (2007) Synthesis of oligo(phenylene ethynylene)s with dendrimer "shells" for molecular electronics. *Org Lett* 9:595
67. Karsten BP, Viani L, Gierschner J, Cornil J, Janssen RAJ (2008) An oligomer study on small band gap polymers. *J Phys Chem A* 112:10764
68. Karsten BP, Viani L, Gierschner J, Cornil J, Janssen RAJ (2009) On the origin of small band gaps in alternating thiophene–thienopyrazine oligomers. *J Phys Chem A* 113:10343

# Chapter 6

## Synthesis and Physical Properties of Three-Dimensionally Insulated Molecular Wires

Jun Terao

**Abstract** Insulated conductive molecules, in which the  $\pi$ -conjugated compounds are covered by a cyclic protective sheath, have attracted considerable attention because of their potential applicability in next-generation molecular electronic devices. New methods of synthesizing three-dimensionally insulated  $\pi$ -conjugated molecules through the polymerization of insulated  $\pi$ -conjugated molecules as monomers are summarized. The obtained insulated molecular wires are highly soluble in organic solvents and have a high coverage ratio, rigidity, and photoluminescence efficiency; further, they show high charge mobility, even in the solid state. This chapter also highlights a new type of molecular wiring method based on the polymerization or copolymerization of an insulated  $\pi$ -conjugated monomer between nanosized electrodes.

**Keywords** Insulated molecular wires • Molecular electronic device • Rotaxane • Polyrotaxane • Permethylyated cyclodextrin • Charge mobility • Molecular wiring

### 6.1 Introduction

Inorganic semiconductor materials such as silicon are still major players in the fabrication of electronic devices in our modern information society. Computer innovations based on the integration of silicon semiconductors have greatly facilitated the expansion of our knowledge base, which in turn has significantly influenced our daily activities. However, the miniaturization of these systems is approaching fundamental limits due to the continuing decrease in feature size (Moore's law) [1]. Therefore, the development of innovative new devices using materials other than

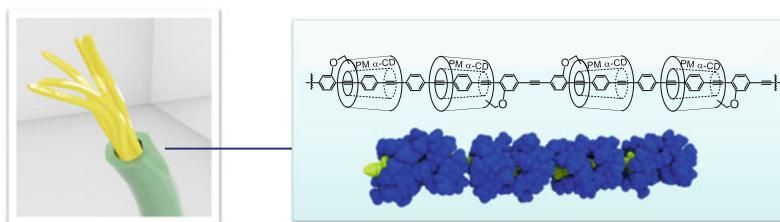
---

J. Terao (✉)

Department of Energy and Hydrocarbon Chemistry, Graduate School of Engineering,  
Kyoto University, Kyoto 615-8510, Japan  
e-mail: [terao@scl.kyoto-u.ac.jp](mailto:terao@scl.kyoto-u.ac.jp)

silicon is necessary for the continued advancement of these systems. The field of molecular electronics is the most promising area for further innovation in information technology [2, 3]. In molecular electronics, each functionalized molecule has the potential to behave as a single device, such as a switch, socket, memory, light emitter, diode [4], sensor, transistor [5], or photoelectric cell [6], which enables extensive integration and miniaturization [7]. To realize such molecular electronics, various functionalized molecules must be wired in between electrodes with nanosized gaps, in an efficient and dense fashion. Therefore, the development of techniques for the synthesis of definite-structure molecular wiring materials with appropriate functional groups and the development of an effective molecular wiring method are eagerly anticipated. In this context, this chapter focuses on the following: (1) the synthesis of functionalized insulated molecular wires possessing high linearity, rigidity, stability, and high charge mobility and (2) the establishment of wiring methods utilizing organic reactions such as cross-coupling or polymerization reaction in between nanosized gaps (Fig. 6.1).

### 1) *Synthesis of functionalized insulated molecular wire*



### 2) *New wiring methods utilizing polymerization between nanosized gap*

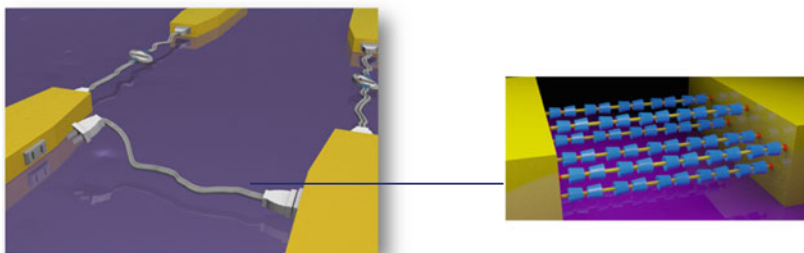


**Fig. 6.1** Synthesis of functionalized molecular wire and molecular wiring method by polymerization

## 6.2 Synthesis of Three-Dimensionally Insulated Molecular Wires

### 6.2.1 *Synthesis of Cyclodextrin-Based Insulated Molecular Wires*

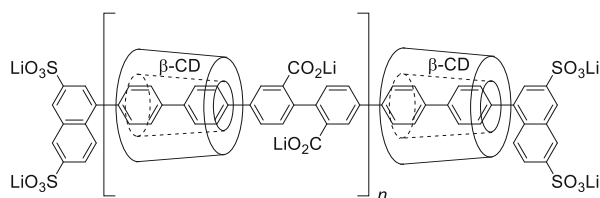
Organic semiconductor materials mainly made of carbon  $\pi$ -conjugated polymers, known as plastics that conduct electricity, have drawn attention because of their advantage in being more suitable than low-molecular organic compounds. Printing technology such as inkjet printing and rotary press can be used in their fabrication, so  $\pi$ -conjugated polymers are expected to reduce production cost. However, their charge mobilities, a parameter for carrier transport property, have not been comparable to those of silicon-based inorganic semiconductor materials. This is the biggest challenge in developing high-polymer materials for semiconductors, and the development of such materials with high charge mobility is being eagerly awaited. As one of the methods to solve these, research is actively conducted for insulating the conductive  $\pi$ -conjugated polymer chain one by one with insulation synthesizing chemically, as though a coated conductor wire is created [8–10]. This insulation reduces the interaction between the  $\pi$ -conjugated chains, and it is expected to provide stability to the conjugated chain along with improvement in solubility, fluorescence characteristics, and charge mobility characteristics of the conjugated chain. The synthetic method for insulated  $\pi$ -conjugated polymer (insulated molecular wire) is broadly classified into the method of sterically introducing bulky side chain to the  $\pi$ -conjugated polymer chain [11] and method of insulating the polymer chain three-dimensionally with cyclic molecules such as cyclodextrin (CD) [12] or cyclophane [13]. The former can impart solubility to the  $\pi$ -conjugated polymer chain, by sterically linking the bulky dendrimers with covalent bonds as the side chain and preventing contact between the  $\pi$ -conjugated polymer chains. Moreover, the constituent units of the insulated  $\pi$ -conjugated polymer synthesized by this method are unique, and the structural regularity is extremely high. The latter using the comparatively weak interactions of hydrophilic–hydrophobic interactions or coordination can efficiently coat the main chain three-dimensionally with cyclic compounds. This chapter explains the overview of the synthesis method for cyclodextrin-based insulated molecular wires and the physical properties.

It is known that water-soluble cyclic molecules capture organic molecules with hydrophilic–hydrophobic interactions forming rotaxanes (inclusion complexes) in water. Among these, water-soluble CD derivatives are easily available at low cost, and they are widely used as insulation molecules (host molecules) of various organic compounds. There are two methods for synthesizing insulated molecular wires using CD: the first method is to form polyrotaxane by inclusion of multiple CDs in the  $\pi$ -conjugated polymer chain and the second method is to form by the inclusion of  $\pi$ -conjugated monomer molecule in CD and the subsequent polymerization reaction.

Harada et al. were able to form polyrotaxane by stirring polyethylene glycol and CD in water and were successful in synthesizing molecular necklace [14, 15] and molecular tube [16]. Ito et al. found that insulated  $\pi$ -conjugated polymers with a pseudo-polyrotaxane structure are formed below 275 K by stirring the conductive polymer polyaniline and  $\beta$ -CD using *N*-methyl-2-pyrrolidinone (NMP) as the solvent [17–19]. This molecular wire dissociates into polyaniline and  $\beta$ -CD at 275 K or more. Moreover, even when cross-linked molecular tubes between CDs are used instead of CD, the polymer enters the tube holes and provides the same insulated  $\pi$ -conjugated polymer chain. The same technique, as will be explained later, has been applied to the insulated  $\pi$ -conjugated polymer chain synthesis of conductive polymers such as polythiophene. When polyaniline insulated molecular wires were placed on a microelectrode substrate having 100–200 nm electrode gap, with platinum as the electrode metal and thermal oxide film on the insulating substrate, using scanning probe microscope (SPM)-based lithography, the resistance was above a few T $\Omega$  when measured in vacuum. Moreover, the resistance value was approximately 47 K $\Omega$  and conductivity  $4 \times 10^{-2}$  S cm $^{-1}$  with the doping of the polyaniline chain. This value is comparable to the conductivity  $10^{-1}$  S cm $^{-1}$  of polyaniline in the bulk state [20].

Anderson et al. succeeded in the synthesis of water-soluble insulated  $\pi$ -conjugated polymers with the copolymerization reaction of pseudo-rotaxane monomer, obtained by the inclusion of  $\pi$ -conjugated monomer chain with boronic acid reaction points at both ends to CD in water and dihalides having a water-soluble functional group under the Suzuki–Miyaura coupling reaction conditions [21]. In this method, since it is carried out by sterically adding a bulky monohalide as a polymerization terminator, the molecular wire is obtained as a polyrotaxane structure having a stopper portion at both ends (Fig. 6.2); hence, the CD does not fall off. Since the feature of this method is to synthesize the  $\pi$ -conjugated chain using a polymerization reaction, it is possible to synthesize insulated molecular wires with different  $\pi$ -conjugated chains using monomers with various  $\pi$ -conjugated structures [22–24]. The resulting molecular wires show high fluorescence quantum yield compared to the corresponding  $\pi$ -conjugated polymers without insulation. That is, the respective  $\pi$ -conjugated polymer chains in the excited state exist independently because of the insulation, and this is considered to be due to the suppression of energy transfer between the chains.

**Fig. 6.2** Chemical structures of water-soluble insulated molecular wire by Suzuki coupling



## 6.2.2 Synthesis of Permethyated Cyclodextrin-Based Insulated Molecular Wires

Polyrotaxane insulated molecular wires are cyclic compounds containing  $\pi$ -conjugated polymer that can move relatively freely and can be moved along the main polymer chain. However, this shuttling may reduce the solubility of the polyrotaxane itself in addition to frequent aggregation of cyclic compounds leading the formation of  $\pi$ -conjugated part without insulation. Moreover, its poor structural regularity is an unfavorable factor for application to molecular electronics where synthesis of identical molecules with good reproducibility is required. Furthermore, when CD is used, ionic insulated  $\pi$ -conjugated polymers are formed due to the CD hydroxyl group, and removal of water molecules and salts influencing the conductivity are the issues faced when developing a device. Development of a nonionic  $\pi$ -conjugated polymer synthesis method with structural regularity and solubility which retains the properties of the  $\pi$ -conjugated polymer that is the main chain while achieving a high insulation for the main chain is required for the realization of molecular electronics using  $\pi$ -conjugated polymers.

One method to satisfy these requirements is to use permethylated cyclodextrin as a macrocycles for the synthesis of insulated molecular wire instead of native cyclodextrin. The methylation of all the hydroxyl groups of cyclodextrin provides permethylated cyclodextrin which has deeper vacancy and higher solubility in organic solvents as compared to the native cyclodextrin. New synthetic route to organic-soluble insulated molecular wires is shown in Fig. 6.3. The self-inclusion of guest-branched permethylated cyclodextrin forms pseudo-rotaxane [25], which is capped with a stopper molecule to afford a linked [2]rotaxane ([1]rotaxane). Polymerization sites are introduced at both ends of this rotaxane to form a fixed [2]rotaxane monomer. Then, this monomer is polymerized to afford  $\pi$ -conjugated polyrotaxane as an organic-soluble insulated molecular wire [26].

Crystals of fixed [2]rotaxane were grown from a mixture of DMSO and H<sub>2</sub>O. The X-ray structure is shown in Fig. 6.4. It is clear that the permethylated cyclodextrin is displaced from the center of the guest moiety, and the main axis of the guest exhibits a slight torsion.

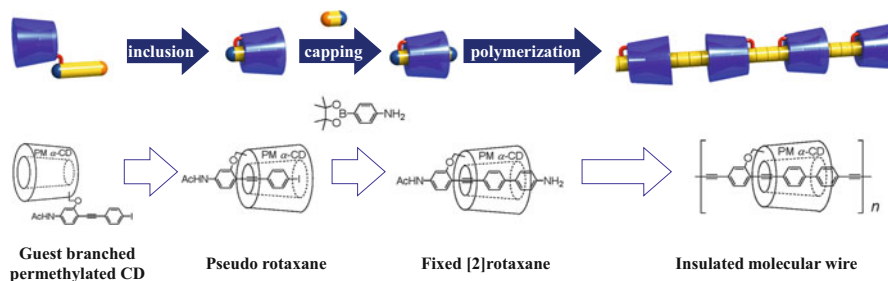
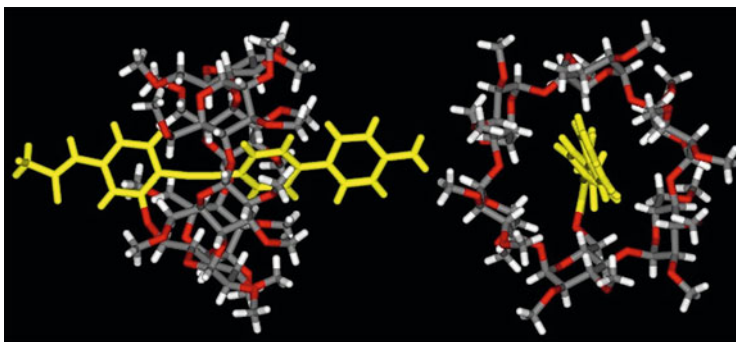
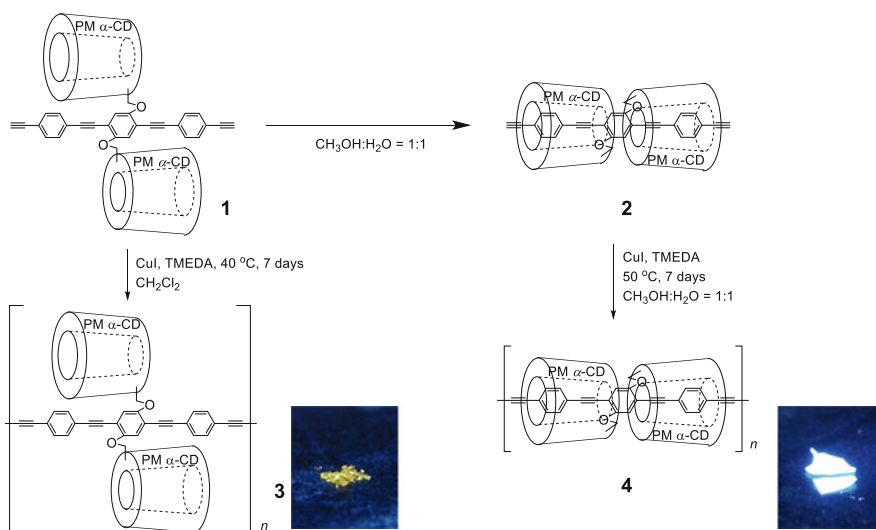


Fig. 6.3 Synthetic route to permethylated cyclodextrin-based insulated molecular wire

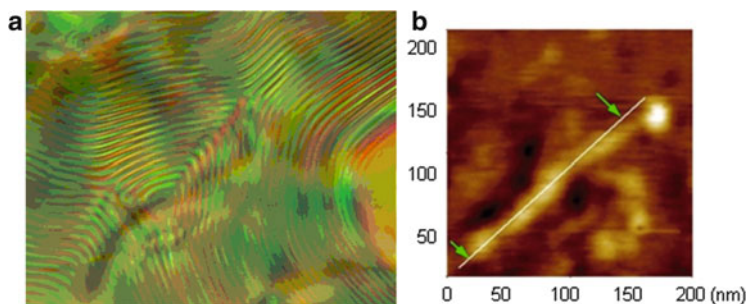


**Fig. 6.4** X-ray crystallographic structure of fixed [2]rotaxane



**Fig. 6.5** Selective synthesis of insulated and uninsulated molecular wires

To decrease the number of reaction steps and increase coverage, a simple methodology for the synthesis of regioregular insulated molecular wires by polymerization of pseudo-linked [3]rotaxane monomer **2** by sequential intramolecular self-inclusion of a phenylene ethynylene oligomer with two permethylated cyclodextrins was developed (Fig. 6.5) [27, 28]. In order to examine the covering effect of permethylated cyclodextrin, an uncovered polymer **3** was also synthesized as a reference by the polymerization of **1** in a lipophilic solution ( $\text{CH}_2\text{Cl}_2$ ) instead of a hydrophilic solution (1:1  $\text{CH}_3\text{OH}:\text{H}_2\text{O}$ ) [29]. The absolute quantum yields of **3** and **4** were determined using a calibrated integrating sphere system. The fluorescence quantum yields of **4** revealed that its fluorescence efficiency was better than that of **3**, particularly in the solid state.



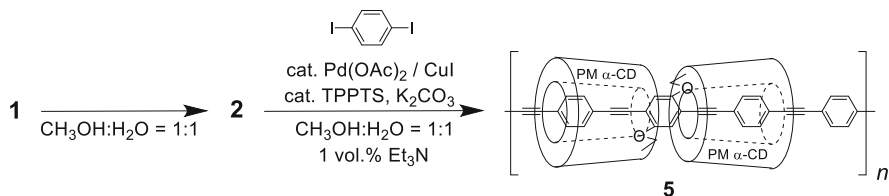
**Fig. 6.6** (a) Polarized optical micrographs of **4** in  $\text{CHCl}_3$  solution, (b) tapping-mode AFM topographic image of **4** on a mica substrate [29]

Figure 6.6a shows polarized optical micrographs of **4** in concentrated  $\text{CHCl}_3$  solutions. It should be noted that **4** forms a cholesteric phase, as confirmed from its indisputably clear fingerprint texture, while **3** forms only an isotropic liquid even at high concentrations. The observed cholesteric phase can be attributed to the presence of permethylated cyclodextrin in **4** since a nematic LC phase should be observed if a polymer chain threads through achiral macrocycles. This is the first report of the formation of a cholesteric LC phase whose chirality originates from the inclusion of a polymer main chain into the permethylated cyclodextrin cavity. The morphology of **4** was investigated by performing AFM experiments using cleaved mica substrates (Fig. 6.6b). Highly dilute solutions of high-molecular-weight **4** that was separated by GPC (gel permeation chromatography) were used to avoid the aggregation of individual assemblies. From the AFM image and a section analysis, the expected average contour length and height of the polymer chains were determined to be  $\sim 200$  nm and  $\sim 1.5$  nm, which is equal to the outer diameter of the free permethylated cyclodextrin calculated using the CPK model.

### 6.2.3 Synthesis of Insulated Molecular Wires with High Charge Mobility

To increase the effective conjugation length in the core molecules, polyrotaxane **5**, with only a poly(phenylene ethynylene) (PPE) backbone, was synthesized by the Sonogashira copolymerization of **2** with 1,4-diiodobenzene (Fig. 6.7).

The kinetic traces of the transient conductivity and optical absorption of **5** upon irradiation by UV light (355 nm) were examined. For the quantitative analysis of photogenerated charge carriers, *N,N*-bis(2,5-di-*tert*-butylphenyl)-3,4,9,10-perylene-dicarboximide (PDCI) was used as an electron acceptor because of its high extinction coefficient in the radical anion form ( $\epsilon\text{-PDCI}^{\cdot-} = 7.4 \times 10^4 \text{ cm}^{-1} \cdot \text{mol}^{-1} \cdot \text{dm}^3$ ). The excellent correlation between the two transients clearly suggests that the positive charge on the  $\pi$ -conjugated core



**Fig. 6.7** Synthesis of insulated molecular wire bearing PPE backbone unit

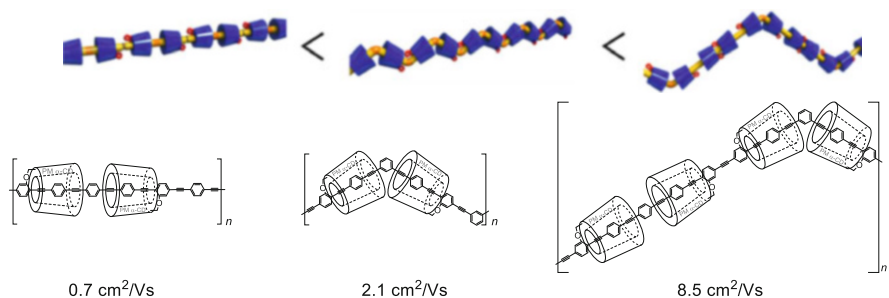
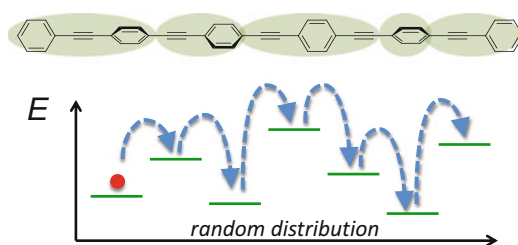


**Fig. 6.8** Structures of linear and twisted insulated molecular wires bearing PPE backbone unit

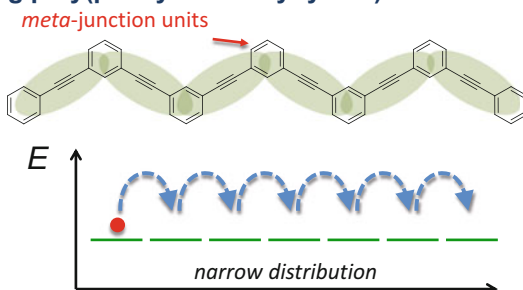
of the molecules in **5** contributed to the high conductivity of this compound over the entire time range. It is noteworthy that the minimum value of anisotropic hole mobility ( $\mu^+$ ) in the core estimated from the maximum value of the quantum yield of charge carriers ( $\phi$ ) ( $3.4 \times 10^{-4}$ ) was  $0.5 \text{ cm}^2 \text{ V}^{-1} \text{ s}^{-1}$ . This is the first report of the formation of an almost perfectly insulated organic semiconductor wire in which the hole mobility along the  $\pi$ -conjugated polymer chain is extremely high and is comparable to that of amorphous silicon [30, 31]. To achieve much higher charge mobilities in the polymer chain, a new strategy to achieve efficient charge hopping has been developed by regularly localizing polymer molecular orbitals to achieve an ideal orbital alignment and, at the same time, by equalizing energy strength and making use of thermal energy. To test this theory, defect-free insulated molecular wires with meta-junctioned poly(phenylene ethynylene) as the backbone units were synthesized to equalize the distance and molecular orbital levels between the hopping sites. Rewardingly, the twisted insulated molecular wire exhibited a higher intramolecular charge mobility ( $2.1 \text{ cm}^2 \text{ V}^{-1} \text{ s}^{-1}$  is the first time that intramolecular charge mobility above  $1 \text{ cm}^2 \text{ V}^{-1} \text{ s}^{-1}$  has been achieved as charge carrier hopping processes in  $\pi$ -conjugated polymers) along the designed  $\pi$ -conjugated polymer chain compared with that of the corresponding linear wire (Fig. 6.8). This was probably because uncontrolled structural deformations owing to rotation and fluctuation in linear  $\pi$ -conjugated polymers will result in widely distributed orbital levels, which should be disadvantageous for charge mobility via hopping processes. On the other hand, *meta*-junction units regularly break the orbital delocalization resulting in a narrow distribution of the orbital levels, which

**Fig. 6.9** Schematics of the orbital distribution and orbital localization in the linear and twisted PPE

### Linear poly(phenylene–ethynylene)



### Zigzag poly(phenylene–ethynylene)



should be suitable for efficient charge hopping processes, like in the crystal structure of pentacene (Fig. 6.9). Interestingly, when the length of the insulated para-segments in the twisted insulated molecular wire was increased to ten phenylene ethynylene units, an intramolecular charge mobility of  $8.5 \text{ cm}^2 \text{ V}^{-1} \text{ s}^{-1}$  was obtained [32]. It was determined that an increase in the planarity of the meta-junctioned systems with an increase in the number of phenylene ethynylene units plays an important role in the enhancement of the charge mobility, and the longer para-segments also enhance the charge mobility via a coherent charge transport process. It is important to note that the value of  $8.5 \text{ cm}^2 \text{ V}^{-1} \text{ s}^{-1}$  for intramolecular charge mobility in the cross-boundary range of hopping and band transport is comparable to the highest value in amorphous silicon ( $1\text{--}10 \text{ cm}^2 \text{ V}^{-1} \text{ s}^{-1}$ ). The application of this technology to  $\pi$ -conjugated polymer backbones will lead to the possible creation of  $\pi$ -conjugated polymers with higher charge exchange. Insulated  $\pi$ -conjugated polymers are expected to be used as organic semiconductor materials and wires in molecular devices.

#### 6.2.4 Synthesis of Functionalized Insulated Molecular Wires

For use as wiring materials, molecular wires must satisfy two requirements: (I) compatible processability resulting from high solubility and defined molecular structure and (II) appropriate material properties such as high linearity, rigidity,

and, in particular, high conductivity. As described above, the synthesis of insulated molecular wires which adequately satisfied properties (I) and (II) was developed; in these wires, the conjugated moieties were isolated through insulation using CD derivatives [33, 34]. However, it is not necessary for molecular wiring materials to strictly mimic their conventional inorganic counterparts. In other words, molecular wires that contain stimuli-responsive units in their polymer chains are expected to perform as higher-order nanodevices owing to their functionalities; i.e., electrodes connected to functionalized molecular wires could exhibit not only conductivity but also physical property change by external stimuli. In order to synthesize functionalized insulated molecular wires by copolymerization of insulated monomer with various functionalized monomers, the insulated OPE **6** as a monomer having a fixed [3]rotaxane structure in the organic solvents was employed. The synthesis of defect-free insulated poly(phenylene ethynylene) (PPE) was executed via Sonogashira copolymerization of **6** with 1,4-diiodobenzene in the presence of a catalytic amount of  $\text{Pd}_2(\text{dba})_3$  and  $\text{PPh}_3$  in the organic medium ( $\text{THF}/\text{Et}_3\text{N} = 2/1$ ). This method was subsequently applied to the synthesis of functionalized insulated molecular wires **7a–e** by Sonogashira copolymerization of **6** with functionalized dihalides having a tetrathiafulvalene (TTF) unit as a redox group, a porphyrin unit as a metal ion-sensing group, and an azobenzene or diarylethene unit as a photoswitching group (Fig. 6.10) [35].

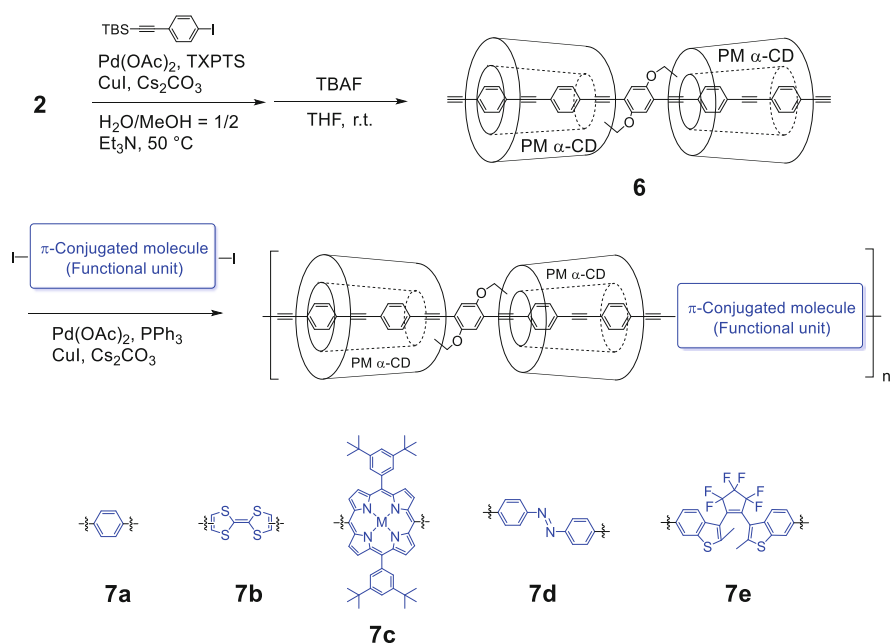


Fig. 6.10 Chemical structures of functionalized insulated molecular wires **7**

A significant fluorescence enhancement in response to oxidation was observed for the insulated molecular **7b** wire bearing tetrathiafulvalene units as compared with the corresponding uninsulated molecular wire. The porphyrin insulated molecular wire **7c** switches conductivity in response to variation of the coordinated metal ion and to the absence or presence of a metal ion. The insulated monomer unit prevents the  $\pi$ -stacking of the conjugated main chains, even in the solid phase, leading to prolongation of the lifetime of the charged radicals on the conjugated backbone through blockage of the charge recombination processes. Conformational changes of the azobenzene insulated molecular wire **7d** in response to sequential irradiation with UV and visible light were clearly observed by AFM measurements and are believed to result because encapsulation of the  $\pi$ -conjugated polymer chains precludes a high degree of aggregation through a decrease in the strong interactions between the  $\pi$ -conjugated chains.

### 6.2.5 *Synthesis of Insulated Metallopolymers*

Over the past few decades, many scientists have focused on the integrated property of molecular wires and metal elements, and the synthesis and properties of conjugated metallowires have gained considerable importance [36–40]. The transition metal complexes are directly inserted into their conjugated main chains producing interesting phosphorescent [41, 42], magnetic [43, 44], and redox behaviors [45, 46] in addition to the reversibility derived from d-electrons or coordination bonding [47]. In conjugated metallowires, transition metal complexes strongly affect  $\pi$ -conjugation because they are placed in between the conjugated wire backbones [48]. Further, conjugated metallowires promise higher-order, unique functionalized materials that have novel properties combined with those of the conventional  $\pi$ -conjugated materials. However, the unique electronic properties of the metal complexes are known to decrease their solubility because of metal–metal interactions and the polycation state. Typical metallowires have very low solubility and can exist only as solids in their crystal packing state [39]. The limitations of conjugated metallowires render their usage as practical functionalized materials difficult. Overcoming these drawbacks can produce highly functionalized materials with excellent physical properties and high processability, such as wet processing. In recent decades, a number of insulated conjugated metallowires have been successfully synthesized and interesting properties have been reported. In addition to the conventional features derived from  $\pi$ -conjugation and transition metals, their insulated structures can compensate for solubility, a disadvantage in conventional metallowires, and enhance their stability and functionalities, such as sensing and luminescence.

Schanze et al. demonstrated the effect of insulation on the phosphorescent behavior of platinum acetylide wires **8** because of its bulky side chains [49] (Fig. 6.11). Launay et al. reported an insulation behavior of metallowire **9a** bearing coordination bonds, wherein bulky Ru(II) porphyrins on the outer edges, closely connected by

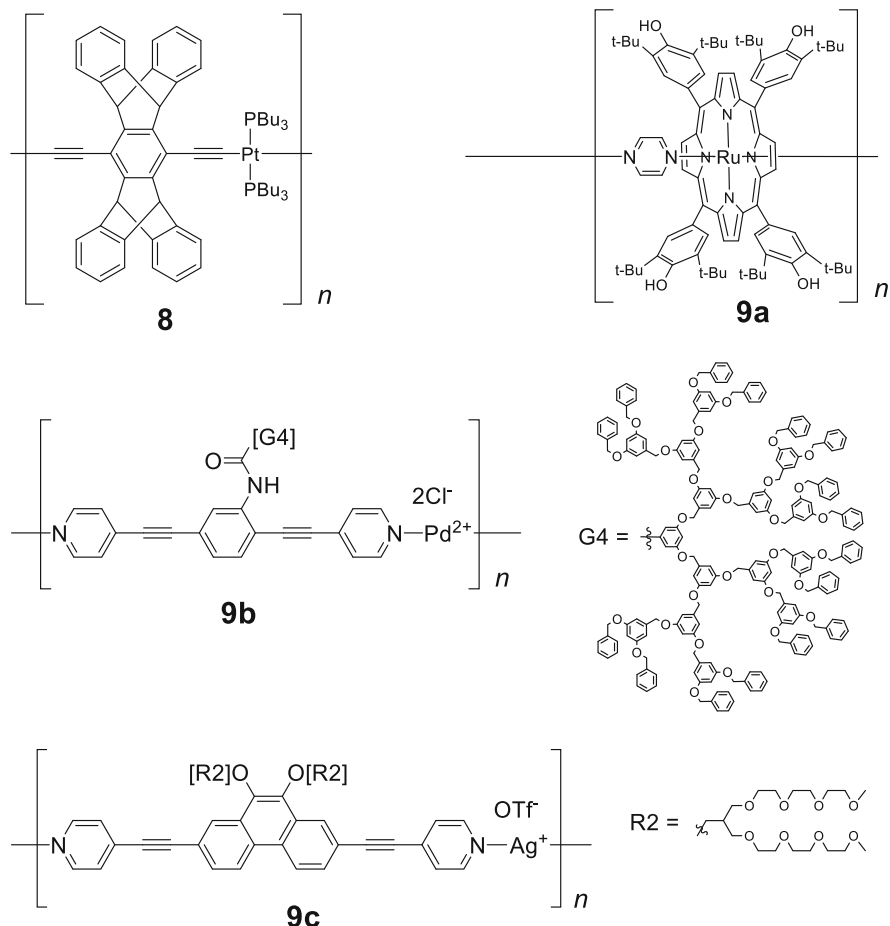


**Fig. 6.11** Chemical structures of insulated metallowires wires with bulky side chains

short bridging ligands, exhibited an insulation effect, as the interactions between the oxidant and the polymer backbone consisting of metals and bridging ligands were inhibited [50]. These results indicated the protective effects of other reagents or interactions on the metallowires. A coordinative metallowire **9b** composed of Ag(I)–pyridyl bonds covered with dendrons, displaying depolymerization by the cleavage of the coordination bonds, was reported, unusual to the nature of the coordinative metallowire [51]. Lee et al. reported an insulated metallowire **9c** with Ag(I)–pyridyl bonds that showed interconversion between the gel and the nematic phases, triggered by an external solvent system through weak interactions of the exposed Ag(I) ions [52]. These wires were significantly affected by the external environment, peculiar to the nature of coordination bonds.

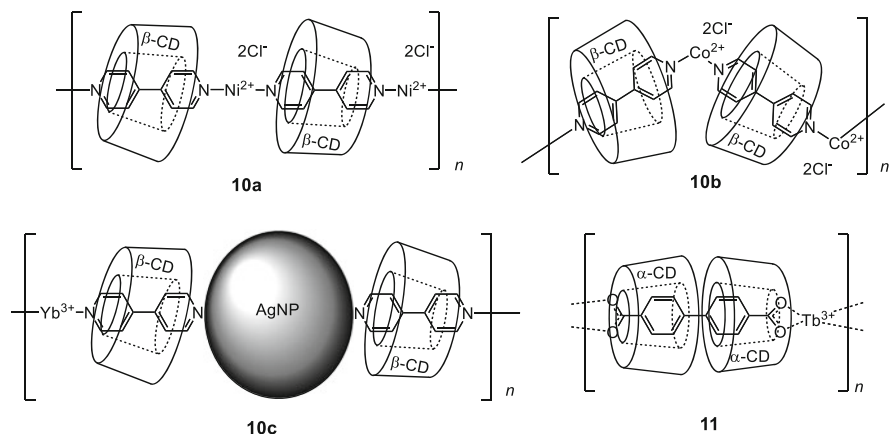


**Fig. 6.12** Chemical structures of insulated metallowires with macrocycles

Liu et al. reported the first coordinative metallowire with conjugated chains insulated by cyclic molecules (Fig. 6.12) [53]. The host–guest inclusion complex between  $\beta$ -CD and 4,4'-bipyridine, based on hydrophilic–hydrophobic interactions in water, was then subjected to coordination polymerization with one equivalent of  $\text{NiCl}_2 \cdot 6\text{H}_2\text{O}$  to form an insulated metallowire **10a** with pyridyl–metal coordination bonds. The effect of the various types of cyclodextrins, metals, and counter-anions on the insulated metallowires was reported [54]. They demonstrated that the counter-anion sensing for chloride by the metallowires **10b** was attributed to the limited space between the CDs that disturbed the coordination between the  $\text{Co}(\text{II})$  ions and water [55]. Li and coworkers reported another functionalized material using Liu's strategy [56]. The color of the solution of the modified Ag nanoparticles with the inclusion complex in water was selectively changed to a metallowire **10c** by  $\text{Yb}(\text{III})$  among seven other lanthanide ions owing to its small ionic radius. Shinkai et al. reported a  $\text{Tb}(\text{III})$ -based insulated metallowire **11** with carboxylate–metal coordination bonds, as a chiral sensing material, estimated to stem from the steric repulsion of  $\text{D/L}$ -tartaric acids around  $\text{Tb}(\text{III})$  ions induced by the chiral  $\alpha$ -CDs [57].

### 6.2.5.1 Synthesis of Solid-State Phosphorescence Insulated Metallopolymers

Transition metal complexes have gained importance as components for light-emitting diodes (LEDs) [41, 58, 59] and in optical sensing [60, 61] and bio-imaging [62] devices because of their highly effective and long-wavelength phosphorescence at room temperature. In the solid state, they are expected to produce higher-density phosphorescent materials, which will display brighter emissions per unit volume than their dilute counterparts [63]. However, their desirable phosphorescence in the

solid state decreases or changes drastically [64, 65] as a result of their indiscriminate molecular interactions with adjacent molecules [66]. Therefore, they exhibit high performance only under highly dilute conditions (such as in a matrix with a very low doping concentration). Several examples of exceptional solid-state phosphorescence have been achieved through the adequate control of molecular arrangements or the inhibition of undesirable molecular interactions in crystalline systems [67–69]. However, the simple concentration of diluted phosphorescent materials cannot increase their emission densities, but rather can lead to unpredictable changes in emission behavior [70–73]. As practical device materials, polymers are of interest owing to their high processability and thermodynamic stability as compared with low-molecular-weight materials. However, their intrinsic disorder in the solid state, which is due to their high degrees of freedom, makes it difficult to organize a well-ordered structure, such as in the crystalline solid state. For this reason, applications of phosphorescent polymer materials have been limited to highly diluted systems, which are usually formed by doping a polymer matrix or through copolymerization with a low mixing ratio [74]. Thus, to achieve high-density phosphorescence in polymer solid materials, two contradictory requirements must be simultaneously satisfied: (i) a higher concentration for brighter emission and (ii) a lower concentration to inhibit molecular interactions. Nevertheless, because of their potential application in solid-state phosphorescent polymer devices, the development of such materials has been eagerly pursued; the insights obtained would contribute to progress in the field of device science. By using macrocycles for higher-order inhibition, only the desired area of a polymer chain can be covered, without any interstitial space, to achieve higher-density phosphorescence. In 2014, poly(phenylene ethynylene) (PPE), covered with permethylated cyclodextrin, omnidirectionally insulated metallopolymers composed of platinum acetylide, and oligoPE as the polymer backbone was synthesized (Fig. 6.13) [75, 76]. Two unprecedented cyclic insulation effects on the phosphorescence behavior of the metallopolymers are described: (i) the cyclic insulation enhances phosphorescence and (ii) identical phosphorescence behaviors are observed in the high-density solid state as well as in dilute solution. The uninsulated platinum acetylide polymer **12** was synthesized by copper-catalyzed transmetalation of **1** with trans-PtCl<sub>2</sub>(PEt<sub>3</sub>)<sub>2</sub> in a hydrophobic solvent (piperidine). The corresponding insulated polymer **13** was obtained from the same monomers in the hydrophilic solvent, MeOH/H<sub>2</sub>O (2:1), from insulated complex **2**. To examine the effects of the cyclic insulation area and PE units, insulated polymer **14** was also synthesized from **6** bearing different oligoPE units. As expected, **13** displays a strong orange emission. In contrast, uninsulated polymer **12**, which exhibited phosphorescence in dilute solution, shows very weak phosphorescence in the solid state, despite its bulky permethylated cyclodextrin side chains which cover the polymer backbone (Fig. 6.13). These results indicate that the insulation in polymer **13** prevents interactions with adjacent molecules, even in the solid state, achieving high-density phosphorescence. Because **13** also tolerated oxygen, as described above, it even exhibits phosphorescence in the solid state under an air atmosphere. In contrast, despite its insulation, **14** does not show any phosphorescence in the solid state, but only fluorescence. The

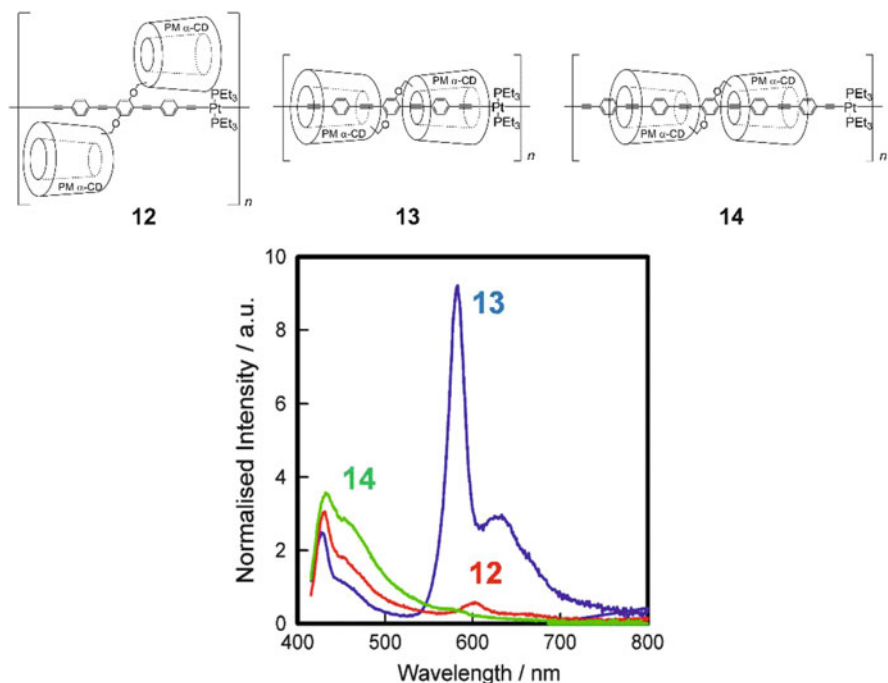


**Fig. 6.13** Emission spectra of polymer solids of **12** (red), **13** (blue), and **14** (green) under degassed conditions (excitation: 405 nm) [76]

triplet-state quenching observed in the polymer **14** solid should be caused by intermolecular interactions, similar to the case of **12**, because **14** also displayed phosphorescence in dilute solution. Higher-order inclusion effects were observed on the phosphorescence behavior of platinum acetylide polymers fully covered with permethylated cyclodextrins. To our knowledge, this is an unprecedented example which integrates the features of phosphorescence and rotaxane structure. Complete three-dimensional insulation generated almost identical phosphorescence emission behaviors in solid systems as in dilute solutions because of protection from all interactions. Moreover, such insulation also led to oxygen tolerance: phosphorescence was observed under an air atmosphere in the solid state. This is the first example of the unimolecular phosphorescence of a polymer material in the high-density solid state.

### 6.2.5.2 Synthesis of One-Dimensional Insulated Coordination Polymers

One-dimensional coordination polymers containing transition metals, which combine the advantages of organic insulated molecular wires mentioned above, with those of transition metal complexes have recently received much attention [77].

They are expected to form wiring materials with novel properties including (1) various characteristics derived from the transition metal complexes such as redox behavior and triplet-state properties and (2) enhanced processability such as recyclability and self-healing through reversible monomer–polymer interconversion brought on by the reversible nature of the non-covalent bonds as opposed to covalently bonded molecular wires. Insulated molecular wire **17** displayed novel processability as a result of its non-covalent bonding motif that was synthesized through the coordination polymerization of Ru(II) porphyrin complex **16** with insulated bridging ligand **15** having well-defined structures [78]. A remarkable property of coordination polymer **17** is its interconversion between monomer and polymer states under certain conditions due to the reversibility of its coordinate bonds (Fig. 6.14). Carbon monoxide (CO) underwent ligand exchange with the pyridyl groups on Ru(II) porphyrin complexes of **17**, because of its stronger coordination ability, thereby yielding monomers **15** and **16**. The resulting monomeric porphyrin complex was expected to subsequently release CO upon UV irradiation to reform **17**. Although **17** was stable in toluene/EtOH even at 55 °C, decomplexation into monomers **15** and **16** occurred with 1 atm of CO, as confirmed by size-exclusion chromatography. Recomplexation of the air-stable monomers could subsequently be induced by UV irradiation of the resulting solution. The degree of polymerization after recomplexation was perfectly consistent with that before decomplexation. Thus, in spite of the stability of **17** and its monomeric components under normal conditions, monomer-to-polymer interconversion could be induced under specific conditions, i.e., either 1 atm of CO or UV irradiation. This property is unique to metal-containing molecular wires bearing coordinate bonds and may be applied in molecular wiring applications such as recycling and self-healing of wiring materials, in addition to as sensory materials for CO.

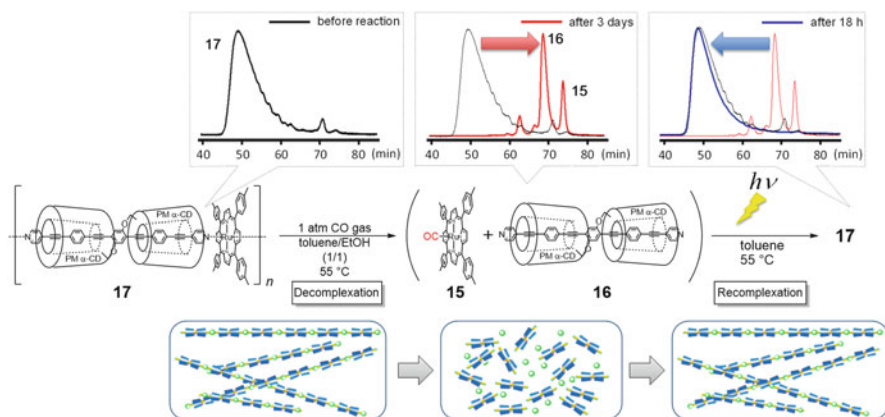


**Fig. 6.14** Schematic and SEC monitoring of polymer–monomer interconversion (eluent: THF) [78]

### 6.3 The Establishment of Wiring Methods Utilizing Organic Reactions Between Nanosized Gaps

The fabrication of molecular devices that use organic molecules, such as  $\pi$ -conjugate polymers and DNA, and carbon compounds, such as carbon nanotubes, as wiring materials is currently being widely studied [79, 80]. Three types of single molecular junction methods have been reported thus far: the break junction method, which is the connection of conjugated molecules via sulfur in the nanogap formed by bending a thin line made of gold; the electrostatic orientation method, which establishes a connection between DNA-coated nanoelectrodes using an electric field; and the junction method, which involves the vacuum deposition of carbon nanotubes over nanoelectrodes (though the probability of achieving a junction is low with this method). Many problems exist with such physical wiring methods including the low obtained current values, extremely low reproducibility, and small number of molecular line connection. A method for connecting conjugated molecules using a thiol group on both ends of the nanoelectrodes, by forming gold and sulfur bonds, with chemisorption of thiol groups on gold has been used for this purpose. However, there are issues, such as low probability and reproducibility of line connections because of (i) poor bonded sections reacting on the same electrodes (because the directionality and linearity of the conjugated chains are low), (ii) aggregation of conjugated chains due to  $\pi$ - $\pi$  interactions, and (iii) occupation of chemisorption sites by heteroatomic species before a bridge can be formed; low transfer efficiency due to electron hopping between conjugated chains; and difficulty in fabricating nanoelectrodes with identical gaps (because conjugated chains corresponding to the electrode distance must be synthesized) [81, 82]. This research will make molecular junctions that do not rely on the distance between electrodes possible, by performing synthesis reactions in the nanospace between them. This buildup method involves the assembly of conjugated molecular units that are shielded from the electrode surfaces. In other words, there will be no need to fabricate or synthesize nanoelectrodes and wiring molecules of the same lengths. It will become possible to perform wiring simultaneously and with greater numbers of conjugated molecules than conventional methods because molecular junctions will be formed by chemical reactions. High conductivity is expected because charge transfers should only occur within conjugated chains, because the chains are shielded and no aggregations should develop between them. Furthermore, applications for practical electrically conductive luminescent materials are expected, because the conductivity and fluorescence quantum yield will increase because of the independent nature of the conjugated polymer chains. The application of spin coating or inkjet methods, which are cheap manufacturing processes, will be possible because the materials are soluble in most organic solvents.

In 2006, Taniguchi et al. developed a new wiring method for fabricating nanosized photoswitching devices (Fig. 6.15) [83]. In this process, electrodes with nanosized gaps were sequentially dipped into a solution of benzenethiol possessing a reactive site, immersed into a solution of wiring molecules, and finally exposed

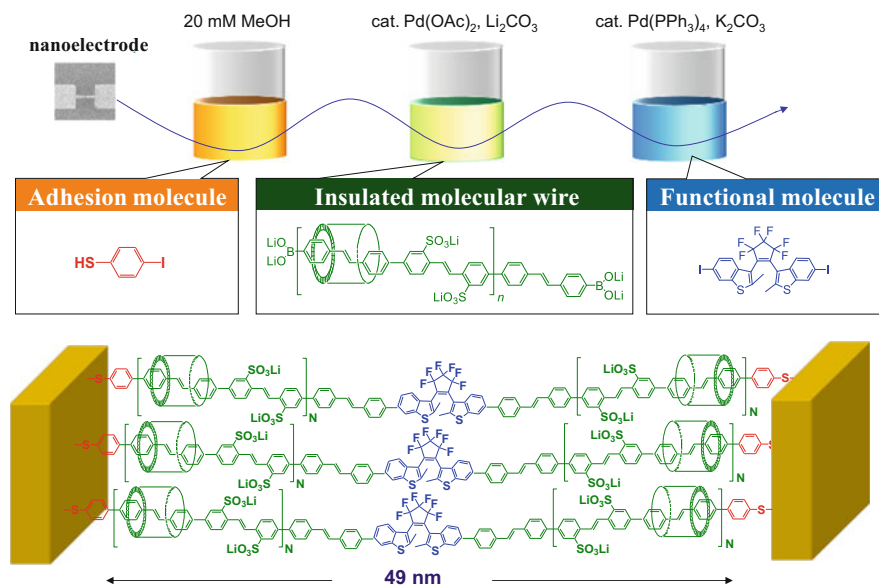


**Fig. 6.15** Schematic images of the molecular wiring between nanogaps via sequential Suzuki coupling reaction

to a solution of functional molecules; the three molecules were then connected via a transition metal-catalyzed cross-coupling reaction. The key to the success of this method lies in the use of CD-based  $\pi$ -conjugated polyrotaxane as the wiring molecule to maintain structural linearity and isolate the  $\pi$ -conjugated polymer chain.

However, this “buildup” method was limited because the synthesis of molecular wires with defined lengths and the fabrication of nanosized electrodes of appropriate lengths were elaborate processes. Therefore, it would be ideal to develop a new wiring method that would be independent of the lengths of the molecular wires and the gaps [84]. To overcome these issues, attempts were made to wire between the nanogaps by polymerizing the insulated monomer **6**, which was characterized by excellent organic solubility and a high coverage ratio and linearity (Fig. 6.16) [85]. Nanosized electrodes with a 20 nm gap were fabricated via electron beam lithography and a lift-off process, using a silicon dioxide layer and gold/titanium electrodes. The fabricated electrode was then dipped into 4 mM 1,2-bis(4-ethynylphenyl)diselenide **18** in dichloromethane to form a Au–Se bond by chemical adsorption, which could serve as a reaction site. After washing with dichloromethane, the surface-modified nanosized electrode was placed in a dichloromethane solution of **3** and stirred for 2 days under Hay coupling conditions to elongate the  $\pi$ -conjugated chain from the surface of the nanosized electrodes, followed by washing. GPC analysis of the solution after the wiring reaction showed that **3** disappeared completely and confirmed that the

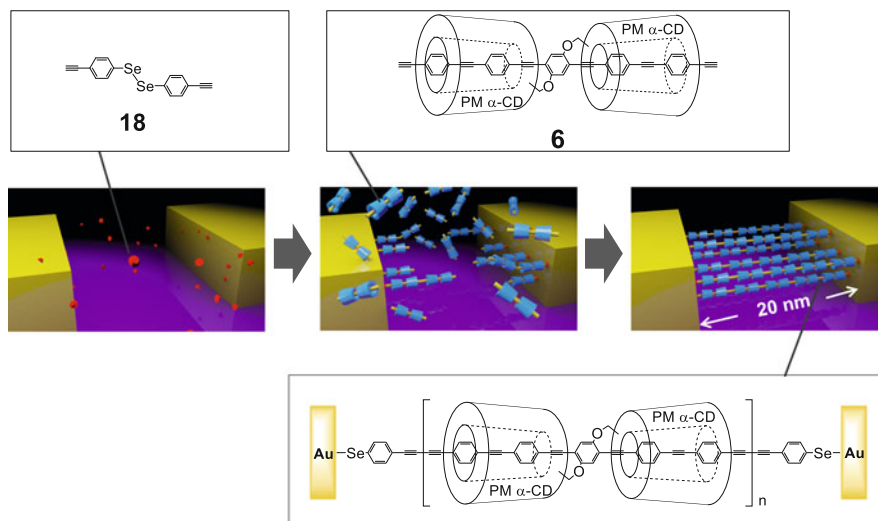


**Fig. 6.16** Schematic images of the molecular wiring between nanogaps via polymerization of **6**

insulated molecular wires **7** had formed. The electric current was 8 pA for 1 V. These results clearly demonstrated that molecular wiring was achieved using this polymerization method. To evaluate the covering effect of the insulated conjugated monomer, the same wiring method was performed using the uninsulated monomer and five nanosized electrodes. Although GPC analysis of the solution after the wiring reaction confirmed that the uninsulated polymer had formed, none of the electrodes exhibited current values over the measurement limit.

This result indicated that the molecular wiring efficiency using the uninsulated monomer was much less efficient than that with the insulated monomer, which maintains structural linearity and isolation of the  $\pi$ -conjugated moiety. This difference was probably due to the high degree of  $\pi$ - $\pi$  interactions or flexibility of the former, leading to low-molecular wiring efficiency by aggregation and bending. As shown in Fig. 6.17, a newly developed wiring technique between the nanogaps to fabricate a nano-optical switching device has been developed by copolymerizing the insulated monomer with the photochromic molecule. The resultant electrode was dipped into a solution of **18** to fabricate the modified nanosized electrode with surface polymerization sites. After washing, the electrode was placed in a solution of **6** and diiododiarylethene, which was stirred for 2 days under Sonogashira copolymerization conditions, to form connections between the electrodes and, under ultraviolet irradiation, to drive the photochromic diarylethene segments into the ring-closing state. GPC analysis of the solution after the wiring reaction confirmed that **11** had formed. To confirm the connection of each molecule by this copolymerization wiring method, electric conduction between the electrodes was measured. The initial electric current was 80 nA for 1 V (ON state). Irradiation of the molecules with visible light required to drive the photochromic diarylethene

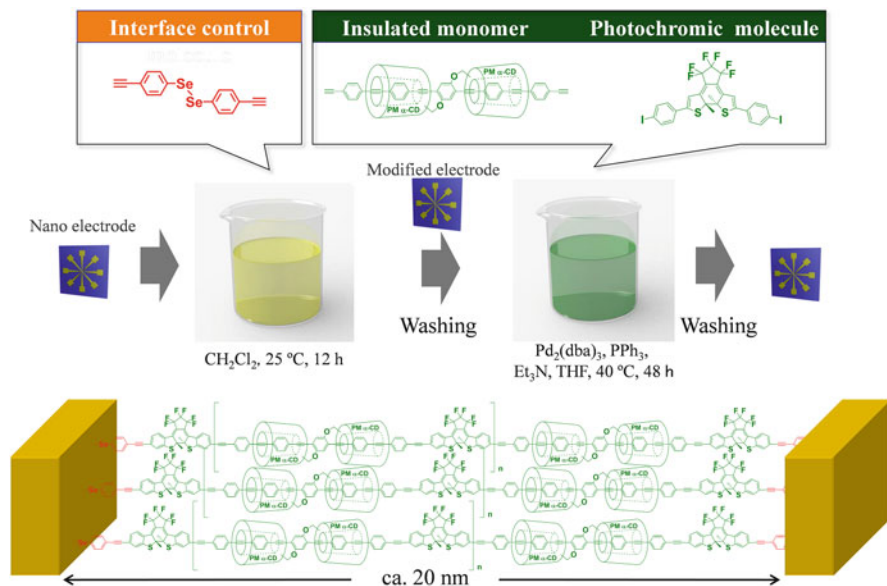


Fig. 6.17 Schematic images of the molecular wiring between nanogaps via copolymerization

residues into the ring-opening state (OFF state), and then UV radiation required to switch them into the ring-closing state (ON state). The electric current in molecular wire **11** C nanogap decreased to 45 nA for 1 V under visible light, but increased to 70 nA for 1 V under ultraviolet radiation, indicating a reversible switching property with light. The observed switching behavior strongly supported the assertion of binding of the molecules between the nanosized electrodes, affording molecular wiring by our newly developed technique to fabricate photoswitching nanodevices.

## 6.4 Summary and Conclusions

This chapter highlights a new method for synthesizing insulated molecular wires through the polymerization of structurally defined permethylated cyclodextrin-based rotaxane monomers. The insulated molecular wires thus formed have a high coverage ratio, rigidity, and PL efficiency and showed high charge mobility in the solid state; further, they are readily soluble in a variety of organic solvents. There was significant fluorescence and phosphorescence enhancement in the insulated molecular wires, especially in the solid state, which suggests that encapsulation of the  $\pi$ -conjugated polymer chains by permethylated cyclodextrin is essential to attain efficient fluorescence properties. A cholesteric LC phase was observed for polyrotaxanes because of the polymer's high rigidity and structure featuring a  $\pi$ -conjugated polymer chain threaded through chiral macrocycles. A highly insulated

organic semiconductor wire in the solid state was demonstrated with hole mobility along the  $\pi$ -conjugated polymer chain achieving close to that of amorphous silicon. The thus-formed polyrotaxane structure prevents  $\pi$ -stacking of the conjugated main chains even in the solid phase, leading to prolongation of the lifetime of charged radicals on the conjugated backbone by blocking the charge recombination processes.

This chapter also highlights a new type of molecular wiring method based on the polymerization or copolymerization of an insulated  $\pi$ -conjugated monomer between nanosized electrodes. Measuring the conductivity of  $\pi$ -conjugated polymers has thus far been either impossible or difficult, because of hopping conduction between neighboring conjugated chains. Taking conductivity measurements of singly conjugated chains will be possible, because using our wiring method will produce  $\pi$ -conjugated chains that are independent of their environment. This is expected to clarify the electrical conduction mechanisms of  $\pi$ -conjugated polymers, which has been considered difficult until now. The proposed research is a unique concept of the applicant, and as such, no studies that are similar to this are being conducted elsewhere.

This research is expected to drastically reduce manufacturing costs. It is also expected to be environmentally friendly and to make a contribution to green innovation because petroleum products are used instead of rare elements, such as Ge or Ir, which are currently used for highly integrated devices. To successfully make molecular electronics, it is important to gain access to synthesize single  $\pi$ -conjugated polymers with metal terminals and understand the behavior of their electrons.

Once the our fabrication method of molecular electronics are established, quantities of single molecule devices can be fabricated in a solution process at lower cost and with higher reproducibility than the conventional physical methods, which involve top-down fine processing technology and require expensive equipment. This technology for innovative nanosized molecular electronics is expected to overcome "Moore's law" and dramatically change industry and society. Currently large amounts of energy are required to prepare integrated circuits by photon and electron beam lithography in clean rooms. The proposed method would offer immense energy-saving effects by preparing molecular electronics in comparatively inexpensive chemical reactors. This method would be advantageous for mass production, because molecular devices, prepared by the assembly of molecular elements, could be prepared in the order of moles.

**Acknowledgments** I greatly acknowledge the experimental and intellectual contribution of my coworkers listed in the references that have made possible the research described herein.

## References

1. Moore GE (1985) *Electron Mag* 38:114
2. Jalabert A, Amara A, Clermidy F (2008) *Molecular electronics materials devices and applications*. Springer, Berlin
3. Petty MC (2007) *Molecular electronics from principles to practice*. Wiley, Chichester
4. Pope M, Kallmann HP, Magnate P (1963) *J Chem Phys* 38:2042
5. Kudo K, Yamashina M, Moriizumi T (1984) *Jpn J Appl Phys* 23:130
6. Tang CW (1986) *Appl Phys Lett* 48:183
7. Forrest SR (2004) *Nature* 428:9113
8. Wenz G (2009) *Inclusion polymers*. Springer, Berlin
9. Frampton MJ, Anderson HL (2007) *Angew Chem Int Ed* 46:1028
10. Pan C, Zhao C, Takeuchi M, Sugiyasu K (2015) *Chem Asian J* 10:1820–1835
11. Schlüter AD, Rabe JP (2000) *Angew Chem Int Ed* 39:864
12. Wenz G, Han B-H, Müller A (2006) *Chem Rev* 106:782
13. Sleiman H, Baxter P, Lehn J-M, Rissanen K (1995) *J Chem Soc Chem Commun* 715
14. Harada A, Kamachi M (1990) *Macromolecules* 23:2823–2824
15. Harada A, Li J, Kamachi M (1992) *Nature* 356:325
16. Harada A, Li J, Kamachi M (1992) *Nature* 364:516
17. Yoshida K, Shimomura T, Ito K, Hayakawa R (1999) *Langmuir* 15:910
18. Akai T, Abe T, Shimomura T, Ito K (2001) *Jpn J Appl Phys* 40:L1327
19. Shimomura T, Akai T, Abe T, Ito K (2002) *J Chem Phys* 116:1753
20. Shimomura T, Akai T, Fujimori M, Heike S, Hashizume T, Ito K (2005) *Synth Met* 153:497
21. Taylor PN, O'Connell MJ, McNeill LA, Hall MJ, Aplin RT, Anderson HL (2000) *Angew Chem Int Ed* 39:3456
22. Michels JJ, O'Connell MJ, Taylor PN, Wilson JS, Cacialli F, Anderson HL (2003) *Chem Eur J* 9:6167
23. Cacialli F, Wilson JS, Michels JJ, Daniel C, Silva C, Friend RH, Severin N, Samorì P, Rabe JP, O'Connell MJ, Taylor PN, Anderson HL (2002) *Nat Mater* 1:160
24. Terao J, Tang A, Michels JJ, Krivokapic A, Anderson HL (2004) *Chem Commun* 56
25. Tsuda S, Terao J, Kambe N (2009) *Chem Lett* 38:76
26. Terao J, Tsuda S, Tanaka Y, Okoshi K, Fujihara T, Tsuji Y, Kambe N (2009) *J Am Chem Soc* 131:16004
27. Tsuda S, Terao J, Tsurui K, Kambe N (2009) *Chem Lett* 38:190
28. Tsuda S, Terao J, Tanaka Y, Maekawa T, Kambe N (2009) *Tetrahedron Lett* 50:1146
29. Terao J, Tanaka Y, Tsuda S, Kambe N, Taniguchi M, Kawai T, Saeki A, Seki S (2009) *J Am Chem Soc* 131:18046
30. Terao J, Ikai K, Kambe N, Seki S, Saeki A, Ohkoshi K, Fujihara T, Tsuji Y (2011) *Chem Commun* 47:6816–6818
31. Terao J, Kimura K, Seki S, Fujihara T, Tsuji Y (2012) *Chem Commun* 48:1577
32. Terao J, Wadahama A, Matono A, Tada T, Watanabe S, Seki S, Fujihara T, Tsuji Y (2013) *Nat Commun* 4:1691
33. Terao J (2011) *Chem Rec* 11:269
34. Terao J (2011) *Polym Chem* 2:2444
35. Terao J, Homma K, Konoshima Y, Imoto R, Masai H, Matsuda W, Seki S, Fujihara T, Tsuji Y (2014) *Chem Commun* 50:658
36. Wong W-Y, Ho C-L (2010) *Acc Chem Res* 43:1246
37. Wild A, Winter A, Schlütter F, Schubert US (2011) *Chem Soc Rev* 40:1459
38. Mas-Ballesté R, Gómez-Herrero J, Zamora F (2010) *Chem Soc Rev* 39:4220
39. Leong WL, Vittal JJ (2011) *Chem Rev* 111:688
40. Koepf M, Chérioux F, Wytko JA, Weiss J (2012) *Coord Chem Rev* 256:2872
41. Evans RC, Douglas P, Winscom CJ (2006) *Coord Chem Rev* 250:2093
42. Zhao Q, Li F, Huang C (2010) *Chem Soc Rev* 39:3007

43. Dul M-C, Pardo E, Lescouëzec R, Journaux Y, Ferrando-Soria J, Ruiz-García R, Cano J, Julve M, Lloret F, Cangussu D, Pereira CLM, Stumpf HO, Pasán J, Ruiz-Pérez C (2010) *Coord Chem Rev* 254:2281
44. Bodenthin Y, Schwarz G, Tomkowicz Z, Lommel M, Geue T, Hasse W, Möhwald H, Pietsch U, Kurth DG (2009) *Coord Chem Rev* 253:2414
45. Nijhuis CA, Ravoo BJ, Huskens J, Reinhoudt DN (2007) *Coord Chem Rev* 251:1761
46. Tam AY, Yam VW (2013) *Chem Soc Rev* 42:1540
47. Burnworth M, Tang L, Kumpfer JR, Duncan AJ, Beyer FL, Fiore GL, Rowan SJ, Weder C (2011) *Nature* 472:334
48. Ho C-L, Wong W-Y (2011) *Coord Chem Rev* 255:2469
49. Zhao X, Cardolaccia T, Farley RT, Abboud KA, Schanze KS (2005) *Inorg Chem* 44:2619
50. Marvaud V, Launay JP (1993) *Inorg Chem* 32:1376
51. Tokuhisa H, Kanesato M (2005) *Langmuir* 21:9728
52. Kim H-J, Jung E-Y, Jin LY, Lee M (2008) *Macromolecules* 41:6066
53. Liu Y, Zhao Y-L, Zhang H-Y, Song H-B (2003) *Angew Chem Int Ed* 42:3260
54. Yang Y-W, Chen Y, Liu Y (2006) *Inorg Chem* 45:3014
55. Zhao Y-L, Zhang H-Y, Guo D-S, Liu Y (2006) *Chem Mater* 18:4423
56. Han C, Zhang L, Li H (2009) *Chem Commun* 3545
57. Yoshida D, Tsuchiya Y, Noguchi T, Yamamoto T, Dawn A, Shinkai S (2013) *Chem Eur J* 19:15485
58. Costa RD, Ortí E, Bolink HJ, Monti F, Accorsi G, Armaroli N (2012) *Angew Chem Int Ed* 51:8178
59. Xiao L, Chen Z, Jiayou BQ, Luo J, Kong S, Gong Q, Kido J (2011) *Adv Mater* 23:926
60. Ma D-L, Ma VP, Chan DS, Leung KH, He HZ, Leung CH (2012) *Coord Chem Rev* 256:3087
61. Liu Z, He W, Guo Z (2013) *Chem Soc Rev* 42:1568
62. Mou X, Wu Y, Liu S, Shi M, Liu X, Wang C, Sun S, Zhao Q, Zhou X, Huang W (2011) *J Mater Chem* 21:13951
63. Baggaley E, Weinstein JA, Williams JAG (2012) *Coord Chem Rev* 256:1762
64. Zhu YC, Zhou L, Li HY, Xu QL, Teng MY, Zheng YX, Zuo JL, Zhang HJ, You XZ (2011) *Adv Mater* 23:4041
65. Juliá F, Bautista D, Fernández-Hernández JM, González-Herrero P (2014) *Chem Sci* 5:1875
66. Wagner PJ, Hammond GS (1968) In: Noyes WA Jr, Hammond G, Pitts JN Jr (eds) *Advances in photochemistry*, vol 5. Interscience Publishers, New York
67. Hong Y, Lam JWY, Tang BZ (2011) *Chem Soc Rev* 40:5361
68. Komiyama N, Okada M, Fukumoto K, Jomori D, Naota T (2011) *J Am Chem Soc* 133:6493
69. Bolton O, Lee K, Kim HJ, Lin KY, Kim J (2011) *Nat Chem* 3:205
70. Lo SC, Harding RE, Shipley CP, Stevenson SG, Burn PL, Samuel IDW (2009) *J Am Chem Soc* 131:16681
71. Lo SC, Male NAH, Markham JPJ, Magennis SW, Burn PL, Salata OV, Samuel IDW (2002) *Adv Mater* 14:975
72. Kim JJ, You Y, Park YS, Kim JJ, Park SY (2009) *J Mater Chem* 19:8347
73. Tang MC, Tsang DPK, Chen MMY, Wong KMC, Yam VWW (2013) *Angew Chem Int Ed* 52:446
74. Gong S, Yang C, Qin J (2012) *Chem Soc Rev* 41:4797
75. Terao J, Masai H, Fujihara T, Tsuji Y (2012) *Chem Lett* 41:652
76. Masai H, Terao J, Makuta S, Tachibana Y, Fujihara T, Tsuji Y (2014) *J Am Chem Soc* 136:14714
77. Masai H, Terao J, Tsuji Y (2014) *Tetrahedron Lett* 55:4035
78. Masai H, Terao J, Seki S, Nakashima S, Kiguchi M, Okoshi K, Fujihara T, Tsuji Y (2014) *J Am Chem Soc* 136:1742
79. Tao NJ (2006) *Nat Nanotechnol* 1:173
80. Jalabert A, Amara A, Clermidy F (2008) *Molecular electronics materials devices and applications*. Springer, New York

81. Tang J, Wang Y, Klare JE, Tulevski GS, Wind SJ, Nuckolls C (2007) *Angew Chem Int Ed* 46:3892
82. Kiguchi M, Nakashima S, Tada T, Watanabe S, Tsuda S, Tsuji Y, Terao J (2012) *Small* 8:726
83. Taniguchi M, Nojima Y, Yokota K, Terao J, Sato K, Kambe N, Kawai T (2006) *J Am Chem Soc* 128:15062
84. Meng F, Hervault Y–M, Shao Q, Hu B, Norel L, Rigaut S, Chen X (2014) *Nat Commun* 5:3023
85. Terao J, Homma K, Konoshima Y, Taniguchi M, Kimoto Y, Horikawa M, Naito Y, Fujihara T, Tsuji Y (2014) *Bull Chem Soc Jpn* 87:871

# Chapter 7

## Orbital Rule for Electron Transport of Molecular Junctions

Tomofumi Tada

**Abstract** Constructive and destructive interference are typical features of electron transport in molecular junctions, which appear as parabolic curves and sharp dips of transmission functions, respectively. To understand the quantum interference properties in molecular junctions, the Green's function method with tight-binding models was adopted, and the quantum interference was analyzed in terms of orbitals, which leads to an efficient *orbital rule* for qualitative predictions of electron transport in molecular junctions. A minimum model, a two-site tight-binding model, was used to explain the *orbital rule* for electron transport without ambiguity. The orbital bases in tight-binding models are typically atomic orbitals, and thus the tight-binding model can be easily extended to larger molecules by simply adding atomic sites. As the next example, a three-site triangular tight-binding model was introduced. The quantum interference that appears in the three-site model can be easily understood using the *orbital rule*. With regard to the orbital bases as molecular orbitals, the triangular tight-binding model could efficiently explain the destructive interference recently observed in a large molecular unit. In the final part, we also examine the applicability of the *orbital rule* for molecular spin systems including spin-flip processes.

**Keywords** Electron transport • Green's function • Tight-binding model • Orbital rule

### 7.1 Introduction

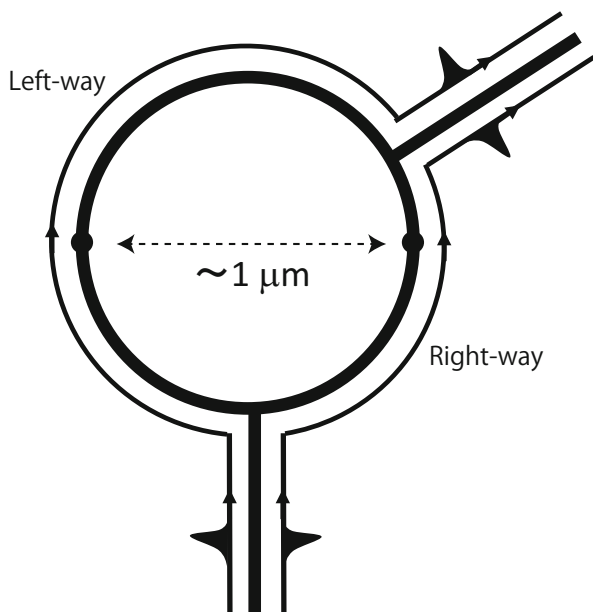
Quantum interference that appears as the result of superposition between possible electronic propagations is a typical phenomenon in quantum mechanics. The simplest picture of quantum interference can be explained with the concept of path-interference. Let us assume that only the left- and right-pathways are allowed for conduction electrons in the ring system shown in Fig. 7.1. When the difference of the transport distance between the two pathways is an integral multiple of the

---

T. Tada (✉)

Materials Research Center for Element Strategy, Tokyo Institute of Technology, Tokyo, Japan  
e-mail: [tada.t.ae@m.titech.ac.jp](mailto:tada.t.ae@m.titech.ac.jp)

**Fig. 7.1** Schematic of two different electron pathways in a ring-shaped apparatus. We can easily expect that no interactions occur between the two propagating states at *dotted mid-points* in a large ring, but such interaction will appear in molecular-sized rings



wavelength of conduction electrons, the two propagation states are superposed in a constructive manner, whereas when half of the wavelength remains in the distance difference, the two propagation states are superposed in a destructive manner. It is well known that quantum interference is a key in the quantum physics of the Aharonov-Bohm (AB) effect [1, 2], and the AB-ring is a very efficient apparatus for quantum physics. This explanation assumes that the two electron pathways are absolutely distinct; therefore, the size of the ring must be sufficiently large to avoid unexpected interactions<sup>1</sup> between the two propagations at mid-points (e.g., dotted points in Fig. 7.1). However, what happens when the macroscopic size of the ring is decreased to a molecular size? In molecular rings, the assumption (i.e., no interactions between the two propagations at mid-points) will be broken. Thereby, the emergence of quantum interference in molecular rings as a result of path interference may become ambiguous.

Theoretical investigations on the quantum interference effect in molecular junctions began from 1988 to the early 2000s [3–6], mainly with the use of ring-shaped molecules. The first report on the quantum interference effect in molecular junctions by Sautet and Joachim was based on the benzene molecule [3], and the constructive or destructive interference in electron transport via the benzene ring was obtained

<sup>1</sup>The so-called *measurement problem* in quantum mechanics is still not resolved; therefore, we cannot deny the presence of any suspicious interactions between two propagating states that are separated by large distances. The term *interaction* used in this chapter denotes an apparent interaction that is explicitly represented in Hamiltonian.

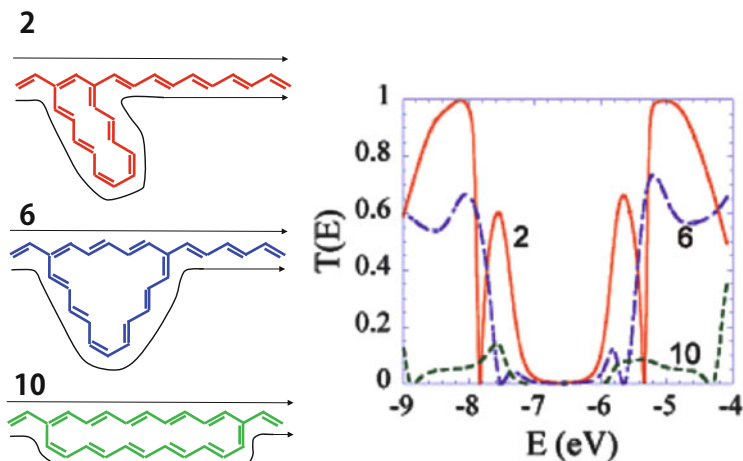


**Fig. 7.2** Carbon molecular junctions theoretically investigated and the calculated transmission functions by Baer and Neuhauser (Reprinted with permission from Ref. [6]. Copyright 2002 American Chemical Society)

using scattering state theory. In addition, the model junctions introduced by Baer and Neuhauser [6] were probably designed for investigation of the quantum interference effect in molecular junctions along the concept of path-interference. Figure 7.2 shows their molecular junctions and calculated transmission functions in which parabolic curves and abrupt drops of transmission functions appear depending of the junction structures and energy of the transmitted electrons. However, quantum interference was also confirmed in larger complicated molecules where the electron pathways cannot be identified. To understand the quantum interference in molecular junctions, the concept of interorbital interference rather than path-interference was proposed based on the Green's function approach [7]. According to interorbital interference, the key quantity of the quantum interference in molecular junctions is not the distance differences but the orbital-phase differences between connection points.

## 7.2 Tight-Binding Model for Molecular Junctions

In this section, the Green's function method based on a single-orbital per single-site model, the simplest tight-binding (TB) model, is introduced, and an orbital-phase rule to achieve a qualitative understanding of electron transport in single molecular junctions is explained. The model corresponds to the Hückel approximation when a single orbital is regarded as a  $\pi$  atomic orbital (AO) in a planar molecule composed of carbon atoms. The simplest TB model can also be useful for more general systems by considering that the base of the single orbital is given in the molecular orbital

(MO) space or in the AO-and-spin direct product space, as shown in the latter part of this section. Here, a qualitative relationship between orbitals and quantum transport is explained as a result of constructive or destructive interference, regardless of the base type for the orbitals.

Quantum interference is typically understood in terms of phase-related matters, and thus the interference effect may not be expected to appear in a phase-broken process (i.e., incoherent transport). However, a similar quantum interference effect can appear even for spin-dependent transport including spin-flip processes (i.e., incoherent transport). The key factor that leads to the quantum interference effects in many different cases is the similarity of the matrix form used to represent the junctions.

For electrodes, a one-dimensional (1D) metallic chain is adopted for simplicity. The base adopted for the orbitals of 1D electrodes does not have any limitations, that is, AO, MO, spin-spin direct product, etc. are acceptable, depending on the orbital base of the system sandwiched between the electrodes. It is also assumed that the interaction between the sandwiched system and the left/right 1D electrode is represented by a single hopping parameter (Fig. 7.3). Although these conditions are extensively simplified compared with the realistic conditions for nanojunctions, they are rather efficient for the derivation of a qualitative relationship between orbitals and conductance.

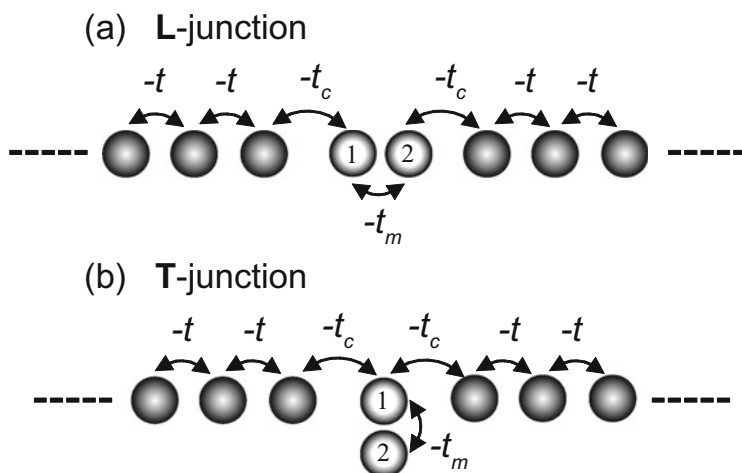


**Fig. 7.3** 1D tight-binding molecular junctions for the two-site model. The sandwiched diatomic molecule is composed of atoms 1 and 2. We adopted the nearest-neighbor hopping;  $-t$  in the electrode,  $-t_c$  for electrode-molecule hopping, and  $-t_m$  for intramolecular hopping parameters. Atoms 1 and 2 are respectively connected to the left- and right-electrodes in (a) a L-junction (Line-contact), and atom 1 is only connected to both electrodes in (b) a T-junction (T-shaped contact)

Let us start from the matrix representation of the 1D tight-binding model. The Hamiltonian of the system can be represented as

$$\mathbf{H} = \begin{pmatrix} \mathbf{H}_L & \mathbf{t}_L^\dagger & \mathbf{0} \\ \mathbf{t}_L & \mathbf{H}_M & \mathbf{t}_R^\dagger \\ \mathbf{0} & \mathbf{t}_R & \mathbf{H}_R \end{pmatrix}, \quad (7.1)$$

where  $\mathbf{H}_M$  represents the Hamiltonian of a sandwiched molecule and the Hamiltonian matrices  $\mathbf{H}_L$  and  $\mathbf{H}_R$  for the electrodes are shown as

$$\mathbf{H}_L = \begin{matrix} & \dots & m-4 & m-3 & m-2 & m-1 \\ \vdots & \begin{pmatrix} \ddots & \ddots & \ddots & \ddots & & \\ \ddots & \varepsilon_0 & -t & 0 & 0 & \\ \ddots & -t & \varepsilon_0 & -t & 0 & \\ \ddots & 0 & -t & \varepsilon_0 & -t & \\ 0 & 0 & 0 & -t & \varepsilon_0 & \end{pmatrix} & \end{matrix}, \quad (7.2)$$

$$\mathbf{H}_R = \begin{matrix} & n+1 & n+2 & n+3 & n+4 & \dots \\ n+1 & \begin{pmatrix} \varepsilon_0 & -t & 0 & 0 & & \\ -t & \varepsilon_0 & -t & 0 & \ddots & \\ 0 & -t & \varepsilon_0 & -t & \ddots & \\ 0 & 0 & -t & \varepsilon_0 & \ddots & \\ \vdots & \ddots & \ddots & \ddots & \ddots & \ddots \end{pmatrix} & \end{matrix}, \quad (7.3)$$

$$\mathbf{t}_L = \begin{matrix} & \dots & m-3 & m-2 & m-1 \\ m & \begin{pmatrix} \dots & 0 & 0 & -t & \\ & & 0 & 0 & \\ & & & 0 & \\ & & & & \vdots \end{pmatrix} & \end{matrix}, \quad (7.4)$$

and

$$\mathbf{t}_R = \begin{matrix} & \dots & n-2 & n-1 & n \\ n+1 & \left( \dots & 0 & 0 & -t \right) \\ n+2 & & & 0 & 0 \\ n+3 & & & & 0 \\ \vdots & & & & \vdots \end{matrix}, \quad (7.5)$$

where the base index of  $\mathbf{H}_M$  is running from  $m$  to  $n$  (i.e., the matrix size of  $\mathbf{H}_S$  is  $n - m + 1$ ). For the coupling matrices,  $\mathbf{t}_L$  and  $\mathbf{t}_R$  in Eqs. 7.4 and 7.5, it was assumed that the atoms connecting with the left and right electrodes are different, and the matrix indices for the two atoms are defined as  $m$  and  $n$  in  $\mathbf{H}_M$ . When the atoms connecting with the left and right electrodes are identical (i.e., the index is  $m$  in  $\mathbf{H}_M$ ), the coupling matrix  $\mathbf{t}_R$  is changed as

$$\mathbf{t}_R = \begin{matrix} & m & m+1 & \dots & n \\ n+1 & \left( -t & 0 & \dots & 0 \right) \\ n+2 & & 0 & \dots & 0 \\ n+3 & & 0 & & 0 \\ \vdots & & \vdots & & \vdots \end{matrix}, \quad (7.6)$$

Note that the matrix forms of  $\mathbf{H}_M$  are dependent on the sandwiched molecule. Examples for the matrices are given in the following sections.

### 7.2.1 Two-Site Model

A two-site TB model (i.e., diatomic molecule) connected to 1D electrodes is introduced first. Figure 7.3 shows two typical contact structures (i.e., L- and T-junctions) in the two-site TB model. The matrix elements for the two contact models are given as

$$\mathbf{H}^L = \begin{matrix} & \dots & & 1 & 2 & & \dots \\ \vdots & \left( \begin{array}{cccccc} \ddots & \ddots & & & & \\ \ddots & \ddots & & & & \\ \ddots & \epsilon_0 & -t & & & \\ & -t & \epsilon_0 & -t_c & & \\ & & -t_c & \epsilon_\alpha & -t_m & \\ & & & -t_m & \epsilon_\alpha & -t_c \\ & & & & -t_c & \epsilon_0 & -t \\ & & & & & -t & \epsilon_0 & \ddots \\ & & & & & & \ddots & \ddots \end{array} \right) & \vdots \\ 1 & & & & & & & & \\ 2 & & & & & & & & \\ \vdots & & & & & & & & \end{matrix}, \quad (7.7)$$

and

$$\mathbf{H}^T = \begin{matrix} & \dots & & 1 & 2 & & \dots \\ \vdots & \begin{pmatrix} \ddots & & & & & & \\ & \ddots & & & & & \\ & & \epsilon_0 & -t & & & \\ & & -t & \epsilon_0 & -t_c & & \\ & & -t_c & \epsilon_\alpha & -t_m & -t_c & \\ & & & -t_m & \epsilon_\alpha & 0 & \\ & & & -t_c & 0 & \epsilon_0 & -t \\ & & & & & -t & \epsilon_0 & \ddots \\ \vdots & & & & & & & \ddots & \ddots \end{pmatrix} & \end{matrix}, \quad (7.8)$$

where the base indices of  $\mathbf{H}_s$  are 1 and 2, and  $\epsilon_0$  and  $\epsilon_\alpha$  are the on-site energies of atoms in the electrodes and in the molecule, respectively. The hopping parameters,  $-t_m$  and  $-t_c$ , correspond to those for the sandwiched molecule itself and molecule-electrode coupling, respectively.

In the non-equilibrium Green's function method for electron transport [8], the transmission probability  $T$ , which is related to conductance as  $G = 2e^2/h$  in Landauer's formula [9], is expressed with the advanced/retarded Green's functions,  $\mathbf{G}^{A/R}$  of the molecule and the local density of states  $\rho$  of the apex atom in each electrode, as follows [10]:

$$T_{rs}(E) = \frac{(2\pi t_c^2)^2}{2} G_{sr}^A(E) G_{rs}^R(E) \rho(E) \rho(E). \quad (7.9)$$

The orbital index  $r/s$  corresponds to the AO connected to the left-/right-electrode.  $G^{A/R}(E)$  is the advanced/retarded Green's function  $\mathbf{G}^{A/R}(E)$ , which is represented as  $\mathbf{G}^{A/R}(E) = [E\mathbf{1} - \mathbf{H}_{\text{mol}} - \Sigma_L^{A/R} - \Sigma_R^{A/R}]^{-1}$ , where  $\mathbf{H}_{\text{mol}}$  is the  $2 \times 2$  Hamiltonian matrix in the basis of AOs in the two-site models, and  $\Sigma_{L/R}$  is the  $2 \times 2$  self-energy matrix of the left-/right-electrode. The interaction between the sandwiched molecule and each electrode is represented with a single hopping parameter  $t_c$  so that only a single element takes a non-zero value in the  $2 \times 2$  self-energy matrix (e.g.,  $(\Sigma_L)_{ij} = t_c^2 g_{\text{elec}} \delta_{ij} \delta_{i1}$  and  $(\Sigma_R)_{ij} = t_c^2 g_{\text{elec}} \delta_{ij} \delta_{i2}$  for the Line-contact, where  $g_{\text{elec}}$  is the Green's function for the electrodes). The transmission probability in the matrix-based Green's function for electron transport is generally represented as  $T(E) = \text{Tr}[i\{\Sigma_L^R(E) - \Sigma_L^A(E)\} \mathbf{G}^R(E) i\{\Sigma_R^R(E) - \Sigma_R^A(E)\} \mathbf{G}^A(E)]$  [8]. Using the matrix elements for the two-site TB model, the expression of  $T(E)$  shown in Eq. 7.9 is easily obtained.

Figure 7.4 shows the calculated transmission probabilities for L- and T-junctions. In both cases, the transmission probabilities have sharp peaks at energies of  $-0.5t$  and  $0.5t$ , which are the orbital levels of the highest occupied MO (HOMO)  $-0.5t$ , and lowest unoccupied MO (LUMO)  $0.5t$ , of the diatomic molecule. However, at the mid-gap between the HOMO and LUMO, the two contacts show a clear

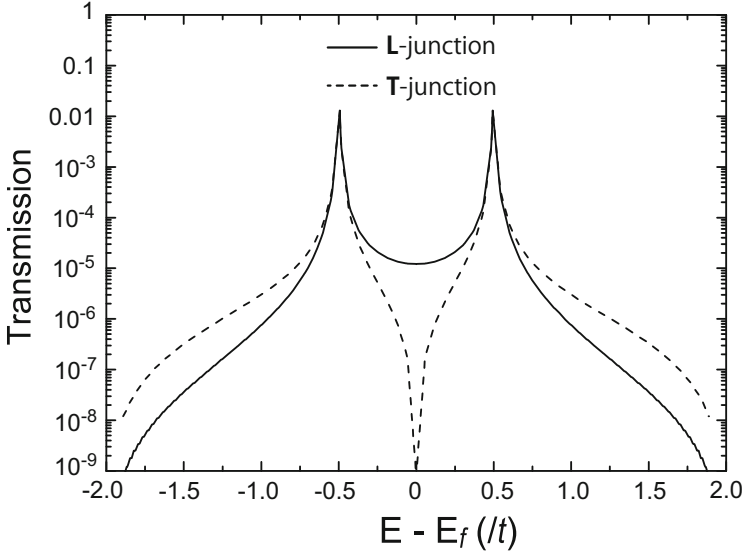


**Fig. 7.4** Calculated transmission probabilities for the two contact cases, L- and T-junctions. The tight-binding parameters used in these calculations are  $t_c = 0.1t$ ,  $t_m = 0.5t$ , and  $\varepsilon_\alpha = \varepsilon_0 = 0$

difference in the transmission probabilities; the transmission of the T-junction drops sharply to zero (i.e., anti-resonance), whereas that for the L-junction has a parabolic shape without anti-resonance. Analysis of Green's function  $G_{rs}(E)$  is quite useful to elucidate the clear difference in the transmission curves at the mid-gap. According to the pioneering study for electron tunneling by Caroli and co-workers [10], the Green's function  $G_{rs}(E)$  is given in terms of the unperturbed Green's function  $G_{rs}^{(0)}(E)$ , as

$$G_{rs} = \frac{G_{rs}^{(0)}}{D}, \quad (7.10)$$

where

$$D = (1 - t_c^2 G_{ss}^{(0)} g_{\text{elec}})(1 - t_c^2 G_{rr}^{(0)} g_{\text{elec}}) - t_c^4 G_{rs}^{(0)} G_{sr}^{(0)} g_{\text{elec}} g_{\text{elec}}. \quad (7.11)$$

Here the notation for retarded/advanced and the energy  $E$  is left off for simplicity. To derive a qualitative relationship between the orbitals and conductance, a weak coupling condition between the electrodes and sandwiched molecule is convenient; therefore, a weak coupling case was adopted in this section (i.e., the hopping parameter  $t_c$  between electrodes and a molecule is small with respect to  $t_m$  and  $t$ ). According to Eq. 7.11, the renormalization term  $D$  in the weak coupling case can be clearly approximated as 1. The calculated renormalization term  $D$  for the T-junction is shown in Fig. 7.5. In weak coupling cases (i.e., smaller  $t_c$  than  $t$ ), the

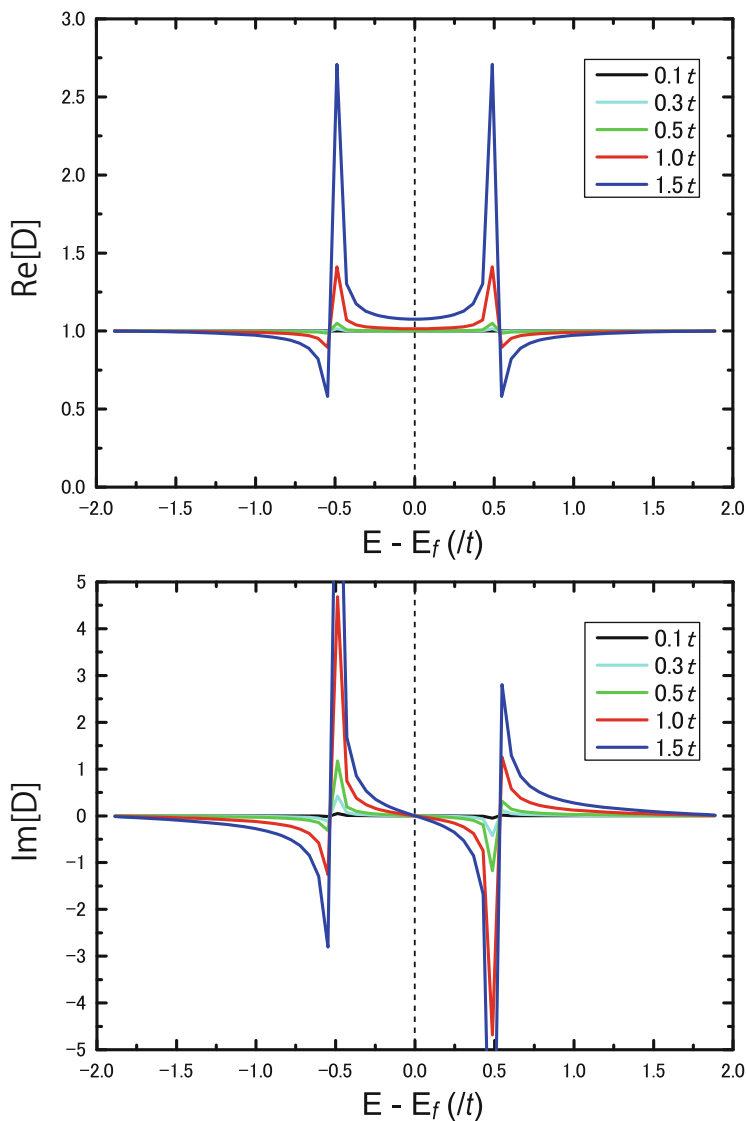


**Fig. 7.5** Calculated real (Re) and imaginary (Im) parts of the renormalization term  $D$  for the T-junction. Electrode-molecule coupling  $t_c$  of 0.1, 0.3, and  $0.5t$  are adopted as weak coupling cases, and  $t_c$  of 1.0 and  $1.5t$  are adopted as strong coupling cases. Other TB parameters are the same as those used in the transmission calculation for the T-junction

real part of the renormalization term  $D$  ( $\text{Re}[D]$ ) is almost equal to 1 at any energy; although some peaks and dips are confirmed at around eigenlevels ( $-0.5t$  and  $0.5t$ ),  $\text{Re}[D]$  at the mid-gap is apparently close to 1. In addition, the deviation of  $\text{Re}[D]$  from 1 at the mid-gap is not so large, even for strong coupling cases (i.e., larger  $t_c$

than  $t$ ), and the imaginary part of  $D$  is perfectly zero at the mid-gap, regardless of the strength of the electrode-molecule coupling  $t_c$ . We therefore unambiguously use the unperturbed Green's function  $G^{(0)}$  instead of the perturbed Green's function  $G$  to figure out the relationship between the Green's function and transmission function.

We are interested in the electronic states of molecules in terms of eigenlevels (e.g., molecular orbitals of molecules); therefore, the following unperturbed Green's function expanded in terms of molecular orbitals is quite efficient:

$$G_{rs}^{(0)}(E) = \sum_k \frac{C_{rk}C_{sk}}{E - \varepsilon_k}, \quad (7.12)$$

where the  $k$ -th eigenvalue of the isolated molecule is  $\varepsilon_k$ , and its eigenvector (i.e., orbital coefficient) on the site  $r$  is  $C_{rk}$ . Here the orbital representation of Eq. 7.12 is valid because the coefficients  $C$ 's of the molecule are real numbers. At the mid-gap between the HOMO and LUMO of the molecule, the contributions from the HOMO and LUMO in the summation of Eq. 7.12 are clearly significant. In the present two-site model, this situation is exactly true because we have only the two MOs, HOMO, and LUMO, and we have confirmed that the assumption also works quite well for multi-orbital systems, even with degenerate orbitals [11].

Let us consider the relationship between the MOs and Green's function. The energy differences  $E - \varepsilon_k$  appear in the denominator and the orbital coefficients in the numerator in  $G^{(0)}$ ; therefore, we can readily derive the following orbital relation for electron transport [7]: (i) large orbital coefficients at the contact sites,  $C_{rk}$  and  $C_{sk}$  for  $k = \text{HOMO}$  or  $\text{LUMO}$ , lead to a large transmission probability, and (ii) opposite signs between the two terms,  $C_{r\text{HOMO}}C_{s\text{HOMO}}$  and  $C_{r\text{LUMO}}C_{s\text{LUMO}}$ , are required for constructive interference from the HOMO and LUMO in the transmission function at the mid-gap due to the sign difference in the denominator  $E - \varepsilon_k$  in  $G^{(0)}$  for the HOMO and LUMO. Using the mathematical notation  $\text{Sgn}(a)$ , which returns the sign of the quantity  $a$ , the second condition is written as

$$\text{Constructive}(\text{HOMO} : \text{LUMO}) : \text{Sgn}(C_{r\text{HOMO}}C_{s\text{HOMO}}C_{r\text{LUMO}}C_{s\text{LUMO}}) = -, \quad (7.13)$$

On the other hand, when the two terms,  $C_{r\text{HOMO}}C_{s\text{HOMO}}$  and  $C_{r\text{LUMO}}C_{s\text{LUMO}}$ , have the same sign, the contributions from the HOMO and LUMO are canceled out at the mid-gap. In the notation using "Sgn", the relation is

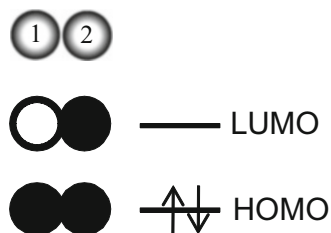
$$\text{Destructive}(\text{HOMO} : \text{LUMO}) : \text{Sgn}(C_{r\text{HOMO}}C_{s\text{HOMO}}C_{r\text{LUMO}}C_{s\text{LUMO}}) = +. \quad (7.14)$$

Although we have focused on the HOMO and LUMO in Eqs. 7.13 and 7.14 as a frontier orbital rule for electron transport, the interference relationship between two neighboring energetically non-degenerate orbitals  $\varepsilon_k$  and  $\varepsilon_{k+1}$  can be represented as

$$\text{Constructive}(k : k + 1) : \text{Sgn}(C_{rk}C_{sk}C_{rk+1}C_{sk+1}) = -, \quad (7.15)$$

$$\text{Destructive}(k : k + 1) : \text{Sgn}(C_{rk}C_{sk}C_{rk+1}C_{sk+1}) = +. \quad (7.16)$$

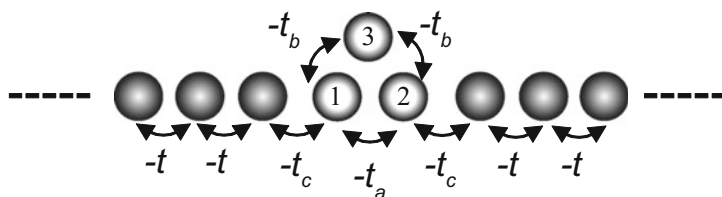
**Fig. 7.6** Orbital phases of the HOMO and LUMO for the two-site molecule. The black and white symbols represent positive and negative coefficients, respectively



According to the orbital rule, the clear difference of the transmission functions at the mid-gap in L- and T-junctions can be readily understood. The orbital phases (i.e., the sign of MOs) of the HOMO and LUMO of the two-site molecule are shown in Fig. 7.6. In this model, the amplitude of the orbital coefficients is  $1/\sqrt{2}$  for both sites. Thus, the orbital rule to consider is rule (ii). In the L-junction, the sites connected to the electrodes are sites 1 and 2. The numerator in  $G^{(0)}$  for HOMO,  $C_{1\text{HOMO}}C_{2\text{HOMO}}$ , is a positive number, but for the LUMO,  $C_{1\text{LUMO}}C_{2\text{LUMO}}$  is a negative number. This is the case for constructive interference of the electron transmission at the Fermi level, which leads to the parabolic transmission at the Fermi level without anti-resonance, as shown in Fig. 7.4. However, in the T-junction, the only site connected to the electrodes is site 1, and the terms  $C_{1\text{HOMO}}C_{1\text{HOMO}}$  and  $C_{1\text{LUMO}}C_{1\text{LUMO}}$  have the same sign (i.e., positive) and the same value. Therefore, the unperturbed Green's function  $G^{(0)}$  at the Fermi level for the T-junction is exactly zero, which results in the sharp drop of the transmission function at the Fermi level, as shown in Fig. 7.4. This is the molecular orbital rule available for the understanding of electron transport. Application of the orbital rules for electron transport in more complicated molecules can be found elsewhere [7, 12–26].

### 7.2.2 Three-Site (Triangular) Model

Figure 7.7 shows  $\Lambda$ - and V-junctions adopted as typical three-site TB junctions, in which only a single site is connected with the left/right electrode. Figure 7.8 shows the calculated transmission functions for the  $\Lambda$ - and V-junctions. There are two peaks of transmission in both junctions that correspond to the eigenlevels of the triangular molecule shown in Fig. 7.9 (i.e.,  $-1.0t$  and  $0.5t$ ). When the triangular system is regarded as a planar  $\pi$ -molecule, the molecule has three  $\pi$ -electrons, and the HOMO is the degenerate  $\varepsilon_2$  or  $\varepsilon_3$ . In that sense, the mid-gap position must be recognized at the degenerate orbital level ( $0.5t$ ), but no pronounced feature appears at this position, just a single transmission peak. On the other hand, transmission functions between  $-1.0t$  and  $0.5t$  show a clear difference between the  $\Lambda$ - and V-junctions; the  $\Lambda$ -junction shows a parabolic transmission, whereas the V-junction shows a sharp drop (i.e., anti-resonance) of transmission at  $-0.5t$ . The V-junction has only one site for coupling with the electrodes (i.e., site 3); therefore, the same explanation for the sharp drop in the T-junction also holds for the V-junction. On

(a)  $\Lambda$ -junction

## (b) V-junction

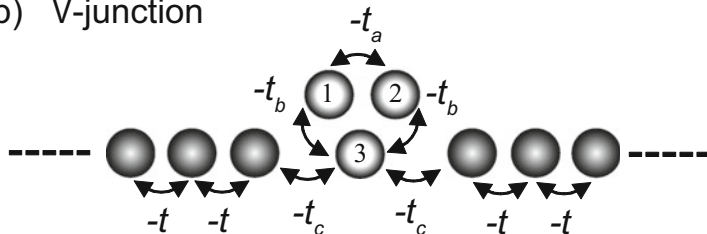


**Fig. 7.7** 1D tight-binding molecular junctions for the three-site triangular model. The sandwiched triangular molecule is composed of atoms 1, 2, and 3.  $-t$  in the electrode,  $-t_c$  for electrode-molecule hopping, and  $-t_a$  and  $-t_b$  for intramolecular hopping were adopted as the nearest-neighbor hopping parameters. Atoms 1 and 2 are respectively connected to the left- and right-electrodes in (a) the  $\Lambda$ -junction, and only atom 3 is connected to both electrodes in (b) the V-junction

the other hand, the orbital pairs of focus in the  $\Lambda$ -junction are  $(\varepsilon_1, \varepsilon_2)$  and  $(\varepsilon_1, \varepsilon_3)$ . Considering the orbital phases of  $\varepsilon_1$ ,  $\varepsilon_2$ , and  $\varepsilon_3$ , the pair of  $(\varepsilon_1, \varepsilon_2)$  is a constructive type of interference, whereas the pair of  $(\varepsilon_1, \varepsilon_3)$  represents destructive interference. However, according to the additive property in the Green's function of Eq. 7.12, a parabolic transmission from the constructive interference remains. In this sense, observation of the sharp drop of transmission (anti-resonance) is more difficult than that of the parabolic type of transmission.

Using the three-site triangular system, let us consider an orbital engineering for electron transport. Figure 7.10a shows the triangular system with three-fold rotational symmetry identical to the sandwiched molecule in Figs. 7.7, 7.8, and 7.9; the system is renamed as  $\Lambda_s$ . When the on-site parameters are changed depending on the atoms (e.g., the on-site parameters of atoms 1 and 2 are changed to negative and that of atom 3 to positive), the three-fold rotational symmetry is easily broken, and thus, the orbital degeneracy for  $\varepsilon_2$  and  $\varepsilon_3$  is also broken, which leads to three different energy levels, the  $\Lambda_a$ -junction in Fig. 7.10b. In the  $\Lambda$ -junction (i.e., the connecting atoms are 1 and 2), the orbital relationship between  $\varepsilon_1$  and  $\varepsilon_2$  corresponds to the *constructive* case, and that between  $\varepsilon_2$  and  $\varepsilon_3$  is also *constructive*. Thus, the calculated transmission function shows parabolic transmission in both the  $(\varepsilon_1:\varepsilon_2)$  and  $(\varepsilon_2:\varepsilon_3)$  regions, as shown in Fig. 7.11. When the base of the Hamiltonian matrix of the triangular system is  $\pi$ -AO, the system corresponds exactly to a

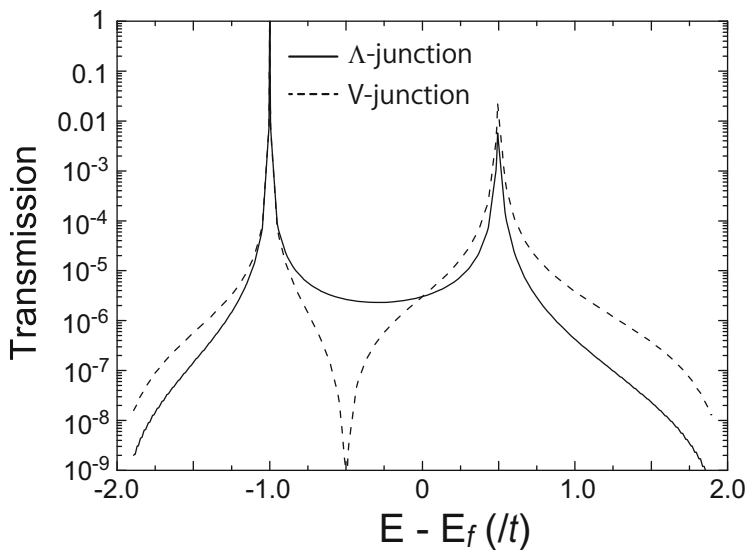


**Fig. 7.8** Calculated transmission probabilities for the three-site models,  $\Lambda$ - and V-junctions. The tight-binding parameters used in the calculations are  $t_c = 0.1t$ ,  $t_a = t_b = 0.5t$ , and  $\varepsilon_\alpha = \varepsilon_0 = 0$

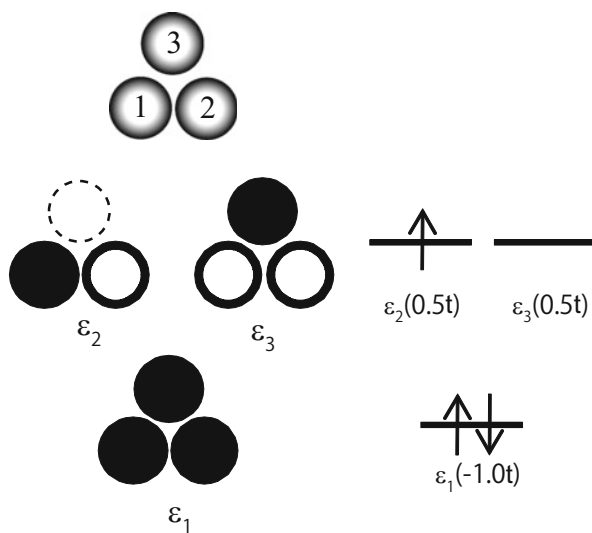


**Fig. 7.9** Orbital phases of  $\varepsilon_1$ ,  $\varepsilon_2$ , and  $\varepsilon_3$  for the three-site triangular molecule. The *black* and *white* symbols represent positive and negative coefficients, respectively. The *dotted* circle indicates the zero orbital amplitude

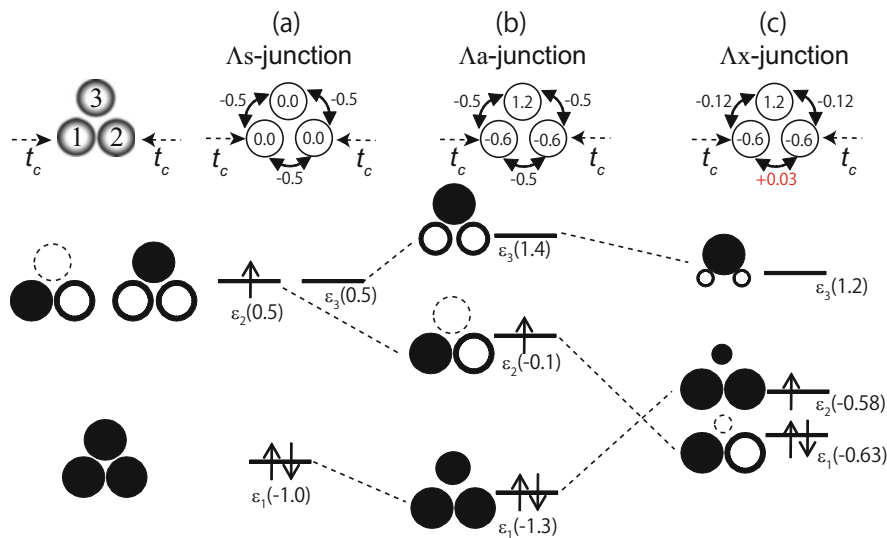


**Fig. 7.10** Orbital schematics for orbital engineering in the triangular system. (a)  $\Lambda_s$  junction: TB parameters maintain the threefold rotational symmetry, and this junction is identical to the original triangular junction in Fig. 7.9. (b)  $\Lambda_a$  junction: the threefold rotational symmetry is broken by changing the on-site parameters. (c)  $\Lambda_x$  junction: the sign of the hopping parameter in  $\Lambda_a$  junction is changed from negative to positive (red). The dotted circles represent the zero orbital amplitudes

planar triangular molecule, and thus the intramolecular hopping parameter (i.e.,  $-t_a$  and  $-t_b$ ) is a negative value because of the  $\pi - \pi$  orbital interactions. Thus, the resultant transmission functions in the triangular molecular system have basically the same features as the transmission functions of the  $\Lambda_s$ - and  $\Lambda_a$ -junctions shown in Fig. 7.11.

However, when the Hamiltonian matrix is given as an MO base, the hopping parameters between the neighboring sites (MOs) can be both positive and negative, whereby an intrinsically different transmission appears, compared with those of the  $\Lambda_s$ - and  $\Lambda_a$ -junctions. When the hopping parameter between sites 1 and 2 is changed to a positive number, the orbital order for  $\varepsilon_1$  and  $\varepsilon_2$  in the  $\Lambda_s$ - and  $\Lambda_a$ -junctions can be exchanged, as shown in Fig. 7.10c,  $\Lambda_x$ -junction. As a result of the orbital order exchange in the  $\Lambda_x$ -junction, the orbital relationship between  $\varepsilon_2$  and  $\varepsilon_3$  becomes *destructive*, and a clear drop of transmission appears in between the orbital  $\varepsilon_2$  and  $\varepsilon_3$  (i.e.,  $-0.58t$  and  $1.2t$ ), as shown in Fig. 7.11. In this way, orbital engineering based on the orbital rule for electron transport is useful to predict the qualitative properties of transport.

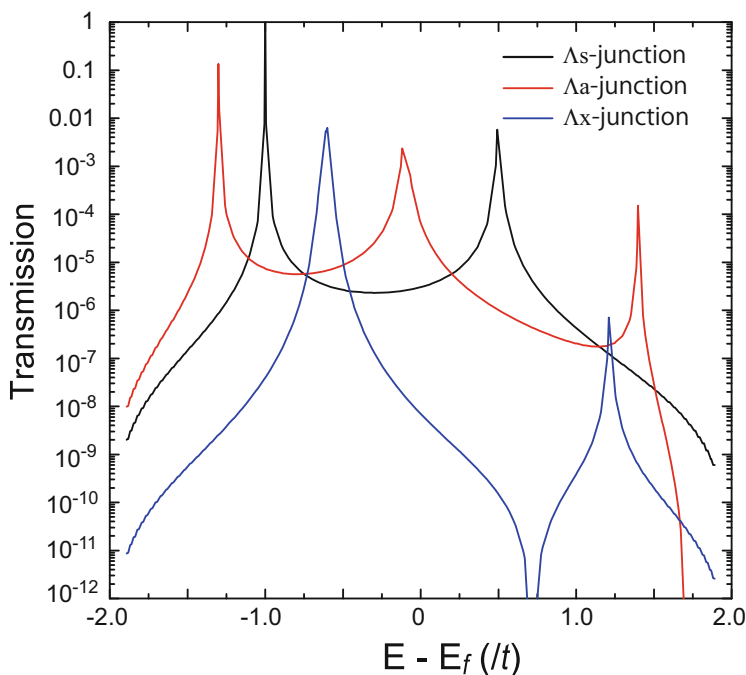


**Fig. 7.11** Calculated transmission probabilities for the  $\Lambda_s$ ,  $\Lambda_a$ , and  $\Lambda_x$  junctions. The tight-binding parameters used in the calculations are given in Fig. 7.10

### 7.2.3 Orbital Rule from Experimental Observations

Now that the relationship between orbitals and transmission functions from a theoretical perspective is explained, the next concern is the experimental validation of the orbital rule. In the experimental observation of electron transport in molecular junctions, sulfur atoms are typically introduced as an alligator clip with gold electrodes because Au-S bonding is sufficiently strong (strong coupling) to trap a single molecule between electrodes; dithiolate molecules are frequently adopted to make single molecular junctions. Therefore, whether the orbital rule using the simplest TB model can be applicable to such realistic Au-dithiole-Au junctions must be discussed first. As for this point, basic analysis and more sophisticated calculations based on density functional theory (DFT) for electron transport have been successful for validation of the orbital rules [25]. In addition, analysis of the renormalization term  $D$  in a strong coupling case, as shown in Fig. 7.5, supports the applicability of the orbital rule derived in a weak coupling case.

Let's move on to the experimental observations related to the orbital rule. The direct observation of the transmission function requires a more careful handling of junctions than in current measurements; therefore, the electrical current would be an easier quantity available for such validation. In fact, validation of the orbital

rule was performed based on the observed current first, and validation using the observed transmission (i.e., derivative conductance) was then accomplished. The first experimental validation was conducted by Taniguchi and co-workers [27], in which naphthalenedithiolenes (ND) molecules were adopted in current measurements. In the experimental work, four ND molecules, shown in Fig. 7.12a, were synthesized, and the tunneling current of the junctions using gold electrodes was calculated and measured. According to the orbital phases of the ND molecules (Fig. 7.12a), four molecules appear to have the constructive pattern of MOs at first inspection; however, 2,7-ND is the exception because only 2,7-ND has two singly-occupied MOs (SOMOs), i.e., a case of degenerate frontier MOs. The two SOMOs can be transformed into another two pairs of MOs by unitary transformation, and the resultant MOs can be perfectly localized frontier MOs, left-edge localized MO and right-edge localized MO. Orbital rule I for electron transport tells us that non-zero orbital amplitudes at the connecting atoms are required in frontier orbitals. Therefore, the zero amplitudes at the connecting atoms cannot be used for transport, and 2,7-ND is an undesirable molecule in terms of the orbital amplitudes, which results in extremely low transmission (Fig. 7.12b). The details of the orbital rule for the degenerate case, which is not addressed in the chapter, has been described in a recent work using a benzene molecular junction [11]. Figure 7.12c shows the clear correspondence with the theoretical predictions based on the orbital rule.

After the experiment using ND molecules, Guédon and co-workers accomplished more direct observations of *constructive/destructive* interference [28] using the anthraquinone molecular unit shown in Fig. 7.13. According to their explanation, the anthraquinone molecular unit can be regarded as a three-site model, in which the interorbital interactions correspond to the  $\Lambda_x$  triangular system shown in Fig. 7.10c.<sup>2</sup> Therefore, *destructive* interference is expected to appear in the molecular junction, and a sharp drop of the transmission function at the Fermi level was actually observed. In this way, the validity of the orbital rule was successfully confirmed from indirect/direct measurements of the transmission probabilities in molecular junctions.

## 7.2.4 Spin-Dependent Transport in Molecular Spin Junctions

In this section, we discuss the applicability of the orbital rule for spin-dependent transport. When a sandwiched molecule has a localized spin and the molecular-spin junction shows a spin-dependent transport without spin-flip processes, the orbital rule introduced in the previous part is straightforwardly applicable for the

<sup>2</sup>According to their three-site model, the hopping parameters between sites 1 and 3 (2 and 3) are also positive, whereas  $\Lambda_x$ -junction is negative for these. However, it was confirmed that the intrinsic property (anti-resonance) in the  $\Lambda_x$ -junction was not sensitive to the sign of the 1–3 and 2–3 hopping parameters. The key parameter for the anti-resonance is the sign for hopping between sites 1 and 2 because the key factor is the orbital exchange between  $\varepsilon_1$  and  $\varepsilon_2$  from  $\Lambda_a$  to  $\Lambda_x$ .

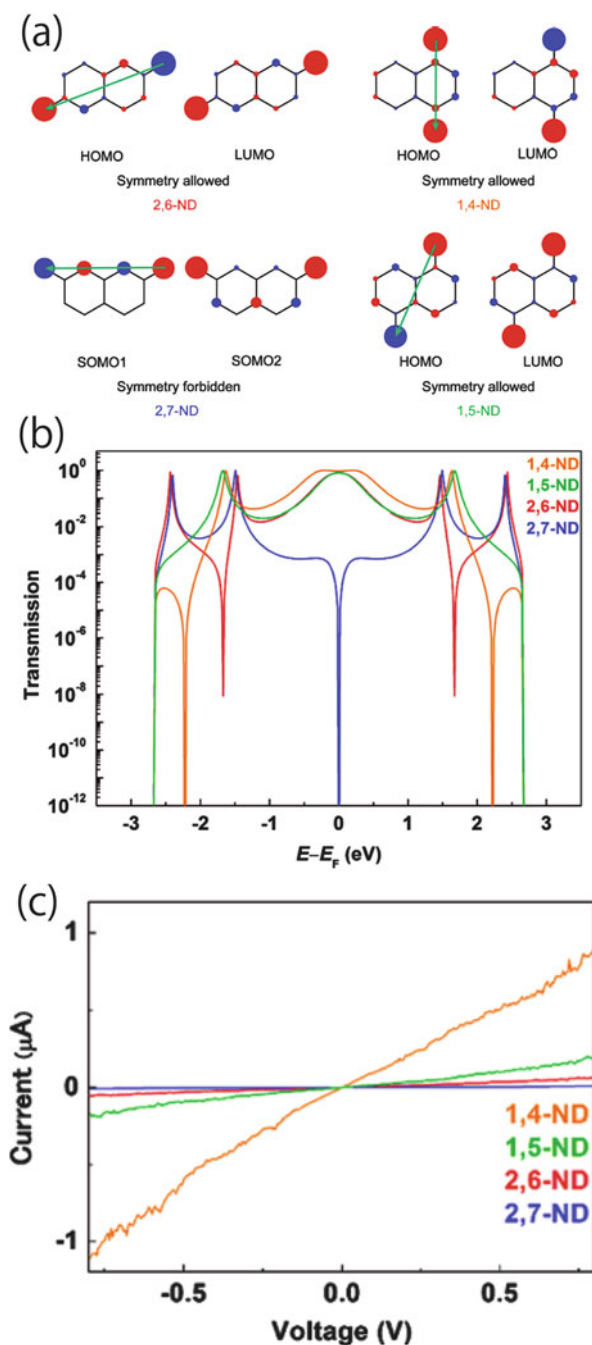


**Fig. 7.12** (a) Naphthalene dithiolate (ND) molecules, (b) calculated transmission functions of the ND molecules, and (c) measured current reported by Taniguchi and co-workers (Reprinted with permission from Ref. [27]. Copyright 2011 American Chemical Society)

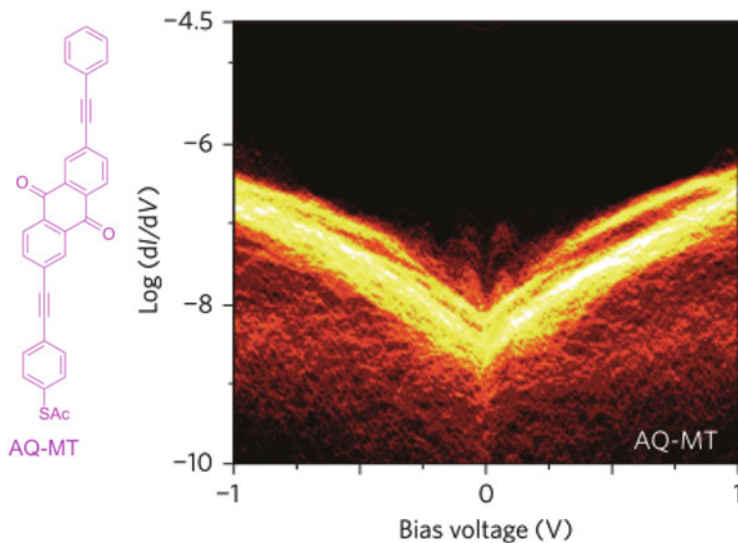


**Fig. 7.13** Anthraquinone molecular unit showing an anti-resonance transmission of the Fermi level, and the measured transmission function (i.e., derivative conductance) by Guédon and co-workers (Reprinted with permission from Ref. [28]. Copyright 2012 Nature Publishing Group)

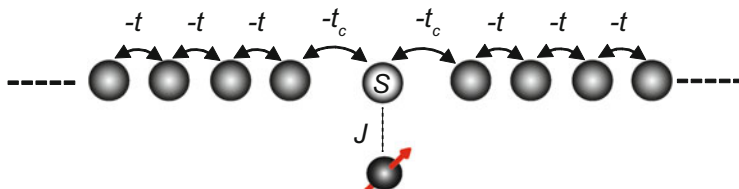


**Fig. 7.14** Tight-binding 1D model including a localized electron spin. The gray atom (or molecule) indexed with  $s$  is coupled to electrodes and to a localized spin (red) through the spin-spin exchange coupling,  $J$ . The nearest-neighbor hopping integrals are represented by  $t$  and  $t_c$

spin-dependent transport because the matrix elements for each spin can be written independently. Thus, we can discuss the transmission properties in both spin cases (e.g., up- or down-spin) separately. However, when spin-flip processes are allowed by the spin exchange coupling between a conduction electron and localized spin, the matrix elements are not divided into submatrices in terms of up- or down-spin. For example, the 1D system shown in Fig. 7.14 corresponds to such a spin system,

and the Hamiltonian matrix is written as

$$\mathbf{H}_{\text{spin}} = \begin{matrix} & \begin{matrix} s-2\downarrow & s-1\uparrow & s-1\downarrow & s\uparrow\downarrow & s\downarrow\uparrow & s+1\uparrow & s+1\downarrow & s+2\uparrow \end{matrix} \\ \begin{matrix} s-2\downarrow \\ s-1\uparrow \\ s-1\downarrow \\ s\uparrow\downarrow \\ s\downarrow\uparrow \\ s+1\uparrow \\ s+1\downarrow \\ s+2\uparrow \end{matrix} & \left( \begin{array}{cccccccc} \varepsilon_0 & 0 & -t & & & & & \\ 0 & \varepsilon_0 & 0 & -t_c & & & & \\ -t & 0 & \varepsilon_0 & 0 & -t_c & & & \\ & -t_c & 0 & \frac{-J}{4} & \frac{J}{2} & -t_c & & \\ & & -t_c & \frac{J}{2} & \frac{-J}{4} & 0 & -t_c & \\ & & & -t_c & 0 & \varepsilon_0 & 0 & -t \\ & & & & -t_c & 0 & \varepsilon_0 & 0 \\ & & & & & -t & 0 & \varepsilon_0 \end{array} \right), \end{matrix} \quad (7.17)$$

where  $\uparrow$  and  $\downarrow$  are the spin directions of conduction electrons and  $\uparrow\downarrow$  and  $\downarrow\uparrow$  are the spin directions of the localized spin (red arrow in Fig. 7.14). The spin exchange coupling  $J$ , between the conduction and localized electron spins, was taken into account through the s-d tight-binding Hamiltonian in Eq. 7.17. In this sense, the spin-junction is a mimic of an aromatic molecule including a d-metal center, such as the metal-phthalocyanine molecular junction with gold chains fabricated by Nazin and co-workers (see Fig. 7.15) [29]. The presence of the spin-spin coupling term  $J/2$  with the matrix elements ( $s\uparrow\downarrow$ ,  $s\downarrow\uparrow$ ) and ( $s\downarrow\uparrow$ ,  $s\uparrow\downarrow$ ) of  $\mathbf{H}_{\text{spin}}$  means that the incoming up-spin electron can be transmitted/reflected as up- or down-spin; the same situation is also observed for the incoming down-spin. Thus, the Hamiltonian  $\mathbf{H}_{\text{spin}}$  cannot be divided into spin-dependent Hamiltonians. In this case, a straightforward method for the transport calculation is a wave-packet propagation; the simulation is useful to calculate the transport processes including spin-flip, and multiple spin-flip processes can also occur at the spin site  $s$ , which corresponds to incoherent transport. Although the wave-packet propagation method is a very useful method, the calculation for the transmission curves from wave-packet dynamics requires numerical propagations of the wave-packet for each energy level, and thus it could be time consuming, depending on the system size and the required energy width and resolution. Therefore, if the Green's function method is also applicable for the present spin-flip case, then it would be better to use it.

#### 7.2.4.1 Coherent Approach for the Spin-Flip Process

For the Green's function approach, the first step is a division of the entire process into coherent and incoherent processes because the transport process including spin-flip is a mixture of coherent and incoherent processes. Let us consider a simple

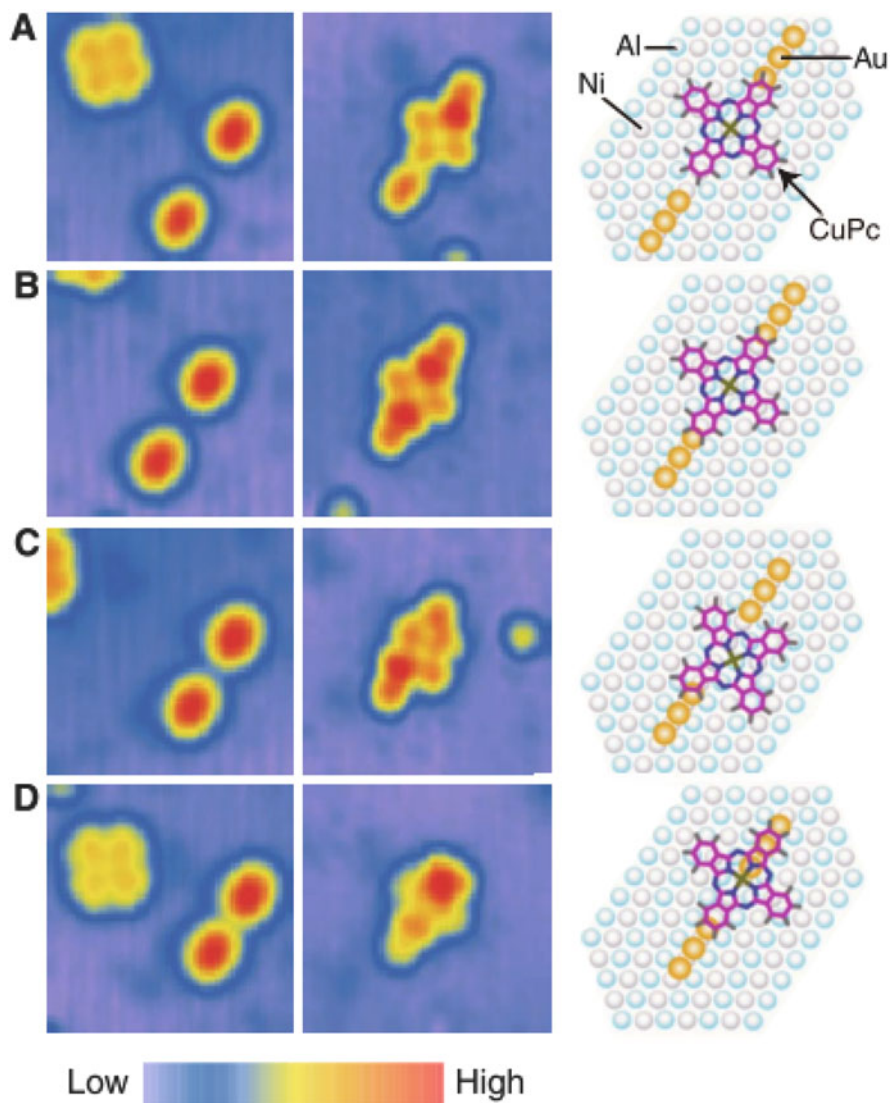


**Fig. 7.15** Scanning tunneling microscopy (STM) image of a gold-Cu phthalocyanine-gold junction on a NiAl substrate taken by Nazin, Qiu, and Ho (Reprinted with permission from Ref. [29]. Copyright 2003 AAAS)

case, in which the incoming electron is initially spin polarized as up-spin. Under this condition, there are two coherent processes:

$$\begin{aligned}
 \text{[Spin-Flip case:]} & \quad \cdots \uparrow_{s-2} \rightarrow \uparrow_{s-1} \rightarrow \uparrow_s \rightarrow \downarrow_s \rightarrow \downarrow_{s+1} \rightarrow \downarrow_{s+2} \cdots \\
 \text{[No Flip case:]} & \quad \cdots \uparrow_{s-2} \rightarrow \uparrow_{s-1} \rightarrow \uparrow_s \rightarrow \uparrow_{s+1} \rightarrow \uparrow_{s+2} \cdots
 \end{aligned}$$

The corresponding submatrices for the spin-flip (SF) and no-flip (NF) processes are respectively given as

$$\mathbf{H}_{s\uparrow-\downarrow}^{(\text{SF})} = \begin{matrix} \vdots \\ s-2\uparrow \\ s-1\uparrow \\ s\uparrow\downarrow \\ s\downarrow\uparrow \\ s+1\downarrow \\ s+2\downarrow \\ \vdots \end{matrix} \begin{pmatrix} \cdots & s-2\uparrow & s-1\uparrow & s\uparrow\downarrow & s\downarrow\uparrow & s+1\downarrow & s+2\downarrow & \cdots \\ \ddots & \ddots & & & & & & \\ \ddots & \ddots & \varepsilon_0 & -t & & & & \\ & & -t & \varepsilon_0 & -t_c & & & \\ & & & -t_c & \frac{-J}{4} & \frac{J}{2} & 0 & \\ & & & & \frac{J}{2} & \frac{-J}{4} & -t_c & \\ & & & & 0 & -t_c & \varepsilon_0 & -t \\ & & & & & & -t & \varepsilon_0 & \ddots \\ & & & & & & & \ddots & \ddots \end{pmatrix}, \quad (7.18)$$

and

$$\mathbf{H}_{s\uparrow-\uparrow}^{(\text{NF})} = \begin{matrix} \vdots \\ s-2\uparrow \\ s-1\uparrow \\ s\uparrow\downarrow \\ s\downarrow\uparrow \\ s+1\uparrow \\ s+2\uparrow \\ \vdots \end{matrix} \begin{pmatrix} \cdots & s-2\uparrow & s-1\uparrow & s\uparrow\downarrow & s\downarrow\uparrow & s+1\uparrow & s+2\uparrow & \cdots \\ \ddots & \ddots & & & & & & \\ \ddots & \ddots & \varepsilon_0 & -t & & & & \\ & & -t & \varepsilon_0 & -t_c & & & \\ & & & -t_c & \frac{-J}{4} & \frac{J}{2} & -t_c & \\ & & & & \frac{J}{2} & \frac{-J}{4} & 0 & \\ & & & & -t_c & 0 & \varepsilon_0 & -t \\ & & & & & & -t & \varepsilon_0 & \ddots \\ & & & & & & & \ddots & \ddots \end{pmatrix}. \quad (7.19)$$

These matrices clearly have the same matrix form already introduced in the two-site TB model, L-, and T-junctions. Replacement of the tight-binding parameters  $\varepsilon_\alpha$  in Eqs. 7.7 and 7.8 with  $-J/4$  and  $-t_m$  in Eqs. 7.7 and 7.8 with  $J/2$  leads to the matrices  $\mathbf{H}_{s\uparrow-\downarrow}^{(\text{SF})}$  and  $\mathbf{H}_{s\uparrow-\uparrow}^{(\text{NF})}$  being easily determined as exactly equal to  $\mathbf{H}_L$  and  $\mathbf{H}_T$ , respectively. Therefore, the coherent spin-flip process corresponds to *constructive* transport, and the coherent no-flip process corresponds to *destructive* transport. We can understand the validity of the consideration in another point of view as follows. As for the coherent no-flip process, the Hamiltonian matrix can be expressed in a spin-dependent form because spin-exchange does not occur, and the junction structure in Fig. 7.14 is the same as that of the T-junction where a single atom is connected to both electrodes. Therefore, *destructive* transport must appear in the no-flip transport of the junction in Fig. 7.14.

Figure 7.16 shows the calculated transmission probabilities for the  $\uparrow$ -to- $\uparrow$  and  $\uparrow$ -to- $\downarrow$  processes using the matrices of Eqs. 7.18 and 7.19. The eigenlevels of the spin junction system are  $-0.15t$  singlet state, and  $0.05t$  triplet state ( $0.2t$  of  $J$

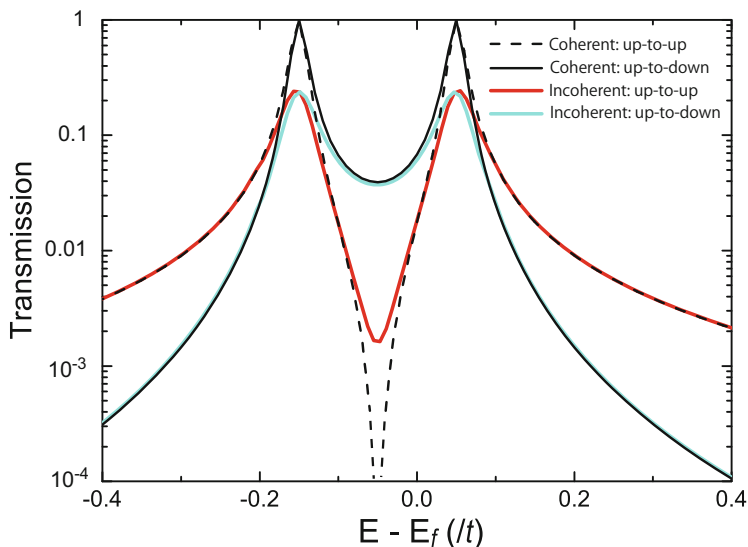


**Fig. 7.16** Calculated transmission probabilities for the  $\uparrow$ -to- $\uparrow$  and  $\uparrow$ -to- $\downarrow$  processes with the coherent two-probes Green's function and incoherent four-probes Green's function approaches. The tight-binding parameters adopted in the calculations are  $0.1t$  of  $t_c$  and  $0.2t$  of  $J$

was used in Fig. 7.16); therefore, two transmission peaks appear at the positions in both processes. As expected in the matrix forms, the spin-flip process shows a parabolic transmission between the two peaks, and the no-flip process shows a clear drop at the mid-gap of the two eigenlevels. This confirms that the process-dependent matrix division is a useful way to understand the intrinsic transport properties (i.e., *constructive* or *destructive*). The next point to be considered is the influence of the incoherent processes that are neglected in the previous framework. In order to discuss this point, the differences between the results from the Green's function based only on coherent processes and wave-packet propagation have to be recognized, and the relationship between the results from the wave-packet method and Green's function including incoherent processes has to be discussed. These comparisons were made in the previous study [24], and excellent correspondence between the Green's function with incoherent processes and the wave-packet method was confirmed. Therefore, in the next section, the Green's function including incoherent processes is introduced. The simulations for charge transport using wave-packet dynamics can be found in applications for organic molecular systems [30–33].

### 7.2.4.2 Incoherent Approach for the Spin-Flip Process

The coherent approximation made in the previous part includes a clear shortcoming in that the division of the entire process into  $\uparrow$ -to- $\downarrow$  and  $\uparrow$ -to- $\uparrow$  processes eliminates the interference between the two processes. Thus, the missing processes in the coherent  $\uparrow$ -to- $\downarrow$  are i) the escape (transmission) of an electron with up-spin at site  $s$  to the right-electrode  $s + 1$  with the same spin, and ii) the reflection back effect of this process into the  $\uparrow$ -to- $\uparrow$  process. This is related to the hopping integrals  $-t_c$  at  $(s\uparrow\downarrow, s+1\uparrow)$  and  $(s+1\uparrow, s\uparrow\downarrow)$  of  $\mathbf{H}_{\text{spin}}$ , which are neglected in  $\mathbf{H}_{s\uparrow\downarrow}^{(\text{SF})}$ . To take the missing effects into account in the Green's function approach, an excess probe can be introduced using an appropriate self-energy [8]. The incoherent effect to be included is the interaction  $-t_c$  between site  $s$  and the right electrode site  $s+1$  with the same spin; therefore, the  $2 \times 2$  self-energy matrix can be written as

$$(\Sigma_{s\uparrow\downarrow}^s)_{ij} = t_c^2 g_{\text{elec}} \delta_{ij} \delta_{i1}. \quad (7.20)$$

Similarly, the missing processes in the coherent  $\uparrow$ -to- $\uparrow$  are iii) the escape (transmission) of an electron with down-spin at site  $s$  to the right-electrode  $s + 1$  with the same down-spin, and iv) the reflection back effect of this process into the  $\uparrow$ -to- $\downarrow$  process. This is related to the hopping integrals  $-t_c$  at  $(s\downarrow\uparrow, s+1\downarrow)$  and  $(s+1\downarrow, s\downarrow\uparrow)$  of  $\mathbf{H}_{\text{spin}}$ , which are neglected in  $\mathbf{H}_{s\uparrow\downarrow}^{(\text{NF})}$ . The related  $2 \times 2$  self-energy matrix is<sup>3</sup>:

$$(\Sigma_{s\downarrow\uparrow}^s)_{ij} = t_c^2 g_{\text{elec}} \delta_{ij} \delta_{i2}. \quad (7.21)$$

Therefore, the Green's function including the incoherent processes (i.e., the four-probe Green's function) can be written as

$$\mathbf{G}_4^{A/R}(E) = [\mathbf{E}\mathbf{1} - \mathbf{H}^{(s1)} - \Sigma_L^{A/R} - \Sigma_R^{A/R} - \Sigma_{s\uparrow\downarrow}^{sA/R} - \Sigma_{s\downarrow\uparrow}^{sA/R}]^{-1}, \quad (7.22)$$

where  $\mathbf{H}^{(s1)}$  is the  $2 \times 2$  matrix at site  $s$  ( $s\uparrow\downarrow$  and  $s\downarrow\uparrow$ ) in Eqs. 7.18 and 7.19.

The solid blue and red lines in Fig. 7.16 are the calculated transmission functions using the four-probe Green's function, which show almost perfect correspondence with the results obtained with the WP dynamics (not shown). The peak height at the resonance position (i.e., eigenlevels) is slightly decreased as a result of the additional escape processes (incoherent processes). In addition, the anti-resonance observed in the coherent no-flip process is slightly weakened, although it is still recognizable. Thus, the coherent approximation is confirmed as reasonable to capture the transport properties qualitatively, and a quantitative description for the incoherent processes is possible using the Green's function including additional appropriate self-energies.

<sup>3</sup>The explanations for the neglected incoherent processes given in this part are originally from Ref. [24]. However, there is a typographical error in Eq. (21) of Ref. [24]; the equations shown here in this section are correct.

### 7.3 Summary

In this chapter, the orbital rule (or HOMO-LUMO rule) to achieve a qualitative understanding of electron transport in molecular junctions was introduced on the basis of the Green's function method. There is no limitation in the orbital basis used for the orbital rule; AOs, MOs, and spin-spin direct product bases are available for an understanding of the *constructive* and *destructive* interference effects in electron transport. In the AO picture, the two-site tight-binding model was adopted to determine the key factor in *constructive* and *destructive* interference. This model is a minimum model because only the HOMO and LUMO appear as the orbital levels of the two-site model. Many examples of the orbital rule applied to other large molecules (i.e., multi-orbital systems) can be found in the literature; for example, nanographite with armchair and zigzag edges [7, 12, 14], DNA molecules [13], aromatic dithiolate molecules [16], metal-phthalocyanine molecules [17], photochromic molecules [18], and  $\pi$ -stacked molecules [11, 34–37]. In a recent work, a concept for a conductance decay-free junction was derived from the orbital rule. In the molecular orbital picture, the triangular three-site model was used to explain the observed *destructive* interference of an anthraquinone molecular unit in a recent experiment. The key is the orbital-phase exchange that originates from the sign-change of the hopping parameters between neighboring sites.

In the final part of this chapter, the *spin-flip transport* in a simple 1D tight-binding chain including a localized spin was discussed using the Green's function with and without incoherent spin-flip processes on the basis of the spin-spin direct product base. The spin exchange coupling  $J$ , between the conduction and localized electron spins, was taken into account through the s-d tight-binding Hamiltonian. In this sense, the spin-junction is a mimic of an aromatic molecule that includes a d-metal center. The transmission probabilities that depend on the spin directions at the drain electrode were analyzed; the  $\uparrow$ -to- $\uparrow$  process for the incoming up-spin is transmitted as the outgoing up-spin, and the  $\uparrow$ -to- $\downarrow$  process for the incoming up-spin is transmitted as the outgoing down-spin. The Green's function calculations show that the transmission probabilities for both processes have large peaks at the eigenlevels of the spin singlet ( $-3J/4$ ) and triplet ( $J/4$ ) states and that the transmission probabilities exhibit different properties, depending on the spin-flip processes at the mid-gap (anti-resonance level) of the two eigenlevels; the  $\uparrow$ -to- $\uparrow$  process shows an abrupt drop, whereas the  $\uparrow$ -to- $\downarrow$  process shows a parabolic transmission. The similarity of the matrix forms for  $\uparrow$ -to- $\downarrow$  transport and a two-site constructive junction (i.e., L-junction) was easily confirmed with reference to the orbital rule for coherent electron transport in a molecular junction; the similarity between  $\uparrow$ -to- $\uparrow$  transport and a two-site destructive junction (i.e., T-junction) was also recognized.

It should be emphasized that the orbital rule is a qualitative rule for the understanding of transport properties; however, the concepts derived from the rule will lead to a wide range of applications for molecular- and nanojunctions.

**Acknowledgements** T.T. sincerely thanks Prof. Kazunari Yoshizawa for contributions and support toward the development of the orbital rule, and Drs. Masakazu Kondo, Aleksandar Staykov, Daijiro Nozaki, Yuta Tsuji, and Xinqian Li for their extensional applications of the orbital rule. This research was supported by Grants-in-Aid for Scientific Research (Innovative Areas “ $\pi$ -System Figuration: Control of Electron and Structural Dynamism for Innovative Functions”) from the Japan Society for the Promotion of Science and Grant-in-Aid for Young Scientists (B) and from the Ministry of Education, Culture, Sports, Science, and Technology (MEXT) of Japan.

## References

1. Aharonov Y, Bohm D (1959) Significance of electromagnetic potentials in the quantum theory. *Phys Rev* 115:485–491
2. Peshkin M, Tonomura A (1989) *The Aharonov–Bohm effect*. Springer
3. Sautet P, Joachim C (1988) Electronic interference produced by a benzene embedded in a polyacetylene chain. *Chem Phys Lett* 153:511–516
4. Kemp M, Roitberg A, Mujica V, Wanta T, Ratner M A (1996) Molecular wires: extended coupling and disorder effects. *J Phys Chem* 100:8349
5. Emberly E G, Kirczenow G (1999) Antiresonances in molecular wires. *J Phys: Condens Matter* 11:6911
6. Baer R, Neuhauser D (2002) Phase coherent electronics: a molecular switch based on quantum interference. *J Am Chem Soc* 124:4200–4201
7. Tada T, Yoshizawa K (2002) Quantum transport effects in nanosized graphite sheets. *ChemPhysChem* 3:1035
8. Datta S (1995) *Electronic transport in mesoscopic systems*. Cambridge University Press, Cambridge
9. Landauer R (1957) Spatial variation of currents and fields due to localized scatterers in metallic conduction. *IBM J Res Dev* 1:223–231
10. Caroli C, Combescot R, Nozieres P, Saint-James D (1971) Direct calculation of the tunneling current. *J Phys C* 4:916
11. Tada T, Yoshizawa K (2015) Molecular design of electron transport with orbital rule: toward conductance-decay free molecular junctions. *Phys Chem Chem Phys* 17:32099–32110
12. Tada T, Yoshizawa K (2003) Quantum transport effects in nanosized graphite sheets. II. Enhanced transport effects by heteroatoms. *J Phys Chem B* 107:8789–8793
13. Tada T, Kondo M, Yoshizawa K (2003) Theoretical measurements of conductance in an (AT)12 DNA molecule. *ChemPhysChem* 4:1256
14. Tada T, Yoshizawa K (2004) Reverse exponential decay of electrical transmission in nanosized graphite sheets. *J Phys Chem B* 108:7565–7572
15. Kondo M, Tada T, Yoshizawa K (2004) Wire-length dependence of the conductance of oligo (p-phenylene) dithiolate wires: a consideration from molecular orbitals. *J Phys Chem A* 108:9143
16. Tada T, Nozaki D, Kondo M, Hamayama S, Yoshizawa K (2004) Oscillation of conductance in molecular junctions of carbon ladder compounds. *J Am Chem Soc* 126:14182
17. Tada T, Hamayama S, Kondo M, Yoshizawa K (2005) Quantum transport effects in copper (II) phthalocyanine sandwiched between gold nanoelectrodes. *J Phys Chem B* 109:12443
18. Kondo M, Tada T, Yoshizawa K (2005) A theoretical measurement of the quantum transport through an optical molecular switch. *Chem Phys Lett* 412:55
19. Yoshizawa K, Tada T, Staykov A (2008) Orbital views of the electron transport in molecular devices. *J Am Chem Soc* 130:9406–9413
20. Tsuji Y, Staykov A, Yoshizawa K (2009) Orbital control of the conductance photoswitching in diarylethene. *J Phys Chem C* 113:21477–21483

21. Li X, Staykov A, Yoshizawa K (2010) Orbital views of the electron transport through polycyclic aromatic hydrocarbons with different molecular sizes and edge type structures. *J Phys Chem C* 114:9997–10003
22. Li X, Staykov A, Yoshizawa K (2011) Orbital views of the electron transport through heterocyclic aromatic hydrocarbons. *Theor Chem Acc* 50:6200–6209
23. Tsuji Y, Staykov A, Yoshizawa K (2011) Orbital views of molecular conductance perturbed by anchor units. *J Am Chem Soc* 133:5955–5960
24. Tada T, Yamamoto T, Watanabe S (2011) Molecular orbital concept on spin-flip transport in molecular junctions. *Theor Chem Acc* 130:775–788
25. Yoshizawa K (2012) An orbital rule for electron transport in molecules. *Acc Chem Res* 45:1612–1621
26. Li X, Staykov A, Yoshizawa K (2012) Orbital views on electron-transport properties of cyclophanes: insight into intermolecular transport. *Bull Chem Soc Jpn* 85:181–188
27. Taniguchi M, Tsutsui M, Mogi R, Sugawara T, Tsuji Y, Yoshizawa K, Kawai, T (2011) Dependence of single-molecule conductance on molecule junction symmetry. *J Am Chem Soc* 133:11426–11429.
28. Guédon CM, Valkenier H, Markussen T, Thygesen KS, Hummelen JC, van der Molen SJ (2012) Observation of quantum interference in molecular charge transport. *Nat Nanotechnol* 7:305–309
29. Nazin G V, Qiu X H, Ho W (2003) Visualization and spectroscopy of a metal-molecule-metal bridge. *Science* 302:77
30. Troisi A, Orlandi G (2006) Charge-transport regime of crystalline organic semiconductors: diffusion limited by thermal off-diagonal electronic disorder. *Phys Rev Lett* 96:086601
31. Ishii H, Kobayashi N, Hirose K (2010) Order-N electron transport calculations from ballistic to diffusive regimes by a time-dependent wave-packet diffusion method: Application to transport properties of carbon nanotubes. *Phys Rev B* 82:085435
32. Terao J, Wadahama A, Matono A, Tada T, Watanabe S, Seki S, Fujihara T, Tsuji Y (2013) Design principle for increasing charge mobility of pi-conjugated polymers using regularly localized molecular orbitals. *Nat Commun* 4:1691
33. Ito Y, Takai K, Miyazaki A, Sivamurugan V, Kiguchi M, Ogawa Y, Nakamura N, Valiyaveettil S, Tada T, Watanabe S, Enoki T (2014) Anomalous metallic-like transport of Co–Pd ferromagnetic nanoparticles cross-linked with pi-conjugated molecules having a rotational degree of freedom. *Phys Chem Chem Phys* 16:288–296
34. Kiguchi M, Takahashi T, Takahashi Y, Yamauchi Y, Murase T, Fujita M, Tada T, Watanabe S (2011) Electron transport through single molecules comprising aromatic stacks enclosed in self-assembled cages. *Angew Chem Int Ed* 50:5708–5711
35. Tsuji Y, Staykov A, Yoshizawa K (2011) Molecular rectifier based on pi-pi stacked charge transfer complex. *J Phys Chem C* 116:2575–2580
36. Kiguchi M, Inatomi J, Takahashi Y, Tanaka R, Osuga T, Murase T, Fujita M, Tada T, Watanabe S (2013) Highly conductive  $[3 \times n]$  gold-ion clusters enclosed within self-assembled cages. *Angew Chem Int Ed* 52:6202–6205
37. Fujii S, Tada T, Komoto Y, Osuga T, Murase T, Fujita M, Kiguchi M (2015) Rectifying electron-transport properties through stacks of aromatic molecules inserted into a self-assembled cage. *J Am Chem Soc* 137:5939–5947

# Chapter 8

## Theoretical Aspects of Quantum Transport and Computational Modeling of Molecular Electronic Device

Hisao Nakamura

**Abstract** Recent techniques to create regulated nano-contact and precise measurement of transport properties such as current-voltage (IV) characteristics provide new insight of charge transfer and transport in a sub-10 nm-scale device. In this chapter, several theoretical concepts to bridge charge transfer (chemistry) and charge transport (physics) theories are described. “Old and new” problems of molecular electronics such as length and temperature dependence of conductance, unimolecular rectifier, etc. are revisited via a modern theoretical approach.

**Keywords** Quantum transport • Electron-phonon interactions • Molecular rectification • First-principles calculation • Nonequilibrium Green’s function • Marcus theory

### 8.1 Introduction

Research of a molecular-scale device has been improved considerably by recent techniques to create regulated nano-contact [1–3] and precise measurement of transport properties such as current-voltage (IV) characteristics [4–9]. The pioneering work of molecular electronics is the proposal of a molecular rectifier by Aviram and Ratner (AR) [10]. Their idea was based on the analogue of a solid *pn* junction [11] to electron transfer between donor and acceptor molecules. However, several historical concepts of molecular electronics have been renewed [12–15], and, furthermore, potential advantages of molecular junctions have been discussed in broader research areas such as photovoltaic conversion [16–19], thermoelectricity [20–26], biosensor [27–29], memory [30–35], and so on. Hereafter, the terminology “molecular junction” represents a system consisting of a single molecule, molecular wire, or molecular film connected to metal electrodes. The varieties of functions relating to transport phenomena are mainly caused by a quantum confinement

---

H. Nakamura (✉)

Research Center for Computational Design of Advanced Functional Materials (CD-FMat), National Institute of Advanced Industrial Science and Technology (AIST), Tsukuba, Japan  
e-mail: [hs-nakamura@aist.go.jp](mailto:hs-nakamura@aist.go.jp)

effect to electrons passing through molecules [36–39]. A quantum confinement effect often gives a characteristic transport behavior by discrete resonant states, an interference effect, and so on. It depends on competition of the intrinsic molecular property (i.e., molecular orbitals: MO) and the contact effect of the molecular conductor and metal electrodes. In this sense, understanding quantum transport mechanism required fusion of the MO theory and Green's function theory or the scattering theory.

Green's function framework is very convenient to perform theoretical analysis for molecular junctions since correction terms, e.g., field effect, electron-electron interactions, and electron-phonon interactions, can be introduced systematically by self-energy terms. Nonequilibrium Green's function (NEGF) theory is often adopted for modeling transport processes under finite bias voltage [40–43]. In the past decade, the atomistic computational modeling of molecular junctions has been rapidly developed by combination of NEGF and first-principles mean-field theory, in particular density functional theory (DFT) [44–54]. The NEGF-DFT approach becomes now a standard tool since DFT has better computational scalability to the system size than other electronic structure theories. However, there are some limitations in first-principles approach yet. For an example, behavior of conductance and transport mechanism depend on length scale of molecular wire or thickness of the film. It is difficult to analyze these universal behaviors by only first-principles calculations due to huge computational demands. Therefore, theoretical modeling and computational study based on first-principles calculations should be adopted complementarily to understand fundamental mechanisms and design a new functional device.

In this chapter, the aim is to sketch theoretical aspects to understand the quantum transport process in molecular junctions based on concerto of theoretical and computational models with reference to recent experimental studies. Throughout this chapter, the atomic unit ( $e = \hbar = 1$ ) is adopted to present theoretical formulations as far as there is no declining.

## 8.2 Theory of Electric Transport in Molecular Junctions

In order to realize a functional molecular device, the first step is to understand charge migration mechanism and control it. Theoretically, two opposite mechanisms are usually considered. One is coherent transport, which consists of a tunneling (band-like) transport, and the other is hopping mechanism as decoherence limit of charge migration [55, 56]. The former mechanism is dominant when length scale of the conductor is shorter than the mean free path length of the charge carrier (electron/hole). On the contrary, the latter mechanism assumes that the carrier loses its coherence by electron-phonon interaction, i.e., quantum nature of a carrier is lost in the hopping mechanism. In practical molecular junctions, the two mechanisms *coexist*. Coherence can survive locally over several molecular units though the charge migration is sequential hopping between each moiety of unit groups. Hence,

the suitable definition of “hopping site” depends on intrinsic electric structures of molecular units when one applies hopping model to a practical system. However, the two mechanisms show distinct universal length [57–60] and temperature [61, 62] dependence of electric conductance. Crossover of the universal behavior of conductance is expected as its dependence on the molecular wire length ( $L$ ) and temperature ( $T$ ) when the conductance measurement is examined by varying  $L$  and  $T$  in a wide range.

It is well known that the conductance decreases exponentially as a function of  $L$ ,  $\sigma = \sigma_0 \exp(-\beta L)$  [55, 63], for conjugated organic molecular wires when  $L$  is sufficiently short. The constant  $\sigma_0$  is determined by the structure of the contact. The exponential behavior was measured for many conjugated molecular wires, and the  $\beta$  value is  $10^{-1} \sim 10^0 \text{ \AA}^{-1}$  for most conjugated molecules [64–67]. Observation of “length dependence crossover” has been also reported by several groups, and the crossover is usually explained by change of the coherent to hopping mechanism [57, 64, 68–70]. Choi and coworkers made oligophenyleneimine (OPI) wires bounded to Au substrates [64]. They found length dependence crossover at  $L \sim 4.0 \text{ \AA}$ . The fitted  $\beta$  is  $0.30 \text{ \AA}^{-1}$  in short  $L$ , while it is  $0.09 \text{ \AA}^{-1}$  for  $L > 4.0 \text{ \AA}$ . Length dependence was measured systematically for similar oligomers, i.e., oligophenylenetriazole (OPT) [57] and oligonaphthalenefluoreneimine (ONI) [68] wires by Frisbie’s group. In all cases, clear crossover is presented at the length of four or five molecular units, and they claim that the plot behaves as linear function of  $L$ , i.e., “transition” of the mechanism from tunneling to hopping.

As shown later, exponential behavior of conductance  $\sigma$  is the typical feature of the off-resonant tunneling system, where the energy gap of the Fermi level ( $E_F$ ) and conduction band of the molecular conductor is sufficiently large. On the contrary,  $\beta$  can be considerably small and  $\sigma$  becomes nearly constant as a function of  $L$  when tunneling is resonant, e.g., nanowire of metallic atoms. Instead of length dependence crossover, another characteristic behavior of  $\sigma$  is observed for monoatomic metal wires such as Au, Pt, and Ir atoms [71, 72]. Smit et al. observed an oscillatory evaluation of  $\sigma$  depending on the number of atoms in the chain being even/odd parity [71]. They concluded that the parity oscillation was universal for metal monoatomic chain and thus length dependence of  $\sigma$  is not always linear or exponential. These experimental findings suggest difficulty to identify the dominant transport mechanism only by analyzing  $\beta$  obtained by a limited number of wire length samples, and *simultaneous* consideration of  $L$  and  $T$  dependence is necessary. Below, the general theory and qualitative analysis of the universal behaviors are presented by using Green’s function framework. An inelastic transport process by electron-vibron interaction is also treated as the extension of the same Green’s function approach.

### 8.2.1 Length Dependence of Conductance and Charge Migration Mechanisms

In order to describe an analytical theory, the single-level tight-binding model is very useful. Here, the theoretical model and analysis by Asai and Fukuyama [73] is introduced, which consists of a uniform chain and cubic lattice electrodes. The schematic figure and symbols of tight-binding parameters are given in Fig. 8.1. The resulting model Hamiltonian is written as follows [73]:

$$\begin{aligned}
 H &= H_L + H_R + H_{\text{wire}} + H_T \\
 H_{L/R} &= \sum_{0 < i_z} \sum_{k_x, k_y} \left( \varepsilon_{L/R} - 2t_M^{L/R} (\cos k_x a_{L/R} + \cos k_y a_{L/R}) \right) c_{k_x, k_y, i_z}^\dagger c_{k_x, k_y, i_z} \\
 &\quad - t_M^{L/R} \sum_{i_z} \sum_{j_z = i_z \pm 1} \sum_{k_x, k_y} c_{k_x, k_y, i_z}^\dagger c_{k_x, k_y, j_z} \\
 H_{\text{wire}} &= \sum_{i=1}^N \varepsilon c_i^\dagger c_i - t \sum_i \sum_{j=i \pm 1} c_i^\dagger c_j \\
 H_T &= -t_L (c_{I_1}^\dagger c_1 + c_1^\dagger c_{I_1}) - t_R (c_{I_N}^\dagger c_N + c_N^\dagger c_{I_N})
 \end{aligned} \tag{8.1}$$

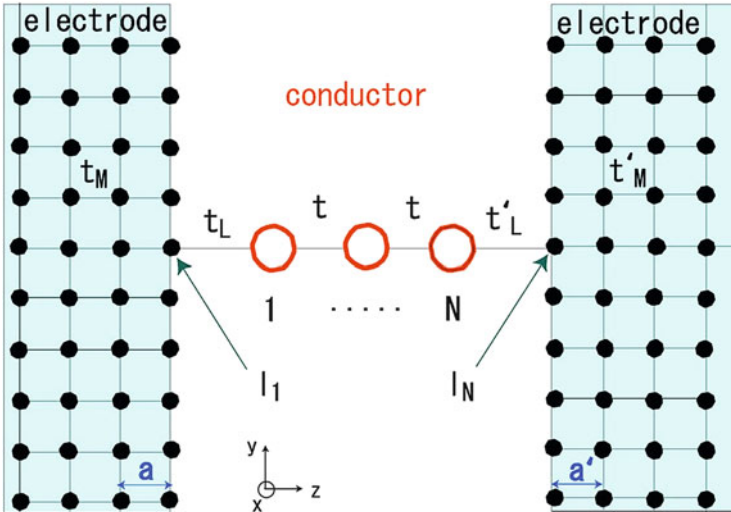


**Fig. 8.1** A schematic view of the tight-binding model for the nano-contact composed of a monoatomic wire and electrodes [73]

The annihilation operator,  $c_{k_x, k_y, z}$ , relates to an electronic state of the electrode labeled by two-dimensional band  $\kappa$  point  $(k_x, k_y)$  and real-space  $z$  (layer  $i_z$ ). The operators  $c_i$ ,  $c_{I_1}$ , and  $c_{I_N}$  are defined by the site in the chain and the left/right contact sites  $I_1/I_N$ , respectively. For simplicity, we take symmetric electrodes, i.e., the parameters are set as  $t_M^L = t_M^R \equiv t_M$ ,  $t_L = t_R \equiv t_c$ ,  $\varepsilon_L = \varepsilon_R$ . The cubic lattice constant is taken as  $a_L = a_R \equiv a$ . We set the metallic site energy of electrodes to zero. Hence,  $E_F$  is also zero when the metal is half-filling. Spin dependence of Hamiltonian is omitted in the present model.

Assuming that left and right electrodes are in thermal equilibrium, i.e., electrons are in Fermi distribution  $f$ , the electric current is expressed by NEGF formalism as follows [40, 43]:

$$I(V) = g_0 \int dE \text{Tr} [\Gamma_L(E) G^r(E) \Gamma_R(E) G^a(E)] (f_L(E, \mu_L, T) - f_R(E, \mu_R, T)) \quad (8.2)$$

where  $V$  is bias voltage and equal to the difference of chemical potential of left and right electrodes and  $\mu_L - \mu_R$ .  $G^{r/a}$  is retarded/advanced Green's function defined in the focused device region, which is usually termed as scattering region.  $\Gamma_{L/R}$  is defined as  $i \left( \Sigma_{L/R}^r - \Sigma_{L/R}^a \right)$ , and  $\Sigma_{L/R}^{r/a}$  is the retarded/advanced self-energy term of (semi-infinite) the left/right electrode. Trace part is transmission coefficient  $\tau(E)$ , and  $g_0$  is conductance unit including spin factor. The conductance at zero bias and temperature  $T$  is obtained by

$$\sigma(T) = g_0 \int dE \tau(E) \left( -\frac{\partial f}{\partial E} \right) \quad (8.3)$$

When  $T$  is not sufficiently high, the derivative of the Fermi function in Eq. 8.3 is close to the delta function. Thus, conductance relates to the transmission coefficient at  $E_F$ . i.e.,  $\sigma(T) \approx \sigma \equiv g_0(E_F)$ .

In the tight-binding model Hamiltonian, Eq. 8.1, Green's function and self-energy terms can be represented by an analytical form. The scattering region is the chain and the self-energy terms are added to the left/right terminal atomic sites of the chain. The resulting conductance  $\sigma$  is [73]

$$\sigma = 4\pi^2 g_0 t_c^4 \tilde{\rho}_c^2 \frac{|\lambda_1 - \lambda_2|^2}{\left| (\lambda_1 + \tilde{\Sigma})^2 e^{i(N-1)\Theta_1} e^{\beta_1(N-1)} - (\lambda_2 + \tilde{\Sigma})^2 e^{i(N-1)\Theta_2} e^{\beta_2(N-1)} \right|^2} \quad (8.4)$$

where  $\lambda_{1/2} = \frac{\Delta}{2} \pm \sqrt{\frac{\Delta^2}{4} - t^2}$  and  $\Delta$  is the energy gap  $E_F - \varepsilon$ .  $\beta_{1/2}$  and  $\Theta_{1/2}$  are defined as  $e^{\beta_{1/2}} \equiv \left| \lambda_{1/2}/t \right|$  and  $e^{i\Theta_{1/2}} \equiv \frac{\lambda_{1/2}/t}{|\lambda_{1/2}/t|}$ , respectively. The retarded self-

energy of each electrode is

$$\tilde{\Sigma} = \pi t_L^2 \left[ P \int \frac{dE'}{\pi} \frac{\rho_c(E')}{E' - E_F} + i\tilde{\rho}_c \right] \quad (8.5)$$

The term  $\tilde{\rho}_c$  is the electron density of state (DOS) on the left (right) electrode terminal site  $I_1$  ( $I_N$ ) at  $E = E_F$ ;  $\tilde{\rho}_{I_1(=N)} E_F$  and  $\tilde{\rho}_c$  are also calculated analytically. Equation 8.4 is useful to figure out the relation between conductance and the site energy level alignment, which is the most essential intrinsic parameter of molecular junctions. The analytical expression of  $\beta$  is derived straightforwardly from Eq. 8.4, and the parameter  $\chi \equiv \left| \frac{\Delta}{2t} \right|$  gives threshold of the tunneling regimes. When  $\chi > 1$ ,  $\Theta_{1/2} \approx 0$  and  $\beta_{1/2} \approx \ln \left( \left| \left| \Delta/2t \right| \pm \sqrt{\Delta^2/4t^2 - 1} \right| \right)$ , respectively. When the tunneling is completely off-resonant, i.e.,  $y \gg 1$ , the values of  $\beta_{1/2}$  are  $e^{\beta_1} \rightarrow \left| \Delta/t \right|$  and  $e^{\beta_2} \rightarrow 0$ . Hence,  $d_0$ , the conductance in the off-resonant tunneling, is expressed by the exponential function of  $L$  as

$$\sigma \approx 4\pi^2 g_0 t_c^4 \tilde{\rho}_c^2 \frac{|\lambda_1 - \lambda_2|^2}{|\lambda_1 + \tilde{\Sigma}|^2} e^{-\beta L} \quad (8.6)$$

where the distance between neighboring sites (molecular units) is set to  $d_0$  and  $\beta$  is

$$\beta = \frac{2 \ln(\Delta/t)}{d_0} \quad (8.7)$$

This analytical expression tells that there are distinct regimes of exponential and non-exponential behavior specified by a threshold value, i.e.,  $\beta_{th} = \frac{2 \ln 2}{d_0}$ .

On the contrary,  $\chi \leq 1$ , and the transport is resonant tunneling or band-like transport. One can find clear conductance oscillation as a function of  $L$  (or number of sites in the chain) by plotting Eq. 8.6 when the parameter is set to  $\chi \leq 1$ . When  $\chi \approx 0$ , the oscillation of  $\sigma$  is even/odd parity for the number of the sites in the wire. Furthermore, theoretical calculation predicts the change of parity (even/odd or odd/even) is reversible by change of  $\chi$ . With increasing  $\chi$  to 1, the periodicity of oscillation becomes large and infinite at  $\chi \rightarrow 1$ . Hence, validity of  $\beta$  estimated by a limited number of data by experiments or first-principles calculations has to be examined carefully when a system is more complex molecular wire (e.g., multilevel sites) and likely quasi-resonant tunneling,  $\chi \approx 1$ . Adding to length dependence, it is worthwhile to note the amplitude of conductance oscillation. The amplitude is governed by a ratio of transfer integrals,  $t_c^2/t_M$  and  $t$ . There is a threshold value,  $\left| \frac{t_c^2/t_M}{t} \right|$ , which gives perfect transmission, and the amplitude becomes large when deviation from the threshold increases.

Formulation of hopping mechanism is derived by the NEGF framework when the decoherence term such as electron-vibron interaction and electron-electron interaction is large. Here, the decoherence term is the coupling term of electron and

inter-/intramolecular vibration (vibron) in the present case though other terms (e.g., impurity scattering, electron-electron scattering) are also possible. It is sufficient to focus on only charge migration between the nearest neighboring sites of the wire. Following the argument by Yeganeh and coworkers [74], the simplified model Hamiltonian is adopted, where only the site “0” couples strongly with vibron (i.e., source of decoherence) of the wire:

$$H_{\text{wire}} = \varepsilon c_0^\dagger c_0 + \sum_i \varepsilon c_i^\dagger c_i - t \sum_i \sum_{j=i\pm 1} c_i^\dagger c_j + M(b + b^\dagger) c_0^\dagger c_0 + \Omega_0 b^\dagger b \quad (8.8)$$

where  $M$  is electron-vibron coupling strength and  $b^\dagger(b)$  is the creation (annihilation) operator of vibron, whose frequency is  $\Omega_0$ . In the strong coupling limit, applying canonical transformation (Lang-Firsov transformation) [75, 76] is convenient:

$$\begin{aligned} \bar{H}_{\text{wire}} &= \exp\left(\frac{M}{\Omega_0} c_0^\dagger c (b^\dagger - b)\right) H_{\text{wire}} \exp\left(-\frac{M}{\Omega_0} c_0^\dagger c (b^\dagger - b)\right) \\ &= \left(\varepsilon - \frac{M^2}{\Omega_0^2}\right) \bar{c}^\dagger \bar{c} - \bar{t} \sum_{i=\pm 1} \left(\bar{c}^\dagger c_i + c_i^\dagger \bar{c}\right) + \varepsilon \sum_{i \neq 0} c_i^\dagger c_i + t \sum_i \sum_{j=i\pm 1} \left(c_i^\dagger c_j + c_j^\dagger c_i\right) \\ &= H_{\text{hop}} + \varepsilon \sum_{i \neq 0, \pm 1} c_i^\dagger c_i + t \sum_i \sum_{j=i\pm 1} \left(c_i^\dagger c_j + c_j^\dagger c_i\right) \end{aligned} \quad (8.9)$$

The site “0” is the source of decoherence. The new operators,  $\bar{c}$  and  $\bar{t}$ , are defined as  $c_0 \exp\left(\frac{-M}{\Omega_0} (b^\dagger - b)\right)$  and  $t \exp\left(\frac{-M}{\Omega_0} (b^\dagger - b)\right)$ , respectively. Focusing on the Hamiltonian of hopping site  $H_{\text{hop}}$ , charge migration rate is derived by using Eq. 8.2 where the left and right electrodes are replaced to the sites of  $i \neq 0$  in Eq. 8.9. Then one gets the hopping conductance as  $\sigma = -2\pi g_0 \bar{t}^2 \text{Im}G^r(\varepsilon)$ . Green’s function is now defined by  $H_{\text{hop}}$ . Since  $H_{\text{hop}}$  consists of the vibron term, we consider finite temperature Green’s function, i.e.,

$$\begin{aligned} G^r(\varepsilon) &= \sum_n \exp\left\{-\left(\frac{M}{\Omega_0}\right)^2 (2N_{BE} + 1)\right\} I_n\left(2\left(\frac{M}{\Omega_0}\right)^2 \sqrt{N_{BE}(N_{BE} + 1)}\right) \\ &\quad \times \exp\left(\frac{n\Omega_0}{2k_B T}\right) \left(\varepsilon - \left(\varepsilon_0 - \frac{M^2}{\Omega_0^2}\right) - n\Omega_0 + i\delta\right)^{-1} \end{aligned} \quad (8.10)$$

where  $I_n$  is the Bessel function. Introducing an asymptotic form of the Bessel function and after several algebras [74], the conductance is expressed as a high-temperature limit

$$\sigma \approx \frac{2\pi g_0 \bar{t}^2}{\sqrt{4\pi \lambda k_B T}} \exp\left[-\frac{(\bar{\Delta} - \bar{\lambda})^2}{4\lambda k_B T}\right] \quad (8.11)$$

where  $\tilde{\Delta}$  relates redox potential of the two sites and  $\tilde{\lambda}$  is equal to  $\frac{M^2}{\Omega_0}$ . Equation 8.11 is formally similar with the electron transfer rate expression by the Marcus theory [55, 77]. The analogue of Marcus's electron transfer rate theory and charge migration by hopping mechanism (polaron) has been often adopted for analysis of organic semiconductor and polymer [78]. For many conjugated molecular wires, one hopping site can consist of two or more molecules and hopping is multi-step. Conductance is independent or linear to  $L$  when transport is dominated by hopping mechanism (decoherence limit). Equation 8.11 predicts Arrhenius-type thermal activation for hopping mechanism.

### 8.2.2 *Universal Temperature Dependence Crossover and Inelastic Scattering Effect by Electron-Vibron Interaction*

In Sect. 8.2.1, universal “length dependence crossover” and the two different charge migration mechanisms were described. Observation of sufficiently large thermal activation energy is considered to be a direct evidence of hopping mechanism. Equation 8.11 was proved by NEGF framework with strong coupling limit of electron-vibron interactions. However, it is not clear whether temperature dependence and relating thermal activation energy is decided uniquely or not by given  $L$ . As a theoretical view, a relating question arises: Is strong electron-vibron coupling a necessary condition to realize the Arrhenius-type behavior? The questions have been opened by Selzer et al. [61]. They used a sufficiently short molecule to avoid strong decoherence caused by large  $L$ : thus, transport is expected to be almost coherent. They observed temperature dependence crossover in the same 1-nitro-2,5-di(phenylethynyl-4-mercapto)benzene molecule. A similar crossover has been reported for biomolecular junctions, e.g., DNA molecule by Yoo et al. [79] and dry bacteriorhodopsin by Sepunaru et al. [80]. Recently, Lee et al. measured temperature dependence of a single oligothiophene molecular wire, where each measured wire contains 5 (5T), 14 (14T), and 17 (17T), respectively [81], as shown in Fig. 8.2. Temperature dependence crossover is not found in the short (5T) and long (17T) wires, and each conductance plot can be explained by coherence and hopping mechanisms as usual. However, in the middle length (14T), the conductance is almost unchanged ( $\sigma \approx 1.8 \times 10^{-5} G_0$ ) up to 350 K, and then it increases with increasing temperature ( $\sigma \approx 1.8 \times 10^{-5} G_0$ ) at  $T = 450$  K. Since the length is fixed, strength of electron-vibron coupling should be the same. Hence, temperature dependence of decoherence term is responsible rather than dependence of coupling strength.

The same model Hamiltonian of Eq. 8.1 was applied, while electron-vibron interaction by the extended Su-Schrieffer-Heeger (SSH) model was added [81]. Contrary to the canonical transformation, the self-consistent Born approximation (SCBA) was adopted to calculate Green's function, i.e., strength of each coupling is

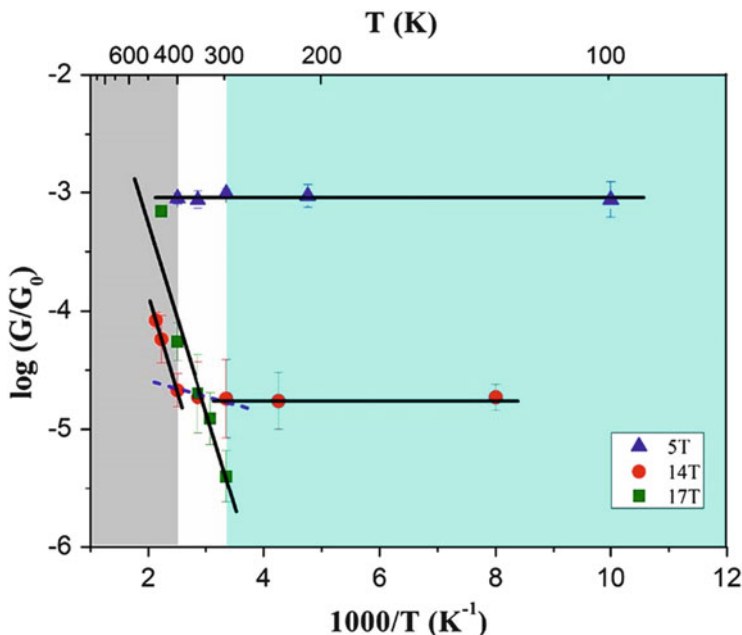


**Fig. 8.2** Plots of temperature dependence of conductance for 5T, 14T, and 17T molecular junctions [81]

assumed to be sufficiently weak. In the SCBA, both nonequilibrium electron and vibron Green's functions (labeled as  $D$ ) are determined simultaneously through electron-vibron self-energy terms,  $\Sigma_{evib}$  (electron) and  $\Pi_{evib}$  (vibron) [82]. Interestingly, SCBA results in successes to reproduce a universal behavior of conductance  $\sigma$  in both low- and high-temperature regimes, i.e., nearly zero and large thermal activation energies. The temperature dependence of the SCBA results was nicely represented by the scaling function  $S(T) = A \exp(-\tanh(B/T)) + C$ , where the form of the function is derived by the single-mode polaron model. The parameter  $B$  represents the activation energy and corresponds to the lowest vibron energy.  $C$  is constant to match the conductance at a low-temperature limit and  $A$  is the adjust parameter. Scaling analysis by  $S(T)$  to the experimental conductance was also applied and showed fairly well agreements with each other. Recall that the present Arrhenius-type behavior is obtained by SCBA of weak electron-vibration coupling approximation. Thus, Arrhenius-type  $\sigma$  and large activation energy are not evidence of the hopping mechanism of strong electron-vibron coupling. High temperature enhances decoherence and provides the thermal activation energy though strength of coupling is weak. In this sense, the concept of "hopping" mechanism should be extended.

As stated above, the electron-vibron interaction affects  $\sigma$  even when the interaction is weak. Only an inelastic process exchanges energy between electron and

vibron, while both of elastic and inelastic scatterings change electric current by resonance of electron and vibron. Rapid change of electric current is observed when the applied bias matches to the energy  $\Omega_\alpha$  of vibrational mode  $\alpha$ . Hence, the plot of the second derivative of electric current by bias,  $\frac{d^2 I}{dV^2}$ , provides a peak or dip at  $V \approx \Omega_\alpha$  and is called inelastic electron tunneling spectroscopy (IETS) [83–90]. IETS is a fingerprint of the bridge molecule and useful spectroscopic tool to prescribe the bridge molecular species and adsorbed molecular conformation [91]. One of interest is that its shape (peak/dip) of IETS depends on a molecular wire [92]. The peak shape was usually observed in organic molecular junctions [87, 93–98], and the early theory of IETS showed that energy exchange of inelastic processes opens a new channel of tunneling electron, i.e., IETS gives a peak shape for positive bias (and dip for negative bias). On the contrary, Agrait et al. measured IETS of some metal atomic nanowires and found that the shape of IETS is dip at positive bias  $V > 0$  [99, 100]. As shown below, peak/dip relates roughly to that tunneling is off-resonant/resonant.

To analyze IETS, use of the normal mode coordinates is convenient to define vibron Green's function. Nonequilibrium effect and details of thermal dissipation of excited vibron energy is often omitted in IETS analysis. Within the model of a single site and single vibrational mode in the wire part like Eq. 8.8, the difference of  $I$  with and without electron-vibron interaction,  $\delta I$ , is evaluated simply by using the lowest-order Born expansion (LOE) [48, 101–103] with omitting the energy shift by the interaction. The second derivative of  $\delta I$  by bias is expressed as follows:

$$\frac{d^2(\delta I)}{dV^2} \approx g_0 M^2 \tau(E_F) \frac{\Delta^2 - (\Gamma_L + \Gamma_R)^2/4}{\left\{ \Delta^2 + (\Gamma_L + \Gamma_R)^2/4 \right\}^2} \frac{d^2 F}{dV^2} \quad (8.14)$$

where the function  $F$  is only a function of  $V$ ,  $T$ , and  $\Omega_\alpha$ :

$$F = (\Omega_\alpha - V) N_{BE}(\Omega_\alpha - V, T) - (\Omega_\alpha + V) N_{BE}(\Omega_\alpha + V, T), \quad (8.15)$$

and  $N_{BE}(\omega, T)$  is the Bose-Einstein function. When  $\Gamma_L$  and  $\Gamma_R$  terms are almost equal, Eq. 8.14 leads to a more simple form as follows:

$$\frac{d^2(\delta I)}{dV^2} \rightarrow g_0 M^2 \tau(E_F) (1 - 2\tau(E_F)) \frac{d^2 F}{dV^2}. \quad (8.16)$$

Equation 8.16 predicts clear peak/dip change at  $\tau(E_F) = 0.5$ , i.e., the sign of IETS depends on that tunneling is resonant (band-like) or off-resonant [104]. More detailed analyses have been performed by SCBA with changing the parameter  $\Delta$  and  $t_M$  [105]. The resulting phase diagram gives the phase boundary of peak and dip as well. The boundary and that calculated by the condition  $\tau(E_F) = 0.5$  agree qualitatively when the correction by real part of self-energies is considered. However, the agreement of SCBA and LOE is not sufficient when the values of  $\Delta$

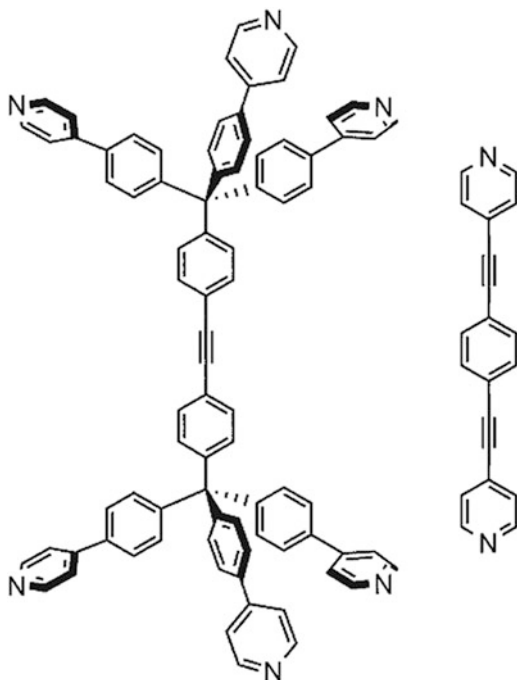
and  $t_M$  are small, which represents resonant tunneling at weak-link contact. In this region, multiple scattering effects will become important for IETS analysis.

### 8.2.3 *MO Engineering and Contact Chemistry via First-Principles Calculations*

Up to now, universal behavior of transport phenomenon of molecular junctions is discussed, and the simple model Hamiltonian approach was very useful for analysis. However, parameterization is very complicated for complex molecules or nanostructured wires, where quantum interference [36, 37, 106–108] due to topology, multi-site effect at an anchoring point, and multilevel effects play essential roles to device functions. Thanks to recent development of computational methods, in particular combination of NEGF and DFT [44, 47–51, 54, 109–112], first-principles transport calculation is possible. Once first-principles results are obtained, we can estimate observables like *IV* characteristic and extract convenient quantities to understand molecular-oriented device feature by using first-principles Green's functions, projected wave functions, and so on.

In the first-principles approach, the scattering region is defined as the region consisting of the molecular part and a sufficiently large number of atomic layers of left and right leads since the electronic structure of the contact (interface) region and deep bulk electrodes must be treated on the equal footings. The self-energy terms are added on the most outer region of the scattering region, i.e., deep bulk region. In NEGF-DFT, Kohn-Sham Hamiltonian is used to define Green's functions: thus, self-energy of electron-electron interaction is incorporated as mean-field potential, Hartree ( $V_H$ ) and exchange-correlation ( $V_{XC}$ ) terms. An external electric field due to bias voltage is also inserted to the Hamiltonian, and perfect screening is assumed in the electrodes. The mean-field approximation makes calculations easy since the relating lesser self-energy term is zero [43, 113]. The most time-consuming step is updating the density matrix and getting a converged result in self-consistent cycles since the numerical integral of the lesser Green's function by energy is necessary. Many algorithms and numerical techniques have been proposed to get fast SCF convergence and reduce computational cost [44, 48, 54, 114, 115]. There are several drawbacks in the standard NEGF-DFT, e.g., underestimating the HOMO-LUMO gap by omitting dynamical correlation, unknown  $V_{XC}$  function applicable to nonequilibrium condition, and so on. Several theoretical efforts have been reported such as an extension to time-dependent DFT framework [116–119], analysis of derivative discontinuity of XC functional [120, 121], and correction by partial GW approximation [122, 123]. In spite of these drawbacks, NEGF-DFT is still a useful and practical tool to perform first-principles transport calculations. Here, we introduce a few examples of the recent NEGF-DFT calculations to show the power of the first-principles transport calculation.

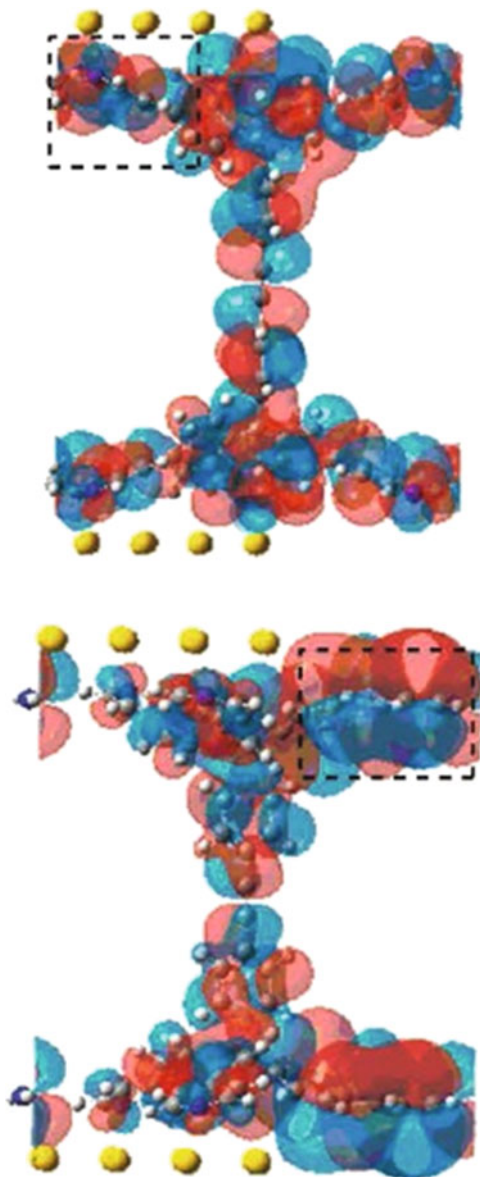
**Fig. 8.3** Chemical structures of diphenylene-ethynylene with single (1Py) and tripodal-leg (3Py) anchors based on pyridine [124]



Designing robust anchoring is as important as synthesizing the conductor to avoid breaks of contact by heating or concentrated electric field. Recently, use of tripodal-leg anchor based on pyridine (**3Py**) was proposed as shown in Fig. 8.3, and better robustness was confirmed by mechanical stability of the three contact points rather than improvement of chemical bond strength [124]. Interestingly, the observed electric conductance of diphenylacetylene anchored by **3Py** is about 140 times larger than that of a single pyridine (**1Py**) anchor unit, in which the tunneling channel is  $\pi$  orbital of N atom. In order to understand the distinct nonadditive contact effect of **1Py** and **3Py**, first-principles calculations are necessary. Two structures of the surface electrodes, (111) and (001), were adopted as computational model systems to perform NEGF-DFT. The resulting  $\sigma$  of the former **3Py** junction was  $1.16 \times 10^{-6} G_0$ , which is close to **1Py**. On the contrary,  $\sigma$  of **3Py** (001) electrodes was  $2.27 \times 10^{-4} G_0$ . The molecular orbital relating to the tunneling is given in Fig. 8.4, and the first-principles results predict formation of  $\pi$  contact at (001) electrode. In other words, the high conductance of the **3Py** anchor can be explained by formation of  $\pi$  contact. The presented example shows importance of “contact chemistry” to design the molecular device [125].

NEGF-DFT is used to calculate not only coherent (ballistic) current but also inelastic electric current by electron-vibron scatterings and is applied to assign IETS [126–134]; however, most of the calculations have been performed within the perturbation theory or LOE theory and applied to assign IETS. The LOE has more simplified expression than that of the rigorous lowest-order Born expansion [103] by

**Fig. 8.4** The plot of wave function of conducting molecular orbital of 3Py junction for Au(111) (*left panel*) and Au(001) electrodes (*right panel*), respectively [124]



introducing approximations like energy averaging [47] and/or WBL [101, 102] and so on. In the standard LOE method implemented to the NEGF-DFT, vibron Green's function  $D$  is represented by normal mode coordinates, and the self-energy  $\Pi'_L + \Pi'_R$  is parameterized to damping constant  $\eta_\alpha$ . This approximation still includes the nonequilibrium term of vibron (vibron excitation) though it is not accurate enough to estimate local heating. LOE is a practical approach to combine first-principles

methods and applicable to simulate inelastic processes at low bias when the tunneling is off-resonant or resonance is not as narrow as the scale of  $\Omega_\alpha$ . Comparison of the IETS signals by experiments and NEGF-DFT calculations has been studied very actively. Typically, agreement of the shape and peak/dip positions is fairly well for alkane-dithiol chain systems and metal atomic wires. Comparing with these alkane chains, agreement is not sufficient quantitatively for aromatic molecular junctions (e.g., benzene-dithiol), in particular for asymmetric low-frequency modes. Since most of aromatic molecular backbones have high symmetry, IETS is very sensitive to conformation of the molecule, electrodes, and adsorbed structure. Small perturbation easily mixes different irreducible representation modes: thus, more precise measurement and careful computational modeling will be necessary to get quantitative agreement. However, for qualitative assignment of IETS signals and active vibrational modes, NEGF-DFT and LOE provide useful insight.

In Fig. 8.5, (a) the first-principles IETS of benzene-dithiol and (b) four Au atomic wires attached on the Au electrodes are presented. Temperature was fixed with 5.0 K. For simplicity, only three longitudinal modes were included for the Au wire, while all molecular internal modes were considered for the benzene-dithiol junction. Difference of IETS shape (dip/peak) is clearly presented. In both cases, some phonon damping parameters  $\eta_\alpha$  were examined. Let us consider the two limited cases. One is  $\eta_\alpha \rightarrow \infty$  (damped limit), which represents that the excitation energy is relaxed instantaneously to the electrodes and vibron is always in thermal equilibrium. The other is  $\eta_\alpha \rightarrow 0$  (undamped limit), where thermal dissipation is assumed to be very slow. With decreasing  $\eta_\alpha$  (i.e., from damped limit to undamped), offset grows in IETS signal. Observed offset is caused by bias dependence of the distribution function of each vibron, which is deviation from  $N_{BE}$ . Since the total number of the internal modes of benzene-dithiol is 36, most of the normal modes are IETS *inactive*. The symmetry rule and propensity of IETS have been discussed for several groups [135–139], but they are not as simple as the rule of IR and Raman spectroscopy [130, 140]: thus, first-principles calculation is highly desirable to analyze experimental IETS signal.

Simulation of IETS is also a useful tool to identify the mechanism of current-induced chemical reaction [141]. Very recently, Ohto et al. examined NEGF-DFT to understand molecular switching mechanism of melamine on Cu electrode by STM [142]. Using nudged elastic band method [143] and IETS calculation, they found that the reaction coordinate of the conformation switch agrees with the highly IETS active mode. By following calculations of current-induced adiabatic force and electric field effect [144, 145], they concluded that switching is dominated by direct vibrational heating of the promoting mode. Then the action spectra are calculated by performing current-induced reaction dynamics using first-principles data. They also found that the backward reaction is forbidden by less vibrational heating because of nearly zero IETS intensity of the relating mode. This is consistent with experimental observation [146].

In addition to NEGF-DFT calculations of observable properties like  $IV$ , extracting some first-principles data and parameterizing model Hamiltonian will be very useful to screening research of device material design and/or to attack challenging

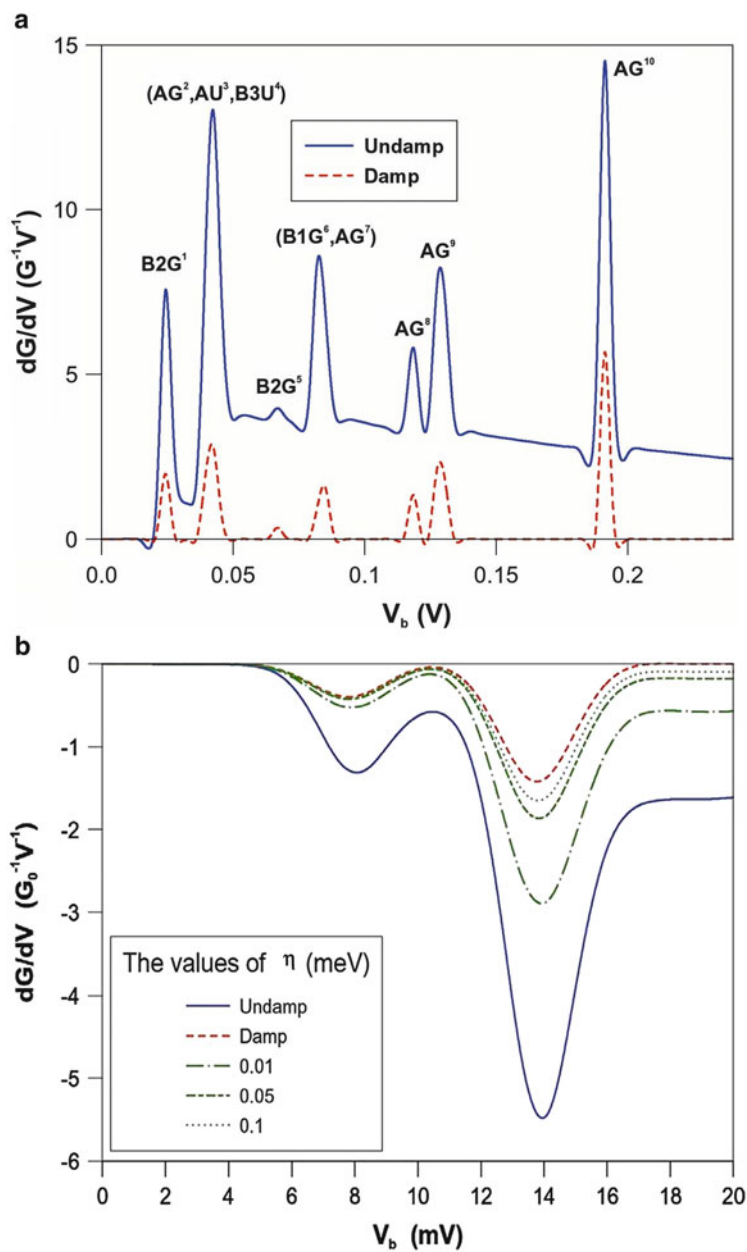


**Fig. 8.5** Calculated IETS of benzene-dithiol (a) and four Au atomic chains (b). Only three longitudinal modes are included in the calculation of the Au chain. The label in the *upper panel* represents irreducible representation of the group of the assigned vibrational modes. The adopted damping factor of each plot is in the insets [48]

transport problems beyond DFT without huge computational demands. In the following, we describe a systematic theoretical method to extract characteristic quantities bridging traditional MO theory and NEGF approach. In order to analyze intrinsic molecular properties, MO theory is the most popular and powerful utility. The design of functional molecules by tuning energy and phase of the frontier MOs (highest occupied MO, HOMO, or lowest occupied MO, LUMO) by chemical modification or chemical substitution is one of (atomistic) chemical engineering, i.e., MO engineering [147]. MO engineering should be a key to create a desired device. However, hybridization of MOs and continuum states of the electrodes changes the electronic structure of “free” molecules and charge donation/back donation through the contact shift energy alignment relative to  $E_F$ . Furthermore, electronic interaction between molecular and metal electronic states governs both mechanical strength and conductance as illustrated in the tripod anchoring system. Hence fusion of MO engineering and contact chemistry is desired.

One of the straightforward approaches is calculating transmission eigenchannel wave functions, and another is adopting an MO picture based on effective Hamiltonian formalism [148]. The former approach is given in Ref. [149]. The latter scheme consists of (i) defining Hamiltonian projected onto the focused molecular region (this projected Hamiltonian is often called molecular projected state Hamiltonian, MPSH) [150] and then (ii) renormalizing the remaining part by projection operator technique [13]. When the projection operators to focused molecular region, left outer region, and right outer region are denoted as  $P$ ,  $Q_L$ , and  $Q_R$ , respectively, the effective Hamiltonian on the  $P$  space is

$$H_{PP}^{\text{eff}}(E) = H_{PP} + H_{PQ_L}G_{QQ}(E)H_{Q_LP} + H_{Q_RP}G_{QQ}(E)H_{PQ_R} \quad (8.20)$$

where  $X_{YY}$  represents  $XYX$ . The  $H_{PP}$  term is the MPSH.  $Q$  is equal to  $Q_L + Q_R$  and  $P + Q_L + Q_R = 1$  as the operator. The eigenstates of MPSH define MO basis  $\{\varphi_\alpha\}$  and this is termed as projected MO (PMO). In contrast to MOs of a free molecule, the PMO has a complex energy term by the last two terms in Eq. 8.20:

$$\begin{aligned} \bar{\varepsilon}_\alpha = & \langle \varphi_\alpha | H_{PP} | \varphi_\alpha \rangle + \langle \varphi_\alpha | \text{Re} (H_{PQ_L}G_{QQ}H_{Q_LP} + H_{Q_RP}G_{QQ}H_{PQ_R}) | \varphi_\alpha \rangle \\ & + i \langle \varphi_\alpha | \text{Im} (H_{PQ_L}G_{QQ}H_{Q_LP}) | \varphi_\alpha \rangle + i \langle \varphi_\alpha | \text{Im} (H_{PQ_R}G_{QQ}H_{Q_RP}) | \varphi_\alpha \rangle \\ = & \varepsilon_\alpha(E) - i\gamma_L(E) - i\gamma_R(E) \end{aligned} \quad (8.21)$$

where the real values  $\varepsilon_\alpha$  and  $\gamma_{L/R}$  represent the PMO energy and electronic coupling strength with the left (right) electrode, respectively. The term  $\varepsilon_\alpha$  consists of an energy shift by orbital hybridization of PMO and wave functions of electrodes. The complex orbital energy  $\bar{\varepsilon}_\alpha$  depends on energy  $E$ . Only when one focuses on low bias voltage  $E$  may be fixed with  $E_F$ . The first-order contribution of  $\varphi_\alpha$  to the

conductance is evaluated by the Breit-Wigner form as

$$\tau_\alpha = \frac{4\gamma_L\gamma_R}{(E_F - \varepsilon_\alpha)^2 + (\gamma_L + \gamma_R)^2}, \quad (8.22)$$

and one can identify the conducting MO by checking each  $\tau_\alpha$ . Note that all parameters can be calculated by NEGF-DFT directly and these parameters include the orbital phase and contact effect implicitly, i.e., straightforward extension of MO engineering unified with contact chemistry.

Using the effective Hamiltonian, site energy alignment for conduction is roughly estimated. To obtain site energies, further division of the  $P$  space to three subspaces and then diagonalization of each sub-block matrix of  $H_{PP}$  (not  $H_{PP}^{\text{eff}}$ ) are performed. The resulting eigenvector relates localized molecular orbitals (MOs) on each site. Then (renormalized) site energy can be obtained as the matrix elements of  $H_{PP}^{\text{eff}}(E_F)$  in the (new) localized MO basis on each group [13].

### 8.3 Rectification by a Single $pn$ Molecule with Symmetric Anchors and Electrodes: Aviram-Ratner or Ellenbogen-Love Diode?

In the following sections, a unimolecular rectifier of a  $pn$  resembled diblock molecule [151–156] is discussed. The diode molecule proposed by AR (AR diode molecule) consists of  $\pi$ -Donor ( $\pi D$ ) and  $\pi$ -Acceptor ( $\pi A$ ) molecular groups separated by a  $\sigma$  spacer bond, and it has often been denoted as  $D$ - $\sigma$ - $A$  [10]. The  $\pi A$  ( $\pi D$ ) part plays an analogous role as  $p$ -type ( $n$ -type) semiconductor of the bulk  $pn$  junction, and the forward direction of the AR diode is same with that of bulk  $pn$  diode. Based on AR's idea, many  $D$ - $\sigma$ - $A$  and several  $D$ - $\pi$ - $A$  structure molecules have been synthesized, and asymmetric  $IV$  characteristics have been observed in a high bias voltage regime (typically above 1.5 V) [157–160]. However, most of the proposed  $D$ - $\sigma$ - $A$  molecules consist of an asymmetric contact because  $D$  and  $A$  groups are usually completely different molecules. Hence, it is not clear that rectification is triggered by the intrinsic electronic structure of the separated  $D$  and  $A$  or by the asymmetric structure of the contact.

In the AR model, the energy alignment of HOMO of  $\pi D$  group and LUMO of  $\pi A$  relative to  $E_F$  is focused and effects of nonequilibrium electronic response of HOMO and/or LUMO to finite bias is omitted. On the contrary to AR, Ellenbogen and Love (EL) focused on the change of energy gap between MOs localized on  $\pi D$  and  $\pi A$  by applied bias direction [12]. The forward direction in the EL mechanism is *opposite* to that of the  $pn$  because the positive bias voltage of  $\pi A \rightarrow \pi D$  direction is expected to lift up the HOMO level of  $\pi D$  while it may diminish the LUMO energy of  $\pi A$ . NEGF-DFT calculations have been examined to various  $D$ - $\sigma$ - $A$  rectification molecules and the results supported EL mechanism [15, 161].

On the side of  $IV$  measurement experiments, a key to make “molecular” rectification mechanism clear is (i) arranging symmetric electrodes and anchors in the junction and (ii) identifying forward direction with regulated orientation in single-molecule level. Only very recently, the precise measurement of the unimolecular rectifier satisfying (i) and (ii) is performed [154, 155]. Recently, several experimental groups have observed clear rectification behavior in a series of self-assembled monolayers (SAMs) made of  $pn$  resembled diblock molecules instead of a  $D-\sigma-A$  structure [151, 154–156]. The forward direction in these cases agrees with that of  $pn$  junctions. The latest study includes single molecular diode property found experimentally in a specific form of the diblock molecules, i.e., bipyrimidinyl-biphenyl molecule with the symmetric thiol anchors.  $IV$  characteristics of the bipyrimidinyl-biphenyl asymmetric molecule were compared with that of its symmetric counterpart, i.e., tetraphenyl molecule [155]. This leads to an experimental finding that the rectification of the asymmetric molecule starts from very low voltage. These experimental findings conflict with EL mechanism: thus, the question is that if rectification is realized by classical AR or alternative mechanism relating an intrinsic  $pn$  feature *built in* the diblock molecule.

The NEGF-DFT was applied to the asymmetric and symmetric molecules, then, clear asymmetry was found in the  $IV$  curve of the single asymmetric. The rectification ration,  $\eta(V) = I_{\text{forward}}/I_{\text{backward}}$ , is 1.34 and 1.58 for  $V=0.5$  and 1.0 volt, respectively. In particular, the rectification ration of first-principles and experimental results agrees well in the low-bias region  $V \leq 0.5$  volt. This result shows that qualitative parameters such as  $\eta(V)$  by NEGF-DFT are sufficiently reliable though NEGF-DFT by local density approximation (LDA) or generalized gradient approximation (GGA) XC functions often overestimate the absolute value of conductance and electric current. The agreement between the theoretical and the experimental results in this region is excellent, while the difference grows rapidly as we increase bias voltage above 0.6 V.

The forward direction of rectification obtained by the calculation agrees with the experiments, i.e., it behaves in the same way as the standard  $pn$  junction. To understand the mechanism of the  $pn$  forward direction, analysis of PMOs for electric transport channels and their bias dependence are useful. According to Eq. 8.22, both  $\varepsilon_\alpha$  and the product of  $\gamma_{\alpha L}$  and  $\gamma_{\alpha R}$  (or square root of  $\gamma_L \gamma_R$ ) are important in characterizing “conducting” molecular orbitals. For example, let us consider an extreme case where  $1 \ll \gamma_L$  and  $\gamma_R = 0$ . The electric current through the molecule is negligibly small in this limit even when  $\varepsilon_\alpha \approx E_F$  (i.e., resonant tunneling) and  $\gamma_L + \gamma_R$  is large. The parameters  $\varepsilon_\alpha$  and the square root of the molecule-electrode coupling product  $\sqrt{\gamma_{\alpha L} \gamma_{\alpha R}}$  were used to identify conducting PMOs.  $E_F$  is set to zero below.

In Table 8.1, values of  $(\varepsilon_\alpha, \sqrt{\gamma_{\alpha L} \gamma_{\alpha R}})$  for HOMO-1, HOMO, and LUMO were listed. Here, note that the terminologies of HOMO/LUMO for the PMOs are defined by a relative energy level of  $\varepsilon_\alpha$  to  $E_F$  for each bias case as usual. They were obtained from our first-principles analyses at  $V = \pm 0.4$  and  $V = \pm 0.8$  volt, respectively. The target molecule projected out by the projection operator  $P$  then is the dithiolated diblock molecule. In the case of the single symmetric molecular

**Table 8.1** PMO energies and the square root product of the molecule-electrode couplings for tetraphenyl (symmetric molecular junction) and bipyrimidinyl-biphenyl (asymmetric molecular junction). Results of HOMO-1, HOMO, and LUMO are listed where  $E_F$  is set to 0. The bold italic parts indicate the dominant PMOs for tunneling. The units of bias and energy (coupling strength) are volt and eV, respectively (Data taken from Ref. [13])

Tetraphenyl						
Bias	$E_{H-1}$	$\sqrt{\gamma_L\gamma_R}$	$E_H$	$\sqrt{\gamma_L\gamma_R}$	$E_L$	$\sqrt{\gamma_L\gamma_R}$
-0.8	-1.90	0.433	-0.97	<b>0.162</b>	2.01	0.090
-0.4	-1.72	0.331	-1.05	<b>0.142</b>	2.01	0.062
0.4	-1.84	0.358	-1.02	<b>0.143</b>	2.08	0.071
0.8	-1.80	0.489	-0.99	<b>0.166</b>	1.95	0.113
Bipyrimidinyl-biphenyl						
Bias	$E_{H-1}$	$\sqrt{\gamma_L\gamma_R}$	$E_H$	$\sqrt{\gamma_L\gamma_R}$	$E_L$	$\sqrt{\gamma_L\gamma_R}$
-0.8	-1.41	<b>0.285</b>	-1.00	0.011	1.63	0.071
-0.4	-1.31	<b>0.152</b>	-1.21	0.044	1.60	0.042
0.4	-1.42	0.018	-1.18	<b>0.106</b>	1.44	0.038
0.8	-1.50	0.048	-1.09	<b>0.144</b>	1.35	0.065

junction system, the most dominant PMO for electric current is the HOMO, and  $\sqrt{\gamma_{\alpha L}\gamma_{\alpha R}}$  is symmetric with respect to the sign change of bias voltage. On the contrary,  $\sqrt{\gamma_{\alpha L}\gamma_{\alpha R}}$  of the single asymmetric molecular junction system depends much more on the voltage sign. At positive bias, drastic asymmetry of electronic coupling strength to electrodes was obtained, i.e.,  $\sqrt{\gamma_{\alpha L}\gamma_{\alpha R}} \ll 1$  for HOMO-1, while it was observed at negative bias voltage for HOMO, i.e., the conducting MO is switched from HOMO to HOMO-1. This switch is an *intrinsic* property as a result of finite bias response of phase and amplitude of MOs, and the complex MO energies should be derived by the effective Hamiltonian. The rectification is realized by this switching because electric current through HOMO-1 should be smaller than that through HOMO because of a larger gap between HOMO-1 and  $E_F$ .

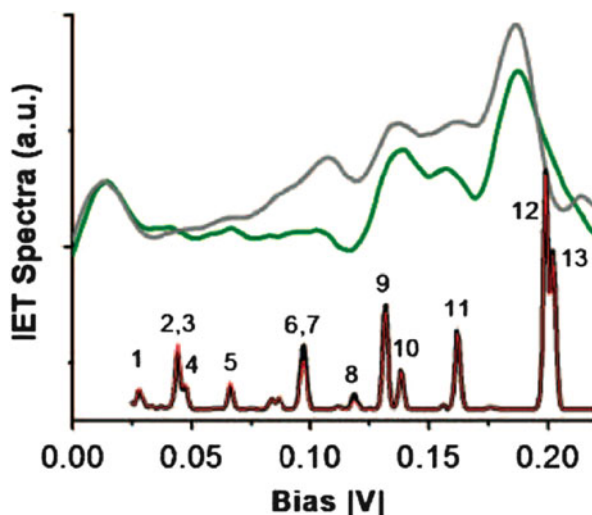
Similar MPSH analysis has been successfully applied to several other molecular diodes [15, 162]. For an example, Stadler et al. discussed a theoretical view of unimolecular rectification by PMO energy curves of a function of bias voltage  $V$ , where they determined PMO energies by the peak position of  $\tau(E)$  [14, 163]. The spaghetti-like PMO energy curves are somewhat similar with Born-Oppenheimer (BO) potential energy curves of a molecular system; however, the latter is defined as a function of reaction coordinate. When one adopts a “diabatic” representation, which can be defined as the states “enforcing smoothness of some physical property or electronic structure” [164, 165], the diabatic MOs can be defined by enforcing smoothness of the value of  $\gamma_L\gamma_R$  as a function of  $V$ . Clear rectification is then a result of avoided crossing by diabatic coupling between conducting and non-conducting diabatic MOs.

In order to get a more intuitive picture, the site energy alignment of the above asymmetric molecule is illustrative. Argument of similarity and difference with AR mechanism or EL mechanism is possible by site (complex) energy alignment as

well. The diblock molecule is represented by four sites, i.e., two phenyl groups and two pyrimidinyl groups for the asymmetric molecule and four phenyl groups for the symmetric molecule, respectively. The most left and right sites include anchor atoms. The site energy alignment of the single symmetric molecular junction changes symmetrically by varying the polarity of  $V$ . The site energy of the right edge phenyl group decreases by 2.01 eV when the  $V$  is increased from  $-0.8$  to  $0.8$  V, although the change of the site energy of the two middle groups is much smaller (0.22 eV) than that of the edge groups. This behavior is consistent with the fact that the phenyl molecule is electron accepting, i.e., it is  $n$  type ( $\pi A$ ). It is also reasonable because we expect that the molecule-electrode interaction effect is mostly limited to the edge molecular groups. On the other hand, the change at the edge pyrimidinyl site (0.63 eV) is much smaller than that of the edge phenyl site. The change of site energy alignment induced by bias voltage is analogous to what is expected in the reduction of built-in potential or smoothed slope of band bending by forward bias in the bulk  $pn$  junction. The intended direction of charge migration is given by  $\pi D$  (pyrimidinyl)  $\rightarrow$   $\pi A$  (phenyl) in the EL mechanism, while  $\pi D$   $\pi A$  favored bias-induced change of electronic coupling strength of  $\pi A$ -LUMO which is much smaller than  $\pi A$ -HOMO ( $<1.0\%$ ) in the present  $pn$  resembled molecule. Thus, the EL mechanism is not likely [13].

After demonstrating the asymmetric  $IV$  characteristics in a low bias voltage regime, the IETS was measured to explore effects of the diode property to inelastic current and heating [155]. According to Eq. 8.16, enhanced asymmetry is expected in the inelastic current of the diode molecule. In Fig. 8.6, the measured and calculated IETS of the bipyrimidinyl-biphenyl is plotted. Note that both plots are obtained by subtracting the derivative of elastic current, and  $-\frac{d^2I}{dV^2}$  is plotted when bias is negative. As same with  $IV$  characteristics, symmetric tetraphenyl was also

**Fig. 8.6** Subtracted IETS in low-bias regime. The *thick green curve* is for positive bias and the *thin gray curve* is the negative bias region rotated  $180^\circ$ . The *black and red curves* are the calculated IETS in positive and negative bias, respectively [155]



examined for comparison. Although slight asymmetries in the peak intensity may be due to either effect from the conformation of the junction or from asymmetry of electron-vibron coupling, they do not show consistent asymmetric intensity across the molecular junction. Asymmetry is much smaller than that expected by Eq. 8.14 and it is almost symmetric for the fingerprint modes. Theoretical results by NEGF-DFT support nearly symmetric intensity. Recall that symmetric electronic coupling strength (in this case,  $\gamma_{\alpha L} \approx \gamma_{\alpha R}$ ) is assumed when Eq. 8.14 is derived. The *bias-dependent* asymmetry of electronic coupling strength as well as the MO energy level works to suppress asymmetry of IETS intensity in the present system.

## 8.4 Summary

In this chapter, modern views of molecular electric transport were presented based on concerto of theoretical models and first-principles calculations. Some illustrative examples of applications to electric and energy-harvesting devices were presented to clarify our views. Actually, study of molecular electronics has a long history, and there are many interesting experimental findings relating to functional devices; however, there are several problems to creating a practical device and circuit, yet. The theory of molecular junction is just a border of the transport theory in solid or mesoscopic physics and electron transfer theory in chemistry. The unified views are very useful to make a bridge of theoretical approaches in physics and chemistry communities.

The basic theory of length and temperature dependence of molecular conductance or electron transfer rate is sometimes considered to be a textbook example; however, there are rooms to deepen the theory and to refine the model in order to explain recent experimental findings such as even/odd oscillation of conductance, crossover of length and temperature dependence, and so on. The last problem relates to a fundamental but difficult issue: how to handle electron-phonon or electron-vibron scatterings in a nano-contact. Effort of theoretical and computational modeling and application to practical systems will give a new insight to local heating and Joule heating in broader nanoelectronics.

A single molecular rectifier by adopting a *pn* diblock molecule rather than a classical *D-σ-A* structure was analyzed to identify really “intrinsic” rectification of the molecule where symmetric anchors, controlled molecular orientation to the electrodes, and clear identification of forward/backward bias polarity to the molecular orientation are required. NEGF-DFT and effective MPSH analysis merged MO and transport theories. A view of MO engineering and contact chemistry provides modern classification of a molecular rectifier. This is one of the successful examples to prove the usefulness and power of first-principles transport calculation. Of course, the present status of first-principles transport calculation is not sufficient because of lack of electron correlation. With developing computational algorithm of “beyond NEGF-DFT,” theoretical development is required for nonequilibrium quantum transport. A molecular rectifier is a good target to tackle this nonequilibrium

electron correlation problem. Potentiality of molecular junctions and designing suitable materials to high-efficiency energy-harvesting devices is more challenging. Theoretical aspects shown in this article are applicable to more general devices like metal oxide bulk heterojunctions, Si materials, and so on, where a sub-10 nm scale is now in the scope. It seems evident that understanding and controlling the quantum nature of transport have large capability to tailor-made functional device.

**Acknowledgments** The author would like to thank for fruitful discussion with Dr. Yoshihiro Asai.

## References

1. van Ruitenbeek JM, Alvarez A, Pineyro I, Grahmann C, Joyez P, Devoret MH, Esteve D, Urbina C (1996) *Rev Sci Instrum* 67:108–111
2. Waitz R, Schecker O, Scheer E (2008) *Rev Sci Instrum* 79. 093901-1-5
3. Tsutsui M, Shoji K, Taniguchi M, Kawai T (2008) *Nano Lett* 8:345–349
4. Rubio G, Agrait N, Vieira S (1996) *Phys Rev Lett* 76:2302–2305
5. Beebe JM, Kim B, Frisbie CD, Kushmerick JG (2008) *ACS Nano* 2:827–832
6. Chen J, Reed MA, Rawlett AM, Tour JM (1999) *Science* 286:1550–1552
7. Markussen T, Chen JZ, Thygesen KS (2011) *Phys Rev B* 83. 155407-1-6
8. Reed MA, Zhou C, Deshpande MR, Muller CJ, Burgin TP, Jones L, Tour JM (1998) *Mol Electron: Sci Technol* 852:133–144
9. Xu BQ, Tao NJJ (2003) *Science* 301:1221–1223
10. Aviram A, Ratner MA (1974) *Chem Phys Lett* 29:277–283
11. Sze SM, Ng KK (2007) *Physics of semiconductor devices*. Wiley, New York
12. Ellenbogen JC, Love JC (2000) *Proc IEEE* 88:386–426
13. Nakamura H, Asai Y, Hihath J, Bruot C, Tao N (2011) *J Phys Chem C* 115:19931–19938
14. Stadler R, Geskin V, Cornil J (2008) *J Phys Condens Matter* 20:374105
15. Stokbro K, Taylor J, Brandbyge M (2003) *J Am Chem Soc* 125:3674–3675
16. Gao J, Yu G, Heeger AJ (1998) *Adv Mater* 10:692–695
17. Halls JJM, Pichler K, Friend RH, Moratti SC (1996) *Appl Phys Lett* 68:3120–3122
18. Steim R, Kogler FR, Brabec CJ (2010) *J Mater Chem* 20:2499–2512
19. Yu G, Gao J, Hummelen JC, Wudl F, Heeger AJ (1995) *Science* 270:1789–1791
20. Bubnova O, Crispin X (2012) *Energ Environ Sci* 5:9345–9362
21. Bubnova O, Khan ZU, Malti A, Braun S, Fahlman M, Berggren M, Crispin X (2011) *Nat Mater* 10:429–433
22. Finch C, García-Suárez V, Lambert C (2009) *Phys Rev B* 79:033405
23. Liu Y-S, Chen Y-R, Chen Y-C (2009) *ACS Nano* 3:3497–3504
24. Malen JA, Yee SK, Majumdar A, Segalman RA (2010) *Chem Phys Lett* 491:109–122
25. Murphy P, Mukerjee S, Moore J (2008) *Phys Rev B* 78:161406
26. Reddy P, Jang SY, Segalman RA, Majumdar A (2007) *Science* 315:1568–1571
27. Bahrami A, Dogan F, Japrun D, Albrecht T (2012) *Biochem Soc Trans* 40:624–628
28. Tsutsui M, Rahong S, Iizumi Y, Okazaki T, Taniguchi M, Kawai T (2011) *Sci Rep UK* 1:1–6
29. Zwolak M, Di Ventra M (2005) *Nano Lett* 5:421–424
30. Browne WR, Feringa BL (2006) *Nat Nanotechnol* 1:25–35
31. Chen J, Wang W, Klemic J, Reed MA, Axelrod BW, Kaschak DM, Rawlett AM, Price DW, Dirk SM, Tour JM, Grubisha DS, Bennett DW (2002) *Ann N Y Acad Sci* 960:69–99
32. Eigler DM, Lutz CP, Rudge WE (1991) *Nature* 352:600–603
33. Huang T, Zhao J, Peng M, Popov AA, Yang SF, Dunsch L, Petek H (2011) *Nano Lett* 11:5327–5332

34. Simonian N, Likharev KK, Mayr A (2013) *J Appl Phys* 113: 044504-1-14
35. Sahu S, Pal AJ (2008) *Org Electron* 9:873–877
36. Bergfield JP, Solomon GC, Stafford CA, Ratner MA (2011) *Nano Lett* 11:2759–2764
37. Ke SH, Yang WT, Baranger HU (2008) *Nano Lett* 8:3257–3261
38. Nakamura H, Yamashita K (2008) *Nano Lett* 8:6–12
39. Solomon GC, Andrews DQ, Van Duyne RP, Ratner MA (2008) *J Am Chem Soc* 130:7788
40. Datta S (1995) *Electronic transport in mesoscopic systems*. Cambridge University Press, Cambridge
41. Kadanoff LP, Baym G (1962) *Quantum statistical mechanics*. Benjamin, New York
42. Keldysh LV (1965) *Sov Phys JETP USSR* 20:1018
43. Wingreen NS, Jauho AP, Meir Y (1993) *Phys Rev B* 48:8487–8490
44. Brandbyge M, Mozos JL, Ordejon P, Taylor J, Stokbro K (2002) *Phys Rev B* 65:165401
45. Kong LT, Denniston C, Muser MH (2011) *Comput Phys Commun* 182:540–541
46. Luisier M, Schenk A (2008) *J Comput Theor Nanosci* 5:1031–1045
47. Nakamura H, Yamashita K (2006) *J Chem Phys* 125:194106
48. Nakamura H, Yamashita K, Rocha AR, Sanvito S (2008) *Phys Rev B* 78:235420
49. Rungger I, Sanvito S (2008) *Phys Rev B* 78:035407
50. Sanvito S, Rocha AR (2006) *J Comput Theor Nanosci* 3:624–642
51. Stokbro K, Taylor J, Brandbyge M, Ordejon P (2003) *Mol Electron III* 1006:212–226
52. Toher C, Sanvito S (2007) *Phys Rev Lett* 99:056801
53. Xue YQ, Datta S, Ratner MA (2002) *Chem Phys* 281:151–170
54. Taylor J, Guo H, Wang J (2001) *Phys Rev B* 6324:245407
55. May V, Kühn O (2000) *Charge and energy transfer dynamics in molecular systems*. Wiley-VHC, Berlin
56. Nitzan A (2006) *Chemical dynamics in condensed phases*. Oxford University Press, Oxford
57. Luo L, Frisbie CD (2010) *J Am Chem Soc* 132:8854
58. Luo LA, Choi SH, Frisbie CD (2011) *Chem Mater* 23:631–645
59. Joachim C, Ratner MA (2005) *Proc Natl Acad Sci U S A* 102:8801–8808
60. Engelkes VB, Beebe JM, Frisbie CD (2004) *J Am Chem Soc* 126:14287–14296
61. Selzer Y, Cabassi MA, Mayer TS, Allara DL (2004) *Nanotechnology* 15:S483–S488
62. Selzer Y, Cabassi MA, Mayer TS, Allara DL (2004) *J Am Chem Soc* 126:4052–4053
63. Mujica V, Nitzan A, Mao Y, Davis W, Kemp M, Roitberg A, Ratner MA (1999) Electron transfer in molecules and molecular wires: geometry dependence, coherent transfer, and control. In: J Jortner, M Bixon (eds) *Electron transfer*, vol 107. Wiley, pp 403–430
64. Choi SH, Kim B, Frisbie CD (2008) *Science* 320:1482–1486
65. He J, Chen F, Li J, Sankey OF, Terazono Y, Herrero C, Gust D, Moore TA, Moore AL, Lindsay SM (2005) *J Am Chem Soc* 127:1384–1385
66. Salomon A, Cahen D, Lindsay S, Tomfohr J, Engelkes VB, Frisbie CD (2003) *Adv Mater* 15:1881–1890
67. Sikes HD, Smalley JF, Dudek SP, Cook AR, Newton MD, Chidsey CED, Feldberg SW (2001) *Science* 291:1519–1523
68. Choi SH, Risko C, Delgado MCR, Kim B, Bredas JL, Frisbie CD (2010) *J Am Chem Soc* 132:4358–4368
69. Yan HJ, Bergren AJ, McCreery R, Della Rocca ML, Martin P, Lafarge P, Lacroix JC (2013) *Proc Natl Acad Sci U S A* 110:5326–5330
70. Lloveras V, Vidal-Gancedo J, Figueira-Duarte TM, Nierengarten JF, Novoa JJ, Mota F, Ventosa N, Rovira C, Veciana J (2011) *J Am Chem Soc* 133:5818–5833
71. Smit RHM, Untiedt C, Rubio-Bollinger G, Segers RC, van Ruitenbeek JM (2003) *Phys Rev Lett* 91: 076805-1-4
72. Smit RHM, Untiedt C, van Ruitenbeek JM (2004) *Nanotechnology* 15:S472–S478
73. Asai Y, Fukuyama H (2005) *Phys Rev B* 72:085431
74. Yeganeh S, Ratner MA, Mujica V (2007) *J Chem Phys* 126:161103
75. Lang IG, Firsov YA (1963) *Sov Phys JETP USSR* 16:1301–1312

76. Mahan G (1990) *Many-particle physics*. Plenum, New York
77. Marcus RA, Sutin N (1985) *Biochim Biophys Acta* 811:265–322
78. Coropceanu V, Cornil J, da Silva DA, Olivier Y, Silbey R, Bredas JL (2007) *Chem Rev* 107:926–952
79. Yoo KH, Ha DH, Lee JO, Park JW, Kim J, Kim JJ, Lee HY, Kawai T, Choi HY (2001) *Phys Rev Lett* 87:198102
80. Sepunaru L, Friedman N, Pecht I, Sheves M, Cahen D (2012) *J Am Chem Soc* 134:4169–4176
81. Lee SK, Yamada R, Tanaka S, Chang GS, Asai Y, Tada H (2012) *ACS Nano* 6:5078–5082
82. Asai Y (2008) *Phys Rev B* 78:045434
83. Gregory S (1990) *Phys Rev Lett* 64:689–692
84. Hahn JR, Lee HJ, Ho W (2000) *Phys Rev Lett* 85:1914–1917
85. Stipe BC, Rezaei HA, Ho W (1999) *Phys Rev Lett* 82:1724–1727
86. Stipe BC, Rezaei MA, Ho W (1998) *Science* 280:1732–1735
87. Ho W (2002) *J Chem Phys* 117:11033–11061
88. Klein J, Leger A, Belin M, Defourne D, Sangster MJ (1973) *Phys Rev B* 7:2336–2348
89. Jaklevic RC, Lambe J (1966) *Phys Rev Lett* 17:1139
90. Lambe J, Jaklevic RC (1968) *Phys Rev* 165:821
91. Reed MA (2008) *Mater Today* 11:46–50
92. Galperin M, Ratner MA, Nitzan A (2004) *J Chem Phys* 121:11965–11979
93. Okabayashi N, Konda Y, Komeda T (2008) *Phys Rev Lett* 100:226604
94. Hihath J, Arroyo CR, Rubio-Bollinger G, Tao NJ, Agrait N (2008) *Nano Lett* 8:1673–1678
95. Hihath J, Bruot C, Tao NJ (2010) *ACS Nano* 4:3823–3830
96. Wang WY, Lee T, Kretzschmar I, Reed MA (2004) *Nano Lett* 4:643–646
97. Taniguchi M, Tsutsui M, Yokota K, Kawai T (2009) *Nanotechnology* 20:434008
98. Tsutsui M, Taniguchi M, Shoji K, Yokota K, Kawai T (2009) *Nanoscale* 1:164–170
99. Agrait N, Untiedt C, Rubio-Bollinger G, Vieira S (2002) *Chem Phys* 281:231–234
100. Agrait N, Untiedt C, Rubio-Bollinger G, Vieira S (2002) *Phys Rev Lett* 88:216803
101. Frederiksen T, Paulsson M, Brandbyge M, Jauho AP (2007) *Phys Rev B* 75:205413
102. Paulsson M, Frederiksen T, Brandbyge M (2005) *Phys Rev B* 72:033408
103. Viljas JK, Cuevas JC, Pauly F, Hafner M (2005) *Phys Rev B* 72:245415
104. Galperin M, Ratner MA, Nitzan A (2007) *J Phys Condens Matter* 19:103201
105. Shimazaki T, Asai Y (2008) *Phys Rev B* 77:115428
106. Andrews DQ, Solomon GC, Goldsmith RH, Hansen T, Wasielewski MR, Van Duyne RP, Ratner MA (2008) *J Phys Chem C* 112:16991–16998
107. Solomon GC, Andrews DQ, Goldsmith RH, Hansen T, Wasielewski MR, Van Duyne RP, Ratner MA (2008) *J Am Chem Soc* 130:17301–17308
108. Arroyo CR, Tarkuc S, Frisenda R, Seldenthuis JS, Woerde CHM, Eelkema R, Grozema FC, van der Zant HSJ (2013) *Angew Chem Int Edit* 52:3152–3155
109. Pecchia A, Penazzi G, Salvucci L, Di Carlo A (2008) *New J Phys* 10:065022
110. Rocha AR, Garcia-Suarez VM, Bailey S, Lambert C, Ferrer J, Sanvito S (2006) *Phys Rev B* 73:085414
111. Sanvito S, Lambert CJ, Jefferson JH, Bratkovsky AM (1999) *Phys Rev B* 59:11936–11948
112. Thygesen KS, Jacobsen KW (2005) *Chem Phys* 319:111–125
113. Jauho AP, Wingreen NS, Meir Y (1994) *Phys Rev B* 50:5528–5544
114. Galperin M, Nitzan A (2003) *Mol Electron III* 1006:48–67
115. Rocha AR, Garcia-Suarez VM, Bailey SW, Lambert CJ, Ferrer J, Sanvito S (2005) *Nat Mater* 4:335–339
116. Kurth S, Stefanucci G, Almladh CO, Rubio A, Gross EKV (2005) *Phys Rev B* 72:035308
117. Kurth S, Stefanucci G, Khosravi E, Verdozzi C, Gross EKV (2010) *Phys Rev Lett* 104:236801
118. Stefanucci G, Kurth S, Rubio A, Gross EKV (2008) *Phys Rev B* 77:075339
119. Uimonen AM, Khosravi E, Stan A, Stefanucci G, Kurth S, van Leeuwen R, Gross EKV (2011) *Phys Rev B* 84:115103
120. Evers F, Schmitteckert P (2011) *Phys Chem Chem Phys* 13:14417–14420

121. Koentopp M, Burke K, Evers F (2006) *Phys Rev B* 73:121403
122. Strange M, Rostgaard C, Hakkinen H, Tygesen KS (2011) *Phys Rev B* 83:115108–1–115108–12
123. Thygesen KS, Rubio A (2008) *Phys Rev B* 77:115333
124. Ie Y, Hirose T, Nakamura H, Kiguchi M, Takagi N, Kawai M, Aso Y (2011) *J Am Chem Soc* 133:3014–3022
125. Chen F, Li XL, Hihath J, Huang ZF, Tao NJ (2006) *J Am Chem Soc* 128:15874–15881
126. Fu QA, Luo Y, Yang JL, Hou JG (2010) *Phys Chem Chem Phys* 12:12012–12023
127. Jiang J, Gao B, Hu ZP, Lu W, Wu ZY, Yang JL, Luo Y (2010) *Appl Phys Lett* 96:253110
128. Lin LL, Wang CK, Luo Y (2011) *ACS Nano* 5:2257–2263
129. Frederiksen T, Lorente N, Paulsson M, Brandbyge M (2007) *Phys Rev B* 75:235441
130. Nakamura H (2010) *J Phys Chem C* 114:12280–12289
131. Okabayashi N, Paulsson M, Ueba H, Konda Y, Komeda T (2010) *Phys Rev Lett* 104:077801
132. Long DP, Troisi A (2007) *J Am Chem Soc* 129:15303–15310
133. Troisi A, Ratner MA, Nitzan A (2003) *J Chem Phys* 118:6072–6082
134. Solomon GC, Gagliardi A, Pecchia A, Frauenheim T, Di Carlo A, Reimers JR, Hush NS (2006) *J Chem Phys* 124:094704
135. Gagliardi A, Solomon GC, Pecchia A, Frauenheim T, Di Carlo A, Hush NS, Reimers JR (2007) *Phys Rev B* 75:17
136. Paulsson M, Frederiksen T, Ueba H, Lorente N, Brandbyge M (2008) *Phys Rev Lett* 100:226604
137. Troisi A, Beebe JM, Picraux LB, van Zee RD, Stewart DR, Ratner MA, Kushmerick JG (2007) *Proc Natl Acad Sci U S A* 104:14255–14259
138. Troisi A, Ratner MA (2006) *J Chem Phys* 125: 214709-1-11
139. Troisi A, Ratner MA (2007) *Phys Chem Chem Phys* 9:2421–2427
140. Beebe JM, Moore HJ, Lee TR, Kushmerick JG (2007) *Nano Lett* 7:1364–1368
141. Cao H, Jiang J, Ma J, Luo Y (2008) *J Phys Chem C* 112:11018–11022
142. Ohto T, Rungger I, Yamashita K, Nakamura H, Sanvito S (2013) *Phys Rev B* 87: 205439-1-7
143. Henkelman G, Uberuaga BP, Jonsson H (2000) *J Chem Phys* 113:9901–9904
144. Todorov TN, Hoekstra J, Sutton AP (2000) *Philos Mag B* 80:421–455
145. Zhang RX, Rungger I, Sanvito S, Hou SM (2011) *Phys Rev B* 84: 085455-1-12
146. Pan SA, Fu Q, Huang T, Zhao AD, Wang B, Luo Y, Yang JL, Hou JG (2009) *Proc Natl Acad Sci U S A* 106:15259–15263
147. Fukui K (1982) *Science* 218:747–754
148. Feshbach H (1991) *Theoretical nuclear physics: nuclear reactions*. Wiley-Interscience, New York
149. Paulsson M, Brandbyge M (2007) *Phys Rev B* 76:201101
150. Stokbro K, Taylor J, Brandbyge M, Mozos JL, Ordejon P (2003) *Comput Mater Sci* 27:151–160
151. Ng MK, Lee DC, Yu LP (2002) *J Am Chem Soc* 124:11862–11863
152. Ng MK, Yu LP (2002) *Angew Chem Int Edit* 41:3598–3601
153. Oleynik II, Kozhushner MA, Posvyanskii VS, Yu L (2006) *Phys Rev Lett* 96:096803
154. Diez-Perez I, Hihath J, Lee Y, Yu LP, Adamska L (2009) *Nat Chem* 1:635–641
155. Hihath J, Bruot C, Nakamura H, Asai Y, Diez-Perez I, Lee Y, Yu LP, Tao NJ (2011) *ACS Nano* 5:8331–8339
156. Morales GM, Jiang P, Yuan SW, Lee YG, Sanchez A, You W, Yu LP (2005) *J Am Chem Soc* 127:10456–10457
157. Metzger RM (2009) *Synth Met* 159:2277–2281
158. Honciuc A, Metzger RM, Gong AJ, Spangler CW (2007) *J Am Chem Soc* 129:8310–8319
159. Jaiswal A, Rajagopal D, Lakshminantham MV, Cava MP, Metzger RM (2007) *Phys Chem Chem Phys* 9:4007–4017
160. Ashwell GJ, Mohib A, Miller JR (2005) *J Mater Chem* 15:1160–1166

161. Pan JB, Zhang ZH, Deng XQ, Qiu M, Guo C (2011) *Appl Phys Lett* 98:013503
162. Ford MJ, Hoft RC, McDonagh AM, Cortie MB (2008) *J Phys Condens Matter* 20:374106
163. Stadler R, Geskin V, Cornil J (2008) *Adv Funct Mater* 18:1119–1130
164. Atchity GJ, Ruedenberg K (1997) *Theor Chem Acc* 97:47–58
165. Nakamura H, Truhlar DG (2001) *J Chem Phys* 115:10353–10372

# Chapter 9

## Single-Molecule Sequencing

Masateru Taniguchi

**Abstract** In this chapter, the use of single-molecule conductance for DNA sequencing, a principle target of the \$1,000 Genome Project, will be discussed. Since starting the project, numerous universities and companies have attempted to develop single-molecule sequencers but have not yet demonstrated a proof of concept. A major challenge has been the fabrication of nanoelectrodes with a 1 nm gap, equal to the diameter of single-stranded DNA molecules. The breakthrough discovery of the use of tunneling currents was required to perform single-molecule electrical sequencing. This discovery led to a proof of concept using a chemically modified scanning tunneling microscope (STM) and mechanically controllable break junction (MCBJ). These single-molecule measurement technologies are now being developed for application studies.

**Keywords** Single molecule • Sequencing • Tunneling currents • DNA • RNA

### 9.1 Introduction

Many people believed that the end of the Human Genome Project in 2003 meant the dawn of personalized medicine and therapeutics based on genomic information [1–4]. However, the long time and exorbitant cost to read an entire human genome have been a significant barrier to realizing personalized medicine [5–7]. To overcome this barrier, the US National Institutes of Health (NIH) that led the Human Genome Project has founded the \$10,000 and \$1,000 genome projects with the goal of reading an entire human DNA sequence in 1 day for the cost of \$10,000 and \$1,000, respectively [8–13]. The final target of the \$1,000 genome project is to develop single-molecule DNA sequencers that can identify the sequences of the four-base molecules in DNA by measuring single-molecule conductance.

First- and second-generation DNA sequencers identify base molecules via light emission by laser excitation of dye molecules that are chemically bonded to base molecules [9–11]. They require polymerase chain reaction (PCR) to amplify

---

M. Taniguchi (✉)

The Institute of Scientific and Industrial Research, Osaka University, Osaka, Japan  
e-mail: [taniguti@sanken.osaka-u.ac.jp](mailto:taniguti@sanken.osaka-u.ac.jp)

sequencing templates so that sufficient material is available for generating detectable signals. Furthermore, first- and second-generation DNA sequencing technologies require fluorescent labels. In contrast, third- and fourth-generation DNA sequencing technologies directly detect single-base molecules by changes in electric current such that neither PCR amplification nor fluorescent probes are necessary [14–17]. Comparing the throughputs and total cost to determine a complete human genome shows that first-generation DNA sequencing technologies take 3 months and cost approximately \$10 million, second-generation technologies take 2 months and cost approximately \$0.1 million, and third- and fourth-generation technologies will take 1 day and cost approximately \$1,000 [9–11]. The use of nanopore devices is expected to result in a technical leap in DNA sequencing technologies.

Nanopore-based sequencers can be classified into two categories based on changes in ionic or tunneling currents (Fig. 9.1) [16, 18]. Ionic current-based nanopores have been studied for over 30 years [16, 19]. When we observe cell surfaces, we can see innumerable holes with diameters of several nanometers. These holes, or nanopores, are what nanopore devices use to sequence DNA. They are formed by channel proteins that allow the transport of specific substances such as ions, small molecules, and DNA across the cell membrane; therefore, nanopores have the ability of molecular recognition. For example, a nanopore may only allow a DNA molecule to enter a cell when it identifies certain DNA sequences. If this single-molecule recognition ability can work on a device chip, the device would be able to identify single molecules with high precision. This idea motivated the creation of bionanopore devices. Bionanopore devices identify base molecules passing through a nanopore by detecting changes in the ionic current flowing parallel to the nanopore when a voltage is applied across the membrane [16, 18, 19]. Negatively charged, single-stranded DNA molecules flow downward through the nanopore due to electrophoresis. When no molecule passes through the nanopore, a large ionic current is able to flow through it. When a molecule enters the nanopore, the ionic current decreases as the molecular volume increases. Bionanopore devices

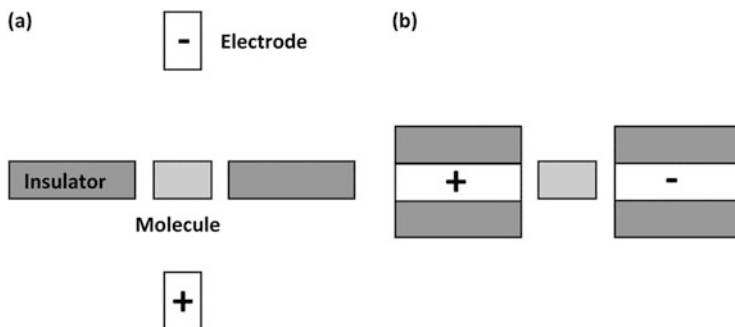


**Fig. 9.1** Schematic figures of (a) ionic current-based nanopore and (b) tunneling current-based nanopores

can read DNA sequences because the devices can identify small differences in the molecular volume by observing the ionic current.

Nanopore-based sequencers that use tunneling currents are presented in Fig. 9.1b [16, 18]. Nanopores of diameter less than 10 nm are formed on a Si substrate covered with a thin  $\text{Si}_3\text{N}_4$  film. Nanogap electrodes with spacing equal to a diameter of approximately 2 nm are assembled in a  $\text{Si}_3\text{N}_4$  membrane. To reduce electrical noise, these electrodes are covered with a thin  $\text{SiO}_2$  film. This nanostructure detects molecules passing through the nanopore using changes in the electric current flowing between the nanogap electrodes, not by changes in the ionic current flowing parallel to the nanopore. The current passing between the nanoelectrodes comes from a tunneling current conducted via molecules passing through the membrane. When a single DNA molecule passes through a nanopore, we can measure the tunneling current, which is potentially different for each nucleotide.

## 9.2 DNA Structures

The entire human genome is composed of three billion base pairs in DNA. Genomic information is obtained by sequencing DNA, where adenine always pairs with thymine with two hydrogen bonds and guanine always pairs with cytosine through three hydrogen bonds. The base molecules are chemically bonded to a sugar and phosphate group. Double-stranded DNA molecules are formed between two single-stranded DNA molecules via hydrogen bonds and can have multiple structures (Fig. 9.2). The *B*-type DNA structure has ten base pairs in a pitch, compared with the 11 base pairs in an *A*-type structure [20]. In the *B*-type DNA structure, the base pair height is 0.34 nm, and the rotation angle is  $36^\circ$ , compared with 0.26 nm and

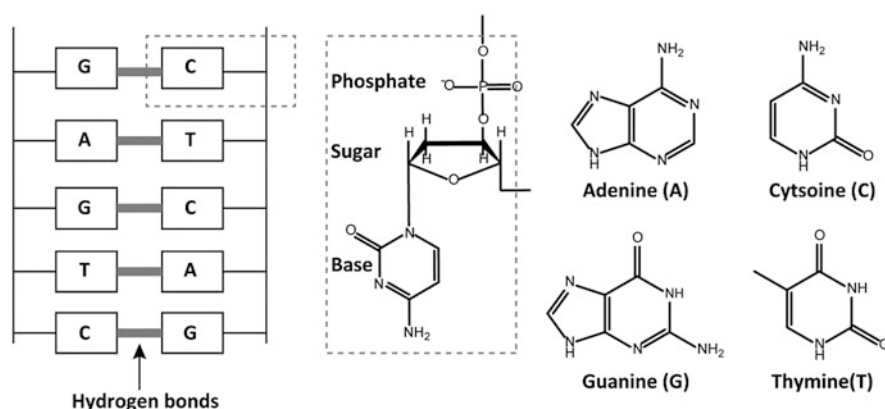
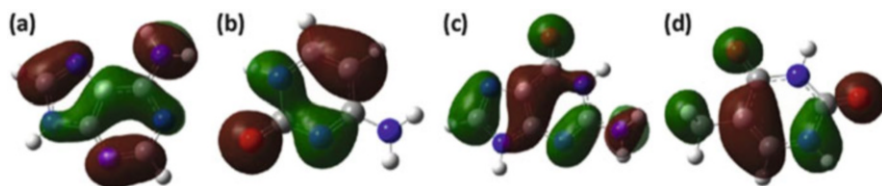


Fig. 9.2 Schematic figures of double-stranded DNA, a monomer unit, and four-base molecules



**Fig. 9.3** The highest occupied molecular orbitals of (a) adenine, (b) cytosine, (c) guanine, (d) thymine

$33^\circ$ , respectively, observed in the A-type structure. In addition, DNA molecules have cations such as  $\text{Na}^+$  to balance the negatively charged phosphate group.

Due to the electrical properties of DNA molecules, only single-stranded DNA can be used for single-molecule sequencing. The four-base molecules in DNA are approximately 1 nm and contain  $\pi$ -electron bonding systems. Their highest occupied molecular orbitals (HOMOs) are distributed over the whole molecule, whereas bonds in the sugar and phosphate groups are localized  $\sigma$  bonds (Fig. 9.3) [15]. Intermolecular  $\pi$ -orbital interactions between base molecules in DNA are expected because base molecules are stacked in parallel. In fact, many researchers expected that double-stranded DNA molecules could function as molecular wires and have examined their electrical conductivity. Although DNA molecules can function as insulators, semiconductors, metals, and superconductors, the best electrical description of DNA molecules is apparently that of a wide-gap semiconductor [21]. Single-molecule sequencing through conductance is difficult because of the strong interactions between base pairs in double-stranded DNA; however, the  $\pi$ -orbital interactions between base molecules are expected to be weak in single-stranded DNA molecules due to their more flexible molecular structures. As a result, single-molecule conductance through base molecules in single-stranded DNA is expected to originate from single-base molecules and can be potentially used for sequencing [22].

### 9.3 The Principle of Single-Molecule Sequencing

There are two ways to identify single-base molecules using tunneling currents (Fig. 9.4) [16, 18]. One is to identify single-base molecules using the tunneling currents generated between the STM and metal substrate that has been modified with recognition molecules. This technique, called recognition tunneling, recognizes base molecules by their hydrogen bonds [23–25]. The second method uses tunneling currents flowing between nanoelectrodes formed by the MCBJ [26–29].

The electric currents obtained using the two measurement methods come from the electron transport mechanism via the HOMO in the coherent tunneling regime where the single-molecule conductance of a base molecule can be expressed by

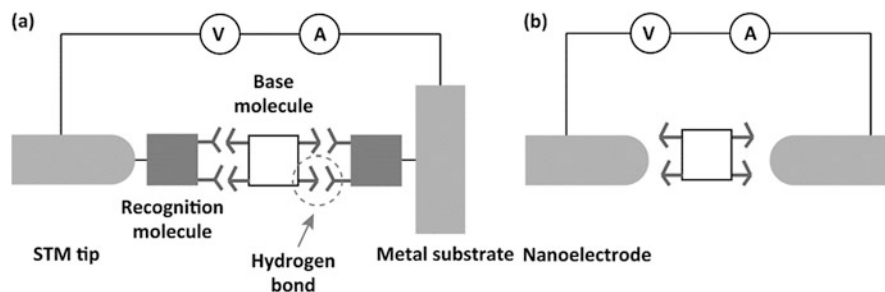


Fig. 9.4 Schematic figures of (a) STM and (b) MCBJ configurations

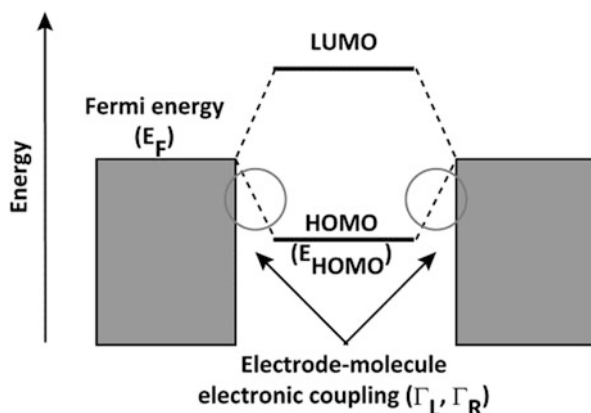


Fig. 9.5 Schematic diagram showing the molecular orbital levels, the Fermi level in the contacts, and the electrode–molecule electronic coupling

Eq. 9.1 [15]:

$$G = \frac{2e^2}{\hbar} \frac{\Gamma_L \Gamma_R}{(E_{\text{HOMO}} - E_F)^2} \quad (9.1)$$

The values  $E_F$ ,  $E_{\text{HOMO}}$ , and  $\Gamma_L$  represent the Fermi energy of the electrodes, the energy of the HOMO, and the left electrode–molecule electronic coupling strength, respectively (Fig. 9.5). Calculations based on density functional theory indicate that the HOMO energy order is guanine > adenine > cytosine > thymine > uracil [27]. Assuming that the electrode–molecule electronic coupling strengths are almost same for the four-base molecules, this order then corresponds to the order of single-molecule electrical conductance.

In an actual measurement system, electrode–molecule electronic coupling strengths strongly depend on the molecular conformation with respect to the nanoelectrodes and their tip structures, resulting in different electrode–molecule electronic coupling strengths for each base molecule. In particular, the coupling

strengths are affected by interactions between the molecules and electrodes when the molecules adsorb onto nanoelectrodes. In addition, molecular conformation is expected to be stabilized in the strong electric field between nanoelectrodes due to the dipole moments of the base molecules [22, 30–32]. Consequently, the single-molecule conductance histogram is expected to show a broad distribution over a single peak; therefore, it is difficult to expect an order in the single-molecule conductance of the base pairs from a chemically modified STM tip, because single-molecule conductance is strongly affected by the electronic structures and conformation of recognition molecules.

In ideal nanopore devices, a single DNA molecule passes through a nanopore at a constant velocity [17, 33]. Similarly, a single DNA molecule is expected to pass through a nanoelectrode gap in one direction and ideally with a constant speed for greater accuracy. Moreover, the throughput has to be higher when single-molecule electrical sequencing technology is applied to a practical sequencer. In other words, single DNA molecules have to enter a nanoelectrode gap at high frequencies. Consequently, identifying single-base molecules and controlling the translocation speed are key for the realization of higher accuracy and throughput. This chapter will only focus on methods for identifying single-base molecules using single-molecule conductance measurements [17, 33].

## 9.4 Measurement and Analysis Methods

The protocols to measure tunneling currents of single-base molecules and single DNA molecules are almost the same for STM-based [23–25] and MCBJ-based [26–29] methods. First, in the STM-based method, an STM tip and a metal substrate are modified with recognition molecules. Second, the distance between the STM, substrate, and spacing between nanoelectrodes are fixed by measuring tunneling currents in solutions containing analytes. Then, the gap spacing is calculated on the basis of tunneling currents. The gap spacing is kept constant via feedback control using piezo devices. In actual experiments, measured electric currents result from tunneling and ionic currents because the sample solutions contain ionic buffers. To reduce ionic currents, an STM tip and nanoelectrodes formed by the MCBJ are covered with insulating materials. After fixing the gap spacing, current–time profiles are measured at a sampling rate of less than 250 KHz by applying a bias voltage of 0.1–0.7 V.

When current–time profiles of single-base and DNA molecules are measured, spikelike signals characterized by the maximum current ( $I_p$ ) and duration ( $t_d$ ) are observed (Fig. 9.6a) [23–29]. Single-molecule conductance histograms are formed by several 100–1,000 points of  $I_p$  data. Generally, single-molecule conductance histograms of the four-base molecules show single peaks with broad distributions [23–29]. Large overlaps of the peaks seem to prevent identifying single-base molecules based on single-molecule conductance (Fig. 9.6b). Let us go back to the method for sequencing DNA using optical measurements.

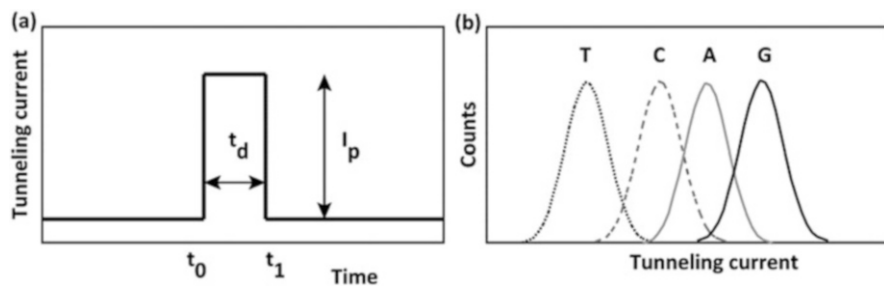


**Fig. 9.6** (a) Tunneling current–time profile characterized by the maximum current  $I_p$  and duration of the current  $t_d$  and (b) schematic figure of tunneling current histograms of four-base molecules

Optical DNA sequencers can identify four-base molecules using four types of dye molecules whose absorption and fluorescent spectra overlap, similar to the conductance histograms [34]. Thus, before processing the spectra, they comprise the sum of the four spectra; however, after processing, all four-base molecules can be identified. The individual spectrum of the four-base molecules corresponds to the probability density function of wavelength  $f_x(\omega)$ . In the simplest case, the spectrum intensity at wavelength  $\omega$  in the measured spectra can be expressed using the probability density function of the four-base molecules:

$$c_A f_A(\omega) + c_C f_C(\omega) + c_G f_G(\omega) + c_T f_T(\omega), \quad (9.2)$$

where  $C_x$  ( $X = A, C, G,$  and  $T$ ) denotes the coefficient at  $\omega$ . For example, the measured spectral intensity at a particular wavelength is obtained by the sum of adenine (80%), cytosine (10%), guanine (8%), and thymine (2%). In this case, the spectral intensity at this wavelength is assigned to adenine.

Similarly, the measured electric currents can be represented as the sum of electric currents multiplied by probability density functions, corresponding to the single-molecule conductance histograms of the four-base molecules:  $G_x(g)$  ( $X = A, C, G,$  and  $T$ ). Therefore, in the simplest model, the measured single-molecule conductance can be expressed by Eq. 9.3:

$$a_A G_A(g) + a_C G_C(g) + a_G G_G(g) + a_T G_T(g), \quad (9.3)$$

where  $a_x$  denotes the coefficient at the measured single-molecule conductance  $g$ . Consequently, small distributions of the probability density functions for single-molecule conductance allow us to sequence DNA with high precision, similar to an optical spectrum. However, peak wavelengths in the fluorescent spectrum are fixed, whereas peak positions in single-molecule conductance histograms alter due to changes in electrode–molecule electronic coupling strengths.

The current–time profiles measured for single-stranded DNA molecules are analyzed using the following procedure [27]. Based on the Eq. 9.3, the measured

conductance ( $G$ ) is assumed to be formed from the sum of the single-molecule conductance of base molecules comprising single-stranded DNA. The ratio of the molecular conductance of each base molecule the overall measured  $G$  must be determined to assign the measured  $G$  to single base. First, single-molecule conductance histograms are constructed from all data points. In an effort to obtain single-molecule conductance histograms of 4 base molecules, Gaussian functions are fitted to conductance histograms. Second, the current–time profiles are transformed into probability–time profiles. The probabilities of the four-base molecules are calculated by inserting probability–time profiles into probability functions of the four-base molecules. Third, the probabilities of individual-base molecules between  $t_0$  and  $t_1$  are integrated using probability–time profiles. Finally, the most likely base molecules are assigned on the basis of the highest integrated probabilities.

However, a significant problem specific to single-molecule DNA analysis remains. Existing DNA sequencers analyze data using machine learning, i.e., a hidden Markov model [34] instead of a simple linear model. Both linear and hidden Markov models assume that the measured values of single-base molecules are independent events. In optical measurements, the observed spectra are independent because the optical methods measure the fluorescence spectrum of dye molecules connected to the terminus of DNA molecules, not the bases themselves. However, in single-molecule identification via tunneling currents, the measured conductance of single-base molecules is not independent because the conductance of single-base molecules can be affected by neighboring base molecules through chemical bonds. In an effort to overcome this issue, single-molecule science should be fused with information technology.

## 9.5 Single-Molecule Identification of Base Molecules

Single-molecule identification of base molecules has been demonstrated using STM and MCBJ methods. Lindsay et al. demonstrated single-molecule resolution of single DNA bases via hydrogen-bond-mediated tunneling currents using a nucleobase-functionalized Au STM probe and nucleoside-functionalized Au substrate in organic solvents [23–25]. This quantum sequencing approach has shown single-base resolution using tunneling currents generated between the Au STM probe and the Au substrate functionalized with 4-mercaptobenzoic acid (Fig. 9.7). This enabled the differentiation of single-molecule conductance in the order of deoxyadenosine > deoxycytidine > deoxyguanosine > thymidine [25]. Furthermore, this approach allowed identification of single-base molecules of DNA with a conductance order of dCMP > dGMP  $\sim$  dmCMP > dAMP, although there were no detectable signals for dT [23]. In addition, the order of peak conductance was d(C)<sub>5</sub> > d(mC)<sub>5</sub>  $\sim$  d(A)<sub>5</sub> for oligomers. Probe drift prevented single-molecule electrical sequencing of d(ACACA) and d(CmCCmCC) [23]; however, two conductance

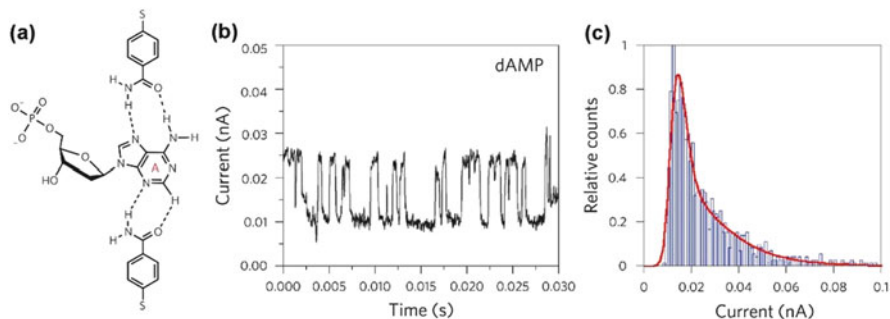


**Fig. 9.7** (a) Schematic of recognition and base molecules, (b) current–time profile of dAMP, and (c) current histogram of dAMP (Reprinted with permission from Macmillan Publishers Ltd: ref. [23], copyright 2010)

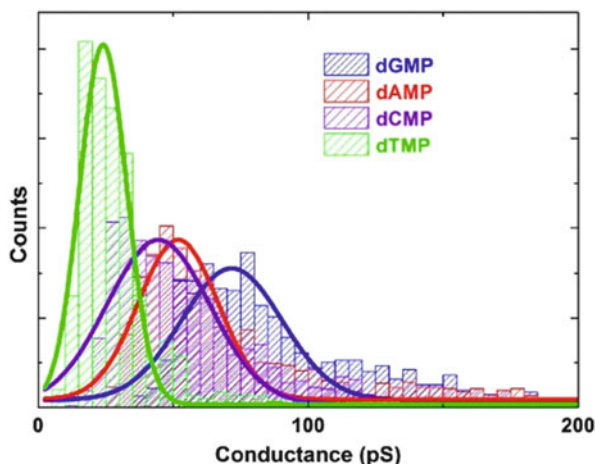


**Fig. 9.8** Single-molecule conductance histograms of four-base molecules. Ref. [27]

plateaus corresponding to each of the two-base molecules were observed in current–time profiles.

In the MCBJ method, when current–time profiles are measured in aqueous solutions containing base molecules, spikelike signals are observed [26, 27, 29]. The corresponding single-molecule conductance histograms of the four-base molecules show single peaks (Fig. 9.8). The peak conductance order is guanine > adenine > cytosine > thymine [27]. Note that this experimental order agrees with HOMO energies obtained from quantum chemical calculations.

If the electron transport mechanism in single-base molecules is coherent tunneling, then methylated dCMP and 8-oxo-dGMP can be identified because their HOMO energies differ from those of other base molecules. Methylated dCMP is the most extensively studied epigenetic mark because of its direct relevance to human

health and disease. 8-Oxo-dGMP is known as a biologically important marker for assessing oxidative stress in humans, such as damage caused by smoking, relevant to aging and diseases. However, existing DNA sequencers cannot identify chemically modified base molecules without chemical modifications and pretreatments. Hence, identifying two chemically modified base molecules is very important. Theoretical calculations show that the HOMO energies of dCMP and methylated dCMP are  $-6.1$  and  $-6.0$  eV, respectively, whereas those of dGMP and 8-oxo-dGMP are  $-5.7$  and  $-5.6$  eV, respectively. Assuming that the electrode–molecule electronic coupling strengths are the same in the original and chemically modified base molecules, single-molecule conductance orders are expected to be methylated dCMP > dCMP and 8-oxo-dGMP > dGMP, consistent with experimental results [29].

## 9.6 DNA Sequencing

Although STM and MCBJ methods have attempted to sequence DNA, only the MCBJ method has achieved DNA sequencing [27]. Here, the cases of TGT and GTG are presented. Spikelike signals were obtained for DNA oligomers as well as single-base molecules. High and low bands show single-molecule conductance from guanine and thymine, respectively (Fig. 9.9). As clearly shown in the single-molecule conductance histogram, three peaks corresponding to baseline, guanine, and thymine are obtained from the current–time profiles of single-base molecules. Next, using the above analysis method, current–time profiles are analyzed to

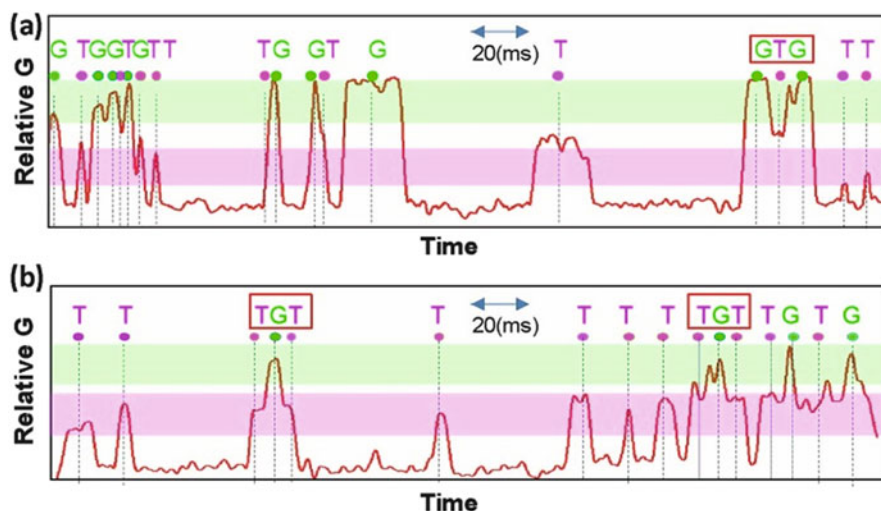


Fig. 9.9 Relative single-molecule conductance–time profiles of GTG and TGT. Ref. [27]

determine the sequences of the base molecules in DNA. In one case, two lower plateaus of thymine were observed in the first and third positions, with guanine forming the middle higher plateau. In the other case, guanine was observed to form the first and third higher plateaus, with thymine in the lower center position. This result demonstrates that the MCBJ method can achieve electrical sequencing of a single DNA molecule. Under the present experimental conditions, not only GTG and TGT but also G, T, TG, and GT can be identified due to the stochastic traps of single DNA molecules.

In the present study, the movement of single DNA molecules is attributed to Brownian motion. When a single TGT DNA sequence approaches the nanoelectrodes and returns, electric signals corresponding to a single thymine molecule are obtained. When a single TGT DNA sequence passes through the nanoelectrodes, electric signals corresponding to TGT are obtained. Similarly, electric signals corresponding to a guanine molecule were obtained when a single TGT DNA sequence approached the electrodes and returned.

## 9.7 RNA Sequencing

RNA is formed from adenine, cytosine, guanine, and uracil, which have two OH groups in a sugar group [20]. Recent studies reveal that microRNA (miRNA) is a small RNA molecule that has approximately 22 base molecules and regulates gene expression at the translational level. MiRNA expression profiling of human tumors has identified the signature associated with diagnosis, staging, progression, prognosis, and response to treatment; however, existing DNA sequencers cannot directly identify sequences of miRNA base molecules [35]. Determination of such sequences is based on transcription of RNA to DNA, i.e., reverse transcription, and transcription errors are expected to result in low accuracy. Instead, single-molecule sequencing technologies can directly sequence RNA, eliminating transcription errors and the need for pretreatments related to reverse transcription.

In addition to DNA, single-molecule conductance histograms of the four-base molecules of RNA are determined using the MCBJ method. Experimental results show that the conductance order for single-molecule RNA is guanine > adenine > cytosine > uracil, corresponding to their HOMO energies. In addition, an RNA molecule of UGAGGUA is sequenced using the MCBJ and analysis methods. Here, three typical current–time profiles are shown (Fig. 9.10). Similar to the current–time profiles of DNA, those of miRNA showed electric currents corresponding to each base molecule. UGAGG is obtained from the upper current–time and U, G, A, and AU in the middle current–time. A long fragmented sequence UGAGGUA was obtained in the lowest profile. Here, 35 fragment sequences were used to assemble the sequence contigs. Sequence contig 1 was assembled as UGA using 13 fragment sequences. Similarly, contigs 2, 3, and 4 were assembled as GAGG, AGGUA, and AGGU, respectively, using the 17-, 9-, and 13-base fragment sequences. The four contigs were assembled as UGAGGUA.

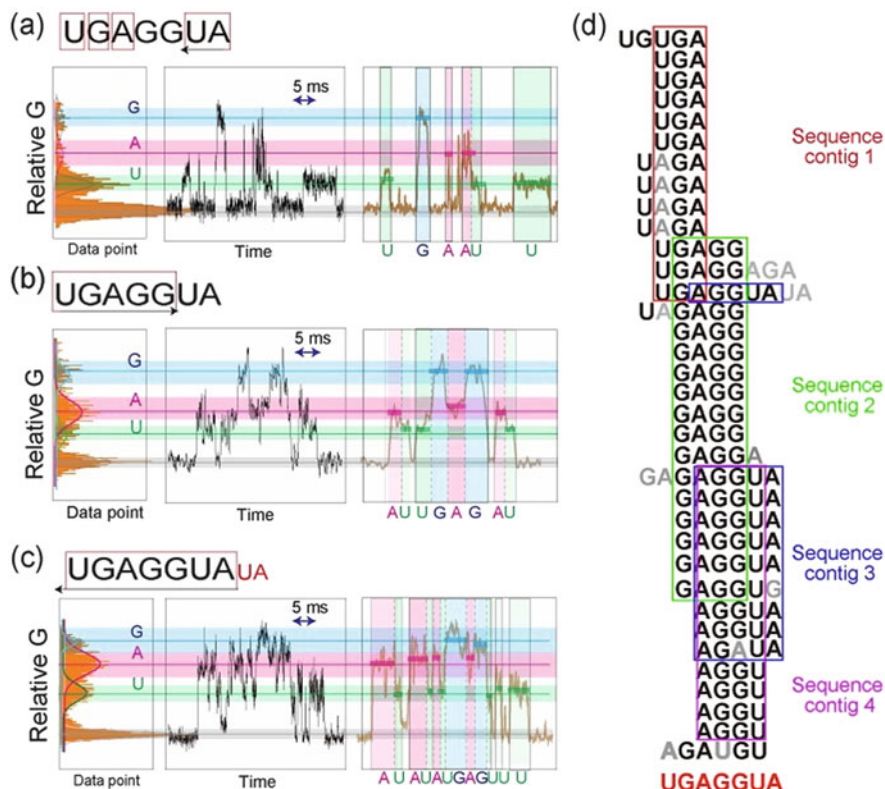


**Fig. 9.10** Relative single-molecule conductance–time profiles of (a) UGA, (b) UGAGG, (c) UGAGGUA, and (d) the 35 fragmented sequences used for resequencing the microRNA of UGAGGUA. Ref. [27]

Single-molecule conductance can be expressed in Eq. 9.1, where electrode–molecule electronic coupling shows a single molecular conformation with respect to nanoelectrodes and their tip structures. Comparing current–time measurements of single-base molecules with single-base molecules in DNA, the degree of freedom in the latter is lower due to restriction of chemical bonds. In fact, the full width at half maximum of single-molecule conductance of single-base molecules for DNA and RNA is lower because the smaller degree of freedom makes variation in electrode–molecule interactions smaller [27].

## 9.8 Peptide Sequencing

Peptides are biomolecules formed by 20 types of amino acids and have many biological functions [36–42]. For example, a peptide formed by 29 amino acids exhibits a hormone action to raise blood sugar levels, whereas another peptide

formed by seven amino acids performs antibacterial action. Based on knowledge of different peptide functions, natural peptides can act as biomarkers of physical conditions and diseases, whereas artificial peptides can be drug discovery targets [37, 38, 41, 43–45].

Sequences of amino acids are very significant to determine peptide functions, although peptides do not perform these functions until one or more amino acids are chemically modified. This chemical modification is called posttranslational modification and enables proteins to exhibit biological functions [46–51]. The phosphorylation of tyrosine is a well-known posttranslational modification that is closely related to cancers and metabolic diseases [46, 51]. Since there are no methods to amplify and directly sequence peptides, preparing peptide samples is time-consuming and expensive. In these cases, single-molecule sequencing technologies are expected to reduce time and cost because sample preparation is not necessary.

As well as all four-base molecules and chemical modified base molecules of DNA and RNA, amino acid molecules and chemical modified amino acid were identified via tunneling currents using the STM tip modified with recognition molecule [52] and MCBJ [28] (Fig. 9.11). In the STM measurements, amino acid molecules are captured via hydrogen bonds formed between amino acids and recognition molecules (Fig. 9.12) [52]. When recognition tunneling currents were measured in buffer solutions of individual amino acid molecules, spikelike signals were observed, similar to the DNA and RNA measurements discussed above. However, recognition tunneling current histograms show exponential decay and the overlaps of the wide range. This is why distinctions between different amino acid molecules are difficult. A machine learning algorithm called support vector machine (SVM) [53–58] was introduced in an effort to overcome this issue. SVM was used to distinguish amino acid molecules into two classes by obtaining large recognition tunneling current–time data of two amino acid molecules and learning from these data parameters. Of course, using SVM to distinguish the signals strongly depends on the signal features of the two chosen amino acid molecules. Two specific signal features (top average amplitude of recognition tunneling currents and Fourier component) of the tunneling current distributions were selected and were able to distinguish glycine (Gly) and methylglycine (mGly) with a probability of  $P = 0.95$ . This is in stark contrast to the probability of  $P = 0.55$  obtained using only recognition tunneling currents [52]. This method was able to identify five amino acids, one chemically modified amino acid, and one pair of enantiomers. In addition, the single-molecule method shows the potential to determine the mix ratio of two amino acid molecules in a solution formed by the two molecules. Because SVM algorithms are binary classifiers in general, the representation of time series data and what feature parameters to select are the key for realizing to identify all 20 amino acid molecules.

The conductance–time profiles of the 20 amino acids are measured using the MCBJ to obtain single-molecule conductivity [28]. Unlike the base molecules of DNA and RNA, there are differences in the molecular size of amino acid molecules. Therefore, single-molecule conductance measurements were performed

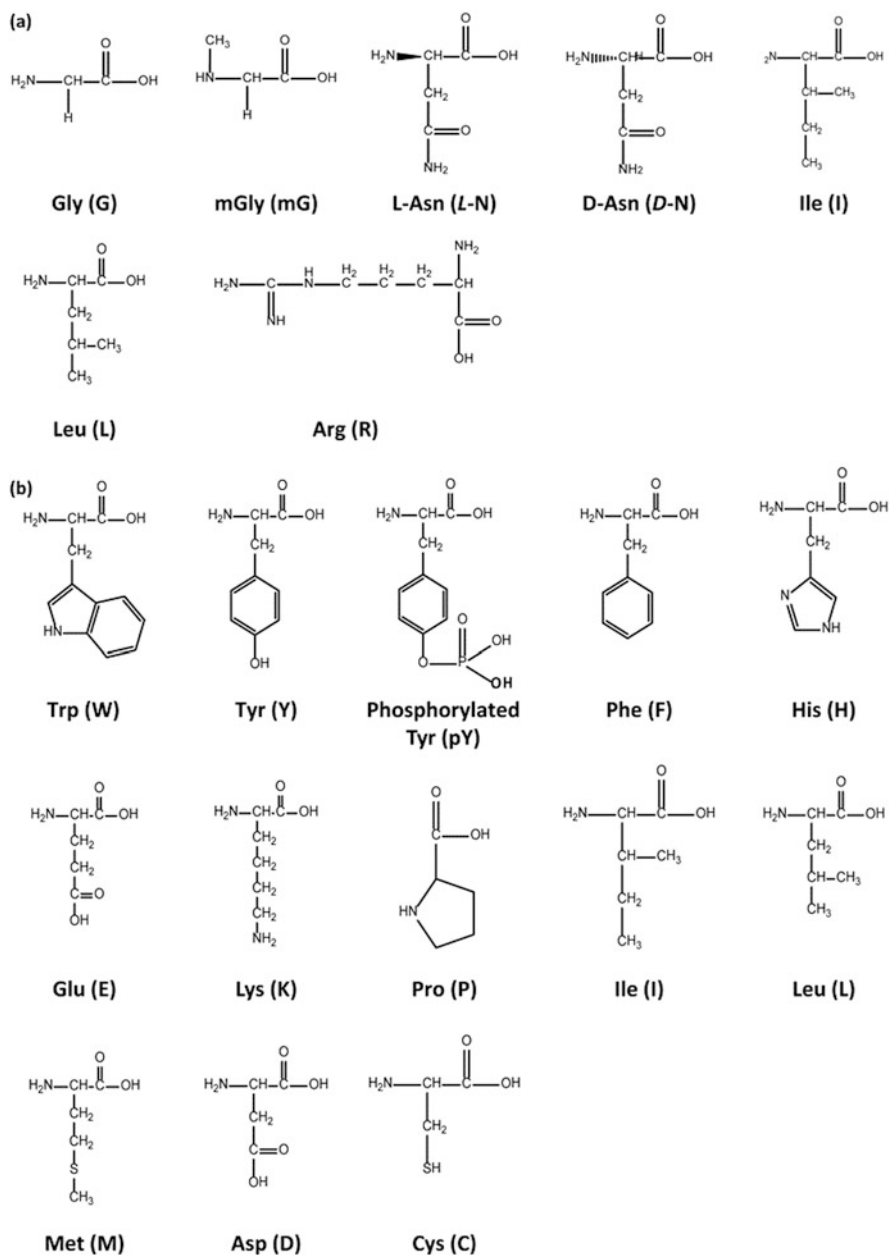


**Fig. 9.11** Amino acids identified via (a) recognition tunneling and (b) tunneling currents

using 0.7- and 0.5-nm-nanogap electrodes. Similar to the base molecules of DNA and RNA, the histograms corresponding to different amino acids show single easily distinguishable peaks. When the 0.7-nm-nanogap electrodes are used, nine

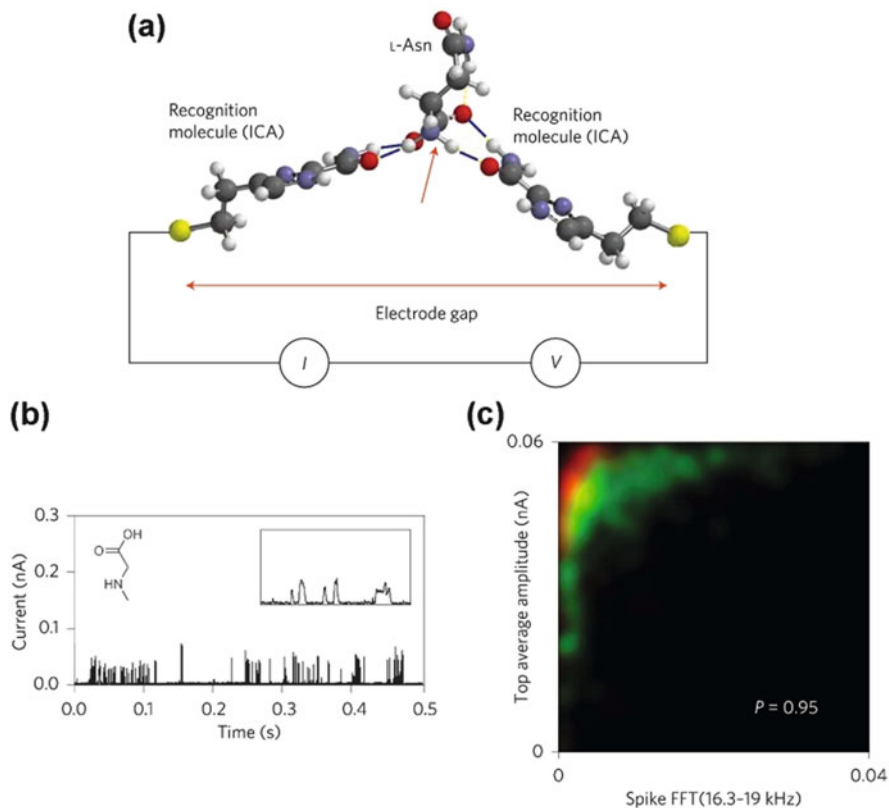


**Fig. 9.12** (a) Schematic of recognition and amino acid molecules, (b) current–time profile of *N*-methylglycine, and (c) two-dimensional plot of probability density as a function of the FFT feature value and top average amplitude (Reprinted with permission from Macmillan Publishers Ltd: ref. [52], copyright 2014)

amino acids can be identified. The nine conductance histograms obtained from conductance–time measurements using the 0.5-nm-nanogap electrodes show single peaks, similar to those observed when using the 0.7-nm-nanogap electrodes. As a result, 12 amino acid molecules could be identified via tunneling currents using the two different nanogap electrodes. Notably, tyrosine and phosphotyrosine could be distinguished by tunneling currents. Estimating the single-molecule conductance order of amino acid molecules using their HOMO energies is difficult because the amino acid molecules are not  $\pi$ -electron systems.

Next, using the 0.7-nm-nanogap electrodes, electrical measurements of the original peptide and the phosphorylated peptide were performed [28]. Based on the single-molecule conductance measurements of individual amino acids and the above analysis method, the three measured peaks were assigned to tyrosine (Y), phenylalanine (F), and phosphotyrosine (pY) (Fig. 9.13a). In this analysis, other

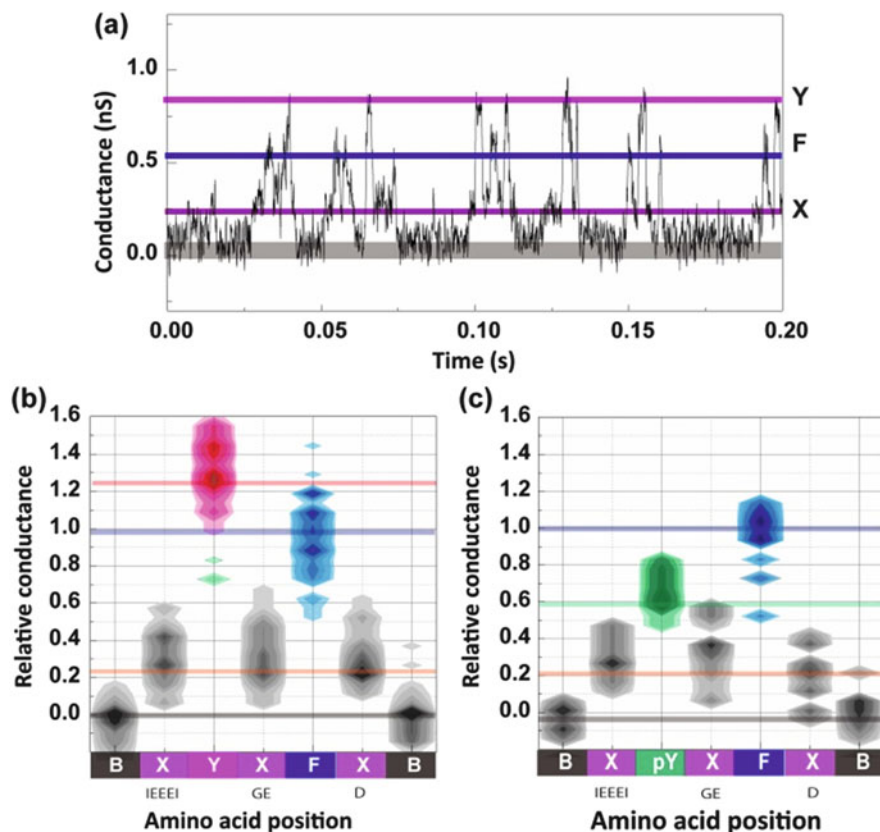


**Fig. 9.13** Conductance–time profile of (a) a peptide, (b) contour map of original peptide, and (c) chemical modified peptide. Ref. [28]

amino acids were assigned to a generic group X. The partial sequence of amino acids that comprises the peptides can be read from their conductance–time profiles. The intensities of the plotted data show the signal numbers as percentages of the total. Based on their conductance intensities, the most likely amino acid sequence can be determined. The left (Fig. 9.13b) and right (Fig. 9.13c) figures correspond to the original peptide and phosphorylated peptide, respectively. These results demonstrate that peptides can be partially sequenced and posttranslational modifications can be detected by conductance profile analysis.

A current–time signal contains information of a fragmented sequence. The original and chemically modified peptides have one tyrosine and phosphotyrosine, respectively. Therefore, the number of electric signals of tyrosine and phosphotyrosine is expected to be the same as in the original and chemically modified peptides in solution. This indicates the possibility of quantitative analysis where sequences of amino acids in peptides and their proportion in a mixture can

be simultaneously determined. When current–time profiles of a solution with a ratio of the original/chemically modified peptide = 1/5 are measured, the ratio of fragmented sequences containing the original and chemically modified peptides is expected to be 1:5. Experimental results obtain a ratio of 1:4.3 [28]. The experimental results confirm that the current–time profile analysis can be used to effectively determine the ratio of original to chemical modified peptides.

## 9.9 Perspective

Tunneling currents can detect small differences in electronic structures of single molecules. Single-molecule electrical sequencing using tunneling currents can identify sequences of base molecules in DNA and RNA and sequences of amino acids in peptides. In addition, unlike existing DNA sequencing techniques, single-molecule sequencing methods can identify base and amino acid molecules, many of which are very important disease markers. Single-molecule sequencing methods may allow us to realize quantitative analysis where sequences of amino acids and the proportion of peptides in a mixture can be determined. This single-molecule quantitative analysis can be applied to DNA and RNA, particularly miRNA.

The development of methods for controlling the speed of single molecules is key for obtaining high accuracy, high throughput, and the length of the sequences that are read [17, 33]. An ideal method is to flow single DNA, RNA, and peptide molecules in one direction at a constant speed. Many research groups are currently working on developing single-molecule speed control technologies [17, 33]; however, technical leaps are required because the hydrodynamics of single molecules in solutions cannot be explained by conventional hydrodynamics.

It is found that information science plays a significant role in distinguishing base and amino acid molecules. Nanoscience and nanotechnology studies based on physics and chemistry require an understanding of the origins of the measurement data, and it is often difficult to completely understand and control the phenomena. For example, large overlaps of distributions of single-molecule conductance appear to be a big barrier for identifying single molecules. However, information science allows us to stochastically identify phenomenon using large data. Hybridization of nanotechnology and information science will lead to remarkable innovations in single-molecule science and technologies.

**Acknowledgment** This work is supported by KAKENHI Grant No. 26220603 for financial support.

## References

1. Levy S et al (2007) *Plos Biol* 5:2113
2. Wheeler DA et al (2008) *Nature* 452:872
3. Manolio TA, Brooks LD, Collins FS (2008) *J Clin Invest* 118:1590
4. Lander ES et al (2001) *Nature* 409:860
5. Feng SH, Jacobsen SE, Reik W (2010) *Science* 330:622
6. Xu X et al (2011) *Nature* 475:189
7. Chen JF et al (2013) *Nat Commun* 4:1595
8. Schloss JA (2008) *Nat Biotechnol* 26:1113
9. Mardis ER (2011) *Nature* 470:198
10. Kircher M, Kelso J (2010) *Bioessays* 32:524
11. Loman NJ, Constantinidou C, Chan JZM, Halachev M, Sergeant M, Penn CW, Robinson ER, Pallen MJ (2012) *Nat Rev Microbiol* 10:599
12. Metzker ML (2010) *Nat Rev Genet* 11:31
13. Holt RA, Jones SJM (2008) *Genome Res* 18:839
14. Rothberg JM et al (2011) *Nature* 475:348
15. Zwolak M, Di Ventra M (2008) *Rev Mod Phys* 80:141
16. Branton D et al (2008) *Nat Biotechnol* 26:1146
17. Venkatesan BM, Bashir R (2011) *Nat Nanotechnol* 6:615
18. Taniguchi M (2015) *Anal Chem* 87:188
19. Dekker C (2007) *Nat Nanotechnol* 2:209
20. Saenger W (1984) *Principles of nucleic acid structure*. Springer, New York
21. Taniguchi M, Kawai T (2006) *Physica E* 33:1
22. Zwolak M, Di Ventra M (2005) *Nano Lett* 5:421
23. Huang S et al (2010) *Nat Nanotechnol* 5:868
24. Chang S, He J, Kibel A, Lee M, Sankey O, Zhang P, Lindsay S (2009) *Nat Nanotechnol* 4:297
25. Chang SA, Huang S, He J, Liang F, Zhang PM, Li SQ, Chen X, Sankey O, Lindsay S (2010) *Nano Lett* 10:1070
26. Tsutsui M, Taniguchi M, Yokota K, Kawai T (2010) *Nat Nanotechnol* 5:286
27. Ohshiro T, Matsubara K, Tsutsui M, Furuhashi M, Taniguchi M, Kawai T (2012) *Sci Rep* 2:501
28. Ohshiro T, Tsutsui M, Yokota K, Furuhashi M, Taniguchi M, Kawai T (2014) *Nat Nanotechnol* 9:835
29. Tsutsui M, Matsubara K, Ohshiro T, Furuhashi M, Taniguchi M, Kawai T (2011) *J Am Chem Soc* 133:9124
30. Krems M, Zwolak M, Pershin YV, Di Ventra M (2009) *Biophys J* 97:1990
31. Lagerqvist J, Zwolak M, Di Ventra M (2006) *Nano Lett* 6:779
32. Lagerqvist J, Zwolak M, Di Ventra M (2007) *Biophys J* 93:2384
33. Yokota K, Tsutsui M, Taniguchi M (2014) *Rsc Adv* 4:15886
34. Durbin R, Eddy S, Krogh A, Mitchison G (1998) *Biological sequence analysis*. Cambridge University Press, Cambridge
35. Kim VN, Han J, Siomi MC (2009) *Nat Rev Mol Cell Biol* 10:126
36. Ganz T (2003) *Nat Rev Immunol* 3:710
37. Zasloff M (2002) *Nature* 415:389
38. Lewis RJ, Garcia ML (2003) *Nat Rev Drug Discov* 2:790
39. Peschel A, Sahl HG (2006) *Nat Rev Microbiol* 4:529
40. Haass C, Selkoe DJ (2007) *Nat Rev Mol Cell Biol* 8:101
41. Hancock REW, Sahl HG (2006) *Nat Biotechnol* 24:1551
42. Brogden KA (2005) *Nat Rev Microbiol* 3:238
43. Hruby VJ (2002) *Nat Rev Drug Discov* 1:847
44. Purcell AW, McCluskey J, Rossjohn J (2007) *Nat Rev Drug Discov* 6:404
45. Fjell CD, Hiss JA, Hancock REW, Schneider G (2012) *Nat Rev Drug Discov* 11:37

46. Mann M, Jensen ON (2003) *Nat Biotechnol* 21:255
47. Bode AM, Dong ZG (2004) *Nat Rev Cancer* 4:793
48. Westermann S, Weber K (2003) *Nat Rev Mol Cell Biol* 4:938
49. Gallego M, Virshup DM (2007) *Nat Rev Mol Cell Biol* 8:139
50. Walsh G, Jefferis R (2006) *Nat Biotechnol* 24:1241
51. Witze ES, Old WM, Resing KA, Ahn NG (2007) *Nat Methods* 4:798
52. Zhao YA et al (2014) *Nat Nanotechnol* 9:466
53. Chang CC, Lin CJ (2011) LIBSVM: a library for support vector machines. *Acm Trans Intell Syst Technol* 2:27
54. Burges CJC (1998) *Data Min Knowl Discov* 2:121
55. Hsu CW, Lin CJ (2002) *IEEE Trans Neural Netw* 13:415
56. Guyon I, Weston J, Barnhill S, Vapnik V (2002) *Mach Learn* 46:389
57. Suykens JAK, Vandewalle J (1999) *Neural Process Lett* 9:293
58. Brown MPS, Grundy WN, Lin D, Cristianini N, Sugnet CW, Furey TS, Ares M, Haussler D (2000) *Proc Natl Acad Sci U S A* 97:262